

# JOHNSON MATTHEY TECHNOLOGY REVIEW

Johnson Matthey's international journal of research  
exploring science and technology in industrial  
applications

Volume 67, Issue 3, July 2023

Published by Johnson Matthey

---

[technology.matthey.com](https://technology.matthey.com)

© Copyright 2023 Johnson Matthey

*Johnson Matthey Technology Review* is published by Johnson Matthey Plc.



This work is licensed under a Creative Commons Attribution 4.0 International (CC BY 4.0) license. You are free to: share: copy and redistribute the material in any medium or format; adapt: remix, transform, and build upon the material for any purpose, even commercially. Under the following terms: attribution: you must give appropriate credit, provide a link to the license, and indicate if changes were made. You may do so in any reasonable manner, but not in any way that suggests the licensor endorses you or your use. No additional restrictions: you may not apply legal terms or technological measures that legally restrict others from doing anything the license permits.

The rights of users under exceptions and limitations, such as fair use and fair dealing, are not affected by the CC licenses.

Johnson Matthey's international journal of research exploring science and technology in industrial applications

## Contents **Volume 67, Issue 3, July 2023**

- 247** Guest Editorial: The Continuing Importance of Platinum Group Metals  
By Emma Schofield
- 249** Advanced Supports for Noble Metal Catalysts in Proton Exchange Membrane Water Electrolysers: A Review  
By Pere L. Cabot, María V. Martínez-Huerta and Francisco Alcaide
- 266** Properties of Additively Manufactured Platinum-Rhodium Alloys  
By Thilo Becker and Thomas Gries
- 278** On the Sustainability of Palladium in Organic Synthesis: A Perspective  
By B. H. Lipshutz
- 285** On the Criticality of Palladium in Organic Synthesis: A Perspective  
By Emma R. Schofield
- 290** Dependence of Mechanical Properties of Platinum-Rhodium Binary Alloys on Valence Electron Parameters  
By Mehrdad Zarinejad, Sajjad Rimaz, Yunxiang Tong, Kiyohide Wada and Farshid Pahlevani
- 300** In the Lab: The Use of Recovered Metal Complexes in Catalysis  
Featuring James Wilton-Ely
- 303** Additive Manufacturing of Platinum Alloys  
By Ulrich E. Klotz and Frank R. König
- 317** Study on Technical Parameters and Suitability of Platinum-Based Metallic Glasses for Jewellery Applications  
By L.-Y. Schmitt, N. Neuber, M. Eisenbart, L. Ciftci, O. Gross, U. E. Klotz and R. Busch
- 333** Moving from Fuel to Feedstock  
By Paul A. Morton and Stephen M. Mansell
- 349** Electrochemical Synthesis of Monodisperse Platinum-Cobalt Nanocrystals  
By Daniel J. Rosen, Duncan Zavanelli and Christopher B. Murray
- 357** "Practical Guidelines for the Chemical Industry: Operation, Processes, and Sustainability in Modern Facilities"  
A book review by Mahmud Juned
- 361** "PGM Market Report May 2023"  
By Alison Cowley
- 364** Advertisement: Johnson Matthey Virtual Platinum Group Metal Conference 2023  
By Emma R. Schofield
- 365** Johnson Matthey Highlights

## Guest Editorial

# The Continuing Importance of Platinum Group Metals

### NON-PEER REVIEWED FEATURE

Received 19th May 2023; Online 8th June 2023

Platinum group metals (pgms) have never been more essential. They are already key contributors to technologies that have global impact: catalytic convertors (platinum, palladium, rhodium) that minimise air pollution; catalysts (platinum, rhodium) to produce nitric acid in fertiliser manufacture, which supports global food production; crucibles (iridium) for making scintillation crystals used in metal scanners and mobile phones; and hard disks (platinum, ruthenium) with enhanced storage capacity.

This special pgm edition of the *Johnson Matthey Technology Review* highlights how some of these long-standing applications are developing. For platinum jewellery, bulk metallic glasses are being investigated for their improved properties compared to cast alloys (1), while the mechanical properties of platinum-rhodium binary alloys and superalloys are being studied based on the impact of the valence electron ratio on metallic bonding (2). Platinum-rhodium alloys are crucial in the production of glass fibres, and here work is presented which investigates additive manufacture as a way to overcome limitations on fabricating equipment (3). The use of additive manufacture is discussed for making platinum-gold alloy jewellery using laser powder bed fusion technology (4).

Catalysis has always been a pivotal application of the platinum group metals, and this special edition features a discussion on progress in C–H activation by rhodium and iridium complexes, a potential future route to making chemical feedstocks from, ideally, sustainably derived hydrocarbons (5). Out of the H2020 Platinum Group Metals Recovery Using Secondary Raw Materials (PLATIRUS) project, novel technologies for improving the recovery of pgms from end-of-life catalysts are

reported, including microwave assisted leaching and gas-diffusion electrocrystallisation (6).

Significant advances have been made in the potential environmental impact of pgm-catalysed processes by carrying out reactions in water instead of organic solvents and decreasing the use of energy and reagents. This is exemplified by a room temperature, aqueous electrochemical route for synthesis of monodisperse platinum-cobalt nanocrystalline catalysts (7) and ground-breaking work reported on aqueous micellar catalysis by palladium in water at ambient temperatures (8).

With particular reference to palladium in organic chemistry, the article by Professor Bruce Lipshutz (8) also raises concerns circulating in the academic community about whether there will be enough palladium to meet future demand in organic synthesis. In reality, Johnson Matthey's pgm market insight indicates that palladium and rhodium will go from their current state of high demand and high price into a surplus position as road transport transitions away from the fossil fuel burning internal combustion engines towards zero tailpipe-emission vehicles (9). As a consequence, in upcoming decades there will be significant opportunities to use palladium and also rhodium in organic chemistry and in a range of new and growing applications.

### Critical Material Constraints

Looking to the future, a mixture of technologies will be needed to achieve the transition to net zero, many of which feature pgms. Critical material constraints (among others) will necessitate that the transport market be shared between lithium- and cobalt-dependent battery electric vehicles, which are best suited for the shorter distances and lower loads of passenger vehicles, and platinum-containing fuel cell vehicles, which have the ability to transport heavier loads over longer



distances with less frequent refuelling. To enable renewable energy (solar power, hydro power, wind power) to be transported from the geographies where they are most plentiful will require iridium- and platinum-based electrolyzers; these generate hydrogen which can then be liquified or captured in a carrier (ammonia or a liquid organic) to be transported cheaply and safely to point of use, significantly easing future demands on electrical infrastructure.

## The Transition to Net Zero

Both mining and recycling are necessary to supply the quantities of pgms demanded by their ever-increasing range of applications, and the high value of pgms means that both continue to be a commercially viable proposition. While miners and refiners of pgm plan to transition their operations to net zero, one way to minimise the environmental impact of processing pgms is to keep using them for as long as possible. Tracking pgms through a closed-loop recycle has been proven to be the most effective way to minimise metal losses resulting from inefficient collection and increase the useful life of pgms. There would be advantage in applying this model to other critical metals as their recycling intensity increases and availability concerns become more urgent.

As this special edition of the *Johnson Matthey Technology Review* illustrates, pgms have an important and unique contribution to make in addressing current global challenges in energy,

food and health and will continue to be essential to the technology portfolio for centuries to come.

EMMA SCHOFIELD

Platinum Group Metal Research Fellow,  
Johnson Matthey, Blounts Court,  
Sonning Common, Reading, RG4 9NH, UK  
Email: [emma.schofield@matthey.com](mailto:emma.schofield@matthey.com)

## References

1. L.-Y. Schmitt, N. Neuber, M. Eisenbart, L. Ciftci, O. Gross, U. E. Klotz and R. Busch, *Johnson Matthey Technol. Rev.*, 2023, **67**, (3), 317
2. M. Zarinejad, S. Rimaz, Y. Tong, K. Wada and F. Pahlevani, *Johnson Matthey Technol. Rev.*, 2023, **67**, (3), 290
3. T. Becker and T. Gries, *Johnson Matthey Technol. Rev.*, 2023, **67**, (3), 266
4. U. E. Klotz and F. R. König, *Johnson Matthey Technol. Rev.*, 2023, **67**, (3), 303
5. P. A. Morton and S. M. Mansell, *Johnson Matthey Technol. Rev.*, 2023, **67**, (3), 333
6. J. Wilton-Ely, *Johnson Matthey Technol. Rev.*, 2023, **67**, (3), 300
7. D. J. Rosen, D. Zavanelli and C. B. Murray, *Johnson Matthey Technol. Rev.*, 2023, **67**, (3), 349
8. B. H. Lipshutz, *Johnson Matthey Technol. Rev.*, 2023, **67**, (3), 278
9. E. R. Schofield, *Johnson Matthey Technol. Rev.*, 2023, **67**, (3), 285

# Advanced Supports for Noble Metal Catalysts in Proton Exchange Membrane Water Electrolysers: A Review

**Improving the performance, stability, durability and cost of iridium- and platinum-based catalytic materials**

## Pere L. Cabot\*

Laboratory of Electrochemistry of Materials and the Environment, Department of Materials Science and Physical Chemistry, Faculty of Chemistry, University of Barcelona, Martí and Franquès 1, 08028 Barcelona, Spain

## María V. Martínez-Huerta

Institute of Catalysis and Petrochemistry, Spanish Council for Scientific Research (CSIC), C/ Marie Curie, 2. Cantoblanco, 28049 Madrid, Spain

## Francisco Alcaide

Laboratory of Electrochemistry of Materials and the Environment, Department of Materials Science and Physical Chemistry, Faculty of Chemistry, University of Barcelona, Martí and Franquès 1, 08028 Barcelona, Spain; CIDETEC, Basque Research and Technology Alliance (BRTA), Paseo Miramón, 196, 20014 San Sebastián, Spain

\*Email: [p.cabot@ub.edu](mailto:p.cabot@ub.edu)

## PEER REVIEWED

Received 29th July 2020; Revised 21st September 2022; Accepted 3rd October 2022; Online 4th October 2022

Renewable and low-carbon hydrogen will contribute to a future climate-neutral economy as a fuel, clean energy carrier and feedstock. One of the main concerns when considering its production

by the present proton exchange membrane water electrolysers (PEMWE) is the use of scarce and expensive noble metals as catalysts for the hydrogen evolution reaction (HER) and oxygen evolution reaction (OER), because they contribute to increase the cost of the technology. Several strategies have been developed to overcome this drawback, such as optimising the catalyst loading in the electrodes and alloying or using alternative catalyst supports, always with the aim to maintain or even increase electrolyser performance and durability. In this review, we examine the latest developments in HER and OER catalysts intended for practical PEMWE systems, which point in the short term to the use of platinum and iridium nanoparticles highly dispersed at low loadings on conductive non-carbon supports.

## 1. Introduction

Renewable energy sources have gained significant attention due to the limited amounts of fossil fuels and their environmental impact. The increasing release of carbon dioxide, nitrogen oxides, heavy metals, ashes, tars and organic compounds from the combustion of fossil fuels to meet global energy demand has led to a rapid increase in pollutants and greenhouse gases in the air (1, 2). Today, concerns about air pollution and climate change drive the search for environmentally friendly, accessible and economically attractive renewable energy sources as alternatives to fossil fuels.

Hydrogen is the 'clean fuel of the future' because water is the only product expected (although residual pollutants can appear depending on the

purity of the fuel and the oxidiser). Pure hydrogen allows clean energy to be obtained (3). However, it is not directly available for use in nature and therefore, it has to be produced (4). The current annual production of hydrogen is about 0.1 billion tonnes, the most part being used for petroleum and metals refining (47%) and ammonia production (45%). A small fraction is applied for electronics fabrication, the food industry and as fuel for transportation (5).

Nikolaidis and Poullikkas (4) have summarised the main advantages and disadvantages of the different methods of hydrogen production. Steam reforming of hydrocarbons is the most developed method, with existing infrastructure and efficiencies in the range 74–85%. Partial oxidation and autothermal steam reforming of hydrocarbons are proven technologies with smaller efficiencies in the range 60–75%. All these methods produce CO<sub>2</sub> as byproduct, depending on the fossil fuel. There are alternative methods using raw materials coming from renewable technologies, namely biomass and water. The pyrolysis of biomass presents efficiencies of 35–50% and is CO<sub>2</sub>-neutral, but its main disadvantages are tar formation and the variable hydrogen content depending on the seasonal availability and impurities of the feedstock. The dark fermentation of biomass also has good efficiencies in the range 60–80% and is CO<sub>2</sub>-neutral, but its major disadvantages are the formation of fatty acids, which are organic pollutants that should be removed, low hydrogen production rates, low yields and the need for large reactor volumes.

Production methods utilising water as the only raw material produce hydrogen through water splitting processes such as electrolysis, thermolysis and photoelectrolysis. Thermolysis of water, with efficiencies in the range 20–45%, is clean and sustainable with oxygen being the only byproduct, but its major disadvantages are the toxicity of the elements used, corrosion problems and the need for high capital investment. Photoelectrolysis of water is also interesting since it is free from emissions and oxygen is the only byproduct, but it requires sunlight, has efficiencies of about 0.06% and suitable photocatalytic materials are needed. Conversely, electrolysis is a proven technology, with existing infrastructures and good efficiencies in the range 40–60%, with only oxygen as byproduct. Although a high capital investment is required and hydrogen produced by this method is still more expensive than that obtained from hydrocarbon

reforming, water electrolysis appears to be an environmentally friendly hydrogen generation process and will be a key technique in the hydrogen economy.

Electrolysis is already a basic technique to provide hydrogen in small quantities for applications such as the food and semiconductor industries (5). Despite this, water electrolysis only contributes about 4% of overall hydrogen production in the world today (5). This may significantly change in the next few decades since solar and wind renewable energy resources are expected to increase, replacing fossil fuels for environmental reasons. If energy production by these methods exceeds the electricity demand, energy storage as hydrogen fuel can be a potential solution (1). This is particularly interesting because renewable resources are intermittent and therefore excess energy in operation can be used in water electrolysis for hydrogen production.

Alkaline electrolysis is the oldest and most mature technique. It uses a thin ceramic porous diaphragm submerged in a liquid alkaline electrolyte (6–8). It is also possible to use anion exchange membrane technology in alkaline water electrolysis. However, this is a long way from commercialisation. In the meantime, water electrolysis using PEMWEs is a recent and very attractive technique from an industrial viewpoint because the PEMWE is a compact device of simple construction and flexible dynamic operation in which a proton exchange membrane (PEM) replaces the liquid electrolyte (9). **Figure 1** shows a schematic of a single cell of a PEMWE (10). The PEM is an acidic solid polymer electrolyte with very good proton conductivity (solid polymer electrolyte in **Figure 1**). Perfluorinated sulfonic-acid (PFSA) PEM membranes such as Nafion® are commonly used (11). The anode and cathode reactions for water electrolysis in acidic media are given by Equations (i) and (ii) for the OER and HER, respectively (3):



The standard (reduction) electrode potentials are 1.23 V and 0.00 V vs. standard hydrogen electrode, respectively, therefore the standard Gibbs energy of the overall Equation (iii) (given by the summation of Equations (i) and (ii)):



is  $\Delta G^0 = -2 \times 96,486 \text{ C mol}_{\text{H}_2\text{O}}^{-1} \times (-1.23 \text{ V}) = 2.37 \times 10^5 \text{ J mol}_{\text{H}_2\text{O}}^{-1} > 0$ , meaning that this process

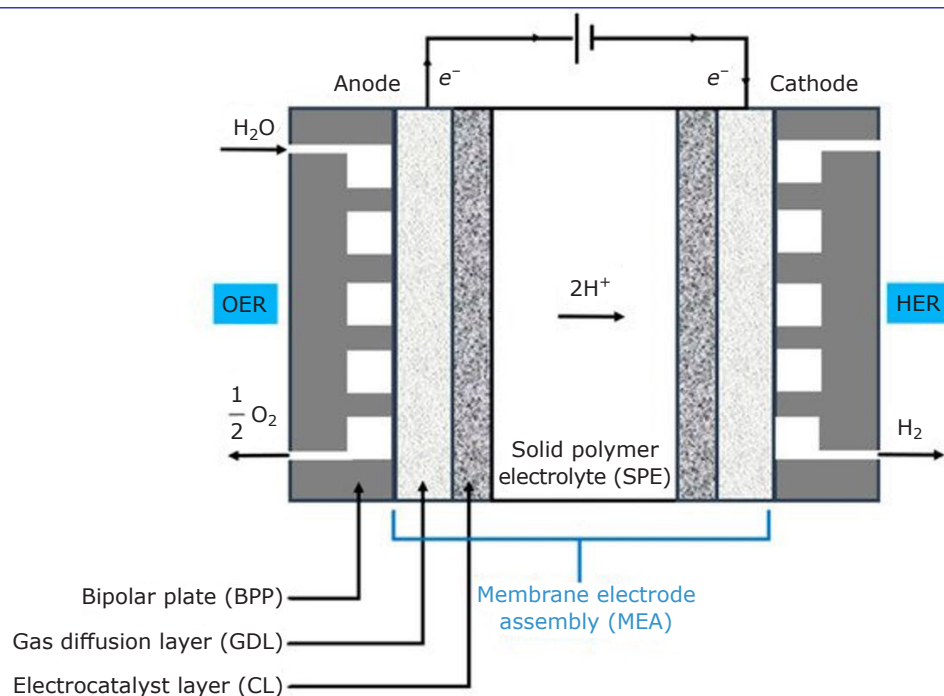


Fig. 1. Scheme of a single cell of a PEMWE. Reproduced from (10) under a Creative Commons CC BY license

requires energy, which can be provided by a power source moving electrons from the anode to the cathode terminals. As shown in **Figure 1**, water is introduced in liquid or vapour form, depending on the temperature, in the anode compartment where Equation (i) takes place. The protons produced through Equation (i) are transported by the electric field through the PEM to the cathode, where they are reduced according to Equation (ii). The acidic solution is retained in the membrane, thus reducing corrosion problems. The PEM must be thin to reduce the ohmic drop, which reduces the voltage needed for water electrolysis. In addition, it is not an electron conductor and behaves as a separator between the anode and the cathode, thus avoiding internal short-circuits. Moreover, it presents good chemical, mechanical and dimensional stability, with low permeability to hydrogen and oxygen. The anode and the cathode catalyst layers or electrocatalyst layers (CLs in **Figure 1**) are placed on each side of the PEM. The gas diffusion layers allow diffusion of reactants through them. The set integrated by the PEM and CLs is known as the membrane electrode assembly (MEA). Note also that the reactants circulate through the gas channels of the bipolar plates (BPPs in **Figure 1**), which allow the complete stack to be built up by means of the electrical connection between the cathode and the anode of adjacent cells.

Although PFSA membranes suffer dehydration over 100°C (11) and there is a consequent thermal limit in its practical use, the PEM offers additional

advantages to the liquid alkaline electrolyte: (a) there are no anionic concentration gradients (as the anionic charges are fixed, fewer species are transported and the complexity of the system is reduced); (b) the gases are evolved at the back of the electrodes and do not contribute to the internal cell resistance, which is mainly due to the PEM (5); and (c) they are free from carbonate formation problems, thus providing highly compressed and pure hydrogen with high efficiency (1).

However, unlike alkaline electrolytes, acidic electrolytes require corrosion-resistant noble metals as electrocatalysts (12). The main components affecting performance and durability of PEMWE stacks are MEAs, in which at present iridium is the electrocatalyst for the OER and platinum for the HER (13–16). Current densities in the range 0.6–2.0 A cm<sup>-2</sup> for applied single cell voltages between 1.8–2.2 V can now be obtained (17). PEMWEs are in the early market introduction phase in the energy sector and the focus is on their durability and reliability rather on their cost (13). A recent estimate is that MEAs represent about 19% of the overall stack cost (18). The PEM itself plays a role because it contributes a significant ohmic loss, increasing with thickness, and must ensure robustness and low hydrogen and oxygen crossover. Nafion® 115 and 117, 120–200 µm in thickness are currently used, typically contributing about 5% of the cost of the PEMWE stack, but there is the possibility of introducing nanoparticles (NPs) or nanofibres in thinner PEMs with lower ionic resistance resulting

in good mechanical stability and low oxygen and hydrogen crossover (14, 15, 19–22).

The MEA is normally fabricated by directly depositing the electrocatalysts onto the PEM or by transferring them onto the PEM by a decal process (23). This latter procedure is known as the catalyst coating membrane approach (24, 25). The OER presents a more sluggish kinetics than the HER, therefore it significantly contributes to the overall polarisation. Iridium metal and IrO<sub>2</sub> are the present state-of-the-art OER catalyst in PEMWEs (12, 14), providing a suitable balance between activity and stability and representing about 8% of the stack cost. With a typical loading of 2 mg<sub>Ir</sub> cm<sup>-2</sup> (23), an amount of about 500 kg of iridium is needed for a gigawatt-plant working at 4 W cm<sup>-2</sup> (14). This is a large amount of iridium considering the annual worldwide production of about 9000 kg year<sup>-1</sup> (2). Therefore, there is a need to reduce the iridium loading while improving the OER performance. The catalyst for the HER is platinum with a loading of about 0.3–0.5 mg cm<sup>-2</sup> (12, 20, 26), contributing about 6% of the MEA cost, although it has been pointed out that this could be significantly reduced without performance loss (25). Other important components of PEMWEs are the bipolar plates and the porous transport layers, which contribute about 68–74% of the overall stack cost. The cell and stack balances account for the remaining percentage (14, 18).

PEMWEs use noble metals because of the advantages mentioned above. After intensive research, new components based on non-noble metals may be possible in the long-term, but in the short-term, there is still room to achieve better performance, durability and cost reduction with iridium and platinum (14). It is estimated that the overall cost could be reduced by about half by using advanced manufacturing techniques, especially for flow fields and separators (18). The catalytic material and catalyst loading are also crucial to obtain suitable performance, durability and cost (14). A good strategy to decrease catalyst cost may be to improve the stability of the support, enabling better dispersion to increase their utilisation.

Feng *et al.* (21) have summarised the degradation mechanisms of PEMWE components. The main problems with the electrocatalysts were dissolution, deactivation and agglomeration together with support passivation which would impede the current flow. This points to promising solutions such as addition of inert oxides, the use of binary or ternary solid-solution catalysts or tailoring the morphology of the catalyst. Recent PEMWE

degradation studies suggested that the measured cell voltage increase was mainly due to reversible changes in the oxidation state of the iridium-based catalyst and that the real degradation took place in the ohmic and mass transport overpotential region at high current densities and long-time operation (13).

In this review, recent approaches to improve performance, stability, durability and cost of iridium- and platinum-based catalytic materials in current use are examined as specific objectives in the short-term development of PEMWEs. Attention is paid to catalyst loading and dispersion onto different supports, especially non-carbonaceous ones, which are particularly important in the anode of the PEMWEs due to the oxidative nature of this environment.

## 2. Supported Catalysts for the Hydrogen Evolution Reaction

As mentioned in the previous section, the most effective electrocatalysts for the HER in practical PEMWE are those based on platinum. However, the high cost and scarcity of platinum are a drawback in the development of PEMWE for large-scale applications. Reducing the amount of platinum is the main strategy to decrease the cathode cost contribution to PEMWEs (25, 27–30). Platinum black has been employed in the cathode of PEMWEs (30), but the platinum loading can be reduced by improving the catalyst dispersion on high specific surface area supports based on carbon or non-carbon materials. A further strategy involves the development of platinum-based alloys.

### 2.1 Platinum-Based Catalysts Supported on Carbon Materials

It is generally accepted that highly dispersed platinum-on-carbon is the benchmark HER catalyst for PEMWEs, the carbon black Vulcan® XC-72 being the most common (15, 19, 22, 23, 25, 26, 29, 31, 32). Carbon-based materials are widely used as electrocatalyst supports because of their large surface area, high electron conductivity and stability. A PEMWE single cell based on Nafion® NR117 containing 0.4 mg<sub>Pt</sub> cm<sup>-2</sup> (40 wt% platinum supported on Vulcan® XC-72) and 2.5 mg cm<sup>-2</sup> of IrO<sub>2</sub> was reported (32) and it showed 1.7 V at 1 A cm<sup>-2</sup> and 90°C. The average voltage degradation rate was *ca.* 35.5 μV h<sup>-1</sup> after 4000 h at these experimental conditions.



Other materials like graphitic nanofibers (GNF) have been proposed as catalyst supports because their textural properties can favour the transport of gases. In particular, the performance of GNF-supported catalysts was found to be better than that of catalysts supported on Vulcan<sup>®</sup> XC-72 (33). A reduced electrolysis cell voltage (1.67 V vs. 1.72 V at 1 A cm<sup>-2</sup> and 90°C) was obtained using Pt/GNF cathodes instead of Pt/XC-72 with the same platinum content (40 wt%).

However, the use of carbon supports for stabilising atomic-scale platinum is challenging because the interaction of the support with platinum atoms must be controlled. Recently, an ultra-low loading of platinum dispersed on single walled carbon nanotubes (SWNTs) (0.19–0.75 at% platinum and a platinum loading of ~114–570 ng<sub>Pt</sub> cm<sup>-2</sup>, respectively) was reported in a three-electrode cell with promising properties in terms of electrocatalytic activity and durability for HER in acidic liquid electrolyte (34). More recently, an electrocatalyst comprising platinum nanowires on SWNTs with ultralow platinum content (340 ng<sub>Pt</sub> cm<sup>-2</sup>) has been used for HER (35). A comparable activity (10 mA cm<sup>-2</sup> at -18 mV vs. reversible hydrogen electrode (RHE)) to that of state-of-the-art Pt/C (10 mA cm<sup>-2</sup> at -16 mV vs. RHE) was reached in acidic aqueous electrolyte. However, it is worth mentioning that HER kinetics cannot be measured accurately in acidic media, because it is limited entirely by hydrogen diffusion (36) which requires suitable gas transport techniques (37). In fact, PEMWE single cell tests recorded at 55°C using Nafion<sup>®</sup> 115 membrane and 0.02 mg cm<sup>-2</sup> of Pt/C or Pt/SWNT at the cathode, while having 3 mg cm<sup>-2</sup> of IrRuO<sub>x</sub> at the anode, revealed similar activity. However, the stability of the electrolyser setup operating the cell at the constant current density of 1 A cm<sup>-2</sup> was better for the MEA containing the Pt/SWNT catalyst.

The hydrogen and oxygen permeation between cathode and anode through the membranes of the PEMWEs has been investigated (38–40) and although oxygen permeation is lower than that of hydrogen, it increased with current density and temperature, as did hydrogen permeation. The oxygen content in the hydrogen product was found to be three to four times greater when using platinum-free instead of platinum cathode catalysts (39). This was explained by the lower activity for the oxygen reduction using the platinum-free catalyst, so that less permeated oxygen was reduced at the cathode of the PEMWE and consequently, the oxygen flow within hydrogen was higher. It has also been

reported that permeated oxygen can be reduced to hydrogen peroxide at the cathode (two-electron reaction), which can be further transformed into hydroxyl radicals, OH<sup>•</sup>, through Fenton's reaction with active metal ion impurities (such as Fe<sup>2+</sup> and Cu<sup>2+</sup>) (40). These radicals produce membrane degradation.

## 2.2 Platinum-Based Catalysts Supported on Non-Carbon Materials

Carbon oxidation of oxygen cathodes has been reported in polymer electrolyte fuel cells (40, 41) and could also be expected in PEMWEs under certain conditions. It is therefore interesting to explore non-carbonaceous supports with high specific surface area. Titania has demonstrated very good chemical resistance and thermal stability (42). Shi *et al.* (43) found that when using a carbon-free Pt/TiO<sub>2</sub> cathode in a PEMWE, the membrane degradation rate was lower compared to a Pt/C cathode. This was explained by the higher rate of hydrogen peroxide generation on the carbon surface of the latter, which led to the formation of OH<sup>•</sup> and OOH<sup>•</sup> radicals responsible for membrane degradation by reaction with residual active ions such as Fe<sup>2+</sup>.

Platinum NPs supported on nitrogen-doped black titania (Pt/N<sub>x</sub>:TiO<sub>2-x</sub>) have been reported to show robust durability and onset potentials for the HER which were somewhat smaller than those of commercial Pt/C catalyst (44). Different platinum catalysts supported on niobium-doped titania nanotubes (TNTs) have been synthesised and tested for the HER in acidic media (45). They showed better electrochemical performance for HER in acidic aqueous solution than those reported in recent literature for synthesised and commercial platinum supported catalysts. These results make Pt/Nb-TNT catalysts, in particular those containing 3 at% niobium, very promising for the HER in PEMWEs.

## 2.3 Platinum-Based Alloy Catalysts

A further way to reduce the platinum loading in the cathode is by developing active platinum-based alloys. An example is a recently developed platinum-iron alloy stabilised with platinum-skin layers supported on carbon black for HER in acidic media (46). The performance and durability of this catalyst were examined in a PEMWE single cell, which incorporated a MEA consisting of Pt<sub>x</sub>AL-PtFe/C (0.20 mg<sub>Pt</sub> cm<sup>-2</sup>) and a conventional anode IrO<sub>2</sub> + platinum black (0.92 mg<sub>Pt+Ir</sub> cm<sup>-2</sup>). The

electrolyte membrane was commercial Nafion® NRE212 (50  $\mu\text{m}$  thick). The initial cell voltage was 1.57 V at 1.0 A  $\text{cm}^{-2}$  and 80°C and presented an average degradation rate of  $\sim 70 \mu\text{V h}^{-1}$  after 1000 h of continuous operation. This relatively high degradation rate at rather moderate operating conditions was mainly due to the anode, since the cathode operated stably with low  $\text{H}_2\text{O}_2$  production (the cathode potential varied only  $\sim 10$  mV during this operating time). The challenge in the case of noble metal-based bimetallic structures is that they may change during the reaction (47).

There is, of course, an alternative way to decrease the cathode platinum loading. Optimising the MEA manufacture would lead to optimal use of the catalyst and, by extension, the cell performance (25). The PEMWE durability at low catalyst loadings is then the issue. Highly active sites may result from synergistic effects between the supporting materials and the electronic properties of the metal when downsizing to single-atom catalysts, as shown in three-electrode cells (47, 48). However, the undesirable tendency to aggregation remains to be solved.

### 3. Catalysts for the Oxygen Evolution Reaction

Even though the electrochemical splitting of water has been known since the 19th century, more knowledge is needed to understand the OER mechanism and to find the ideal catalyst in terms of activity and stability (49). For large-scale production of water electrolyzers, the development of highly active, stable and inexpensive OER catalysts is critical (50).

Due to the sluggish kinetics and the highly oxidative and acidic conditions of the OER, the electrocatalysts used on the anode side must be noble metal-based, mainly iridium and ruthenium, because they show the best performance in terms of activity and stability in the operation conditions (51–53). Considering the industrial importance of PEMWEs, several studies on electrocatalytic properties of iridium- and ruthenium-based catalysts on OER performance in acidic media are discussed in a large body of literature (31, 49, 52–54).

Metallic ruthenium and  $\text{RuO}_2$  are known to be the most active catalysts for the OER in acidic media (51, 55, 56). However, several studies have determined that ruthenium has low stability compared to iridium and other metals, even under

mild operation conditions (53, 57, 58). Danilovic *et al.* (58) used X-ray absorption spectroscopy together with potentiodynamic OER measurements to establish a functional link between activity and stability of monometallic oxides during the OER in acidic media. They found that the most active oxides (gold  $\gg$  platinum  $<$  iridium  $<$  ruthenium  $\gg$  osmium) were, in fact, the least stable (gold  $\gg$  platinum  $>$  iridium  $>$  ruthenium  $\gg$  osmium) materials. Discarding osmium because of its very low stability,  $\text{RuO}_2$  also degrades during OER in acidic media. At potentials higher than 1.4 V, the oxidation of  $\text{RuO}_2$  to non-conductive  $\text{RuO}_4$  is favoured and tends to dissolve rapidly (53, 59). Therefore, this reaction greatly modifies  $\text{RuO}_2$  properties, significantly losing its electrocatalytic activity and stability during extended PEMWE operation (52).

A comparative study carried out during OER using an electrochemical scanning flow cell connected to an inductively coupled plasma mass spectrometer, revealed that  $\text{IrO}_2$  was more stable than  $\text{RuO}_2$ , with a difference in dissolution of *ca.* 30 times under similar conditions (53).  $\text{IrO}_2$  still has outstanding activity and stability and, for this reason, is used as the state-of-the-art catalyst in PEMWE systems (14, 54).

Unfortunately, the loading of iridium in the anode is significantly higher than the noble metal in the cathode due to the sluggish OER kinetics and stability issue. Moreover, iridium is extremely rare and expensive. For relatively small systems (kilowatt range), the iridium and platinum catalysts comprise about 5–10% of the stack cost (60). The catalyst cost is expected to increase for larger systems (megawatt range), whereas the cost of the other stack components will be lower (61). Therefore, reducing the loading of precious metals, while maintaining higher activity and optimal stability, is critical to enable large-scale implementation of PEMWEs. For the anode, several strategies are currently pursued, such as reducing the particle size and assuring uniform distribution over a conductive support to make all nanoparticles electrochemically accessible. When the particle size is reduced (for a given catalyst loading), the effective surface area is increased and thus, more active sites for the OER are formed (62, 63).

#### 3.1 Iridium-Based Core-Shell Catalysts

In a similar way to platinum, the combination of  $\text{IrO}_2$  with other metals in core-shell structures allows

less iridium to be used and, in addition, can display a superior OER activity. Tackett *et al.* (64) described FeN<sub>3</sub> core-IrO<sub>2</sub> shell structures with superior OER activity in which the nitride was protected from the acidic media by the shell. The activity increase was related to electronic effects of the substrate-surface interaction. Nong *et al.* (65) prepared an electrochemically dealloyed IrNi core-IrO<sub>x</sub> shell combined with a mesoporous corrosion-resistant antimony-doped tin oxide support (antimony-tin oxide (ATO)), which behaved as highly efficient and stable OER catalysts in acidic medium. The higher OER activity on both geometric surface and iridium-mass basis compared to the IrO<sub>x</sub>/C and IrO<sub>x</sub>/ATO benchmarks was explained by electronic and strain effects, which could modify the chemisorption and reactivity of intermediates at the surface. More recently, Jiang *et al.* (66) electrodeposited thin iridium films (~68 nm thick) on WO<sub>x</sub> nanorods, thus allowing a uniform iridium dispersion on the poorly conducting WO<sub>x</sub> and the use of a low loading of the precious metal. Current densities of 2.2 A cm<sup>-2</sup> were obtained at 2.0 V in a laboratory PEMWE with improved stability over 1000 h at 0.5 A cm<sup>-2</sup> for a reduced loading of 0.14 mg<sub>Ir</sub> cm<sup>-2</sup>, which was assigned to the stability of WO<sub>x</sub> and the fixed iridium coating.

### 3.2 Iridium-Based Catalysts with Metal Oxides

IrO<sub>2</sub> can also be mixed with different metal oxides to create electrocatalysts with improved activity and stability for the OER such as Ru<sub>x</sub>Ir<sub>1-x</sub>O<sub>2</sub> (59), Ru<sub>60</sub>Pt<sub>30</sub>Ir<sub>10</sub> (67), Ir<sub>0.7</sub>Ru<sub>0.3</sub>O<sub>x</sub> (68–70) and Ir<sub>0.40</sub>Sn<sub>0.30</sub>Nb<sub>0.30</sub>O<sub>2</sub> (71). Computational studies have revealed that the superiority of these mixed metal oxides is due to the stable formation of the intermediates involved in the OER mechanism (72–75). Tang *et al.* (76) found that by switching the host structure of the Ir<sup>4+</sup> oxygen-coordination octahedra from corner- and edge-sharing rutile (IrO<sub>2</sub>) to purely corner-sharing perovskite (SrIrO<sub>3</sub>), the OER activity increased by more than one order of magnitude. Density functional theory calculations revealed that the adsorption energetics on SrIrO<sub>3</sub> depended sensitively on the electron-electron interaction, whereas for IrO<sub>2</sub>, it depended rather weakly. Yang *et al.* (77) reported high-activity face-sharing perovskite structures. Despite that the 6H-SrIrO<sub>3</sub> perovskite contained 27.1 wt% less iridium than IrO<sub>2</sub>, its iridium mass activity was seven times greater than the latter due to the existence of face-sharing IrO<sub>6</sub> octahedral

dimers, which facilitated the OER rate determining step by weakening the iridium-oxygen binding.

Another promising solution to decrease the iridium amount is the use of one-dimensional nanoarray electrodes, which shows promise in high catalyst utilisation and enhanced electron and mass transfer (78–80). Zhao *et al.* (80) prepared IrO<sub>x</sub> nanotube arrays by electrodepositing IrO<sub>2</sub> NPs onto ZnO nanorod surfaces to produce IrO<sub>2</sub>-coated core-shell nanorod arrays, followed by wet chemical etching the ZnO nanorods away. The IrO<sub>x</sub> nanotube arrays showed 2.7 times higher turnover frequency (TOF) than that of commercial IrO<sub>2</sub> NPs in the OER. Lu *et al.* (78) prepared vertically aligned IrO<sub>x</sub> nanoarrays by electrodeposition using titania nanotube arrays as templates. IrO<sub>x</sub> open-end nanotube arrays with tunable length range were obtained by modulating the scan rate in the electrodeposition process. IrO<sub>x</sub> nanoarrays performed almost the same OER current density with one twentieth iridium loading amount compared with commercial IrO<sub>2</sub> NPs.

### 3.3 Iridium-Based Nanostructured Thin Film Catalysts

Another strategy to improve the electrochemically active surface area was the preparation of iridium-based nanostructured thin film (NSTF) electrodes, developed by 3M, USA, which are less sensitive to agglomeration and corrosion due to the special catalyst morphology (21, 81–83). The NSTF catalysts were obtained by physical vapour deposition (PVD) of catalysts onto a supported monolayer of oriented crystalline organic-pigment whiskers. Whiskers are corrosion resistant, therefore eliminating the high voltage corrosion affecting most carbon supports (31). Lewinski *et al.* (81) prepared an ultra-thin continuous film of iridium deposited on arrays of organic nanowhiskers (PR149). NSTF was shown to be able to operate at 0.25 mg<sub>Ir</sub> cm<sup>-2</sup> and attain high current densities of 10 A cm<sup>-2</sup> at ~2 V at 80°C.

More recently, Jensen *et al.* (83) reported the use of a modified PVD technique to prepare interconnected nanoporous thin films by selective leaching of heterogeneous Ir-Co templates formed by an alternating magnetron sputtering process. This approach allowed the preparation of extended surface area catalysts with higher porosity and iridium dispersion, while maintaining high intrinsic activities. Mirshekari *et al.* (84) used reactive spray deposition technology, a flame-based process in which catalyst nanoparticles are synthesised by combusting solutions of metal-organic precursors



in combustible solvents, to fabricate MEAs with very small amounts of catalyst. Anode and cathode contained only  $0.3 \text{ mg}_{\text{Ir}} \text{ cm}^{-2}$  (in the form of Ir/IrO<sub>x</sub> NPs) and  $0.2 \text{ mg}_{\text{Pt}} \text{ cm}^{-2}$  (platinum NPs on Vulcan XC-72R), respectively. With the purpose of reducing the hydrogen crossover, the MEA contained a thin platinum recombination layer (RL) 100–200 nm in thickness ( $0.025 \text{ mg}_{\text{Pt}} \text{ cm}^{-2}$ ) between the Nafion® 211 and the Nafion® 117 membranes of the anode and cathode, respectively. The cell operated for 3000 h at 50°C with  $1.8 \text{ A cm}^{-2}$  with no significant losses in performance.

### 3.4 Iridium-Based Catalysts Supported on Conductive Materials

One of the most remarkable ways to achieve highly active electrode with low loading amount of iridium content is the use of conductive supports (67, 85–88). It has been shown that supports are important not only to increase the active surface area of the catalysts, but also to integrate the catalyst-support feature or to improve the charge transfer efficiency between them (89). Stability under the harsh conditions of the cell is one of the main requirements that catalyst supports should meet.

Conductive supports based on carbon materials are routinely used in fuel cell technology. However, under the high potential of the OER, most carbons are easily corroded. Better results were obtained using advanced carbon supports such as carbon nanobowls (90) and nanotubes (91). The stability and activity of iridium nanocrystals supported on carbon nanobowls during the OER at  $10 \text{ mA cm}^{-2}$  in 0.1 M HClO<sub>4</sub> significantly outperformed that of commercial Ir/C (80). IrO<sub>2</sub> supported on carbon nanotubes also exhibited similar stability during the OER at the same current density in 0.1 M H<sub>2</sub>SO<sub>4</sub> (88).

### 3.5 Iridium-Based Catalysts Supported on Metal Oxides

Alternatively, oxide-based supports such as titania (89, 92–94), Ti<sub>4</sub>O<sub>7</sub> Magneli phases (70, 95–98) and doped tin oxide (60, 85, 87, 99–101) have been proposed.

#### 3.5.1 Titania-Based Supports

Titania supports offer low cost, very high thermal and chemical stability under anode conditions and commercial availability. However, titania suffers

low electric conductivity (about  $10^{-6} \text{ S cm}^{-1}$  at  $T < 200^\circ\text{C}$ ) and low adsorption/desorption capability toward the species and charge in the OER (31, 102–104). Fuentes *et al.* (92) developed IrRu(1:1) electrocatalysts supported on anatase titania with high activity towards the OER, which showed a 53% higher current per gram of metal than that of unsupported electrocatalyst of the same composition. The higher catalyst utilisation of supported electrocatalysts for the OER was consistent with small, well-dispersed nanoparticles. Mazúr *et al.* (102) prepared IrO<sub>2</sub> NPs (60 wt%) supported on commercial titania powders, with specific surface areas from  $10 \text{ m}^2 \text{ g}^{-1}$  to  $90 \text{ m}^2 \text{ g}^{-1}$ . They found that the lower the specific surface area of the support the higher was the electrochemical activity of the catalyst. This was explained by the formation of a thin layer of more conductive IrO<sub>2</sub> on the surface of the non-conductive titania, which was able to cover the support with low specific surface area, thus providing the entire material with enough electron conductivity. Rozain *et al.* (105) synthesised IrO<sub>2</sub> catalysts on micro-sized titanium particles (50 wt% titanium), showing that for IrO<sub>2</sub> loadings less than  $0.5 \text{ mg}_{\text{IrO}_2} \text{ cm}^{-2}$ , the performance of the PEMWE was better than that prepared with unsupported IrO<sub>2</sub>.

Assuming that titanium was oxidised to TiO<sub>2</sub> during the OER, Bernt *et al.* studied the influence of the ionomer content (24) and of the iridium loading (25) on the performance of a PEMWE using IrO<sub>2</sub>/TiO<sub>2</sub> (75 wt% iridium) as the anode electrocatalyst. The best performance was found for 11.6 wt% of the ionomer (24). The performance losses below and over this value were ascribed to a higher proton conduction resistance and to an oxygen higher mass transport resistance, respectively. The iridium loading was varied between  $0.20\text{--}5.41 \text{ mg}_{\text{Ir}} \text{ cm}^{-2}$ . The optimal performance at operational current densities ( $\geq 1 \text{ A cm}^{-2}$ ) was for  $1\text{--}2 \text{ mg}_{\text{Ir}} \text{ cm}^{-2}$ . The CL became very thin and inhomogeneous when its loading was reduced to  $<0.5 \text{ mg}_{\text{Ir}} \text{ cm}^{-2}$ , resulting in a much higher performance loss than expected based simply on the OER kinetics losses (54). This is illustrated in **Figure 2(a)**, where a scanning electron microscopy (SEM) image of the MEA section is shown. On the anode side, there is a porous transport layer (PTL) made of sintered titanium, which facilitates water transport to the CL, composed of IrO<sub>2</sub>/TiO<sub>2</sub> and ionomer. Separated by the Nafion® 212 membrane is the cathode, made of 4.8 wt% Pt/C and ionomer, covered by a carbon paper PTL. The thickness of the iridium-based CL depends on the iridium load, as shown in

**Figure 2(b)**, which shows a couple of examples in the insets. **Figures 3(a)** and **3(b)** depict the cross-sectional and top views in the case of a low iridium loading. **Figures 3(c)** and **3(d)** show schemes of the electrical connections in the case of thick and thin anode CLs, whereas in **Figure 3(e)**, the titanium PTLs have been replaced by a carbon PTL with a microporous layer.

Cheng *et al.* (106) synthesised a composite  $\text{IrO}_x\text{-TiO}_2\text{-Ti}$  catalyst with mixed valence iridium species. It was shown that titania was beneficial for the formation of Ir(III) and mixed Ir(III/IV) oxyhydroxides, resulting in a high surface concentration of adsorbed hydroxyl and controllable iridium valence, thus explaining its high OER activity.

Additional durability studies were performed with titania-supported  $\text{IrO}_2$  (Elyst Ir75 0480 from Umicore, Belgium) with an iridium loading of  $2\text{mg}_{\text{Ir}}\text{cm}^{-2}$  (107). It was observed that the performance of the MEA electrolyser decreased after cycling the anode potential between  $\sim 0\text{ V}_{\text{RHE}}$  in the open

circuit voltage-periods and high potentials when current was applied to the electrolyser. This degradation was due to the formation of the less conductive hydrous  $\text{Ir}(\text{OH})_x$  phase and the gradual passivation of the titanium porous transport layer (titanium-PTL), which increased the internal ohmic resistance.

The conductivity of titania could be significantly improved by doping with donor species such as metal ions. The group of Hong and Lv extensively studied the effect of doping the titania support for  $\text{IrO}_2$  with vanadium (108), niobium (109, 110), tantalum (111) and tungsten (112) on the physical properties and OER activity of the catalysts. They obtained highly active  $\text{IrO}_2$  supported on mesoporous niobium (20 at%)-doped titania with specific surface area of  $132\text{ m}^2\text{ g}^{-1}$  by means of the modified evaporation-induced self-assembly method (109). The authors found that the majority of the OER activity increase was due to the niobium-doping, which enhanced the specific surface area and surface activity of charge and species transfer.

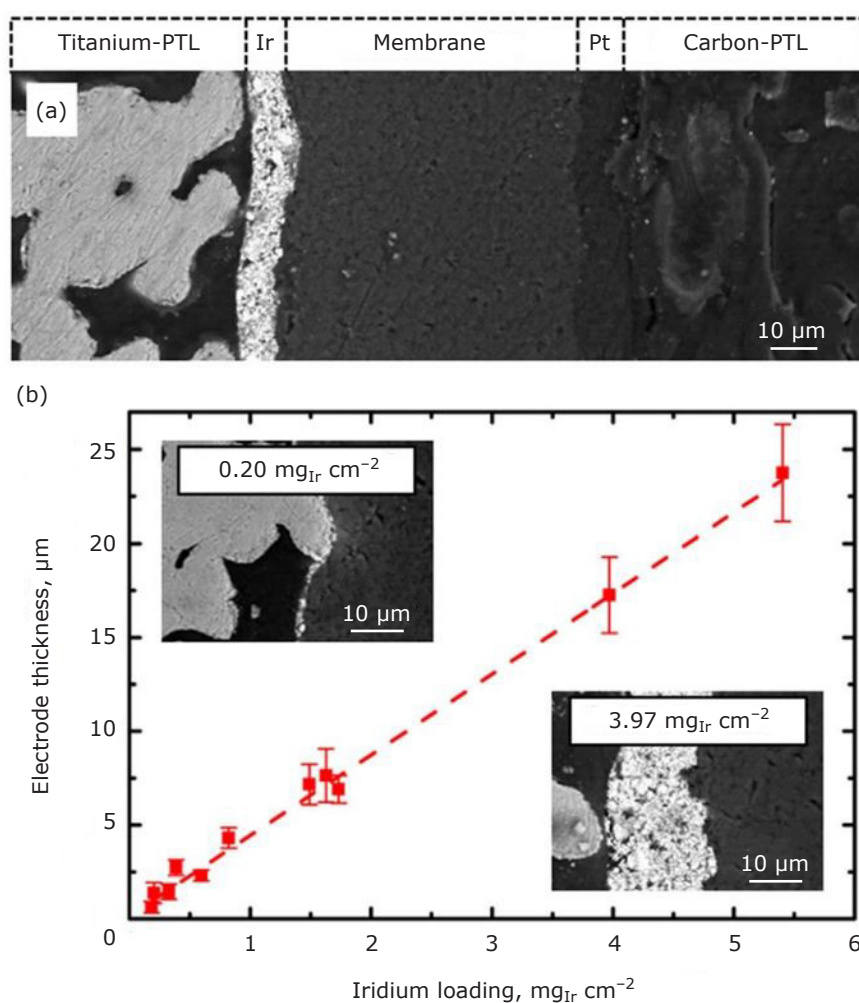


Fig. 2. (a) SEM image of the cross-section of a MEA showing an  $\text{IrO}_2/\text{TiO}_2 + \text{ionomer}$  anode CL and a Pt/C + ionomer cathode CL, separated by a Nafion® 212 membrane. The anode and the cathode PTLs were made of titanium and carbon paper, respectively; (b) anode thickness as a function of the iridium loading, with two SEM cross-sectional pictures for different thicknesses as insets. Reproduced from (25) under Creative Commons Attribution 4.0 License (CC BY)

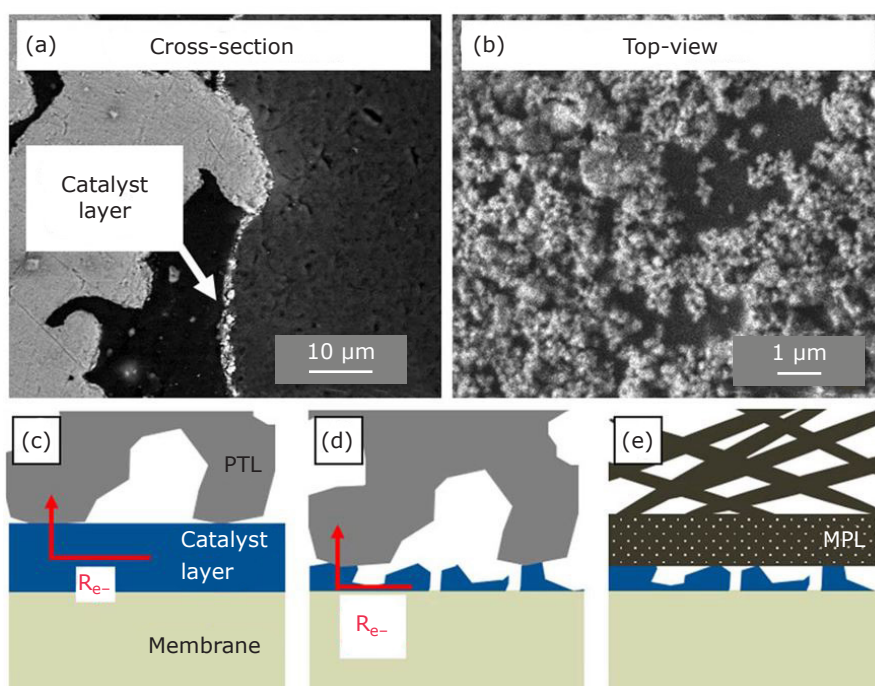


Fig. 3. (a) Cross section; and (b) top-view SEM images of thin iridium-based CLs. The schemes illustrating the electronic transport between the titanium PTLs and the CLs are shown in: (c) for thick; and (d) thin CLs. In (e), the titanium-based PTLs have been replaced by a carbon PTL with a MPL. Reproduced from (25) under Creative Commons Attribution 4.0 License (CC BY)

Subsequent treatment of niobium-doped titania with hydrogen resulted in higher electrical conductivity, increased surface active sites and enhanced OER performance (110). Single cell tests showed that the catalyst treated in hydrogen at 750°C led to the optimum OER activity (1.832 V at 1 A cm<sup>-2</sup>), which was superior to that of unsupported IrO<sub>2</sub> (1.858 V at 1 A cm<sup>-2</sup>) and remained stable for 100 h operating at a current density of 1 A cm<sup>-2</sup>.

They also studied the effect of vanadium doping of the titania support, synthesised by a modified evaporation-induced self-assembly technique (108). IrO<sub>2</sub> supported on titania samples doped with different amounts of vanadium (0 at%, 10 at%, 20 at% and 30 at%) were evaluated. In a single cell, the OER performance gradually increased with vanadium dopant from 0 at% to 20 at%, followed by a performance deterioration with vanadium amount reaching 30 at% due to the corrodible V<sub>2</sub>O<sub>5</sub> precipitate. Recently, the incorporation of tungsten to obtain IrO<sub>2</sub>/Ti<sub>1-x</sub>W<sub>x</sub>O<sub>2</sub> (x = 0.05, 0.1 and 0.2), resulted in an active electrocatalyst for the OER. Of all the Ti<sub>1-x</sub>W<sub>x</sub>O<sub>2</sub> supports, the highest electrocatalytic activity was obtained with Ti<sub>0.9</sub>W<sub>0.1</sub>O<sub>2</sub>. With optimised IrO<sub>2</sub> loading, the applied potential in a single water electrolysis cell was 1.79 V to obtain 1 A cm<sup>-2</sup> at 80°C. Durability tests for 40IrO<sub>2</sub>/Ti<sub>0.9</sub>W<sub>0.1</sub>O<sub>2</sub> at 0.5 A cm<sup>-2</sup> and 1 A cm<sup>-2</sup> indicated that the cell voltages were stable over 100 h.

Hu *et al.* (113) synthesised IrO<sub>2</sub> dispersed on a corrosion-resistant Nb<sub>0.05</sub>Ti<sub>0.95</sub>O<sub>2</sub> support

(83 m<sup>2</sup> g<sup>-1</sup>) by the sol-gel method. The IrO<sub>2</sub> loading of 26 wt% exhibited the best mass normalised OER activity, which was explained by uniform support of the IrO<sub>2</sub> NPs on the surface, thus providing conductive channels to reduce the grain boundary resistance. Recently, Alcaide *et al.* (89) prepared IrO<sub>2</sub> and IrRuO<sub>x</sub> (50 wt%) supported on titania nanotubes and niobium-doped titania nanotubes (3 at% niobium). They observed that niobium doping of titania significantly increased the surface area of the support from 145 m<sup>2</sup> g<sup>-1</sup> to 260 m<sup>2</sup> g<sup>-1</sup>. The highest OER performance of IrO<sub>2</sub>/Nb-TiO<sub>2</sub> nanotubes was assigned to the good dispersion and accessibility of the IrO<sub>2</sub> NPs, the high specific surface area of the support and the electron donor properties of the Nb<sup>4+</sup> species to the conduction band of titania. The stability with the Nb-TiO<sub>2</sub> nanotubes was also better than that of unsupported IrO<sub>2</sub>.

### 3.5.2 Ti<sub>n</sub>O<sub>2n-1</sub>-Based Supports

Non-stoichiometric titanium sub-oxides, TiO<sub>2-x</sub>, have drawn considerable attention due to their high electronic conductivity. In particular, the titanium sub-oxides Magneli phases, Ti<sub>n</sub>O<sub>2n-1</sub>, such as Ti<sub>5</sub>O<sub>9</sub> and Ti<sub>4</sub>O<sub>7</sub> or a mixture, which are known by the commercial name Ebonex<sup>®</sup>, are highly conductive and corrosion resistant in acidic media during the OER (95, 96). Metallic iridium NPs supported on Ti<sub>4</sub>O<sub>7</sub> were synthesised by Wang *et al.* (86) *via* a conventional sodium borohydride reduction method in anhydrous ethanol at room temperature.

The catalyst exhibited improved OER kinetics in acidic media and higher TOF compared to iridium-black. A study comparing IrO<sub>2</sub> electrocatalysts supported on commercial Ebonex<sup>®</sup> and titanium-suboxides (Ti<sub>n</sub>O<sub>2n-1</sub>) prepared in-house was carried out by Siracusano *et al.* (114). The results showed expected electronic conductivity for both electrocatalysts and superior OER activity of the catalyst based on titanium-suboxides prepared in-house compared to the commercial support. These results were attributed to better dispersion and larger occurrence of active catalytic sites on the surface of the suboxide prepared in-house.

### 3.5.3 Antimony-Tin Oxide-Based Supports

ATO has been considered as an alternative support material for OER catalysts because it exhibits relatively high electrical conductivity and corrosion resistance. Some dissolution of the dopant has been reported during the OER at high anodic potentials in sulfuric acid. However, it withstands anodic conditions better than indium-doped tin oxide, known as indium-tin oxide (ITO) (101). Liu *et al.* (115) synthesised antimony-tin oxide nanowires (nw) as supporting materials for IrO<sub>2</sub> NPs which exhibited significant improvement in mass activity when compared to the same catalyst supported on antimony-tin oxide NPs and pure IrO<sub>2</sub>. The OER performance was further confirmed by PEMWE tests at 80°C; the IrO<sub>2</sub>/ATO-nw catalyst reached 2 A cm<sup>-2</sup> at 1.62 V vs. RHE (80°C) with an activity loss of 0.76 mV h<sup>-1</sup> after 646 h at 0.45 A cm<sup>-2</sup>.

Wang *et al.* (116) found that IrO<sub>2</sub> supported on ATO aerogels allowed the use of noble metal to be reduced while keeping the same OER current per unit geometric surface area. Furthermore, the highly porous structure of SnO<sub>2</sub>:Sb aerogel was successfully retained by using vanadium additives under atmospheric drying. However, vanadium did not play an active role in OER catalysis. Similarly, iridium NPs supported on SnO<sub>2</sub>:Sb aerogel allowed the use of precious metal to be decreased by more than 70% while enhancing the electrocatalytic activity and stability (60). *Operando* near-ambient pressure X-ray photoelectron spectroscopy on MEAs revealed a low degree of iridium oxidation, attributed to the oxygen spill-over from iridium to SnO<sub>2</sub>:Sb where the formation of highly unstable Ir<sup>3+</sup> species was mitigated.

A comprehensive overview of the stability and degradation of catalysts during the OER in acidic

media was given by Spöri *et al.* (117). They established that the degree of metal immobilisation on the support depends on the interface between the support surface (groups) and the metal oxide and influences the extent of particle detachment or dissolution during the OER process. These interactions can range from weak electrostatic attraction to stronger connections through surface chemical bonds or formation of an overlayer on the support, which can also affect the activity by decreasing or increasing electron density to the catalyst surface. More recently, several reviews address electrocatalyst performance in terms of activity, stability and efficiency (17, 118, 119). Kim *et al.* (17) have reviewed the latest advances in iridium-based, ruthenium-based and even non-noble metal-based multimetallic electrocatalysts for the OER in acidic media, with emphasis on their stability and reference to machine learning models. Wang *et al.* (118) have summarised the OER performance of selected catalysts in acidic and alkaline media. Also related to this point, an in-depth literature review of the OER mechanism, with special emphasis on the adsorption and lattice oxygen evolution mechanisms to elucidate the catalyst degradation, has recently been published by Chen *et al.* (119).

## 4. Performance of Selected Proton Exchange Membrane Water Electrolysers

**Table I** shows the performance of selected PEMWE single cells in recent years, generally at 80°C, including catalyst loading, operating conditions, type of membrane and degradation rate, which have been discussed in this paper. In this review, we have seen many different anodic and cathodic catalysts which have been studied in three-electrode cells and in laboratory PEMWEs. Note that the latter have been generally tested using platinum supported on carbon cathodes and different PEMs, also applying different voltages, resulting in different current densities. It is therefore not easy to extract the best PEMWEs, since changing the anode, the cathode, the membrane, the temperature, the cell voltage or catalyst loadings can lead to significant changes in the cell performance. Optimisation of all these parameters should be performed. However, promising results can be ascertained.

General trends can be observed: (a) current densities and cell voltages are similar, but the most recent papers use less iridium at the anode due to better dispersion of the precious metal, either

**Table I Performance Data of Selected PEMWE Single Cells Made with Different Components Under the Indicated Conditions from 2009 to 2021**

Catalyst	Anode		Cathode		Operating conditions			Membrane	Degradation rate	Ref.
	Loading, mg cm <sup>-2</sup>		Catalyst		Loading, mg cm <sup>-2</sup>	Voltage, V	Current density, A cm <sup>-2</sup>			
<b>Ir/IrO<sub>x</sub></b>	0.3		Pt/C		0.2	2.09	1.8	50	Nafion <sup>®</sup> 211/Pt RL/ Nafion <sup>®</sup> 117	24 μV h <sup>-1</sup> , 1.8 A cm <sup>-2</sup> , 3000 h (84)
<b>Ir@WO<sub>x</sub></b>	0.14		70 wt% Pt/C		0.4	2.0	2.2	80	Nafion <sup>®</sup> 115	49.7 μV h <sup>-1</sup> , 0.5 A cm <sup>-2</sup> , 1030 h (66)
<b>IrO<sub>2</sub></b>	1.40		60 wt% Pt/C		0.50	1.80	2.0	80	Nafion <sup>®</sup> D520	N/A (15)
<b>IrO<sub>2</sub></b>	0.90		55.5–58.5 wt% Pt/C		0.25	1.80	3.6	80	Nafion <sup>®</sup> 212	N/A (26)
<b>RuO<sub>2</sub></b>	3.0		30 wt% Pd/B <sub>3</sub> -CNPs		0.70	1.86	0.50	80	Nafion <sup>®</sup> 115	2.04 V, 500 h, 1 A cm <sup>-2</sup> (29)
<b>Ir<sub>0.7</sub>Ru<sub>0.3</sub>O<sub>x</sub></b>	0.40		40 wt% Pt/C		0.10	1.82	3.0	80	Aquivion <sup>®</sup> membrane (E98-09S)	90 μV h <sup>-1</sup> , 800 h (69)
<b>Ir/SnO<sub>2</sub>:Sb</b>	0.50 (Ir)		40 wt% Pt/C		1.0	N/A	N/A	N/A	Aquivion <sup>®</sup> membrane (E87-05S)	N/A (60)
<b>IrO<sub>2</sub></b>	1.40		60 wt% Pt/C		0.50	1.80	1.1	80	Nafion <sup>®</sup> 117	200 h, 2 A cm <sup>-2</sup> (22)
<b>IrO<sub>2</sub>/Sb-SnO<sub>2</sub> (7/3)</b>	0.50		40 wt% Pt/C		5.00	1.70	~1.3	80	Nafion <sup>®</sup> 211	N/A (100)
<b>IrO<sub>2</sub> + Pt black (1:1)</b>	0.92		Pt <sub>x</sub> AL-PtFe/C		0.20	1.57	1.0	80	Nafion <sup>®</sup> 212	~70 μV h <sup>-1</sup> , 1 A cm <sup>-2</sup> , 1000 h (46)
<b>IrO<sub>2</sub></b>	2.10		55.5–58.5 wt% Pt/C		0.40	1.80	6.0	80	N/A	N/A (23)
<b>IrO<sub>2</sub> (75%) / TiO<sub>2</sub></b>	1.50–2.0 (Ir)		4.8 wt% Pt/C		0.025 (Pt)	1.79	3.6	80	Nafion <sup>®</sup> 212	N/A (25)
<b>IrO<sub>2</sub> (20%) / gCNH</b>	N/A		Pt/C		4.0 (Pt)	1.80	~0.7	80	Nafion <sup>®</sup> 115	N/A (88)
<b>IrRuO<sub>x</sub></b>	3.0		Pt black		0.086	1.80	~1.8	80	Nafion <sup>®</sup> 115	N/A (30)
<b>Ir black</b>	2.0		Pt/C		1.0	1.80	~1.3	80	Nafion <sup>®</sup> N115/Pt (0.02 mg cm <sup>-2</sup> )/ Nafion <sup>®</sup> NR212	190 μV h <sup>-1</sup> , 1 A cm <sup>-2</sup> (19)
<b>IrO<sub>2</sub></b>	2.50		40 wt% Pt/C		0.40	1.70	1.0	90	Nafion <sup>®</sup> 117	35.5 μV h <sup>-1</sup> (32)
<b>40 wt% IrO<sub>2</sub>/V-TiO<sub>2</sub> (20 at% V)</b>	2.50		40 wt% Pt/C		0.50	1.80	0.6	80	Nafion <sup>®</sup> 117	N/A (108)

(Continued)



**Table I (Continued)**

Anode		Cathode			Operating conditions			Degradation rate	Ref.
Catalyst	Loading, mg cm <sup>-2</sup>	Catalyst	Loading, mg cm <sup>-2</sup>	Voltage, V	Current density, A cm <sup>-2</sup>	Temperature, °C	Membrane		
Ir <sub>0.7</sub> Ru <sub>0.3</sub> O <sub>x</sub>	1.0	40 wt% Pt/C	0.40	1.70	1.0	80	Nafion® NR212	81 μV h <sup>-1</sup> (70)	
IrO <sub>2</sub> /Ti (50 wt% Ti)	0.1	46 wt% Pt/C	0.25	1.73	1.0	80	Nafion® NRE 115CS	1000 h, 20 μV h <sup>-1</sup> (105)	
Ru@Pt (core-shell)	0.10	Pt@WO <sub>3</sub> (core-shell)	0.10	1.80	1.0	80	Nafion® 117	N/A (61)	
IrO <sub>2</sub> /Sb-SnO <sub>2</sub> nanowire	0.75	40 wt% Pt/C	0.20	1.62	2.0	80	Nafion® NR212	0.76 mV h <sup>-1</sup> , 0.45 A cm <sup>-2</sup> at 35°C (115)	
67 wt% IrO <sub>2</sub> /Ti <sub>n</sub> O <sub>2n-1</sub>	1.0	30 wt% Pt/Vulcan XC-72	1.0	1.80	0.700	80	Nafion® 115	N/A (114)	

on a supporting material or unsupported, although obtained using a different synthesis procedure; (b) a gain in the PEMWE stability is also seen, with several factors affecting PEMWE stability including anode structure and membrane degradation; and (c) limiting the permeation of gases through the membrane leads to better PEMWE stability since radicals formed at the cathode produce membrane degradation.

## 5. Concluding Remarks

In this review, an overview of the most recent advances in electrocatalysis for PEM water electrolysis has been provided, both for the HER at the cathode and the OER at the anode, paying special attention to the development of noble metal supported catalysts and their implementation into practical systems. For the former reaction, Pt/C is the most common catalyst, while for the latter the most used catalysts are iridium black and IrO<sub>2</sub>. Both noble metals are scarce and expensive. Several approaches to develop highly structured catalysts leading to high metal dispersion and, ultimately, lower loadings at the electrodes have been thoroughly reviewed. Regarding the HER, platinum supported on advanced carbon materials achieves the expected targets in terms of performance, but in the authors' opinion, durability is an issue that requires the use of alternative titanium-based non-carbon supports. Regarding the OER, among the reviewed approaches and also in the authors' opinion, the development of iridium-based catalysts supported on conductive metal oxides such as those based on niobium-doped titania and antimony-doped tin oxide could lead to the expected performance and durability required by industry players.

Overall, in the short term, the development of advanced supports for metal dispersion will allow the use of these noble metals to be optimised, reducing the cost and increasing the performance and durability of the electrolyzers. In the long term, the development of non-noble catalysts and their implementation in real cells is mandatory to ensure the viability of the technology. In this sense, preliminary studies carried out with non-noble catalysts in half-cell configuration are promising, but further work is necessary to improve their stability and durability in practical cells. Thus, there is still a long way to go before their implementation in commercial PEMWEs.

## References

1. K. Bareiß, C. de la Rúa, M. Möckl and T. Hamacher, *Appl. Energy*, 2019, **237**, 862
2. P. C. K. Vesborg and T. F. Jaramillo, *RSC Adv.*, 2012, **2**, (21), 7933
3. M. Pudukudy, Z. Yaakob, M. Mohammad, B. Narayanan and K. Sopian, *Renew. Sustain. Energy Rev.*, 2014, **30**, 743
4. P. Nikolaidis and A. Poullikkas, *Renew. Sustain. Energy Rev.*, 2017, **67**, 597
5. Y. Naimi and A. Antar, 'Hydrogen Generation by Water Electrolysis', in "Advances in Hydrogen Generation Technologies", ed. M. Eyvaz, Ch. 1, InTechOpen, London, UK, 2018, 18 pp
6. D. M. F. Santos, C. A. C. Sequeira and J. L. Figueiredo, *Quim. Nova*, 2013, **36**, (8), 1176
7. D. Berndt and D. Spahrbier, 'Batteries', in "Ullmann's Encyclopedia of Industrial Chemistry", Wiley-VCH Verlag GmbH, Weinheim, Germany, 2005
8. J. Brauns and T. Turek, *Processes*, 2020, **8**, (2), 248
9. A. S. Aricò, S. Siracusano, N. Briguglio, V. Baglio, A. Di Blasi and V. Antonucci, *J. Appl. Electrochem.*, 2013, **43**, (2), 107
10. X. Sun, K. Xu, C. Fleischer, X. Liu, M. Grandcolas, R. Strandbakke, T. S. Bjørheim, T. Norby and A. Chatzidakis, *Catalysts*, 2018, **8**, (12), 657
11. A. Kusoglu and A. Z. Weber, *Chem. Rev.*, 2017, **117**, (3), 987
12. P. Millet, N. Mbemba, S. A. Grigoriev, V. N. Fateev, A. Aukauloo and C. Etiévant, *Int. J. Hydrogen Energy*, 2011, **36**, (6), 4134
13. M. Suermann, B. Bensmann and R. Hanke-Rauschenbach, *J. Electrochem. Soc.*, 2019, **166**, (10), F645
14. P. Shirvanian and F. van Berkel, *Electrochem. Commun.*, 2020, **114**, 106704
15. P. Holzapfel, M. Bühler, C. Van Pham, F. Hegge, T. Böhm, D. McLaughlin, M. Breitwieser and S. Thiele, *Electrochem. Commun.*, 2020, **110**, 106640
16. T. Reier, M. Oezaslan and P. Strasser, *ACS Catal.*, 2012, **2**, (8), 1765
17. T. Kim, B. Kim, T. Kwon, H. Y. Kim, J. Y. Kim and K. Lee, *Mater. Chem. Front.*, 2021, **5**, (12), 4445
18. K. Ayers, N. Danilovic, R. Ouimet, M. Carmo, B. Pivovar and M. Bornstein, *Annu. Rev. Chem. Biomol. Eng.*, 2019, **10**, 219
19. C. Klose, P. Trinke, T. Böhm, B. Bensmann, S. Vierrath, R. Hanke-Rauschenbach and S. Thiele, *J. Electrochem. Soc.*, 2018, **165**, (16), F1271
20. J. Hu, J. Luo, P. Wagner, O. Conrad and C. Agert, *Electrochem. Commun.*, 2009, **11**, (12), 2324
21. Q. Feng, X.-Z. Yuan, G. Liu, B. Wei, Z. Zhang, H. Li and H. Wang, *J. Power Sources*, 2017, **366**, 33
22. M. Bühler, F. Hegge, P. Holzapfel, M. Bierling, M. Suermann, S. Vierrath and S. Thiele, *J. Mater. Chem. A*, 2019, **7**, (47), 26984
23. M. Stähler, A. Stähler, F. Scheepers, M. Carmo and D. Stolten, *Int. J. Hydrogen Energy*, 2019, **44**, (14), 7053
24. M. Bernt and H. A. Gasteiger, *J. Electrochem. Soc.*, 2016, **163**, (11), F3179
25. M. Bernt, A. Siebel and H. A. Gasteiger, *J. Electrochem. Soc.*, 2018, **165**, (5), F305
26. M. Stähler, A. Stähler, F. Scheepers, M. Carmo, W. Lehnert and D. Stolten, *Int. J. Hydrogen Energy*, 2020, **45**, (7), 4008
27. M. Bajdich, M. García-Mota, A. Vojvodic, J. K. Nørskov and A. T. Bell, *J. Am. Chem. Soc.*, 2013, **135**, (36), 13521
28. S. S. Kumar and V. Himabindu, *Mater. Sci. Energy Technol.*, 2019, **2**, (3), 442
29. S. S. Kumar and V. Himabindu, *Renew. Energy*, 2020, **146**, 2281
30. Z. Kang, G. Yang, J. Mo, Y. Li, S. Yu, D. A. Cullen, S. T. Retterer, T. J. Toops, G. Bender, B. S. Pivovar, J. B. Green and F.-Y. Zhang, *Nano Energy*, 2018, **47**, 434
31. M. Carmo, D. L. Fritz, J. Mergel and D. Stolten, *Int. J. Hydrogen Energy*, 2013, **38**, (12), 4901
32. S. A. Grigoriev and A. A. Kalinnikov, *Int. J. Hydrogen Energy*, 2017, **42**, (3), 1590
33. S. A. Grigoriev, M. S. Mamat, K. A. Dzhus, G. S. Walker and P. Millet, *Int. J. Hydrogen Energy*, 2011, **36**, (6), 4143
34. M. Tavakkoli, N. Holmberg, R. Kronberg, H. Jiang, J. Sainio, E. I. Kauppinen, T. Kallio and K. Laasonen, *ACS Catal.*, 2017, **7**, (5), 3121
35. T. Rajala, R. Kronberg, R. Backhouse, M. E. M. Buan, M. Tripathi, A. Zitolo, H. Jiang, K. Laasonen, T. Susi, F. Jaouen and T. Kallio, *Appl. Catal. B: Environ.*, 2020, **265**, 118582
36. W. Sheng, H. A. Gasteiger and Y. Shao-Horn, *J. Electrochem. Soc.*, 2010, **157**, (11), B1529
37. C. M. Zalitis, D. Kramer and A. R. Kucernak, *Phys. Chem. Chem. Phys.*, 2013, **15**, (12), 4329
38. E. Price, *Johnson Matthey Technol. Rev.*, 2017, **61**, (1), 47
39. P. Trinke, B. Bensmann and R. Hanke-Rauschenbach, *Electrochem. Commun.*, 2017, **82**, 98

40. M. Chandesaris, V. Médeau, N. Guillet, S. Chelghoum, D. Thoby and F. Fouda-Onana, *Int. J. Hydrogen Energy*, 2015, **40**, (3), 1353
41. A. A. Franco and M. Gerard, *J. Electrochem. Soc.*, 2008, **155**, (4), B367
42. X. Chen and S. S. Mao, *Chem. Rev.*, 2007, **107**, (7), 2891
43. Y. Shi, L. Guo, Z. Lu, Z. Wang, Y. Gan, C. Guo, H. Tan and C. Yan, *Energy Technol.*, 2019, **7**, (5), 1800781
44. X. Wang, X. Yuan, X. Liu, W. Dong, C. Dong, M. Lou, J. Li, T. Lin and F. Huang, *J. Alloys Compd.*, 2017, **701**, 669
45. F. Alcaide, R. V. Genova, G. Álvarez, H.-J. Grande, Ó. Miguel and P. L. Cabot, *Int. J. Hydrogen Energy*, 2020, **45**, (40), 20605
46. G. Shi, H. Yano, D. A. Tryk, S. Nohara and H. Uchida, *Phys. Chem. Chem. Phys.*, 2019, **21**, (6), 2861
47. C. Li and J.-B. Baek, *ACS Omega*, 2020, **5**, (1), 31
48. N. Cheng, S. Stambula, D. Wang, M. N. Banis, J. Liu, A. Riese, B. Xiao, R. Li, T.-K. Sham, L.-M. Liu, G. A. Botton and X. Sun, *Nat. Commun.*, 2016, **7**, 13638
49. E. Fabbri and T. J. Schmidt, *ACS Catal.*, 2018, **8**, (10), 9765
50. N.-T. Suen, S.-F. Hung, Q. Quan, N. Zhang, Y.-J. Xu and H. M. Chen, *Chem. Soc. Rev.*, 2017, **46**, (2), 337
51. S. Trasatti, *Electrochim. Acta*, 1984, **29**, (11), 1503
52. S. Park, Y. Shao, J. Liu and Y. Wang, *Energy Environ. Sci.*, 2012, **5**, (11), 9331
53. S. Cherevko, S. Geiger, O. Kasian, N. Kulyk, J.-P. Grote, A. Savan, B. R. Shrestha, S. Merzlikin, B. Breitbach, A. Ludwig and K. J. J. Mayrhofer, *Catal. Today*, 2016, **262**, 170
54. M. Bernt, A. Hartig-Weiß, M. F. Tovini, H. A. El-Sayed, C. Schramm, J. Schröter, C. Gebauer and H. A. Gasteiger, *Chem. Ing. Tech.*, 2020, **92**, (1–2), 31
55. C. Iwakura, K. Hirao and H. Tamura, *Electrochim. Acta*, 1977, **22**, (4), 329
56. E. A. Paoli, F. Masini, R. Frydendal, D. Deiana, C. Schlaup, M. Malizia, T. W. Hansen, S. Horch, I. E. L. Stephens and I. Chorkendorff, *Chem. Sci.*, 2015, **6**, (1), 190
57. M. Escudero-Escribano, A. F. Pedersen, E. A. Paoli, R. Frydendal, D. Friebel, P. Malacrida, J. Rossmeisl, I. E. L. Stephens and I. Chorkendorff, *J. Phys. Chem. B*, 2018, **122**, (2), 947
58. N. Danilovic, R. Subbaraman, K.-C. Chang, S. H. Chang, Y. J. Kang, J. Snyder, A. P. Paulikas, D. Strmcnik, Y.-T. Kim, D. Myers, V. R. Stamenkovic and N. M. Markovic, *J. Phys. Chem. Lett.*, 2014, **5**, (14), 2427
59. R. Kötz and S. Stucki, *Electrochim. Acta*, 1986, **31**, (10), 1311
60. V. A. Saveleva, L. Wang, O. Kasian, M. Batuk, J. Hadermann, J.-J. Gallet, F. Bournel, N. Alonso-Vante, G. Ozouf, C. Beauger, K. J. J. Mayrhofer, S. Cherevko, A. S. Gago, K. A. Friedrich, S. Zafeiratos and E. R. Savinova, *ACS Catal.*, 2020, **10**, (4), 2508
61. K. E. Ayers, J. N. Renner, N. Danilovic, J. X. Wang, Y. Zhang, R. Maric and H. Yu, *Catal. Today*, 2016, **262**, 121
62. X. Xia, L. Figueroa-Cosme, J. Tao, H.-C. Peng, G. Niu, Y. Zhu and Y. Xia, *J. Am. Chem. Soc.*, 2014, **136**, (31), 10878
63. S. Siracusano, V. Baglio, S. A. Grigoriev, L. Merlo, V. N. Fateev and A. S. Aricò, *J. Power Sources*, 2017, **366**, 105
64. B. M. Tackett, W. Sheng, S. Kattel, S. Yao, B. Yan, K. A. Kuttiyiel, Q. Wu and J. G. Chen, *ACS Catal.*, 2018, **8**, (3), 2615
65. H. N. Nong, H.-S. Oh, T. Reier, E. Willinger, M.-G. Willinger, V. Petkov, D. Teschner and P. Strasser, *Angew. Chem. Int. Ed.*, 2015, **54**, (10), 2975
66. G. Jiang, H. Yu, Y. Li, D. Yao, J. Chi, S. Sun and Z. Shao, *ACS Appl. Mater. Interfaces*, 2021, **13**, (13), 15073
67. K. C. Neyerlin, G. Bugosh, R. Forgie, Z. Liu and P. Strasser, *J. Electrochem. Soc.*, 2009, **156**, (3), B363
68. S. Siracusano, N. Van Dijk, E. Payne-Johnson, V. Baglio and A. S. Aricò, *Appl. Catal. B: Environ.*, 2015, **164**, 488
69. S. Siracusano, S. Trocino, N. Briguglio, F. Pantò and A. S. Aricò, *J. Power Sources*, 2020, **468**, 228390
70. L. Wang, V. A. Saveleva, S. Zafeiratos, E. R. Savinova, P. Lettenmeier, P. Gazdzicki, A. S. Gago and K. A. Friedrich, *Nano Energy*, 2017, **34**, 385
71. K. Kadakia, M. K. Datta, O. I. Velikokhatnyi, P. Jampani, S. K. Park, P. Saha, J. A. Poston, A. Manivannan and P. N. Kumta, *Int. J. Hydrogen Energy*, 2012, **37**, (4), 3001
72. I. C. Man, H.-Y. Su, F. Calle-Vallejo, H. A. Hansen, J. I. Martínez, N. G. Inoglu, J. Kitchin, T. F. Jaramillo, J. K. Nørskov and J. Rossmeisl, *ChemCatChem*, 2011, **3**, (7), 1159
73. A. Eftekhari, *Mater. Today Energy*, 2017, **5**, 37
74. J. Rossmeisl, Z.-W. Qu, H. Zhu, G.-J. Kroes and J. K. Nørskov, *J. Electroanal. Chem.*, 2007, **607**, (1–2), 83
75. M. T. M. Koper, *J. Electroanal. Chem.*, 2011,



- 660, (2), 254
76. R. Tang, Y. Nie, J. K. Kawasaki, D.-Y. Kuo, G. Petretto, G. Hautier, G.-M. Rignanese, K. M. Shen, D. G. Schlom and J. Suntivich, *J. Mater. Chem. A*, 2016, **4**, (18), 6831
77. L. Yang, G. Yu, X. Ai, W. Yan, H. Duan, W. Chen, X. Li, T. Wang, C. Zhang, X. Huang, J.-S. Chen and X. Zou, *Nat. Commun.*, 2018, **9**, 5236
78. Z.-X. Lu, Y. Shi, P. Gupta, X. Min, H. Tan, Z.-D. Wang, C. Guo, Z. Zou, H. Yang, S. Mukerjee and C.-F. Yan, *Electrochim. Acta*, 2020, **348**, 136302
79. Q. Shi, C. Zhu, D. Du, J. Wang, H. Xia, M. H. Engelhard, S. Feng and Y. Lin, *J. Mater. Chem. A*, 2018, **6**, (19), 8855
80. C. Zhao, H. Yu, Y. Li, X. Li, L. Ding and L. Fan, *J. Electroanal. Chem.*, 2013, **688**, 269
81. K. A. Lewinski, D. van der Vliet and S. M. Luopa, *ECS Trans.*, 2015, **69**, (17), 893
82. R. T. Atanasoski, L. L. Atanasoska, D. A. Cullen, G. M. Haugen, K. L. More and G. D. Vernstrom, *Electrocatalysis*, 2012, **3**, (3–4), 284
83. A. W. Jensen, G. W. Sievers, K. D. Jensen, J. Quinson, J. A. Arminio-Ravelo, V. Brüser, M. Arenz and M. Escudero-Escribano, *J. Mater. Chem. A*, 2020, **8**, (3), 1066
84. G. Mirshekari, R. Ouimet, Z. Zeng, H. Yu, S. Bliznakov, L. Bonville, A. Niedzwiecki, C. Capuano, K. Ayers and R. Maric, *Int. J. Hydrogen Energy*, 2021, **46**, (2), 1526
85. H.-S. Oh, H. N. Nong, T. Reier, M. Gliach and P. Strasser, *Chem. Sci.*, 2015, **6**, (6), 3321
86. L. Wang, P. Lettenmeier, U. Golla-Schindler, P. Gazdzicki, N. A. Cañas, T. Morawietz, R. Hiesgen, S. S. Hosseiny, A. S. Gago and K. A. Friedrich, *Phys. Chem. Chem. Phys.*, 2016, **18**, (6), 4487
87. L. Solà-Hernández, F. Claudel, F. Maillard and C. Beauger, *Int. J. Hydrogen Energy*, 2019, **44**, (45), 24331
88. A. B. Jorge, I. Dedigama, T. S. Miller, P. Shearing, D. J. L. Brett and P. F. McMillan, *Nanomaterials*, 2018, **8**, (6), 432
89. R. V. Genova-Koleva, F. Alcaide, G. Álvarez, P. L. Cabot, H.-J. Grande, M. V. Martínez-Huerta and O. Miguel, *J. Energy Chem.*, 2019, **34**, 227
90. Q. Xue, W. Gao, J. Zhu, R. Peng, Q. Xu, P. Chen and Y. Chen, *J. Colloid Interface Sci.*, 2018, **529**, 325
91. R. Badam, M. Hara, H.-H. Huang and M. Yoshimura, *Int. J. Hydrogen Energy*, 2018, **43**, (39), 18095
92. R. E. Fuentes, J. Farell and J. W. Weidner, *Electrochim. Solid-State Lett.*, 2011, **14**, (3), E5
93. M. García-Mota, A. Vojvodic, H. Metiu, I. C. Man, H.-Y. Su, J. Rossmeisl and J. K. Nørskov, *ChemCatChem*, 2011, **3**, (10), 1607
94. M. Aizawa, S. Lee and S. L. Anderson, *Surf. Sci.*, 2003, **542**, (3), 253
95. F. C. Walsh and R. G. A. Wills, *Electrochim. Acta*, 2010, **55**, (22), 6342
96. S.-S. Huang, Y.-H. Lin, W. Chuang, P.-S. Shao, C.-H. Chuang, J.-F. Lee, M.-L. Lu, Y.-T. Weng and N.-L. Wu, *ACS Sustain. Chem. Eng.*, 2018, **6**, (3), 3162
97. K. Huang, Y. Li and Y. Xing, *J. Mater. Res.*, 2013, **28**, (3), 454
98. A. Kitada, G. Hasegawa, Y. Kobayashi, K. Kanamori, K. Nakanishi and H. Kageyama, *J. Am. Chem. Soc.*, 2012, **134**, (26), 10894
99. M. P. Gurrola, J. Gutiérrez, S. Rivas, M. Guerra-Balcázar, J. Ledesma-García and L. G. Arriaga, *Int. J. Hydrogen Energy*, 2014, **39**, (29), 16763
100. S.-B. Han, Y.-H. Mo, Y.-S. Lee, S.-G. Lee, D.-H. Park and K.-W. Park, *Int. J. Hydrogen Energy*, 2020, **45**, (3), 1409
101. S. Geiger, O. Kasian, A. M. Mingers, K. J. J. Mayrhofer and S. Cherevko, *Sci. Rep.*, 2017, **7**, 4595
102. P. Mazúr, J. Polonský, M. Paidar and K. Bouzek, *Int. J. Hydrogen Energy*, 2012, **37**, (17), 12081
103. Y.-C. Nah, I. Paramasivam and P. Schmuki, *ChemPhysChem*, 2010, **11**, (13), 2698
104. G. Garcia-Belmonte, V. Kytin, T. Dittrich and J. Bisquert, *J. Appl. Phys.*, 2003, **94**, (8), 5261
105. C. Rozain, E. Mayousse, N. Guillet and P. Millet, *Appl. Catal. B: Environ.*, 2016, **182**, 123
106. J. Cheng, J. Yang, S. Kitano, G. Juhasz, M. Higashi, M. Sadakiyo, K. Kato, S. Yoshioka, T. Sugiyama, M. Yamauchi and N. Nakashima, *ACS Catal.*, 2019, **9**, (8), 6974
107. A. Weiß, A. Siebel, M. Bernt, T.-H. Shen, V. Tileli and H. A. Gasteiger, *J. Electrochem. Soc.*, 2019, **166**, (8), F487
108. C. Hao, H. Lv, Q. Zhao, B. Li, C. Zhang, C. Mi, Y. Song and J. Ma, *Int. J. Hydrogen Energy*, 2017, **42**, (15), 9384
109. C. Hao, H. Lv, C. Mi, Y. Song and J. Ma, *ACS Sustain. Chem. Eng.*, 2016, **4**, (3), 746
110. H. Lv, S. Wang, C. Hao, W. Zhou, J. Li, M. Xue and C. Zhang, *ChemCatChem*, 2019, **11**, (10), 2511

111. H. Lv, G. Zhang, C. Hao, C. Mi, W. Zhou, D. Yang, B. Li and C. Zhang, *RSC Adv.*, 2017, **7**, (64), 40427
112. H. Lv, J. Zuo, W. Zhou, X. Shen, B. Li, D. Yang, Y. Liu, L. Jin and C. Zhang, *J. Electroanal. Chem.*, 2019, **833**, 471
113. W. Hu, S. Chen and Q. Xia, *Int. J. Hydrogen Energy*, 2014, **39**, (13), 6967
114. S. Siracusano, V. Baglio, C. D'Urso, V. Antonucci and A. S. Aricò, *Electrochim. Acta*, 2009, **54**, (26), 6292
115. G. Liu, J. Xu, Y. Wang and X. Wang, *J. Mater. Chem. A*, 2015, **3**, (41), 20791
116. L. Wang, F. Song, G. Ozouf, D. Geiger, T. Morawietz, M. Handl, P. Gazdzicki, C. Beauger, U. Kaiser, R. Hiesgen, A. S. Gago and K. A. Friedrich, *J. Mater. Chem. A*, 2017, **5**, (7), 3172
117. C. Spöri, J. T. H. Kwan, A. Bonakdarpour, D. P. Wilkinson and P. Strasser, *Angew. Chem. Int. Ed.*, 2017, **56**, (22), 5994
118. S. Wang, A. Lu and C.-J. Zhong, *Nano Converg.*, 2021, **8**, 4
119. Z. Chen, L. Guo, L. Pan, T. Yan, Z. He, Y. Li, C. Shi, Z.-F. Huang, X. Zhang and J.-J. Zou, *Adv. Energy Mater.*, 2022, **12**, (14), 2103670

## The Authors



Pere L. Cabot defended his PhD in 1984 at the University of Barcelona (UB), Spain, and is full Professor of the Department of Materials Science and Physical Chemistry (Section of Physical Chemistry) of the UB since 2003. His current research topic is electrocatalysis in fuel cell and electrolyzers, with special interest in polymetallic nanostructures and catalysts supports. He has participated in 50 competitive research projects, 31 contracts with companies and published 170 research papers, three international patents, 23 books and book chapters and about 200 meeting presentations and invited lectures. He has also received three awards from private companies, related to research, development and innovation.



Maria Victoria Martínez Huerta has held a Tenured Scientist position at the Institute of Catalysis and Petrochemistry (ICP) of the Spanish Council for Scientific Research (CSIC) since 2010 and is the head of the Electrocatalysis for Energy and the Environment Group. Her research activity is dedicated to the development of electrocatalysts that improve the activity and stability of electrodes in electrochemical devices for storage and conversion of clean energy, mainly in those applications that use hydrogen as an energy carrier such as fuel cells and electrolyzers. She has participated in 39 competitive research projects and published 89 research papers (indexed in Web of Science™).



Francisco Alcaide holds a PhD in Chemistry (Physical Chemistry) from the University of Barcelona (2002). He has more than 25 years of experience in electrochemical technologies, especially in fuel cells and hydrogen. He has participated in or led about 50 national, European and international research, development and innovation projects and contracts with companies in technology transfer and innovation. He serves as independent expert and advisor for several national, international and European Commission public bodies. His research interests range from electrocatalysis for clean energy and decarbonisation to batteries and water treatment. Alcaide currently works as Principal Investigator and Project manager at CIDETEC, Spain.

# Properties of Additively Manufactured Platinum-Rhodium Alloys

## Investigating the feasibility of additive manufacturing for glass fibre bushings

**Thilo Becker\*, Thomas Gries**

Institut für Textiltechnik of the RWTH Aachen University, Otto-Blumenthal-Str. 1, 52066 Aachen, Germany

\*Email: [thilo.becker@ita.rwth-aachen.de](mailto:thilo.becker@ita.rwth-aachen.de)

### PEER REVIEWED

Received 9th December 2021; Revised 3rd January 2022; Accepted 9th February 2022; Online 5th May 2023

Bushings made of platinum-rhodium alloys are a key component in glass fibre production. While bushings have grown in size and functionality since their introduction in the early 20th century, manufacturing constraints still limit their full potential. Both in terms of design and quality, traditional manufacturing methods such as milling, drilling and welding limit the potential of precious metal bushings. The technical feasibility of the use of additive manufacturing for the production of bushings is greatly dependent on the material properties. For the purpose of this work, an additively manufactured alloy consisting of 90 wt% platinum and 10 wt% rhodium (PtRh10) is investigated with regard to density, electrical resistivity, creep performance and the contact angle of E-glass on the PtRh10 samples.

## 1. Introduction

Glass fibres are inorganic non-crystalline thin filaments that, in their most simple form, date back to ancient Egypt (1). They play a key role in technologies of great commercial importance such as multilayer printed circuit boards (PCBs),

composite wind turbine blades and lightweight boats. At a price of approximately €1.1 kg<sup>-1</sup>, chopped ( $\leq 50$  mm length) and continuous glass fibres dominate the reinforcement fibre market with a total production volume of approximately 700,000 tonnes in the European Union (EU) in 2018. Including imported glass fibres, the total annual demand for glass fibres within the EU in 2018 was just over 1.05 million tonnes (2). Estimates for the global glass fibre production in 2019 vary between 5 million tonnes and 8 million tonnes (3, 4).

The commercial production of glass fibres dates back to the 19th century. In France, glass fibres were produced as early as 1830 in small volumes and woven to produce garments. In 1908, W. v. Paczinsky produced continuous glass fibres using a platinum vessel, a so-called bushing, for the first time in Hamburg (Germany) (5). As defined by ASTM C162-05, a bushing is “a precious metal or refractory/metal structure with single or multiple hole(s) through which glass flows and is attenuated into fiber(s)” (6). The key role of the bushing is to provide a heated vessel for a glass melt, comprising a multiplicity of openings from which glass fibres can be drawn. **Figure 1** depicts the lower section of a bushing, the so-called tip plate. Commercial production of glass fibres *via* this process began in 1930 in the USA and 1939 in Germany (5). Since that time, the underlying principle of drawing glass filaments from a glass melt through narrow tips (nozzles) in precious metal bushings has remained largely unchanged. The same process is also employed in the production of continuous basalt fibres. The bushing forms a critical part of the glass fibre production process. Typical operating temperatures are between 1150°C and 1500°C, depending on the glass composition. While bushing technology has

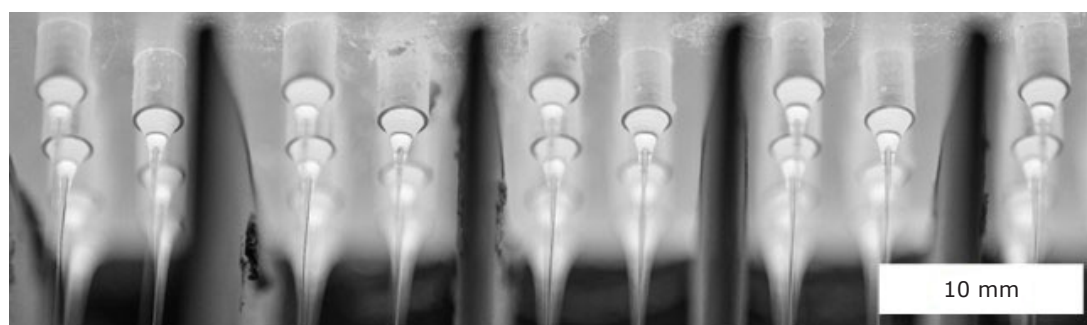


Fig. 1. Section of an operational tip plate of a 203-tip bushing with fin coolers between double rows of tips

advanced with regard to increases in the number of tips and functionality, manufacturing constraints of traditional manufacturing methods such as milling, drilling and welding still limit their full potential both in terms of design and quality.

Manufacturing techniques for bushing tip plates such as deep-drawing and welding feature manufacturing constraints with regard to the design of a bushing, and in particular the complex tip plate of a bushing. Manufacturing the tip plate accounts for approximately 40% of the total manufacturing costs of €12,000–€15,000 for a typical 4000 tip bushing. The conventional production of a bushing is very time-consuming and cost-intensive due to the numerous tips. In addition, every weld seam increases the risk of failure and glass leakage. This must be counteracted by elaborate quality control. The risk of leakage can be reduced by deep-drawing the nozzle plate, but the production of the required tools is very cost-intensive. The additive manufacturing technology shows potential to overcome these deficits, as it enables the production of complex monolithic parts without external weld lines and to a high level of precision. Furthermore, it enables complex design features such as narrow adjacent walls, hollow structures or finely detailed tips which are either impossible to produce through conventional methods or are simply not economical.

Additive manufacturing, also known as '3D printing', is a technology through which parts are produced by adding material, usually layer by layer, to form a desired geometry. The technology emerged in the 1980s, with the first patent in the field of additive manufacturing filed in 1984 by William E. Masters (7). In 2014, the first commercially available additive manufacturing machine for precious metals, the Precious M 080 (EOS GmbH Electro Optical Systems, Munich, Germany), was introduced to the market (8). While initially designated for jewellery production, the new precious metal additive manufacturing systems also show significant potential for

industrial processes. Offering great design freedom in three-dimensional space, the process enables geometries and part functionality which can often not be achieved with conventional subtractive manufacturing methods.

Additive manufacturing of PtRh10 alloys is still a relatively new technology. Little work has gone into optimising the material with regard to the relevant material properties for bushings. However, previous work has shown that metal parts manufactured through laser powder bed fusion (LPBF) can be optimised to achieve similar or even superior properties to cast or rolled parts (9, 10). In this present work, three properties of additively manufactured PtRh10 alloys are investigated, namely electrical resistivity, creep performance and the contact angle of E-glass on the PtRh10 samples. By evaluating these properties, the potential of the additive manufacturing technology for the production of glass fibre bushings is evaluated.

The electrical resistivity is critical for bushings, as they are heated through Joule heating, also referred to as resistive heating. The creep performance of the bushing is of great importance for its service life. Particularly with large bushings featuring 2400 tips or more, the large surface area of the tip plate is prone to sagging due to material creep under the hydrostatic pressure ( $P$ ) of the glass melt, as indicated in **Figure 2**.

In a study conducted by Yang *et al.*, the average lifetime of an industrial 2400 tip bushing was analysed. A total of 84 bushings, 14 bushings each from six different furnaces were analysed. An average lifetime of 368 days with a large standard deviation of 114 days was recorded. Despite the lack of essential information such as bushing geometry, material or processing conditions, these figures provide general insights into typical bushing lifetimes (11). Further values available in literature suggest average bushing lifetimes between 250 and 350 days, with mechanical failure due to excessive creep being a common cause of failure (12).

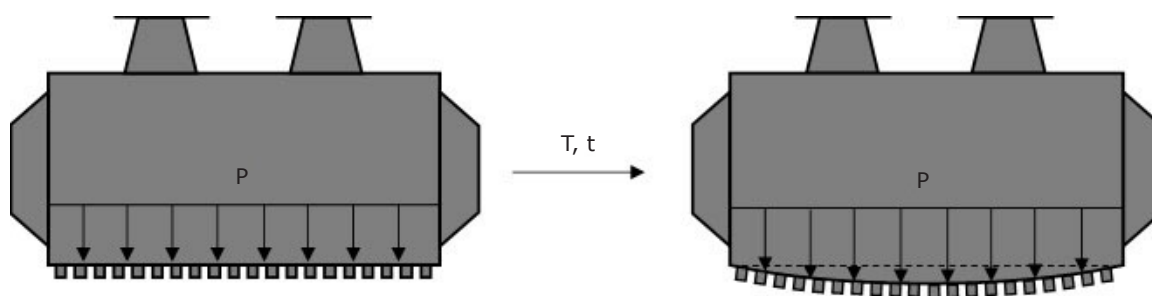


Fig. 2. Schematic of the sagging of a tip plate of a bushing due to the effects of temperature (T), time (t) and pressure (P)

Finally, the contact angle with the glass melt is of great importance for the performance of bushings to enable a stable fibre drawing process and prevent flooding of the tip plate. Flooding describes the phenomenon of molten glass creeping around the tip openings of the bushing, covering large portions or even the entire tip plate. The surface morphology impacts the contact angle between a liquid and a solid, as outlined by Cassie, Baxter and Wenzel (13, 14). The determination of the contact angle of additively manufactured PtRh10 alloys is important as additive manufacturing often leads to rougher surfaces compared to conventional rolled sheet metal, and post-processing of the surfaces is more challenging due to the complex monolithic geometries.

## 2. Sample Preparation and Methodology

All additively manufactured PtRh10 samples were prepared on an EOS M 100 (EOS GmbH, Germany) additive manufacturing machine by Cookson Precious Metals Ltd (Birmingham, UK). Prior to testing, the rhodium content of the samples was evaluated through non-destructive X-ray fluorescence (XRF) analysis using an ADVANT XP device manufactured by Thermo Scientific (Waltham, USA). The impurities were determined *via* inductively coupled plasma optical emission spectrometry using an iCAP<sup>TM</sup> ICP-OES 7400 device by Thermo Fisher Scientific. As all additively manufactured PtRh10 specimens used throughout this work were manufactured from the same batch of raw material powder according to the manufacturer, respective impurities are assumed to be constant across various samples. An additional conventionally manufactured creep specimen was also tested with regard to impurities. The XRF and inductively coupled plasma optical emission spectroscopy (ICP-OES) analyses were conducted

on solid platinum-rhodium samples rather than the powder feedstock, as the material quality is assumed to be homogenous across the powder and therefore also across the part. The producer of the additively manufactured parts was unable to provide feedstock for analysis.

The density of an additively manufactured PtRh10 cube measuring 10 mm × 10 mm × 10 mm was determined using an AccuPyc II 1340 gas pycnometer made by Micromeritics Instrument Corp (Norcross, USA). 10 volume measurements were conducted through the AccuPyc II 1340 gas pycnometer to account for geometric inaccuracies.

The creep behaviour of additively manufactured PtRh10 samples was evaluated *via* constant load tensile creep tests at a temperature of 1200°C. Additively manufactured 'dog bone' shaped samples measuring 48.4 mm in length, 7 mm in width and 1 mm in thickness were prepared for testing. A central creep portion used to visually determine the elongation of the sample measuring 5 mm in length and 2.9 mm in width is indicated by lateral markers on the samples (Figure 3). The creep behaviour was evaluated through the so-called stress rupture time, which describes the time it takes for a sample to fail under a constant stress.

For the determination of the creep rate as well as the rupture time, the PtRh10 samples were inserted into a creep test rig consisting of a furnace, ceramic sample holders and thermocouples. Subsequently the furnace was heated to a temperature of 1200°C at a heating rate of approximately 10°C min<sup>-1</sup> and once the target temperature was reached, a tensile load of 10 MPa was applied. The deformation over time was recorded optically through a suitable camera (Figure 4). A total of three additively manufactured samples were tested with regard to their creep rates and stress-rupture time at a load of 10 MPa at 1200°C. A further three benchmark samples produced through conventional manufacturing were tested.



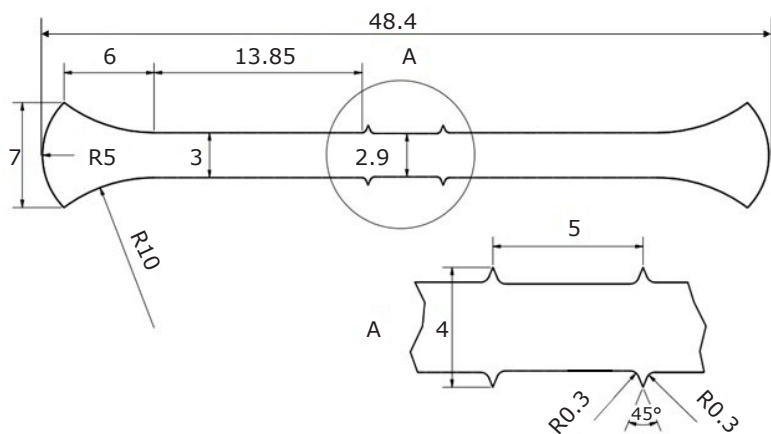


Fig. 3. Geometry of the tensile creep test samples

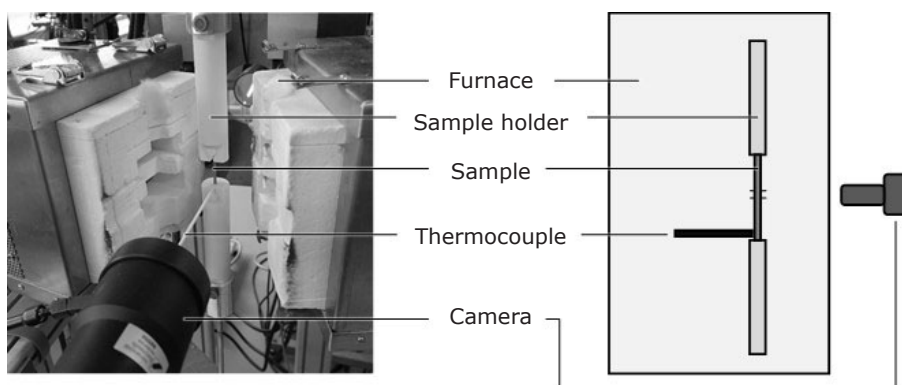


Fig. 4. Overview of the high temperature creep test setup

**Table I Chemical Composition of Typical E-Glass<sup>a</sup> According to the Product Datasheet**

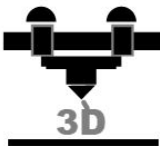
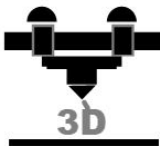
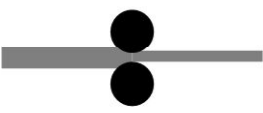
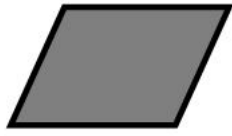
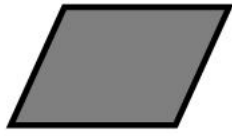
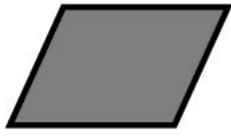
	SiO <sub>2</sub>	CaO	Al <sub>2</sub> O <sub>3</sub>	B <sub>2</sub> O <sub>3</sub>	MgO	Fe <sub>2</sub> O <sub>3</sub>	R <sub>2</sub> O	Other
wt%	53.75	20.18	13.87	6.65	3.59	0.28	0.32	1.36

<sup>a</sup>supplied by Unifrax Dongxiang (Songyuan) Co, Ltd (Shenyang City, China)

A similar experimental setup was previously used by Völkl *et al.*, allowing for a direct comparison of the creep rates with conventionally manufactured PtRh10 components from this study (15). While standards for creep testing of metals such as ISO 204:2018 or ASTM E139-11(2018) (16, 17) exist, they are not suitable for precious metals. Specified clamping methods, heating systems and temperature monitoring systems are often not compatible with the high-temperature regimes required for testing precious metals.

The contact angle between E-glass and additively manufactured PtRh10 parts was evaluated. The chemical composition of the E-glass is outlined in **Table I**. Glass fragments weighing between 0.01 g and 0.015 g were prepared by crushing E-glass droplets collected from a glass fibre bushing.

The PtRh10 substrates measure 15 mm × 15 mm × 1 mm. Four PtRh10 samples (U1–U4) were analysed in an ‘as built’ condition without further post-treatment after the additive manufacturing process. A further four samples (B1–B4) were sand-blasted prior to exposure with the glass. In both cases, the surface facing upward during the additive manufacturing process was investigated. Finally, three conventionally manufactured samples (C1–C3) produced by Saxonia Edelmetalle GmbH (Halsbrücke, Germany) were analysed as a benchmark to ensure the comparability of the tests to the data available in literature. Additional polishing was performed on the conventional samples to remove unidirectional surface grooves. Prior to testing, all samples were cleaned with acetone (**Table II**).

Table II Overview of the Different Sample Types			
	U1-U4	B1-B4	C1-C4
<b>Manufacturing</b>	 AM	 AM	 Conventional, rolled
<b>Surface treatment</b>	Acetone	Sand-blasting acetone	Polishing acetone
<b>Dimensions, mm</b>	 15 × 15 × 1	 15 × 15 × 1	 15 × 15 × 1

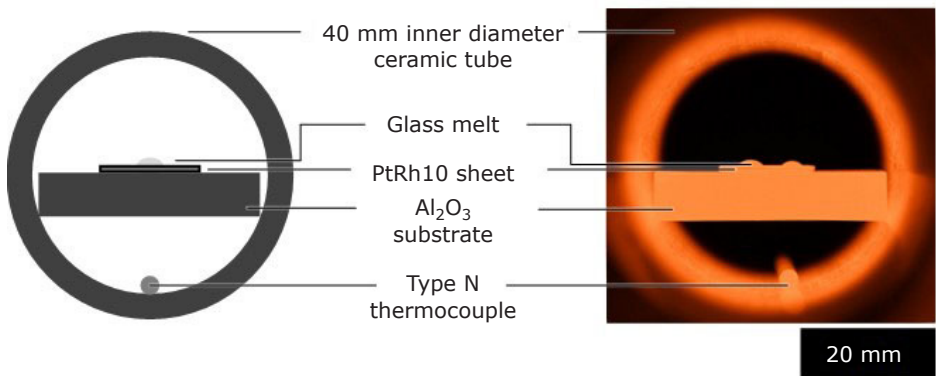


Fig. 5. Schematic and image of the PtRh10 sample within the tube of the tube furnace

A model STF 16-180 tube furnace produced by Carbolite Gero Ltd (Hope Valley, UK) was preheated to 1200°C and an alumina substrate block inserted together with a PtRh10 sample and a glass fragment (Figure 5). The furnace temperature was monitored and maintained within ±5°C of the target temperature using a type N thermocouple attached to a RS PRO 1316 digital thermometer (RS Components Ltd, Corby, UK). Images of the shape of the glass on the metal substrate were captured every 10 s for a period of 1 h using a D850™ digital camera with an AF-S Nikkor 28-300 mm f:3.5-5.6G ED VR lens (Nikon Corp, Tokyo, Japan) at a focal length of 300 mm. The captured images were analysed using the ImageJ software developed and published by the National Institutes of Health (Bethesda, USA) (18). More specifically, the LB-ADSA plugin based on the Young-Laplace equation was used to analyse the imaging data [SMM+10]. For analysis, the images were converted to 32-bit black and white images, cropped and rotated for the PtRh10 samples to align horizontally.

Additionally, a detailed surface roughness analysis was conducted using an InfiniteFocusG5 3D focus variation measurement system produced by Alicona Imaging GmbH (Raaba, Austria). Average surface roughness measurements of the arithmetical mean height ( $S_a$ ) were taken across a central portion of the samples. A 10× magnification lens was used with a specified vertical resolution of 100 nm. A total of nine images were stitched to create a measurement area 4.5 mm × 4.5 mm in size and featuring 27 million measurement points. A Gaussian filter according to ISO 16610-71:2014 (18) was applied through the MeasureSuite 5.3.5 software (Alicona Imaging GmbH) to account for surface curvature.

Three additively manufactured PtRh10 samples measuring 70 mm × 10 mm × 1 mm were produced in different build orientations during the additive manufacturing process (Figure 6). No post-treatment of the samples was undertaken besides the removal from the build platform via wire electrical discharge machining. An additional three conventionally manufactured samples from

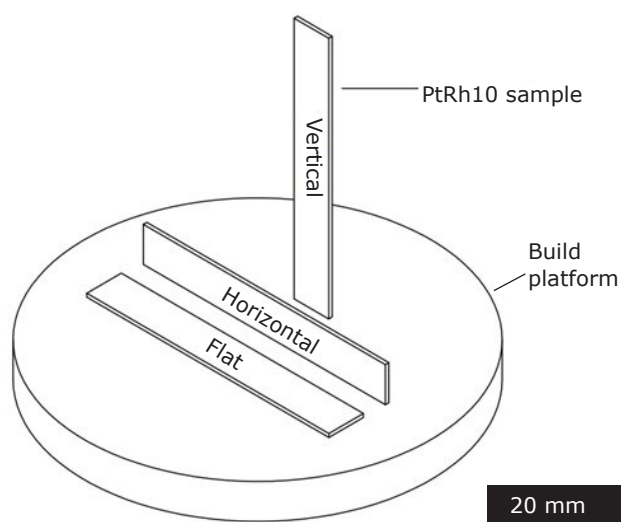


Fig. 6. Build orientation of the different additively manufactured samples

rolled sheet metal of the same geometry were prepared. Based on the work by Silbernagel *et al.*, the four-terminal sensing method, also referred to as Kelvin sensing, was applied to determine the electrical resistivity of the samples (19). Using a 5500A Multi-Product Calibrator (Fluke Corp, Everett, USA), a 10 A current was applied through alligator clips at each end of the sample.

The electrical resistivity of a given object with a known geometry can be calculated according to Equation (i) by measuring the electrical resistance, as the resistance is equal to the resistivity of the material times the length and divided by the cross-sectional area:

$$R = (\rho L)/A \tag{i}$$

where R is electrical resistance in Ω; ρ is electrical resistivity in Ω m; L is length in m; A is cross-sectional area in m<sup>2</sup>.

The potential difference across a central portion measuring approximately 50 mm in length was measured using a high-precision 3458A multimeter (Hewlett Packard, USA). The contact probes were manually placed on the samples in a previously marked position along its central axis. An overview of the experimental setup is shown in Figure 7. Each additively manufactured sample was measured prior to and after annealing for 1 h at 1260°C. The actual cross-sectional area of each sample was measured to account for inaccuracies during sample preparation when calculating the electrical resistance.

### 3. Results

#### 3.1 Metallurgical Impurities

Impurities of approximately 0.33 wt% were detected within the additively manufactured sample. A total platinum and rhodium content of 89.83 wt% and 9.84 wt% respectively was measured. The conventionally manufactured sample featured impurities of 0.03 wt% with 89.94 wt% platinum and 10.03 wt% rhodium. An overview of the various impurities is shown in Table III. The concentrations of zinc, gold, chromium, ruthenium, silver and tungsten were below the detection threshold of 10 ppm for the conventionally manufactured sample.

#### 3.2 Density

Through an average of 10 volume measurements, a density of 19.942 g cm<sup>-3</sup> was determined. The measured volume of the cube of 0.9762 cm<sup>3</sup> with a standard deviation of 0.0003 cm<sup>3</sup> deviated slightly from the expected volume of 1 cm<sup>3</sup>. Compared with

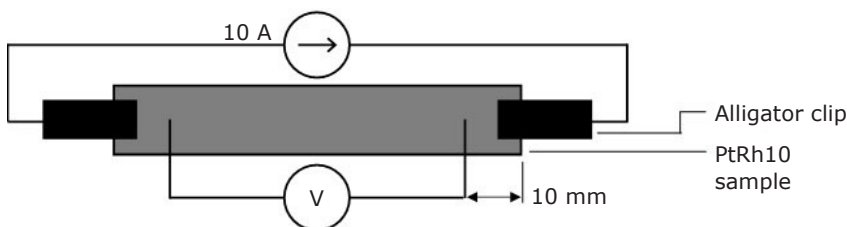


Fig. 7. Schematic of the experimental set-up measuring the potential difference across the PtRh10 samples

Table III Detected Impurities Within the Samples

ppm	Cu	Fe	Zn	Au	Cr	Ir	Ru	Ag	Pd	W	Other
<b>Additive manufacturing</b>	1800	500	460	102	100	60	50	30	29	21	95
<b>Conventional</b>	20	33	-	-	-	78	-	-	94	-	75



the reported density of  $20.00 \text{ g cm}^{-3}$  for PtRh10, a theoretical porosity of 0.29% can be calculated.

### 3.3 Creep Behaviour

The three additively manufactured samples failed after 23.8 h, 26.1 h and 30.3 h respectively, resulting in a mean rupture time of 26.7 h. A mean elongation at failure of 42.9% with a standard deviation of 4.6% was recorded. An additional three conventionally manufactured samples were tested under the same conditions, resulting in failure times of 63.3 h, 72.0 h and 128.8 h respectively. A mean elongation at failure of 65.7% with a standard deviation of 18.8% was recorded.

### 3.4 Contact Angle

The surface roughness and surface area of the additively manufactured samples is greatly increased compared to the polished samples. A macroscopic image of the top surface facing the laser beam during the LPBF process of the as-built and sand-blasted samples is depicted in **Figure 8**. This top surface was investigated in the subsequent analysis of surface roughness and contact angle.

Surface defects are present in both additively manufactured samples, with mean measurements of  $S_a = 5.1 \text{ }\mu\text{m}$  and  $S_a = 5.0 \text{ }\mu\text{m}$  respectively for the sand-blasted and as-built surfaces. The polished conventionally manufactured samples feature a mean surface roughness of  $S_a = 0.2 \text{ }\mu\text{m}$ . Additionally, the increase in size of the measured surface compared to the projected surface of

$4.5 \text{ mm} \times 4.5 \text{ mm}$  was calculated to determine the surface roughness on a smaller scale (**Figure 9**).

The contact angle of the samples was evaluated in a tube furnace. After a rapid decrease in contact angle over the first 5 min within the tube furnace, the equilibrium contact angle is quickly reached. **Figure 10** shows the progression of the contact angle over a period of 30 min for a sand-blasted additively manufactured sample. The curves for all samples, conventional and additive manufacturing, are similar with equilibrium reached after approximately 10 min.

For the samples in 'as-built' condition, a mean contact angle of  $35.1^\circ$  with a standard deviation of  $1.1^\circ$  was measured. The sand-blasted samples showed a slightly increased mean contact angle of  $36.2^\circ$  with a standard deviation of  $1.2^\circ$ , while the conventionally manufactured samples feature a mean contact angle of  $43.1^\circ$  and a standard deviation of  $0.7^\circ$  (**Figure 11**).

According to Wenzel, corresponding roughness factors of 1.12 and 1.10 for the untreated as-built (U) and sand-blasted (B) surfaces can be calculated respectively (13).

### 3.5 Electrical Resistivity

In the horizontally built samples, a change in both mean resistivity and standard deviation can be observed after annealing (**Figure 12**). Similarly, the vertically built samples show little change in resistivity after annealing, with a mean resistivity of  $22.2 \text{ }\mu\Omega \text{ cm}$  both prior to and after annealing (**Figure 12**). Both vertically and horizontally built additive manufacturing samples show a

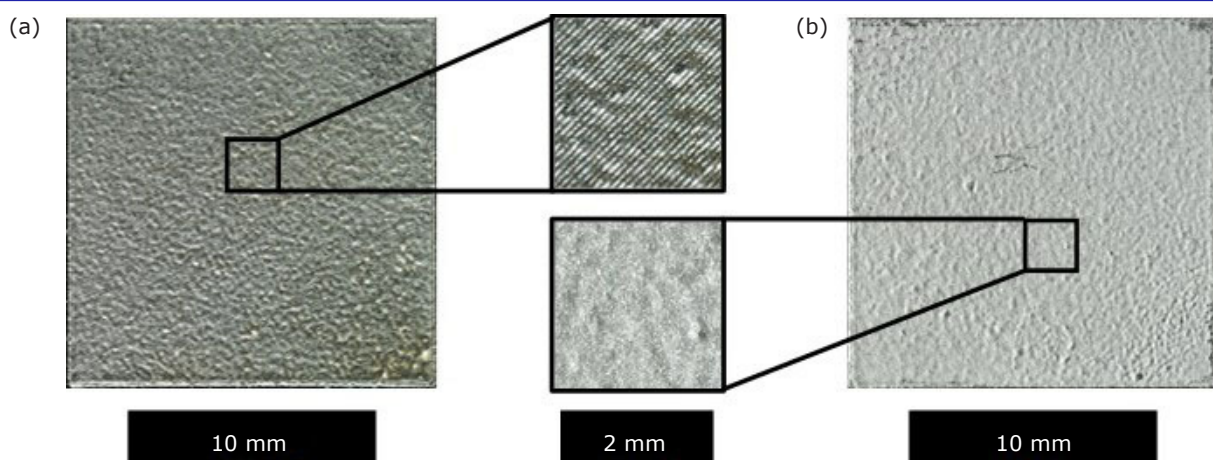


Fig. 8. Surface structure of: (a) as-built; and (b) sand-blasted PtRh10 samples

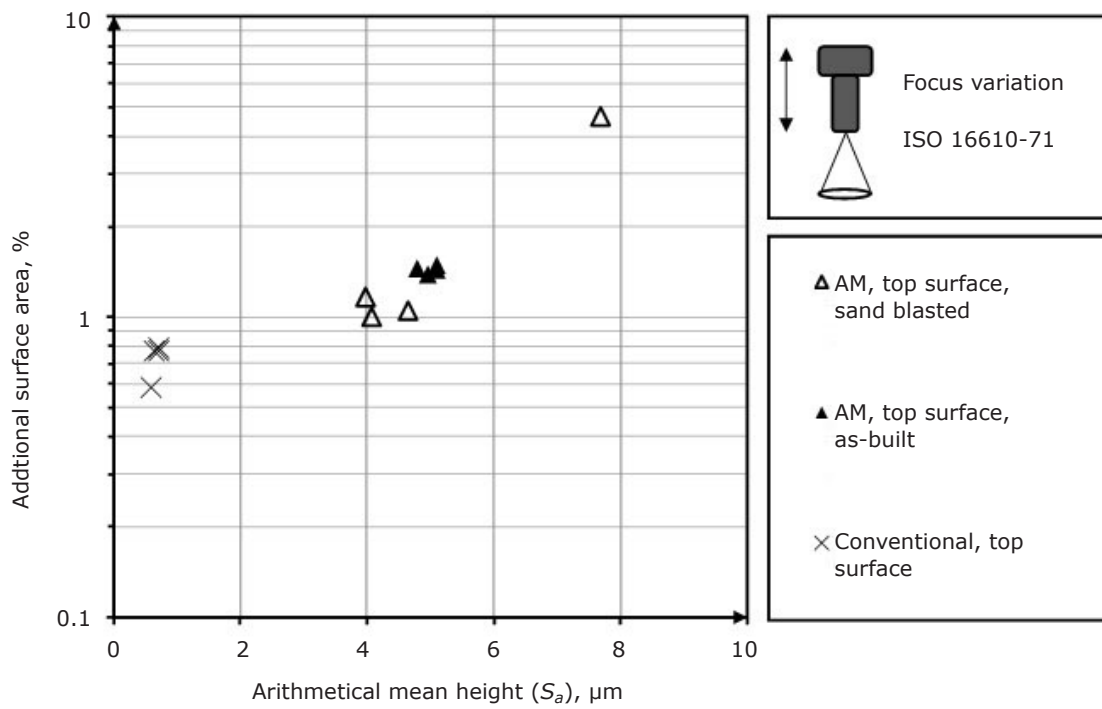


Fig. 9. Additional surface area of the samples plotted on a logarithmic scale against the arithmetical mean height ( $S_a$ )

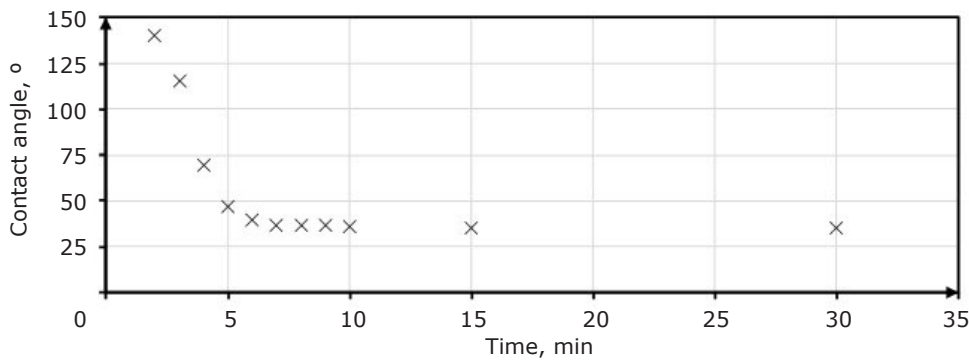


Fig. 10. Measured contact angle between PtRh10 sample and a glass bead over time

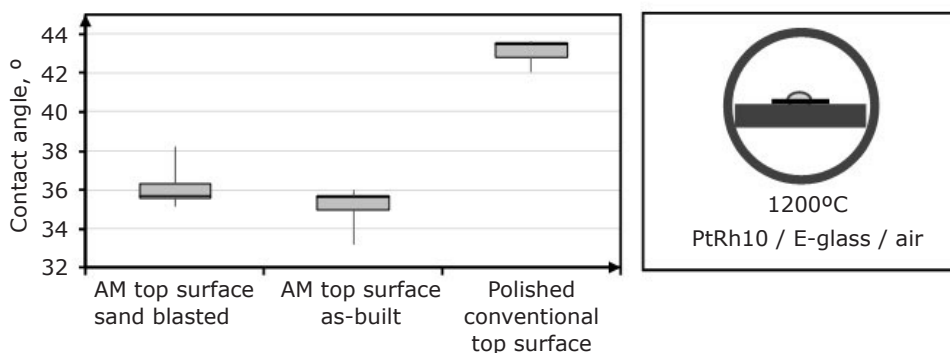


Fig. 11. Box plot diagram of measured contact angles on the various surfaces

higher resistivity than the value of  $19.5 \mu\Omega \text{ cm}$  measured on the conventionally manufactured samples, which exactly matches the value

published by Acken (27). Additional annealing at  $1500^\circ\text{C}$  was undertaken on the horizontally built samples, with no measurable change in mean

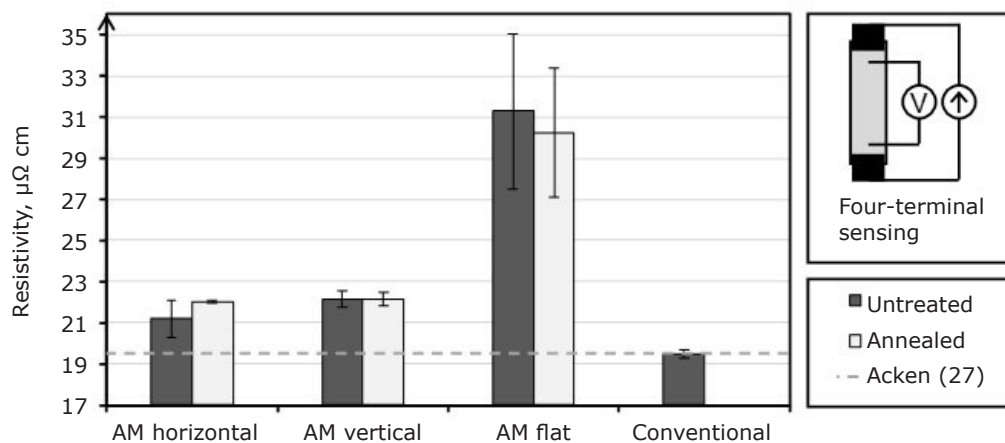


Fig. 12. Electrical resistivity of additively manufactured PtRh10 samples and benchmark value by Acken (27)

resistivity compared to the samples annealed at 1260°C.

The flat additive manufacturing samples feature a mean resistivity of 31.3  $\mu\Omega$  cm and 30.3  $\mu\Omega$  cm and a corresponding standard deviation of 3.8  $\mu\Omega$  cm and 3.1  $\mu\Omega$  cm prior to and after annealing respectively.

## 4. Discussion

### 4.1 Metallurgical Impurities

The detected impurities of the additively manufactured samples significantly exceed those investigated in previous creep related studies of platinum-rhodium alloys (20, 21). While all impurities are undesired, zinc is considered to increase creep rates of platinum-rhodium alloys, and typical permissible values in the glass fibre industry are below 50 ppm. Copper is known to reduce the ductility of the alloy, however no concrete data on the effects of concentrations of nearly 2000 ppm were found in the available literature. The source of the impurities is likely from the feedstock, as the production machines are used exclusively for precious metals. The producer of the additively manufactured parts was unable to provide feedstock for analysis to confirm this.

### 4.2 Density

The reduced volume of the test cube in comparison to the target volume of 1 cm<sup>3</sup> can be attributed to open pores on the surfaces of the cube as well as dimensional inaccuracies during the additive manufacturing and wire cutting process. The porosity of 0.29% is due to a combination of

internal voids and vacancies as well as metallurgical impurities.

### 4.3 Creep Behaviour

The creep behaviour of the additively manufactured samples agrees with data on conventionally manufactured PtRh10 wire published by Trumić *et al.* (21). Though no detailed analysis of impurities is provided in said studies, purities of 99.95% for platinum and 99.5% for rhodium are quoted as well as unquantified impurities of palladium, silver, gold, bismuth, antimony, arsenic and copper. When compared to other studies such as those published by Völkl *et al.* and Hamada however, the observed rupture times are significantly shorter (Figure 13) (15, 22). The short rupture times of the additive manufacturing specimens can therefore be attributed to the impurities of 0.33 wt%.

### 4.4 Contact Angle

The contact angle between an E-glass melt and the additively manufactured platinum-rhodium samples is reduced compared to conventionally manufactured polished samples. The polished samples further show a larger contact angle when compared to the value of 41° published by Selman *et al.* at a temperature of 1200°C (26). As outlined by Selman *et al.* when comparing their own findings to previous studies, this can at least partially be explained by different states of oxidation of the platinum-rhodium alloys. For the purpose of this work however, it can clearly be observed that the PtRh10 samples with a rougher additively manufactured surface show a smaller contact angle with E-glass droplets under air than

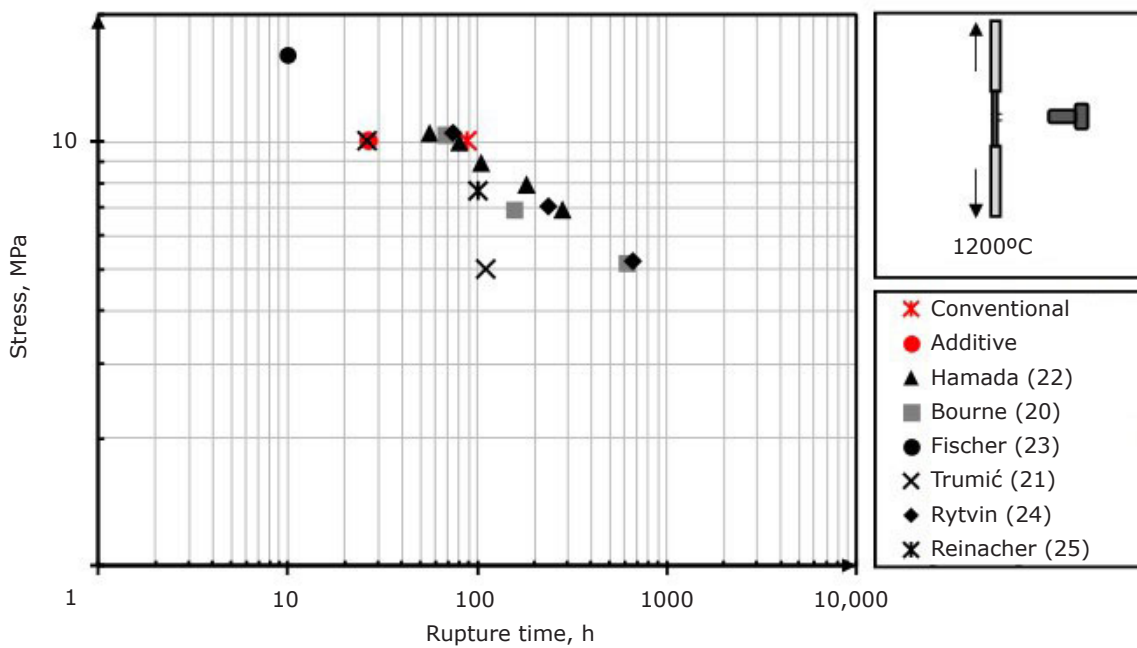


Fig. 13. Stress-rupture time of the mean values of the present study as well as results from previous studies with conventional PtRh10 (21–25)

conventionally manufactured polished surfaces. More specifically, the sand-blasted surfaces (B) show a 16.0% smaller surface angle in comparison to the conventional polished samples.

#### 4.5 Electrical Resistivity

The annealing appears to have little effect on the measured resistivity of the samples. When comparing the resistivity of the horizontally built samples before and after annealing, no statistically significant difference could be detected by applying a two-tailed t-test ( $p = 0.3$ ). The difference in the mean values is likely due to a measurement error, as two of the three measurements prior to annealing are within 1% of the measured resistivity after annealing. Omitting this outlier, the mean resistivity is 21.8  $\mu\Omega$  cm prior to annealing and 22.0  $\mu\Omega$  cm after annealing for the horizontally built samples.

The flat additive manufacturing samples are outliers within this series, with a mean resistivity of 31.3  $\mu\Omega$  cm and 30.3  $\mu\Omega$  cm and a corresponding standard deviation of 3.8  $\mu\Omega$  cm and 3.1  $\mu\Omega$  cm prior to and after annealing respectively. This is likely due to remains of the support structure from the additive manufacturing process attached to the bottom of the samples (Figure 14).

With the supplier of the parts unable to execute a clean cut along the border between the support structure and the sample, the lower surface of the flat samples features an irregular surface. This causes problems during the contacting of the samples through the crocodile clips. Furthermore, the true cross-sectional area is therefore smaller than the product of the width and thickness of the sample, leading to measurement errors. All as-built and tempered additively manufactured samples show a higher resistivity than the reference value of 19.5  $\mu\Omega$  cm. As outlined by Silbernagel *et al.*,

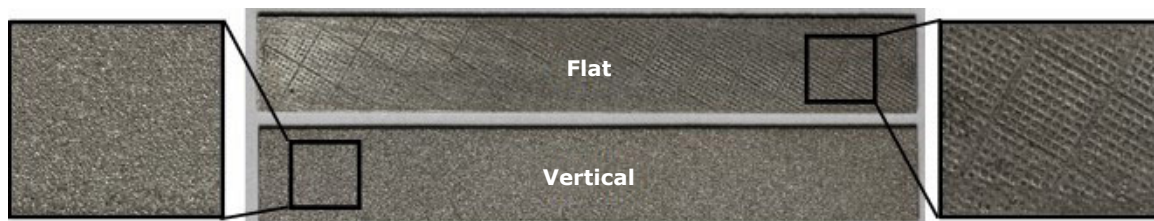


Fig. 14. Comparison of the surfaces of additive manufacturing parts built in the flat and vertical orientation, showing remains of the support structure on the flat samples (right)

disruptions in the atomic lattice structure of pure metals govern the electrical resistance of pure solid metals. These disruptions are generally grain boundaries, vacancies or voids (19). For alloys, such as the PtRh10 alloys present in this study, such disruptions are typically caused by elements other than the main elements of the alloy. The higher resistivity of the additively manufactured samples is therefore likely due to a combination of internal vacancies or voids and the metallurgical impurities. The annealing has little effect on the measured resistivity. The observed increase in resistivity after annealing in the horizontal samples is likely due to a measurement error in the untreated samples, as two out of three measurements are within a 1% margin prior to and after annealing.

## 5. Conclusion

The metallurgical impurities within the additively manufactured samples are outside of common standards within the glass fibre industry. The high level of impurities leads to reduced stress-rupture-times, highlighting the requirement for raw materials of consistently high quality to enable the industrial use of additive manufacturing for the production of glass fibre bushings. The density of the additively manufactured parts is within <0.5% of conventionally manufactured parts and generally suitable for use in bushings. For the manufacturing of bushings, the higher electrical resistivity of the additively manufactured components is generally advantageous, as lower currents are required in the electrical heating system. Components of the electrical heating system such as busbars can be reduced in size with lower currents and system losses reduced.

Finally, the 16% smaller contact angle of the rougher additively manufactured surfaces with E-glass melt is generally disadvantageous with regard to bushing performance. The real-life implications of this however can only be determined through experimental trials investigating the fibre forming and flooding behaviour of additively manufactured tip plates and bushings.

In summary, this work provides a first overview of the feasibility of additive manufacturing for glass fibre bushings by shining a light on the most relevant material properties. Further work is recommended to increase material feedstock quality and additive manufacturing parameters to optimise these properties, and the creep performance in particular.

## References

1. K. L. Loewenstein, "The Manufacturing Technology of Continuous Glass Fibres", 2nd Edn., Elsevier, Amsterdam, The Netherlands, 1983
2. Commission Implementing Regulation (EU) 2020/379, *Official J. Eur. Union*, 2020, **63**, (L69), 14
3. S. Mazumdar, 'The Glass Fiber Market', *Composites Manufacturing*, Winter 2021, pp. 18–19
4. T. Becker, M. Haag, T. Gries, D. Pico, C. Wilms, G. Seide, R. Kleinholz and H. Tiesler, 'Fibers, 12. Glass Fibers', in "Ullmann's Encyclopedia of Industrial Chemistry", Wiley-VCH Verlag GmbH and Co KGaA, Weinheim, Germany, 2022
5. R. Teschner, "Glasfasern: 2. Auflage", Springer-Verlag GmbH, Berlin, Germany, 2019 (in German)
6. 'Standard Terminology of Glass and Glass Products', ASTM C162-05, ASTM International, West Conshohocken, USA, 2015, 16 pp
7. W. E. Masters, 'Computer Automated Manufacturing Process and System', *US Patent* 4,665,492; 1987
8. B. Krassenstein, 'EOS & Cooksongold Team to Launch the PRECIOUS M 080 Jewelry DMLS 3D Printer', 3DR Holdings, New York, USA, 15th September, 2014
9. I. Raffeis, U. Vroomen, F. Adjei-Kyeremeh, D. Großmann, H. Hammelrath, E. Westhoff, S. Bremen, D. Boscolo Bozza and A. Bührig-Polaczek, *Materialwiss. Werkstofftech.*, 2020, **51**, (4), 432
10. J.-R. Zhao, F.-Y. Hung, C.-S. Lu and I.-C. Lai, *Adv. Eng. Mater.*, 2021, **23**, (6), 2001366
11. C.-L. Yang and K.-T. Yu, *J. Fail. Anal. Preven.*, 2013, **13**, (5) 521
12. H. Stiller, 'Material Intensity of Advanced Composite Materials: Results of a Study for the Verbundwerkstofflabor Bremen eV', Wuppertal Papers, No. 90, Wuppertal Institute for Climate, Environment, Energy gGmbH, Wuppertal, Germany, 1999, 38 pp
13. R. N. Wenzel, *Ind. Eng. Chem.*, 1936, **28**, (8), 988
14. A. B. D. Cassie and S. Baxter, *Trans. Faraday Soc.*, 1944, **40**, 546
15. R. Völkl, D. Freund and Fischer, *J. Test. Eval.*, 2003, **31**, (1)
16. 'Metallic Materials – Uniaxial Creep Testing in Tension – Method of Test', ISO 204:2018, International Organization for Standardization, Geneva, Switzerland, 2018, 53 pp
17. 'Standard Test Methods for Conducting Creep, Creep-Rupture, and Stress-Rupture Tests of Metallic Materials', ASTM E139-11, ASTM International, West Conshohocken, USA, 2018, 14 pp



18. 'Geometrical Product Specifications (GPS) – Filtration – Part 71: Robust Areal Filters: Gaussian Regression Filters', ISO 16610-71:2014, International Organization for Standardization, Geneva, Switzerland, 2014, 20 pp
19. C. Silbernagel, I. Ashcroft, P. Dickens and M. Galea, *Addit. Manuf.*, 2018, **21**, 395
20. A. A. Bourne and A. S. Darling, *Platinum Metals Rev.*, 1963, **7**, (2), 42
21. B. Trumić, L. Gomidželović, S. Marjanović, A. Ivanović and V. Krstić, *Mat. Res.*, 2017, **20**, (1), 191
22. T. Hamada, 'High Temperature Creep of Platinum and Its Alloys', Dissertation, Department of Physical Science, Osaka University, Japan, January, 1998, 87 pp
23. B. Fischer, A. Behrends, D. Freund, D. F. Lupton and J. Merker, *Platinum Metals Rev.*, 1999, **43**, (1), 18
24. E. I. Rytvin, "Heat Resistance of Platinum Alloys", Ore and Metals Publishing House, Moscow, Russia, 1987
25. G. Reinacher, *Platinum Metals Rev.*, 1962, **6**, (4), 148
26. G. L. Selman, M. R. Spender and A. S. Darling, *Platinum Metals Rev.*, 1965, **9**, (4), 130
27. J. S. Acken, *Bur. Stand. J. Res.*, 1934, **12**, (2), 249

---

## The Authors



Thilo Becker works as a research associate and group leader of the inorganic fibres research group at the Institut für Textiltechnik (ITA) of the RWTH Aachen University, Germany. His current research focuses on glass fibre production technology. In recent years, he has driven forward the industrialisation of additive manufacturing technology for the production of glass fibre bushings.



Thomas Gries studied at the RWTH Aachen University. He holds a diploma in mechanical engineering and economics and a doctorate in mechanical engineering. From 1995 to 2001, he worked at Lurgi Zimmer AG, Frankfurt am Main, Germany, at the Department of Technologies for Fibres & Textiles in leading positions. From April 2001 onwards, he is Director of the ITA of RWTH Aachen University.

# On the Sustainability of Palladium in Organic Synthesis: A Perspective

## Palladium-based catalysis: its availability and use, today and tomorrow

### B. H. Lipshutz

Department of Chemistry and Biochemistry,  
University of California, Santa Barbara,  
CA 93106, USA

Email: [lipshutz@chem.ucsb.edu](mailto:lipshutz@chem.ucsb.edu)

### PEER REVIEWED

Received 12th August 2022; Accepted 15th November 2022; Online 30th November 2022

What's the long- and short-term prognosis for palladium in organic synthesis, the key platinum group metal (pgm) for transition metal-based catalysis used today by the fine chemicals industries? Are these processes green and sustainable? Are they environmentally respectful of the metals, especially the pgms, so essential to modern day society? Are non-pgm 'earth abundant' metals an attractive alternative? Where does the up-and-coming area of chemoenzymatic catalysis, which combines chemo- and biocatalysis in one-pot processes in water, fit into the future of drug syntheses? And what about agricultural targets also being made that include palladium catalysis? These and related timely topics are discussed in this Perspective.

### 1. Is Palladium in Crisis?

Ask any card-carrying organic chemist which metal reigns supreme today in synthetic organic chemistry and most, if not all, will quickly identify palladium as the clear winner. But this soft, silver-white metal is only one of six that make up the pgms, which also include ruthenium, osmium, platinum, rhodium, and iridium. According to the

American Chemical Society (ACS) Green Chemistry Institute (1), palladium has "limited availability..."; the other five are also endangered, given their "rising threat from increased use". In brief, they are, in one way or another, all at risk. And while neither osmium nor even ruthenium is considered 'precious' usually based on cost, both platinum and palladium are certainly 'expensive', while iridium, and especially rhodium, are borderline prohibitive, typically being reserved for reactions where catalyst loadings must be very low. During the past few years, the price of palladium has jumped on occasion to >US\$3000 per troy ounce, **Figure 1** (2), and even today remains competitive with that of gold (*ca.* US\$2000 per troy ounce). What does this suggest regarding the prognosis for pgms even in the short term, let alone the prospects for long-term availability? How can we continue today with a 'business as usual' mentality, knowing that these particular resources on the planet are finite? Are we not already operating in crisis mode, if only on the basis of price, where palladium may provide, at least on paper, the solution to an important synthetic problem but its use in the laboratory is simply unaffordable? For many contract manufacturing organisations (CMOs) that make crucial intermediates, that time is already here. What now?

### 2. Earth-Abundant Metals?

One prevailing sentiment is that base metals will come to the rescue (3, 4). Do we actually have base metal-catalysed processes ready to step in and allow the community to achieve the same goals? Hardly; the science is simply not there yet. Most notably, reactions looking to replace palladium, for example, with typically 5–10 mol% nickel may offer

academic solutions but, in reality, are just replacing one problem of metal scarcity with others. That is, aside from the additional options for mechanistic variations, for example, with nickel having facile access to various oxidation states normally not commonly involved in palladium catalysis (i.e., Ni(I) and Ni(III)) thereby leading potentially to side-product formation, a different array of ligands is usually required to match nickel for the intended chemistry. More vigorous conditions are also common, thereby requiring greater investments of both energy and time. And lastly, looming large in what is rarely acknowledged in publications using such high loadings in catalysis is the all-but-certain elevated levels of residual metal in each product. This may not be an issue for many practitioners, but it is a crucial consideration in the pharmaceutical industry where the limit according to International Conference on Harmonisation (ICH) Q3D guidelines, for example, for nickel in oral drugs is 20 ppm or less than 200  $\mu\text{g day}^{-1}$  (5–7). Even using 1 mol% of a nickel catalyst is virtually guaranteed to lead to >100 ppm nickel in any product, thereby necessitating additional time and expense required for its removal. Taken together, all of these factors might better be viewed as exchanging the more obvious up-front costs with those overall reaction parameters associated with base metal catalysis. Such considerations, likewise, apply to other base metals beyond nickel (such as copper and cobalt) that, notwithstanding their historic roles played in alchemy, are today also endangered (1). Indeed, focusing on current prices as the sole indicator in the selection process may be leading us into a false sense of security. The reality is that this metric

alone is not an accurate measure in choosing a catalyst, whether considering pgms or otherwise.

While the catalyst selection process, therefore, perhaps argues for more widespread use of pgms, we must recognise that pgm availability, eventually, will begin to drop; that for decades the chemistry community continues to be unwilling to accept the shortages that will likely appear at some point, perhaps within the next 5–10 years, **Figure 1** (2). Is it acceptable today, therefore, or at any time in the near future for all 'consumers' to simply ignore this reality? It seems to always be the 'other guy' using pgms at scale in industrial laboratories who is the big offender, since academicians, for example, typically do chemistry with far smaller quantities. Of course, there are far more users in academia (both at the graduate and undergraduate levels, worldwide), and hence, the major offenders from the overall green chemistry perspective are... academicians! Let's also appreciate that while (transition metal) catalysis at any level of usage may be one of the fundamental "12 Principles of Green Chemistry" (1), it is listed at number nine. In other words, while pgms should be an integral part of environmentally responsible synthetic chemistry, where recycling must figure prominently (8), its usage should be viewed as part of a holistic picture.

### 3. Do We Have Options?

Today, most catalysis is still done, unfortunately, with far too much metal, precious or otherwise. Proof of this pervades the chemical literature and is easily seen; for example, recent work by big pharmaceutical companies (9–10). But beyond



Fig. 1. Price of palladium (per troy ounce) over time (2)



these catalyst issues, synthetic chemistry was developed in, and is 'matched' to, waste-generating organic solvents (6), thereby consuming enormous amounts of our limited petroleum reserves. Rarely acknowledged, of course, is that most of this organic waste is burned giving rise to CO<sub>2</sub>, much of which is released into the atmosphere. In addition, there are temperature requirements for catalytic processes, which typically means heating reactions (i.e., investing energy) that lead to byproducts that generate even more waste from subsequent product purification.

Along with transitioning away from organic solvents into alternative reaction media (11) come changes in the rules for doing organic synthesis (12); rules that embrace new opportunities as they appear, and that are in harmony with nature. With all these issues facing traditional organic chemistry, perhaps the overriding question that must be addressed is: should we be betting our future on 200 years of modern synthetic organic chemistry in organic solvents, or millions of years of chemistry by nature in water?

Fortunately, the beginnings of environmentally friendly and economically attractive alternatives are becoming more apparent on a regular basis. Not surprisingly, nature continues to provide guidance that is leading to viable solutions for the practice of organic chemistry that include: (a) minimising the need for organic solvents of any type, thereby dramatically reducing organic waste and allowing for telescoping to become routine, rather than limited due to individual reaction solvent needs; (b) reliance on lower levels of pgm-based catalysts, thereby extending the lifetime of available supplies; and (c) reactions being run under ambient temperatures, thereby avoiding higher temperature-induced byproduct formation,

along with associated investments of time and effort to effect separations.

Recognition of the path forward comes easily once an appreciation of nature's success is recognised... success realised all in water. But most chemistry of carbon involves water-insoluble materials, so what's nature's secret? Answer: 'dirty water'. The 'dirt', of course, corresponds to the numerous chemicals present in the oceans that might have assisted the evolutionary process: vesicles, membranes, salts and yes, micelles in which chemistry of water-immiscible compounds took place. Clearly, the Earth's water through time was not pristine.

Some of this 'dirt' that has led to numerous opportunities for transitioning several of the most heavily used reactions away from organic solvents focuses on development of 'benign by design' surfactants that enable chemistry 'in water'. Newly introduced amphiphiles such as the vitamin E-containing TPGS-750-M (13), proline-derived PS-750-M (14) and the rosin-based APGS-2000-M (15) (**Figure 2**) each spontaneously form micellar arrays upon dissolution in water (above their critical micellar concentrations, which tend to be very low). These are just a few examples of technologies that continue to show considerable promise for use in synthesis.

The potential for modernised micellar catalysis 'in water' to significantly extend pgm usage almost indefinitely (admittedly only with respect to synthetic chemistry) is represented by recently reported processes for the most heavily utilised palladium-catalysed cross-couplings; for example, Nobel Prize-winning Suzuki-Miyaura reactions (16). Hence, by varying either the ligand, as with HandaPhos (17), (**Figure 3**) or more recently biaryl N<sub>2</sub>Phos (18), or the substitution pattern on a palladacycle (especially with the most atypical

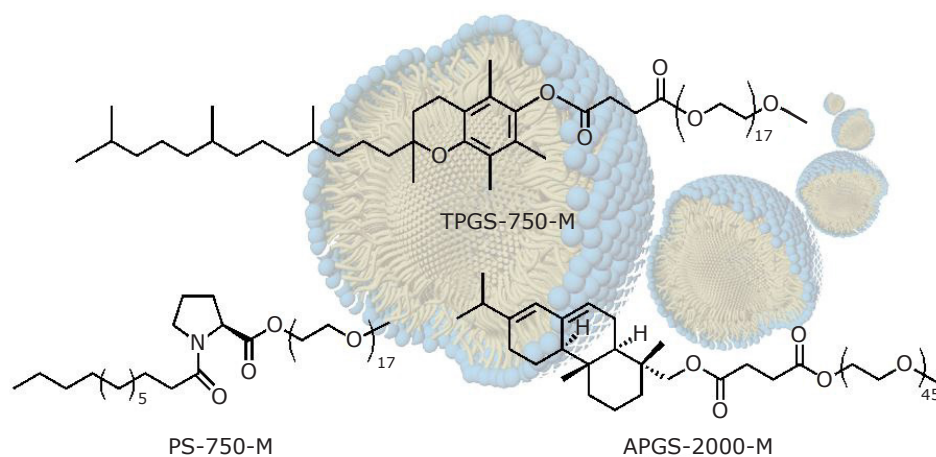


Fig. 2. Structures for three common surfactants used in aqueous micellar catalysis

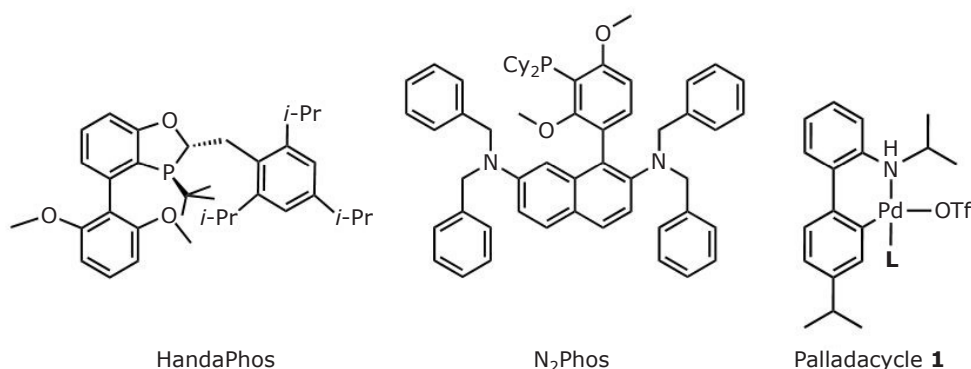
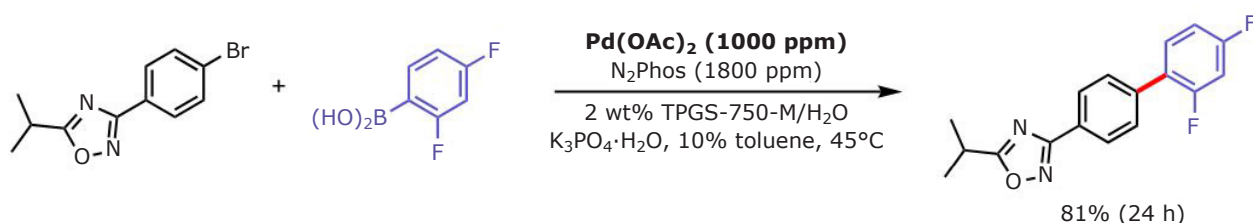


Fig. 3. Structure of ligands HandaPhos and N<sub>2</sub>Phos, and palladacycle **1**, for use in parts per million level palladium catalysis



Scheme I. Representative example of a Suzuki-Miyaura coupling in water using parts per million level palladium catalysis

but synthetically significant isopropyl group on nitrogen) (19) as in palladacycle **1**, key biaryl bonds involving highly functionalised reaction partners can now be made in water with loadings of palladium in the parts per million range (for example, as in **Scheme I**; 1000 ppm palladium = 0.1 mol%). Very similar options exist as well for related parts per million level palladium catalysis applied to Sonogashira (20), Stille (21), Mizoroki-Heck (22) and Negishi (23) couplings. The same is true for aminations (i.e., C-N bond formations), also now achievable in water using parts per million loadings of palladium (24–26). As industrial laboratories, especially in the pharmaceutical and agrochemical areas, face continuing regulatory scrutiny and demands that place restrictions on environmentally allowable chemistry (27), not to mention costs to the consumer, the importance of extending access to pgms *via* usage at parts per million levels becomes all-the-more obvious.

#### 4. Platinum Group Metals and Biotechnology, or Platinum Group Metals vs. Biotechnology?

Another area impacted, perhaps to the greatest extent by 'dirty water' that is destined to play an increasingly important role in the future of organic

synthesis, is chemoenzymatic catalysis (28). That is, featuring one-pot reaction sequences where both chemocatalysis and biocatalysis occur utilising the same 'solvent': water. The presence of an aqueous micellar medium accommodates the requirements of each type of catalysis: chemocatalysis, focusing on the type and amounts, for example, of pgms being used, and biocatalysis that relies mainly on enzymes present in the water, whether natural or engineered *via* directed evolution (29). Thus, as shown in **Figure 4**, the combination is especially powerful not only in allowing for tandem processes to take place, but also in its avoidance of unsustainable levels of precious metal catalysts (note the use of only 2500 ppm palladium, or 0.25 mol%). Moreover, the switch to water (11), rather than using organic solvents that typically involve aqueous workups of any intermediate(s), avoids waste-generating purification(s). The enzymes involved, with all their innate virtues, can thus be used either in the initial reaction; for example, a lipase, leading to esterification (30), or, in a subsequent step, for example, an initial transition pgm-catalysed reaction (such as a palladium-catalysed Sonogashira coupling) followed by an asymmetric carbonyl reduction mediated by a ketoreductase (KRED; such as, ADH101) to give a nonracemic

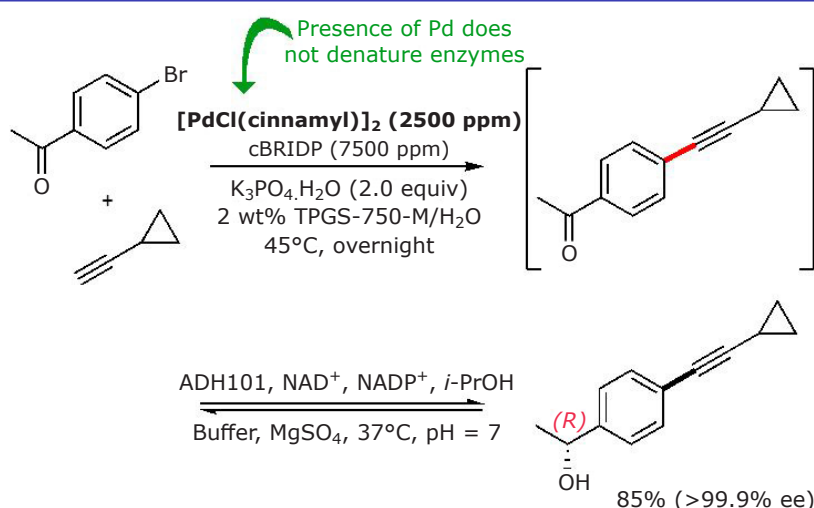


Fig. 4. Representative example of chemoenzymatic catalysis, where parts per million levels of palladium suffice

product alcohol, not surprisingly in high ee's (31). It should also be noted that the same surfactant technology that enables chemoenzymatic catalysis also ensures minimal enzyme denaturing due to the presence of pgms that continue being used in the unsustainable 1–10 mol% range (9, 10). Presumably, the nanomicelles provide alternative 'housing' for the pgm-based ligated catalyst, rather than its typical localisation in the aqueous buffered medium. Thus, with an order of magnitude less pgm present in the reaction medium, which is all that is now needed for chemocatalysis, chances are that the compatibility question associated with even highly sensitive enzymes might soon end up as a solved problem.

## 5. What's 'Wrong' with this Picture?

While the issues of sustainability noted above apply to all users of pgm catalysts, what's the view from industrial companies that process the raw materials leading up to the availability of pgm catalysts? After all, isn't there an implied assumption that they have unlimited access to metals, and pgms, in particular, needed by the chemistry enterprise? Assumptions aside, where are we today on this front (8), and just how much do other factors, such as geopolitical issues figure into the equation, for example, given that >40% of the world's supply of palladium comes from Russia (32)? In other words, what is being done to address future needs of pgms? Even when nature provides unexpected sources; for example, the finding that palladium is present to varying degrees as an 'impurity' in the mining of the truly Earth-abundant iron ore (33), the community at large still sees most of these discoveries not as opportunities (34) but as

experimental failures (35). These attitudes must change, and these questions must be addressed sooner than later. Otherwise, fundamental organic synthesis that depends so heavily on pgm-based catalysis in organic solvents will simply continue digging that 'rabbit hole', using more and more resources being taken from future generations. How much longer will it take before the obvious is acknowledged: that organic chemistry as currently practiced is unquestionably unsustainable?

Perhaps the graph in **Figure 1** illustrating the price of palladium over time helps tell the story (2). What will this picture look like 5–10 years from now? And even as society gradually moves away from gasoline-powered engines that dramatically increases supply as the need for catalytic converters eventually dwindles, in terms of long-term availability, aren't we just postponing the inevitable? Isn't the solution obvious: let's find a way, today, to do more with less. Just moving the decimal point in terms of usage one unit to the left solves the problem, both short and long term. And while hints that technology that relies on only parts per million loadings of palladium is already in hand (25, 33, 36, 37), any workable solution must include collaborations with industrial colleagues, especially those who not only share this vision for the future of pgms, but who also have their fingers at all times on the pulse of the field as to where we are and, perhaps more importantly, where we are going (8).

## 6. Conclusions

In summary, pgm-containing catalysts will continue to play crucial roles in processes currently in use or under development in academic and many

industrial laboratories, alike. Technologies already exist in the toolbox for reducing consumption of pgms to ensure that access to these absolutely essential metal-containing catalysts are available for both immediate and future use, with many more additions to this toolbox coming. Nonetheless, in the big picture sense, how pgms are viewed today must include both short-term and long-term perspectives. Short-term swings in availability are just that: short term. But overall, the chemistry community must appreciate that we are, today, stewards of a very important finite planetary resource requiring a holistic approach that ensures that tomorrow's needs in catalysis, mainly defined by having similar access to pgms, can be met.

## References

1. 'Endangered Elements', American Chemical Society, September, 2019, Washington, USA
2. 'Palladium Prices - Interactive Historical Chart', MacroTrends, Seattle, USA: <https://www.macrotrends.net/2542/palladium-prices-historical-chart-data> (Accessed on 28th July, 2022)
3. M. J. Goldfogel, X. Guo, J. L. Meléndez Matos, J. A. Gurak, M. V. Joannou, W. B. Moffat, E. M. Simmons and S. R. Wisniewski, *Org. Process Res. Dev.*, 2022, **26**, (3), 785
4. S. Handa, E. D. Slack and B. H. Lipshutz, *Angew. Chem. Int. Ed.*, 2015, **54**, (41), 11994
5. 'ICH Q3D Elemental Impurities - Scientific Guideline', European Medicines Agency, Amsterdam, The Netherlands: <https://www.ema.europa.eu/en/ich-q3d-elemental-impurities> (Accessed on 28th July 2022)
6. A. M. Thayer, 'Trace Metals Debate', *Chemical Engineering News*, Washington, DC, USA, August, 2013
7. 'Committee for Human Medicinal Products (CHMP): Guideline on the Specification Limits for Residues of Metal Catalysts', Doc. Ref. CPMP/SWP/QWP/4446/00 corr., European Medicines Agency, Amsterdam, The Netherlands, January, 2007, 32 pp
8. E. Schofield, *Johnson Matthey Technol. Rev.*, 2023, **67**, (3), 285
9. S. Pithani, M. Malmgren, C.-J. Aurell, G. Nikitidis and S. D. Friis, *Org. Process Res. Dev.*, 2019, **23**, (8), 1752
10. G. L. Beutner, E. M. Simmons, S. Ayers, C. Y. Bemis, M. J. Goldfogel, C. L. Joe, J. Marshall and S. R. Wisniewski, *J. Org. Chem.*, 2021, **86**, (15), 10380
11. B. H. Lipshutz, *J. Org. Chem.*, 2017, **82**, (6), 2806
12. B. H. Lipshutz, *Curr. Opin. Green Sus. Chem.*, 2018, **11**, 1
13. B. H. Lipshutz, S. Ghorai, A. R. Abela, R. Moser, T. Nishikata, C. Duplais, A. Krasovskiy, R. D. Gaston and R. C. Gadwood, *J. Org. Chem.*, 2011, **76**, (11), 4379
14. J. Brals, J. D. Smith, F. Ibrahim, F. Gallou and S. Handa, *ACS Catal.*, 2017, **7**, 7245
15. Y. Zhang, B. Zhu, Y. Zheng and S. Huang, *J. Organomet. Chem.*, 2022, **965-966**, 122321
16. N. Miyaura and A. Suzuki, *J. Chem. Soc. Chem. Commun.*, 1979, (19), 866
17. S. Handa, M. P. Andersson, F. Gallou, J. Reilly and B. H. Lipshutz, *Angew. Chem. Int. Ed.*, 2016, **55**, (16), 4914
18. N. Akporji, R. R. Thakore, M. Cortes-Clerget, J. Andersen, E. Landstrom, D. H. Aue, F. Gallou and B. H. Lipshutz, *Chem. Sci.*, 2020, **11**, (20), 5205
19. R. R. Thakore, B. S. Takale, F. Gallou, J. Reilly and B. H. Lipshutz, *ACS Catal.*, 2019, **9**, (12), 11647
20. B. Jin, F. Gallou, J. Reilly and B. H. Lipshutz, *Chem. Sci.*, 2019, **10**, (12), 3481
21. B. S. Takale, R. R. Thakore, G. Casotti, X. Li, F. Gallou and B. H. Lipshutz, *Angew. Chem. Int. Ed.*, 2021, **60**, (8), 4158
22. H. Pang, Y. Hu, J. Yu, F. Gallou and B. H. Lipshutz, *J. Am. Chem. Soc.*, 2021, **143**, (9), 3373
23. Y. Hu, M. J. Wong and B. H. Lipshutz, *Angew. Chem. Int. Ed.*, 2022, **61**, (39), e202209784
24. Y. Zhang, B. S. Takale, F. Gallou, J. Reilly and B. H. Lipshutz, *Chem. Sci.*, 2019, **10**, (45), 10556
25. R. R. Thakore, K. S. Iyer and B. H. Lipshutz, *Curr. Opin. Green Sustain. Chem.*, 2021, **31**, 100493
26. J. R. A. Kincaid, M. J. Wong, N. Akporji, F. Gallou, D. M. Fialho and B. H. Lipshutz, *J. Am. Chem. Soc.*, 2023, **145**, (7), 4266
27. J. Becker, C. Manske and S. Randl, *Curr. Opin. Green Sustain. Chem.*, 2022, **33**, 100562
28. L. Bering, J. Thompson and J. Micklefield, *Trends Chem.*, 2022, **4**, (5), 392
29. F. H. Arnold, *Angew. Chem. Int. Ed.*, 2018, **57**, (16), 4143
30. V. Singhania, M. Cortes-Clerget, J. Dussart-Gautheret, B. Akkachairin, J. Yu, N. Akporji, F. Gallou and B. H. Lipshutz, *Chem. Sci.*, 2022, **13**, (5), 1440
31. M. Cortes-Clerget, N. Akporji, J. Zhou, F. Gao, P. Guo, M. Parmentier, F. Gallou, J.-Y. Berthon and B. H. Lipshutz, *Nat. Commun.*, 2019, **10**, 2169
32. 'Value of Palladium Exports from Russia from 2018

- to 2021 (in Million US Dollars)', Statista Inc, New York, USA, May, 2022
33. S. Handa, Y. Wang, F. Gallou and B. H. Lipshutz, *Science*, 2015, **349**, (6252), 1087
34. S. K. Ritter, 'A More Natural Approach to Catalysts', *Chemical Engineering News*, Washington, DC, USA, February, 2017
35. L. K. Boerner, 'Metal-Free? The Mistake that Chemists Seem Doomed to Repeat', *Chemical Engineering News*, Washington, DC, USA, February, 2022
36. B. H. Lipshutz, J. C. Caravez and K. S. Iyer, *Curr. Opin. Green Sustain. Chem.*, 2022, **38**, 100686
37. B. H. Lipshutz, *Synlett*, 2021, **32**, (16), 1588

---

## The Author



Bruce Lipshutz is currently a Distinguished Professor of Chemistry at the University of California, Santa Barbara (UCSB), USA. His research group continues to develop new technologies that are environmentally responsible by enabling key transition metal-catalysed cross-couplings and many other of the most common reactions to be carried out in water under mild conditions. The Lipshutz group has also focused its attention on developing new catalysts for key palladium and several other transition metal-catalysed reactions that enable C–C, C–N and C–H bond formation, typically involving both precious and base metals at the parts per million level. Most recently, these newly developed technologies in chemocatalysis have been merged with biocatalytic processes, commonly referred to as 'chemoenzymatic catalysis', which allow for tandem, one-pot reactions, all enabled by designer surfactants in water.

---



# On the Criticality of Palladium in Organic Synthesis: A Perspective

## Palladium-based catalysis: a field with scope for expansion

### Emma R. Schofield

Johnson Matthey, Blounts Court, Sonning Common, Reading, RG4 9NH, UK

Email: [Emma.schofield@matthey.com](mailto:Emma.schofield@matthey.com)

### PEER REVIEWED

Received 12th October 2022; Revised 28th November 2022; Accepted 28th November 2022; Online 30th November 2022

The palladium price has been rising because emissions legislation necessitates using more palladium in catalytic converters. However, this trend will not continue as the energy transition progresses, and in the future there will be considerably more palladium available to use in other applications, including chemicals, pharmaceuticals and agrochemicals catalysts. This is both opportunity and justification for the organic chemistry research community to develop new and significant uses for palladium that can be of global benefit. Any catalyst research needs to include optimisation of circular economy, offering sustainable process and recovery options to support life cycle assessment (LCA).

### Palladium as a Critical Metal

Palladium is the metal of choice for many catalytic coupling reactions in organic synthesis. It is particularly useful in the homogeneous synthesis of high-value target molecules in the pharmaceutical and agrochemical industries. It features on the UK (1), USA (2) and European

Union (EU) (3) critical minerals lists as one of a set of platinum group metals (pgms) which are simultaneously technologically significant, difficult to substitute and sourced in parts of the world where there can be political instability.

Because of its critical metal status, and because metals are by their nature finite resources, some have expressed concern about the future of palladium in organic synthesis (4, 5). For those of us who grew up with a palladium price that was comfortably below those of gold and platinum, the recent price highs (**Figure 1**) stir fears about whether palladium will price itself out of catalyst markets (6).

Why is the palladium price currently so high? Anyone who reads Johnson Matthey's 'PGM Market Report' will be aware that there is currently more demand for palladium than there is palladium to fulfil it (7). This is because palladium is a vital



Fig. 1. Johnson Matthey palladium base price showing variability from 2015 to 2022

metal in catalytic converters, which are required to minimise exhaust emissions. Vehicle emissions limits are subject to increasingly strict legislation in many parts of the world, including China, the USA and Europe. To achieve these stricter emissions limits, the loading of pgm on the catalysts is increasing so more and more palladium is being used by the catalytic converter market.

### Palladium in the Chemicals Sector

It may come as a surprise to catalyst chemists to discover that only about 6% of global palladium demand was used in the chemicals sector in the year to April 2022. 83% of the available palladium (Figure 2) was used in automotive catalytic converters. This, however, is expected to change as a result of international initiatives to replace the internal combustion engine with battery and fuel cell powered vehicles. In the USA, an executive order for cars and light duty trucks states that “half of all new vehicles sold in 2030 be zero-emissions vehicles” (8), the UK has announced the end of the sale of new non-zero emission cars and vans by 2035, and the European Parliament is backing a European Commission proposal for a total ban on new CO<sub>2</sub>-emitting cars and vans by 2035. Declining production of the internal combustion engine will result in declining demand for palladium in its major market. In the later years of the transition, palladium consumption by the chemicals sector has the scope to increase six-fold without constraining supply.

### Supply vs. Demand

If the demand for palladium in catalytic converters goes down, will market forces not ensure decreased supply of palladium to compensate?

Neither historical supply data, nor the economics of palladium refining, indicate that this will occur.

The supply of pgms in a given year comes from three sources: mining, recycling and reserves of above-ground metal (for example, investment bars and jewellery). Over the past 10 years the ratio for palladium of recycled to primary supply has been approaching 1:2 (Figure 3). In this period there has been no marked increase in the outputs from mining in response to market demand nor marked decreased due to finite supplies. In fact, mined supply has been relatively flat: while some mines have expanded, and surface stocks have been mobilised in response to strong demand, there has been declining production at other, older mines. Open-loop recycled supply has increased gradually ever since 1984.

Palladium supply is not directly controlled by the market because 90% of palladium mined every year is produced as a byproduct of either platinum or nickel mining. As a result, the availability of palladium is inextricably linked with the supply of the metals it is mined with, and the economics of mining palladium depend on the combined worth of the coextracted metals. In reporting the value of mine output, pgm producers refer to the basket price, which is the combined price of a troy ounce of the particular ratio of pgms, or pgms and gold, that are extracted together. It is the ore, not the market, that determines what that ratio is. The mining sector can influence the longer-term future palladium supply to some degree by selecting whether to develop palladium-rich or palladium-poor deposits but, irrespective of whether palladium is in surplus or deficit, it will continue to be produced as one of a basket of valuable metals.

The same co-dependencies exist in palladium supply from recycling processes. Recycling autocatalysts, which will continue for many years

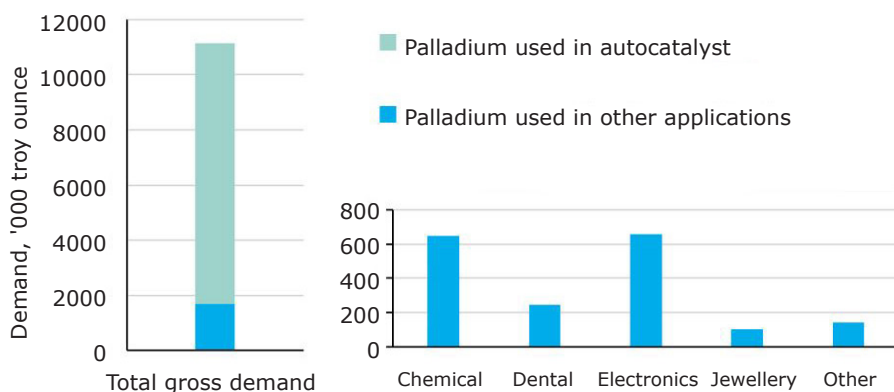


Fig. 2. Proportion of the 2021 demand for palladium taken up by autocatalysts and other applications

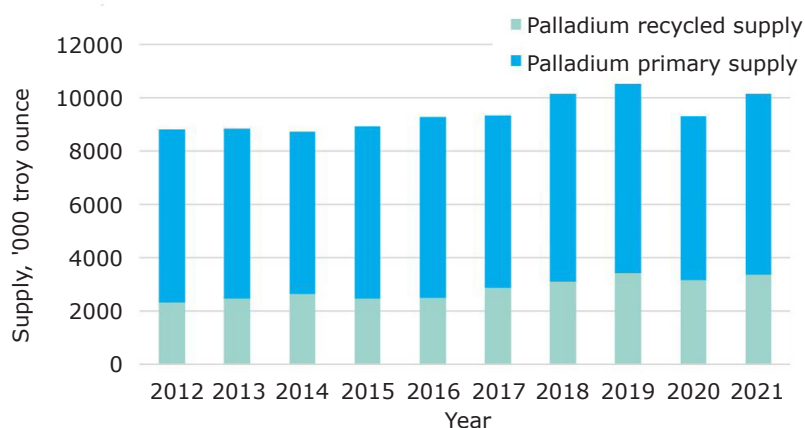


Fig. 3. Amount of palladium produced by mining and by refining over the past 10 years

after the 2030/2035 turning point, necessitates refining palladium along with rhodium and platinum. Even in jewellery platinum can be alloyed with some palladium. As long as alloys and mixtures of pgms are recycled, palladium will continue to be produced.

## Palladium for the Future

The fact that in the longer term there will be plenty of palladium for use in manufacturing is good news for the synthetic organic chemist, and for global dependence on agriculture and the pharmaceutical industry. But if the availability of palladium results in its price decreasing long term, what impact is that likely to have on the other pgms which are palladium's coproducts?

Technologies for the energy transition need metals with good electrochemical and catalytic properties, that withstand extreme conditions and do not corrode. The pgms are unique in their ability to do this. Examples include platinum in fuel cells, iridium in proton exchange membrane electrolyzers and all the pgms in process catalysts for sustainable and bio-derived fuels (9). But if the price of palladium goes down because future availability exceeds market demand, it will become economically less favourable to mine and recycle all of the pgms. This will have little impact on the availability of palladium to the chemicals sector but could limit supply of other pgms into alternative energy technologies, which the world urgently needs.

The solution to this problem is that we are going to need to use more palladium in the future. Only by using more palladium will it be possible to justify continuing to mine and recycle all the pgms. Having more applications of palladium will put supply of all the pgms on a more sustainable footing by making

mining and processing more economically viable, but also by ensuring that the valuable byproducts are not wasted. And as long as that palladium becomes part of the circular economy, it will contribute to long-term future availability.

From the perspective of pgms being a scarce and finite resource, this solution may appear counterintuitive. However, the thesis of this paper is that finding new applications for palladium is a necessary step in protecting the future availability of all the pgms. This conclusion is justification and opportunity for the scientific community, and particularly for the fine chemicals industry, to focus efforts on inventing the new, high-volume applications of palladium that will be required. And given it can take 10 years to go from laboratory to plant, the time to start inventing those applications is now.

Recognising this, the pgm industry is actively searching for new applications for palladium. The Global Palladium Fund was established in 2016 with the remit "to advance the development of world-changing technologies in essential areas such as aerospace, electronics, and the automotive industries" and in 2022, with sponsorship from Nornickel, the International Precious Metals Institute issued the Palladium Challenge (on hold at the time of writing due to subsequent developments) to expand the scope of applications that use palladium. Johnson Matthey, too, is giving away samples of palladium and other pgms to encourage research into new applications (10).

## Palladium Sustainability

Achieving net-zero goals is a challenge that has been taken to heart by the chemistry community. Where previously cost and catalyst performance were the deciding indicators of success, the

past decade reveals an increasing focus on the conditions and environmental impact of catalyst-mediated processes (5). Reaction conditions that have the potential to contribute to a sustainable process include: using less palladium (thrifting); avoiding organic solvents in favour of water (11); processing at ambient temperature; one-pot reactions; using recycled palladium; recovering ligands; using stoichiometric reagent instead of excess. Which of these parameters actually contribute to a sustainable process is a complex question.

Take thrifting. Metal is generally thrifted to decrease manufacturing costs and minimise the value locked up in a batch of catalyst. Ground-breaking research has proved that it is possible to decrease palladium catalyst loadings significantly while maintaining and, in some cases, improving catalyst performance (12). Thrifting is unquestionably a good way to ensure scarce metals are more widely available. The drawback is that thrifting can make recycling more difficult. The less pgm there is in a catalyst, or the more performance additives it contains, the more difficult the metal can be to recover at the end of life and the more waste can be produced. In a market-driven industry, if the cost of recycling exceeds the value of the pgm, there is no economic motivation to recover the metal.

A significant step towards solving this would be to include circular economy as an intrinsic parameter of catalyst performance, alongside yield, selectivity, cost and turnover number. In this paradigm, a good catalyst is one from which the palladium (or any critical metal) can easily be recovered at end of life. And it's not just about reusing the metal. Currently, in recovering the palladium from some homogeneous catalysts, the sophisticated and expensive ligands required to tune the catalytic reaction are burned. Being able to recover undegraded ligands as well as metal from the end-of-life mixture has the potential to decrease both the cost and environmental impact of a process. This is an avenue of investigation that the research community is ideally placed to follow: those who put the catalyst together are surely best placed to understand how it can be taken apart again most efficiently at end of life. Doing the recycling research alongside new catalyst development builds design for recycle into the catalyst discovery process and creates a product tailored for the net zero future.

Does using recycled palladium contribute to a sustainable process? With today's technology, recycled pgms have much less environmental

impact than newly mined pgms, so using recycled palladium improves the sustainability metrics of the individual process. The global picture is more complicated. The world currently uses all of the palladium available, whether mined or recycled. If the size of the market were unchanging, one process using recycled metal would just mean another process has to use mined metal and there would be no global impact of using one over the other. However, at the moment the demand for palladium is greater than what is produced. If that demand can be met by producing more recycled metal rather than mining more metal, then there is a global sustainability benefit to using recycled palladium in a catalyst.

Throughout this section, care has been taken to use 'potential' in phrases such as 'decrease in environmental impact'. Actually it's impossible to know whether adopting 'sustainable' reaction conditions will result in a lower environmental impact across the whole life cycle of the catalyst. The only way to be sure is to do the LCA. However, it is essential to do research to develop more eco-friendly process options that avoid ecotoxic solvents, excesses of reagents or high energy use because it gives the process chemist the best range of alternatives when it comes to comparing process options in the LCA.

## Conclusion

Palladium will become increasingly available in the longer term as the energy transition proceeds towards and beyond the 2030/2035 turning point. Rather than constraining research or substituting less satisfactory alternative metals because the palladium price is currently high, this is the time when synthetic organic chemists need to be developing the future palladium catalysts on which the chemical, pharmaceutical and agrochemical sectors depend.

New catalysts will need to become part of a circular economy where recovery and reuse of the palladium and its ligands are an intrinsic feature of catalyst design. And using tools such as LCA to evaluate routinely which process options have minimum environmental impact will ensure chemical processes are ever more sustainable.

Beyond this opportunity in palladium catalysis, there is a need for broader use of palladium in the future. The circular economy of the pgms depends on all of the metals that are co-mined or co-recycled contributing to the economic viability of processing. Making beneficial use of more palladium in future

safeguards the availability of the other pgms which are critical to the net zero transition.

## Acknowledgements

Particular thanks are owed to Marge Ryan, Lucy Bloxham and the excellent Precious Metals Marketing team at Johnson Matthey, and to Professor Bruce Lipshutz (University of California, Santa Barbara, USA) who inspired the research.

## References

1. 'Resilience for the Future: The UK's Critical Minerals Strategy', Policy Paper, Department for Business, Energy & Industrial Strategy, London, UK, 13th March, 2023
2. 'US Geological Survey Releases 2022: List of Critical Minerals', US Geological Survey, Reston, USA, 22nd February, 2022
3. 'Critical Raw Materials Resilience: Charting a Path Towards Greater Security and Sustainability', Document 52020DC0474, COM(2020) 474 Final, European Commission, Brussels, Belgium, 3rd September, 2020
4. L. Poli, *McGill Green Chem. J.*, 2015, **1**, 56
5. S. McCarthy, D. C. Braddock and J. D. E. T. Wilton-Ely, *Coord. Chem. Rev.*, 2021, **442**, 213925
6. B. H. Lipshutz, *Johnson Matthey Technol. Rev.*, 2023, **67**, (3), 278
7. A. Cowley, "Pgm Market Report", Johnson Matthey, London, UK, May, 2021, 60 pp
8. 'FACT SHEET: Biden-Harris Administration Proposes New Standards for National Electric Vehicle Charging Network', The White House, Washington, DC, USA, 9th June, 2022
9. C. Xu, E. Paone, D. Rodríguez-Padrón, R. Luque and F. Mauriello, *Renew. Sust. Energy Rev.*, 2020, **127**, 109852
10. E. Schofield, *Johnson Matthey Technol. Rev.*, 2021, **65**, (4), 595
11. M. Cortes-Clerget, J. Yu, J. R. A. Kincaid, P. Walde, F. Gallou and B. H. Lipshutz, *Chem. Sci.*, 2021, **12**, (12), 4237
12. Y. Hu, M. J. Wong and B. H. Lipshutz, *Angew. Chem. Int. Ed.*, 2022, **61**, (39), e202209784

---

## The Author



Emma Schofield is the Platinum Group Metal Research Fellow at Johnson Matthey, UK. Having spent over a decade researching improvements to pgm recycling technologies, her focus over the past few years has increasingly been on circular economy of critical metals. She was a Commissioner for the April 2021 UK Policy Commission on Securing Strategic Elements and Critical Materials, and as a member of the Critical Minerals Expert Group supported development of the UK Government's July 2022 Critical Minerals Strategy.



# Dependence of Mechanical Properties of Platinum-Rhodium Binary Alloys on Valence Electron Parameters

## Increasing valence electron ratio improves alloy properties

### Mehrdad Zarinejad\*

Department of Materials Science and Technology, PB Research Centre, Oshawa, ON, L1H 7K4, Canada

### Sajjad Rimaz

Department of Chemical and Biomolecular Engineering, National University of Singapore, 4 Engineering Drive 4, 117585, Singapore

### Yunxiang Tong

Institute of Materials Processing and Intelligent Manufacturing, College of Materials Science and Chemical Engineering, Harbin Engineering University, Harbin, 150001, China

### Kiyohide Wada

Faculty of Science and Engineering, Swansea University, Bay Campus, Fabian Way, Crymlyn Burrows, Swansea, SA1 8EN, UK

### Farshid Pahlevani

Centre for Sustainable Materials Research and Technology, SMaRT@UNSW, School of Materials Science and Engineering, UNSW Sydney, NSW 2052, Australia

\*Email: [mehr0003@e.ntu.edu.sg](mailto:mehr0003@e.ntu.edu.sg)

### PEER REVIEWED

Received 21st February 2022; Revised 28th April 2022; Accepted 16th May 2022; Online 16th May 2022

Dependence of mechanical properties of binary platinum-rhodium alloys on valence electron

ratio (VER), number of valence electrons ( $e_v$ ) and average atomic number of the alloys ( $Z$ ) are investigated. The alloys have a high number of valence electrons ( $9 \leq e_v \leq 10$ ) and a wide range of average atomic numbers ( $Z = 45-78$ ). Clear correlations between VER of the alloys and their mechanical properties are found. By increasing the VER of the alloy from 0.13 to 0.20 following the increase of rhodium content in the composition, the hardness, elastic modulus and ultimate tensile strength (UTS) of the alloy increases. Creep rates of the selected alloys clearly decrease with increasing VER at high temperatures (1500–1700°C), while stress rupture time at different temperatures consistently increases because of higher rhodium content in the alloy solid solution chemistry. Dependence of mechanical properties on valence electron parameters is discussed with reference to the atomic bonding.

## 1. Introduction

Platinum alloys attract considerable attention as new areas of application are found and continuously explored. Platinum alloys are used to produce jewellery (1, 2), thermocouples (3), resistance thermometers (4), resistance temperature detector sensors (5), catalysts (6) and glass fabrication equipment (7–9) due to their high strength, good workability and corrosion resistance at high temperatures (10, 11). The analysis of Gavin clearly indicates increased attention to platinum alloys (12). Hu *et al.* have recently presented research into platinum-based superalloys for high-temperature applications (13). Solid solution strengthened platinum-based alloys have been

the subject of research and development for some time. All transition group elements have considerable solid solubility in platinum. The elements near platinum in the periodic table form a continuous solid solution with platinum and have different degrees of solid solution strengthening effect on the platinum matrix. Platinum-based alloys are also being developed for high-temperature structural applications with the aim of replacing some of the currently used nickel-based superalloys (NBSAs) (13). Platinum-based superalloys have a similar structure to NBSAs and can potentially be used at higher temperatures and in more aggressive environmental conditions. Platinum-based superalloys show strong chemical stability and excellent mechanical properties such as high creep strength and ductility and can be used for next generation gas turbine materials and in chemical, glass and space technologies (14–21).

Of all platinum alloys, currently the most widely used are alloys of platinum with rhodium. Their range of application temperature is extended up to 1600°C (10). Luyten *et al.* have examined the platinum-rhodium, platinum-palladium, palladium-rhodium and platinum-palladium-rhodium phase diagrams using the Monte Carlo simulation method in combination with the modified embedded atom method (MEAM) and optimised parameters (22). Thermodynamics and phase equilibria of the binary platinum-rhodium system were studied by Jacob *et al.* (23) and Okamoto (24). To adjust the properties of these intermetallics, rhodium as the alloying element is added to platinum. Platinum and rhodium are completely miscible and form a single-phase solid solution at all concentrations of rhodium as shown by Okamoto (24).

New materials based on dispersion strengthening of platinum-rhodium alloys have been developed for high-temperature applications (25–27). Microstructural analyses of selected platinum alloys used in industry and jewellery (including PtRh10 and PtRh30) were performed by Battaini (28). Fischer *et al.* (29) studied the stress-rupture strength and creep behaviour of platinum, platinum-rhodium and platinum-iridium alloys, dispersion hardened platinum materials, rhodium and iridium. Investigations of elastic properties (Young's modulus, modulus of rigidity and Poisson's ratio) for platinum, platinum alloys, rhodium and iridium at high temperatures using a resonance technique have been carried out by Merker *et al.* (30). They observed that Young's modulus and the modulus of rigidity of platinum, rhodium, iridium and various platinum alloys in the as-cast condition decrease

linearly with increasing test temperature. Platinum-rhodium alloys have more stable properties: an increase in rhodium content leads to higher temperature durability, extended creep life and decreased creep rate (13, 29). At higher rhodium content, however, the machinability of the alloys may be negatively affected (13). Darling presented the high-temperature and room-temperature properties of platinum-rhodium alloys as a function of rhodium content and service temperature in earlier work (31), while the work of Ackmen on the mechanical properties of platinum-rhodium was the first published report available in the literature (32). Rdzawski and Stobrawa studied the microstructural evolution and mechanical properties of yttrium- and boron-alloyed platinum-rhodium (33). Garbacz *et al.* studied the microstructure and mechanical properties of a platinum-rhodium alloy produced by powder metallurgy and subjected the alloy to plastic working (34).

One of the research goals in this area is to develop materials with better high-temperature mechanical properties (for example, tensile, fracture, creep and thermomechanical fatigue properties) and environmental stability (for example, resistance to high-temperature oxidation and hot corrosion) than NBSAs (13, 35). Platinum and its alloys represent a major challenge because of the high cost of materials and need for special experimental conditions (10). Finding fundamental correlations between structural factors of these alloys and their mechanical properties can help reduce the cost with less trial-and-error and difficulty.

To understand the factors that control the elastic and mechanical properties and transformation temperatures in alloy systems, Zarinejad suggested the need to acquire in-depth knowledge of how the atomic bonding strength of the solid solutions can be influenced by the chemical composition of the alloys (36). Apart from microstructural features such as precipitates and grain boundaries, the mechanical properties of the matrix crystals of solid solution alloys in several alloy systems such as nickel-titanium (37–41), titanium-palladium, titanium-platinum (42), titanium-gold titanium-iridium (43) and many other alloy systems (44) were shown to be influenced by the alloy chemistry and how the metallic bonding changes with chemical composition change. Hence, the dependence of mechanical properties of solid solutions on electron variables in alloys was introduced (36–44). It was shown that the mechanical properties (elastic moduli and plastic deformation characteristics) of the solid solution crystals are influenced by

changes in the chemical composition. Knowing that in metallic materials, the delocalised valence electrons dominate the bond strengths and elastic properties (45, 46), it is of particular importance to study the electronic parameters of alloys. In this study, the investigation is extended to the platinum-rhodium binary alloys to help understand the dependence of the mechanical properties on alloy chemistry.

The aim of this study is to show the dependence of mechanical properties of binary platinum-rhodium alloys on the VER of the alloys, which is related to the chemical composition, or the atomic fraction of platinum and rhodium in the alloys. The study focuses on existing data on hardness, tensile strength, creep rate and rupture time for the platinum-rhodium binary alloys. We reveal and explain the dependence of the mechanical properties of platinum-rhodium binary alloys on these parameters with a focus on the correlation of the mechanical properties to VER of the alloys. The correlations found in this study will provide important understanding towards effective alloy design.

## 2. Materials and Methods

Mechanical properties data including creep rate, rupture time, tensile strength and hardness of single-phase platinum-rhodium binary alloys (without precipitate or mechanical work) made to date were investigated. The data were extracted from the relevant literature especially the works of Trumic *et al.* (10, 11), Fischer *et al.* (29), Darling (31), Acken (32), Hu *et al.* (47) and other sources (48, 49) as listed in tables or presented in graphs. For the analyses in this study, three simple parameters were considered: (a) the average atomic number of the alloys; (b) the number of valence electrons and (c) VER of the alloys.

The average atomic numbers of the alloys were calculated based on the atomic fractions and atomic numbers of the elements comprising the alloys as follows, Equation (i):

$$Z = f_{Pt}Z_{Pt} + f_{Rh}Z_{Rh} \quad (i)$$

where  $Z$  is the fraction-averaged atomic number of the alloy.  $Z_{Pt}$  and  $Z_{Rh}$  are the atomic numbers of platinum and rhodium, respectively.  $f_{Pt}$  and  $f_{Rh}$  are the corresponding atomic fractions of platinum and rhodium in the alloy. To study the dependence of the transformation temperatures on the chemistry of alloys, the basic electron configurations of the alloys are analysed in the following section.

The number of valence electrons in a transition metal atom is usually considered as the number of  $d$  and  $s$  electrons. The valence electrons per atom of platinum-rhodium binary alloys can be calculated based on the atomic fractions of the elements in the alloy by Equation (ii):

$$\frac{e_v}{a} = f_{Pt}e_v^{Pt} + f_{Rh}e_v^{Rh} \quad (ii)$$

where  $f_{Pt}$  and  $f_{Rh}$  represent the atomic fractions of platinum and rhodium in the alloy, respectively, and  $e_v^{Pt}$  and  $e_v^{Rh}$  are the corresponding numbers of valence electrons of elements platinum and rhodium.

The VERs of the alloys were calculated. VER is defined as the ratio of the number of valence electrons to the total number of electrons of the alloy,  $VER = (e_v/e_t)$ , which can be simply calculated by Equation (iii):

$$VER = \frac{e_v}{e_t} = \frac{f_{Pt}e_v^{Pt} + f_{Rh}e_v^{Rh}}{f_{Pt}Z_{Pt} + f_{Rh}Z_{Rh}} \quad (iii)$$

where, following the earlier Equations (i) and (ii),  $Z_{Pt}$  and  $Z_{Rh}$  represent the atomic numbers of platinum and rhodium, respectively, whilst  $f_{Pt}$  and  $f_{Rh}$  represent their corresponding atomic fractions in the alloy.

## 3. Results and Discussion

### 3.1. Average Atomic Number

**Table I** presents eighteen binary platinum-rhodium alloy compositions (31, 32, 48, 49), together with their available mechanical properties including hardness, modulus of elasticity ( $E$ ) and UTS in ascending order as reported in the literature and from the present study. The maximum hardness in the fully annealed alloys (130 HV) corresponds to pure rhodium (maximum rhodium content percentage in the alloy). The lowest hardness corresponds to pure platinum (45 HV). Platinum ( $Z = 78$ ) has a higher atomic number than rhodium ( $Z = 45$ ). This means that by increasing the rhodium content of the alloy, the average atomic number of the binary alloy decreases whereas the hardness increases (**Table I**, **Figure 1**). Similarly, for the available data on  $E$  and UTS of these binary alloys, the decrease in average atomic number of the alloy with increasing rhodium content results in higher values (**Table I**). The values of  $E$  and UTS of platinum with no rhodium content and atomic number  $Z = 78$  increase from  $E = 151.7$  GPa and UTS = 144.7 MPa to  $E = 221$  GPa and UTS = 413.7 MPa, respectively, in a binary alloy

**Table I Number of Valence Electrons ( $e_v$ ), Average Atomic Number ( $Z$ ), Valence Electron Ratio and Mechanical Properties of Binary Platinum-Rhodium Alloys (31, 32, 48, 49)**

Pt-Rh, wt%	Pt-Rh, at%	$e_v$	$Z$	VER	Hardness, HV	E, GPa	UTS, MPa	Reference		
								Hardness	E	UTS
0	0	10	78	0.128	45	151.7	144.7	(31)	(31)	(31)
5	9.1	9.909	74.997	0.132	63	172.4	206.8	(31)	(31)	(31)
10	17.4	9.826	72.258	0.136	79	191.7	292.3	(48)	(31)	(48)
10.01	17.5	9.825	72.225	0.136	80	-	-	(49)	-	-
13	22.1	9.779	70.707	0.138	82	196.5	318.5	(31)	(31)	(31)
15	25.1	9.749	69.717	0.140	86	201.3	343.3	(48)	(31)	(48)
18.1	29.5	9.705	68.265	0.142	88	206.8	355	(48)	(31)	(48)
20	32.2	9.678	67.374	0.144	90	213.7	372.3	(31)	(31)	(31)
25	38.8	9.612	65.196	0.147	97	218	386.1	(31)	(31)	(31)
30	44.9	9.551	63.183	0.151	102	221	413.7	(31)	(31)	(31)
35	50.6	9.494	61.302	0.155	105	-	-		(31, 32)	
40	55.9	9.441	59.553	0.159	108	-	-		(31, 32)	
50	65.5	9.345	56.385	0.166	112	-	-		(31, 32)	
60	74.1	9.259	53.547	0.173	118	-	-		(31, 32)	
70	81.6	9.184	51.072	0.180	122	-	-		(31, 32)	
80	88.4	9.116	48.828	0.187	124	-	-		(31, 32)	
90	94.5	9.055	46.815	0.193	127	-	-		(31, 32)	
100	100	9	45	0.2	130	-	-		(31, 32)	

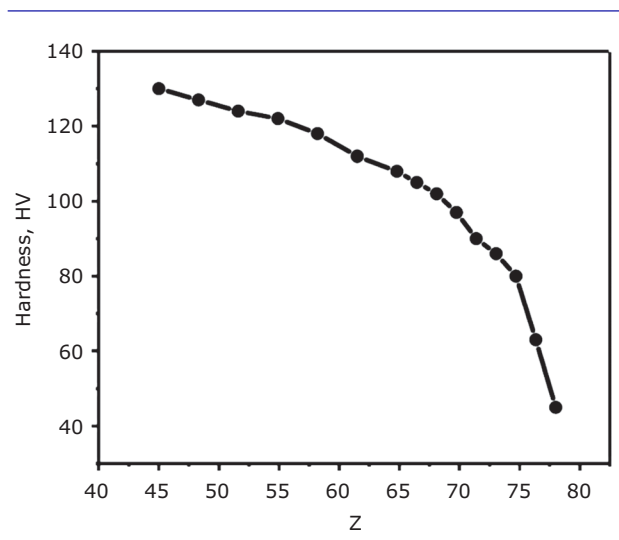


Fig. 1. Alloy atomic number: variations of hardness with average atomic number of binary platinum-rhodium alloys ( $Z$ )

with 44.9 at% rhodium and average  $Z = 63.183$ . Furthermore, the hardness increases from 45 HV to 102 HV by the reduction of average  $Z$  due to increasing rhodium content of the alloy and higher hardness is achieved by increasing rhodium content.

The average atomic numbers of the alloys in this study are tabulated in **Table I**. The mechanical

properties (hardness, E and UTS) of these alloys clearly increase with decreasing average  $Z$  as shown in **Figure 1**. In transition metals and intermetallics, it is known that when the average atomic number is halfway through the transition metal rows of the Periodic Table, i.e., either  $Z = 25-26$ , or  $Z = 43-44$ ,  $Z = 75-76$  and so on, the elastic properties and hardness of the solid solution crystal can be improved to some extent as the properties hit maxima at or around these atomic numbers (46) as a consequence of optimal orbital occupancy. This effect is not observed in platinum-rhodium binary alloys, as in most cases the average atomic number of the alloy is not close to the aforementioned  $Z$  numbers (**Table I**). As shown in the table, the existing platinum-rhodium alloys can have higher hardness, E and UTS with decreasing average atomic number. In other words, the mechanical properties of the alloys improve with decreasing total number of electrons (average atomic number) of the alloy. Non-valence electrons do not contribute to bonding and together with the protons comprise the ion kernels in the metallic bonding of transition metal alloys. Decreasing the non-valence electrons or the size of the kernels at constant (or nearly constant) valence electron numbers leads to stronger elastic bonding (45, 46).

This, in turn, means that the resistance to atomic displacement, crystal shape and volume change will be higher (at least in some crystallographic directions) resulting in the improved mechanical properties. The presence of rhodium ( $Z = 45$ ) compared to platinum ( $Z = 78$ ) in the alloys causes the total number of non-valence electrons to extensively decrease due to its lower  $Z$  value (Table I).

### 3.2. Number of Valence Electrons

Platinum-rhodium alloys with 0 to 100 at% rhodium were included in this study. In transition metal alloys, a wide range of number of valence electrons can be observed ( $3 \leq e_v \leq 12$ ) as categorised by Zarinejad and Liu (36, 44). The alloys were divided into low ( $e_v < 5$ ), medium ( $5 \leq e_v \leq 7.50$ ) and high ( $e_v > 7.50$ ) valence electron groups. Following this categorisation, platinum-rhodium binary alloys all belong to the high valence electron group with  $e_v > 7.50$  in a range between 9 and 10 (Table I, Figure 2).

By increasing rhodium content percentage in the binary alloys, the number of valence electrons of the alloy decreases as the number of valence electrons of platinum ( $s + d$  orbital electrons) is 10 and that of rhodium is 9. By decreasing the number of valence electrons in the alloys, the hardness,  $E$  and UTS are consistently increased (Table I). This indicates the dependence of the mechanical properties on number of valence electrons in the

binary solid solution alloy and that although  $e_v$  is a factor in bonding, its effect must be studied along with other influencing factors such as  $Z$ . Increasing the rhodium content of binary alloys accompanied by lowering  $e_v$  results in a lower average  $Z$  for the alloy crystal. These two opposing trends not only affect the number of valence and non-valence electrons of the alloys but also the dynamics of metallic bonding. Decreasing the number of non-valence electrons because of a decrease in the average atomic number of the alloys, even when accompanied by slight reductions in the number of valence electrons, affects the interatomic bonding that keeps the ion kernels in the metallic bonds together as it affects the size and density of the kernels (41). The higher numbers of non-valence electrons and protons in this condition reduce the bonding effects of the valence electrons and therefore reduce the mechanical properties of the solid solution crystal at least in some crystallographic directions.

### 3.3. Valence Electron Ratio

#### 3.3.1 Hardness

Depending on the atomic fractions of rhodium in the platinum-rhodium alloys, different VER values have resulted. The values for the alloys examined are tabulated in Table I. The variations of hardness vs. VER and vs. atomic percentage of rhodium in the alloy are plotted in Figure 3. A trend can

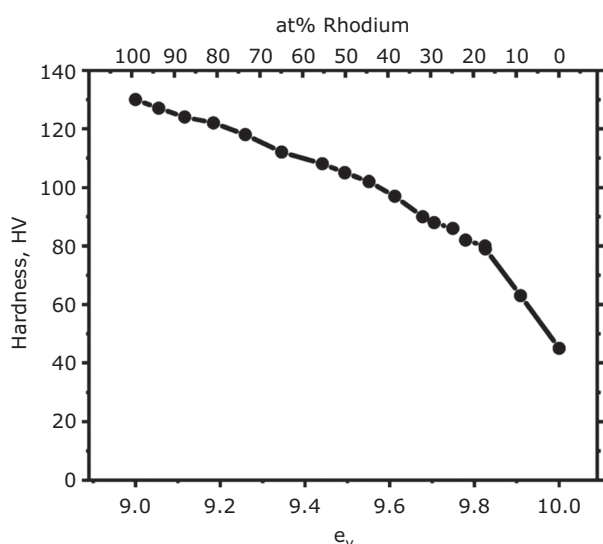


Fig. 2. Hardness vs. number of valence electrons: variations of hardness with number of valence electrons of binary platinum-rhodium alloys ( $e_v$ ) and rhodium content of the alloy (at% rhodium)

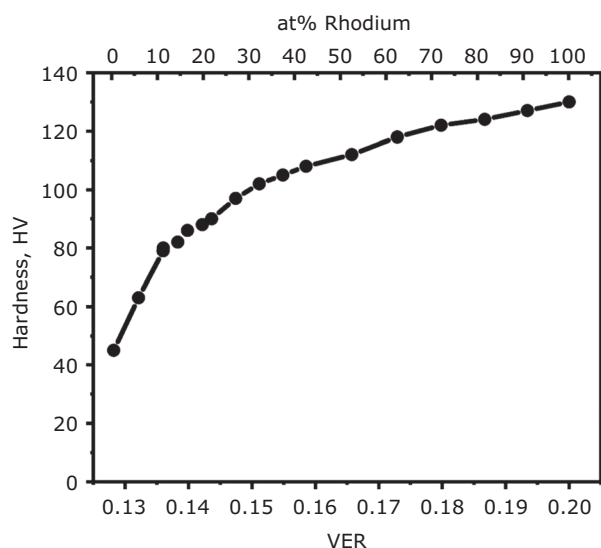


Fig. 3. Hardness vs. VER and rhodium content: variations of hardness with VER and rhodium content of the of binary platinum-rhodium alloys (at% rhodium)



be observed with increasing VER. By increasing rhodium content, the hardness of the binary alloy increases consistently from values as low as 45 HV with VER 0.13 to values as high as 130 HV with VER 0.20. The general trend in the variation of hardness with VER and rhodium content is identical (Figure 3). It is evident that the varying direction of hardness with VER is ascending. VER represents the compound effect of both  $e_v$  and Z.

### 3.3.2 Tensile Strength and Elastic Modulus

Figure 4 shows the variation of E and UTS of the alloys as a function of rhodium content and VER. It is evident that both E and UTS increase with VER, which is brought about by increasing rhodium content of the binary alloys. The gradient of UTS with increasing VER and rhodium content is more pronounced than the gradient of E, although in both cases the variations with VER as it represents chemical composition are remarkably high (Figure 4). It should be noted that microstructural factors including grain boundary characteristics

and defect populations can have a major influence especially on UTS. However, the intrinsic properties of the solid solution are dictated by bonding and valence electron parameters.

### 3.3.3 Creep Rate and Rupture Time

Table II presents the four binary platinum-rhodium alloy compositions and their creep rate characteristics at 1500°C, 1600°C and 1700°C (10, 11). Table III presents the seven binary platinum-rhodium alloy compositions and their stress rupture time characteristics at various test temperatures from 1200°C to 1700°C (10, 11, 29). With reference to the tables, it is evident that the creep rate of the binary alloys at all tested temperatures decreases with VER. This means that with the presence of more rhodium in the binary alloy the creep resistance of the alloy is improved (Figure 5). Moreover, the stress rupture time of the binary alloys at any temperature of creep testing (1200°C to 1700°C) increases with VER and rhodium content (Figure 6). In all the variations of mechanical properties, VER follows the change in

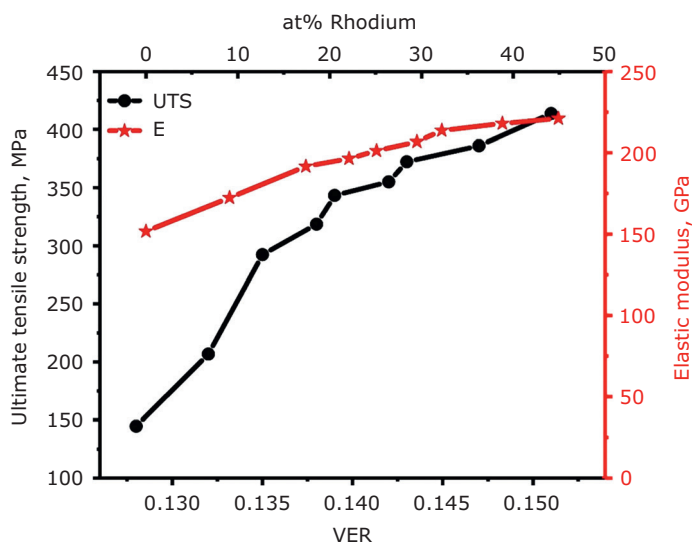


Fig. 4. UTS and E vs. VER and rhodium content: variations of UTS and E with VER and rhodium content of the binary platinum-rhodium alloys (at% rhodium)

**Table II Valence Electron Ratio and Creep Rate of Binary Platinum-Rhodium Alloys at Different Temperatures (10, 11)**

Pt-Rh, wt% Rh	Pt-Rh, at% Rh	VER	Creep rate $\xi$ , % h <sup>-1</sup>			Reference
			1500°C	1600°C	1700°C	
15	25.1	0.140	2.5	5.5	12	(10, 11)
20	32.2	0.144	2	4	9.5	(10, 11)
30	44.9	0.151	0.8	2.5	6	(10, 11)
40	55.9	0.158	0.1	1.3	5	(10, 11)

**Table III Valence Electron Ratio and Stress Rupture Time of Binary Platinum-Rhodium Alloys at Different Temperatures (10, 11, 29)**

Pt-Rh, wt% Rh	Pt-Rh, at% Rh	VER	Rupture time, h					Reference	
			1200°C	1300°C	1400°C	1500°C	1600°C		1700°C
0	0	0.128	1.5	0.2	0.1	–	–	–	(10, 11, 29)
7	12.5	0.133	10	6	3.5	–	–	–	(10, 11)
10	17.4	0.136	26	12	6	–	2	–	(10, 11, 29)
15	25.1	0.140	31	21	11	6	3.5	2.5	(10, 11)
20	32.2	0.144	–	–	–	9	4	2.8	(10, 11)
30	44.9	0.151	–	–	–	17	5	3.5	(10, 11)
40	55.9	0.158	–	–	–	–	6	3.7	(10, 11)

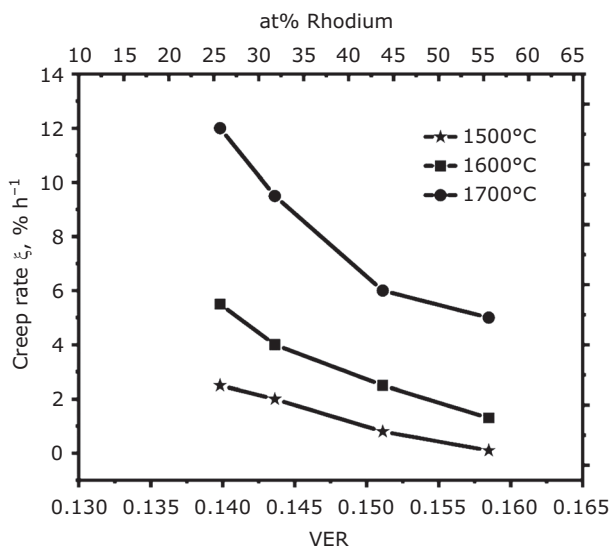


Fig. 5. Creep rate vs. VER and rhodium content: variations of creep rate with VER and rhodium content of the binary platinum-rhodium alloys (at% rhodium) at different temperatures

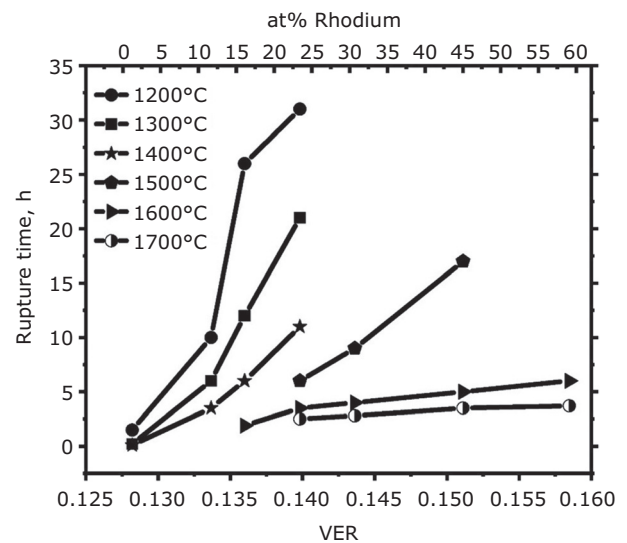


Fig. 6. Stress rupture time vs. VER and rhodium content: variations of stress rupture time with VER and rhodium content of the binary platinum-rhodium alloys (at% rhodium) at different temperatures

rhodium content. Hence, the relationship between VER and mechanical properties of platinum-rhodium alloy is discussed.

In metallic bonding, valence electrons act like 'glue' to bond non-valence electrons and nuclei units together (45, 46), whereas non-valence electrons contribute to the total atomic volume of the alloy. Increasing VER could mean thickening of the 'glue' to bond the ionic kernels together. The elastic response coefficients are the most fundamental of all the properties of solid crystals. The most important subset of properties are the shear and bulk moduli. Bulk modulus is a measure of the resistance of a solid to volume change. Shear modulus is a measure of resistance to shape change. Shear moduli have the highest influence on the mechanical properties of crystals (45, 46).

Furthermore, stacking-fault energy, dislocation mobility and plastic deformation characteristics of crystals are also dictated by metallic bonding (41). Bonding type (metallic, covalent, ionic and molecular) and solidity index of a crystal (which is simply the ratio of the shear modulus to the bulk modulus, multiplied by a coefficient of the order of unity) have been used to classify crystals (46). Hardness, tensile properties and other mechanical properties at elevated temperatures are also dominated by the nature and change in the metallic bonding in transition metal alloys. Metallic bonding is in turn controlled by valence electrons, which are altered by the chemistry of the alloys. The chemical factors that affect the mechanical properties of platinum-rhodium-based alloys in this study are discussed as follows.

An established empirical relationship between the valence electron density and bulk modulus of metallic materials and intermetallic compounds is known. Higher VER usually results in higher bulk and therefore higher shear moduli (46). Increasing VER of the platinum-rhodium alloys, therefore, is expected to result in higher elastic and shear moduli, lower dislocation mobility and more difficult local plastic deformation at least in some crystallographic directions. The change of VER by altering the platinum:rhodium ratio in the alloy is accompanied by a change in the elastic properties, dislocation mobility and stacking-fault energy as the interatomic bonding is affected.

A key factor controlling bonding is the VER of the alloy. When the properties of a solid solution crystal of a platinum-rhodium alloy are enhanced because of higher VER, the crystal's resistance to shape or volume change, atomic displacement and dislocation mobility increases. In this way mechanical properties such as hardness, elastic modulus, tensile strength and creep rate are enhanced. More rhodium content in the alloy increases VER and contributes to improvement of the mechanical properties.

From the work of Okamoto (24), we know that platinum-rhodium alloys are complete solid solutions and second phase precipitation does not take place at any rhodium content. Therefore, all the rhodium contributes to the change in VER and mechanical properties. We assume that impurity trace elements at very low concentrations do not contribute significantly to grain boundary precipitations in the alloys. The comprehensive work of Termic *et al.* (50) has shown that impurity elements might influence the mechanical properties by the formation of grain boundary effects. However, addition of any other element to this binary system that may cause precipitation can change the influence of the VER and warrants further study. The VER dependence of mechanical properties discussed above is limited to platinum-rhodium binary alloys, although it might be extended to other solid solution alloy systems after careful future studies. The trends shown are general and indicative of the major underlying influence of VER on the intrinsic mechanical properties of platinum-rhodium alloy systems.

#### 4. Conclusions

The main correlations shown in this study reveal clear dependence of the intrinsic creep, tensile and hardness properties of binary platinum-rhodium

solid solution alloys on VER. Alloy chemistry influences the number and ratio of valence electrons and average atomic number of platinum-rhodium alloys and thereby changes the mechanical properties of the solid solution alloy crystals. All the mechanical properties improve with increasing VER of binary platinum-rhodium alloys. VER presents itself as a dominant intrinsic parameter that can be utilised to take steps toward successful alloy design to achieve the desired mechanical properties.

#### References

1. B. T. Biggs, S. S. Taylor and E. van der Lingen, *Platinum Metals Rev.*, 2005, **49**, (1), 2
2. J. C. Wright, *Platinum Metals Rev.*, 2002, **46**, (2), 66
3. B. Wu and G. Liu, *Platinum Metals Rev.*, 1997, **41**, (2), 81
4. R. Price, *Platinum Metals Rev.*, 1959, **3**, (3), 78
5. S. Sarkar, *Cogent Eng.*, 2018, **5**, (1), 1558687
6. M. Saternus, A. Fornalczyk and J. Cebulski, *Arch. Metall. Mater.*, 2014, **59**, (2), 557
7. E. Preston, *Platinum Metals Rev.*, 1960, **4**, (2), 48
8. D. F. Lupton, J. Merker, B. Fischer and R. Völkl, 'Platinum Materials for the Glass Industry', 24th International Precious Metals Conference, Williamsburg, USA, 11th–14th June, 2000, International Precious Metals Institute, Pensacola, USA, 18th July, 2000
9. F. Xiao, F. Zhao, D. Mei, Z. Mo and B. Zeng, *Biosens. Bioelectron.*, 2009, **24**, (12), 3481
10. B. Trumić, L. Gomidželović, S. Marjanović, V. Krstić, A. Ivanović and S. Dimitrijević, *Arch. Metall. Mater.*, 2015, **60**, (2), 643
11. B. Trumić, L. Gomidželović, S. Marjanović, V. Krstić, A. Ivanović and S. Dimitrijević, *Mater. Test.*, 2013, **55**, (1), 38
12. H. Gavin, *Platinum Metals Rev.*, 2010, **54**, (3), 166
13. C. Hu, Y. Wei, H. Cai, L. Chen, X. Wang, X. Zhang, G. Zhang and X. Wang, *Johnson Matthey Technol. Rev.*, 2021, **65**, (4), 535
14. Y. Yamabe, Y. Koizumi, H. Murakami, Y. Ro, T. Maruko and H. Harada, *Scr. Mater.*, 1996, **35**, (2), 211
15. Y. Yamabe-Mitarai, Y. Ro, T. Maruko, T. Yokokawa and H. Harada, 'Platinum Group Metals: Base Refractory Superalloys for Ultra-High Temperature Use', Structural Intermetallics, 2nd International Symposium on Structural Intermetallics, 21st–25th September, 1997, Champion, USA, eds. M. V. Nathal, R. Darolia, C. T. Liu, P. L. Martin, D. B. Miracle, R. Wagner and M. Yamaguchi, The Minerals Metals & Materials Society, Pittsburgh,

- USA, 1997, pp. 805–814
16. Y. Yamabe-Mitarai, Y. Koizumi, H. Murakami, Y. Ro, T. Maruko and H. Harada, *Scr. Mater.*, 1997, **36**, (4), 393
  17. Y. Yamabe-Mitarai, Y. Ro, H. Harada and T. Maruko, *Metall. Mater. Trans. A*, 1998, **29**, (2), 537
  18. Y. Yamabe-Mitarai, Y. Ro, T. Maruko and H. Harada, *Scr. Mater.*, 1998, **40**, (1), 109
  19. Y. Yamabe-Mitarai, Y. Gu, Y. Ro, S. Nakazawa, T. Maruko and H. Harada, *Scr. Mater.*, 1999, **41**, (3), 305
  20. X. Yu, Y. Yamabe-Mitarai, Y. Ro and H. Harada, *Intermetallics*, 2000, **8**, (5–6), 619
  21. I. M. Wolff and P. J. Hill, *Platinum Metals Rev.*, 2000, **44**, (4), 158
  22. J. Luyten, J. De Keyzer, P. Wollants and C. Creemers, *Calphad*, 2009, **33**, (2), 370
  23. K. T. Jacob, S. Priya and Y. Waseda, *Metall. Mater. Trans. A*, 1998, **29**, (6), 1545
  24. H. Okamoto, *J. Phase Equilib. Diffus.*, 2013, **34**, (2), 176
  25. L. A. Cornish, J. Hohls, P. J. Hill, S. Prins, R. Süß and D. N. Compton, *J. Min. Metall. Sect. B-Metall.*, 2002, **38**, (3–4), 197
  26. L. A. Cornish, R. Süß, A. Watson and S. N. Prins, *Platinum Metals Rev.*, 2007, **51**, (3), 104
  27. A. Watson, R. Süß and L. A. Cornish, *Platinum Metals Rev.*, 2007, **51**, (4), 189
  28. P. Battaini, *Platinum Metals Rev.*, 2011, **55**, (2), 74
  29. B. Fischer, A. Behrends, D. Freund, D. Lupton and J. Merker, *Platinum Metals Rev.*, 1999, **43**, (1), 18
  30. J. Merker, B. Fischer, R. Völkl and D. F. Lupton, *Mater. Sci. Forum*, 2003, **426–432**, 1979
  31. A. S. Darling, *Platinum Metals Rev.*, 1961, **5**, (2), 58
  32. J. S. Acken, *Bur. Stand. J. Res.*, 1934, **12**, (2), 249
  33. Z. M. Rdzawski and J. P. Stobrawa, *J. Mater. Process. Technol.*, 2004, **153–154**, 681
  34. H. Garbacz, J. Mizera, Z. Laskowski and M. Gierej, *Powder Technol.*, 2011, **208**, (2), 488
  35. J. K. Odusote, L. A. Cornish and J. M. Papo, *J. Mater. Eng. Perform.*, 2013, **22**, (11), 3466
  36. M. Zarinejad, 'Influence of Alloy Chemistry on the Transformation Temperatures and Local Atomic Structure of Shape Memory Alloys: With a Focus on NiTi-Based Intermetallics', PhD Thesis, School of Mechanical and Aerospace Engineering, Nanyang Technological University, Singapore, September, 2009, 176 pp
  37. M. Zarinejad, Y. Liu and T. J. White, *Intermetallics*, 2008, **16**, (7), 876
  38. M. Zarinejad and Y. Liu, *Adv. Funct. Mater.*, 2008, **18**, (18), 2789
  39. M. Zarinejad, Y. Liu and Y. Tong, *Intermetallics*, 2009, **17**, (11), 914
  40. M. Zarinejad, Y. Liu, T. Liu, T. White, P. Yang and Q. Chen, *Philos. Mag.*, 2011, **91**, (3), 404
  41. Y. Tong, Y. Liu, Z. Xie and M. Zarinejad, *Acta Mater.*, 2008, **56**, (8), 1721
  42. M. Zarinejad, K. Wada, F. Pahlevani, R. Katal and S. Rimaz, *Shape Mem. Superelasticity*, 2021, **7**, (1), 179
  43. M. Zarinejad, K. Wada, F. Pahlevani, R. Katal and S. Rimaz, *J. Alloys Compd.*, 2021, **870**, 159399
  44. M. Zarinejad and Y. Liu, 'Dependence of Transformation Temperatures of Shape Memory Alloys on the Number and Concentration of Valence Electrons', in "Shape Memory Alloys: Manufacture, Properties and Applications", ed. H. R. Chen, Ch. 12, Nova Science Publishers Inc, Hauppauge, USA, 2010, pp. 339–360
  45. C. Kittel, "Introduction to Solid State Physics", 8th Edn., John Wiley & Sons Inc, Hoboken, USA, 2005
  46. J. J. Gilman, "Electronic Basis of the Strength of Materials", Cambridge University Press, Cambridge, UK, 2003
  47. B. X. Hu, Y. Ning, L. Chen, Q. Shi and C. Jia, *Platinum Metals Rev.*, 2012, **56**, (1), 40
  48. F. Cardarelli, "Materials Handbook", 2nd Edn., Springer-Verlag London Ltd, London, UK, 2008
  49. "ASM Handbook: Properties and Selection: Nonferrous Alloys and Special-Purpose Materials", 10th Edn., Vol. 2, ASM International, Materials Park, USA, 1990
  50. B. Trumić, L. Gomidželović, S. Marjanović, A. Ivanović and V. Krstić, *Mater. Res.*, 2017, **20**, (1), 191

## The Authors



Mehrdad Zarinejad is a senior academic at PB Research Centre, currently located in Ontario, Canada. Previously, he served as a Lead Scientist at Singapore Institute of Manufacturing Technology of the Agency of Science Engineering and Research (A\*STAR). With a PhD in materials science and engineering, he worked at Nanyang Technological University (NTU), Singapore; McGill University, Canada; Precision H2 Inc, Canada; University of Tehran, Iran; and Sharif University of Technology, Iran. His research focus is on structure-processing-property relationships in alloys, engineering ceramics, catalysts and waste materials reuse. He has also led technology development, knowledge transfer and training activities for industry in the last decade.



Sajjad Rimaz received his bachelor's degree (2013) and master's degree (2015) in Chemical Engineering from Amirkabir University of Technology (Tehran Polytechnic, Iran). In 2017 he received the Singapore International Graduate Award (SINGA) for PhD studies and finished his PhD in 2021 in chemical engineering from National University of Singapore (NUS). His research focus is on bimetallic catalysis and alloys.



Yunxiang Tong is a professor in the College of Materials Science and Chemical Engineering, Harbin Engineering University, China. He received his PhD degree from NTU in 2008. His current research interest focuses on development of alloys including shape memory alloys and their applications.



Kiyohide Wada received his PhD in mechanical and aerospace engineering from NTU in 2008. Thereafter he worked as a satellite space engineer dealing with various commercial space programmes between 2009 and 2013. Currently, he is a senior lecturer in aerospace engineering, and a member of Institution of Mechanical Engineers (IMechE) as chartered engineer and a fellow of Association for Project Management (APM). His research interests include aerospace materials, shape memory alloy applications in space, origami folds and models, deployable structures, space debris removal and satellite design.



Farshid Pahlevani is an associate professor at the Centre of Sustainable Materials Research and Technology at the School of Materials Science and Engineering of the University of New South Wales (SMaRT@UNSW) in Australia. He earned his PhD from Tohoku University, Japan. Farshid is an international expert on innovative solutions for waste challenges, materials development and processing. His international research career, spanning high profile research institutes in Japan, Singapore and Australia, includes considerable experience working closely with industry to improve existing processes to achieve better environmental outcomes and greater cost efficiencies.



## In the Lab

# The Use of Recovered Metal Complexes in Catalysis

**Johnson Matthey Technology Review features laboratory research**

## NON-PEER REVIEWED FEATURE

Received 1st December 2022; Online 1st June 2023

Research in the group led by James Wilton-Ely focuses on catalysis, imaging and sensing. All of this work involves *d*- and *f*-elements and is underpinned by the group's wide-ranging expertise in synthesis. Collaborations with researchers in engineering, medicine and bioimaging allow these discoveries to be used to address major healthcare and sustainability challenges. Professor Wilton-Ely is the author of more than 100 publications and was the recipient of the 2021 Sir Geoffrey Wilkinson Award from the Royal Society of Chemistry for his work on metal-based carbon monoxide sensing. He has a strong interest in sustainability, having directed the MRes Green Chemistry course at Imperial College for over 12 years (2010–2022). He has published on the use of recovered metals in catalysis (1–5), the catalytic transformation of biomass to platform chemicals (6–11) and magnetically-recoverable nanoscale catalysts (12, 13). Elemental sustainability is a pressing concern for all researchers using precious metals and this has led Wilton-Ely to work with colleagues to explore the potential for using gold (3) and palladium (4, 5) complexes recovered from end-of-life products in catalysis.

## The Researcher



- **Name:** James Wilton-Ely
- **Position:** Professor of Inorganic Chemistry
- **Department:** Department of Chemistry
- **University:** Imperial College London
- **Address:** Molecular Sciences Research Hub, 82 Wood Lane, London
- **Postcode:** W12 0BZ
- **Country:** United Kingdom
- **Email:** [j.wilton-ely@imperial.ac.uk](mailto:j.wilton-ely@imperial.ac.uk)

## About the Research

Catalysis using precious metals is a cornerstone of synthetic chemistry, yet many of these metals are extremely scarce. Palladium is found in concentrations of 1–10 parts per trillion in the earth's crust in only a few locations. The demand for this metal is driven by its use in automotive three-way catalysts (TWCs) and the limited

supply has resulted in a significant palladium deficit, rendering current palladium consumption unsustainable. An attractive solution is to recycle and reuse rather than continuing to draw on primary sources, thereby also reducing waste. Johnson Matthey has played a leading role in adopting this approach through their pyrometallurgical and chemical leaching process for recovering and reusing spent TWCs. However, only around 20–30% of palladium is currently recovered worldwide. New technologies, such as those investigated in the Platinum Group Metals Recovery Using Secondary Raw Materials (PLATIRUS) programme, offer promising alternatives to the current energy-intensive processes for the recovery of TWC metal content for reuse in new automotive TWCs.

In contrast, there has been relatively little research aimed at the recovery of precious metals for use in the catalytic transformations needed to make fine chemicals, pharmaceuticals and fertilisers (1, 2) with the majority of these catalysts still being sourced directly from mining. While efforts have been made to use catalysts based on more abundant metals, the use of palladium catalysts in industry and academia is well established due to its high activity and reliability. Professors Angela Serpe and Paola Deplano (University of Cagliari, Italy) have pioneered low-energy, environmentally-benign processes for the recovery of palladium from TWCs and gold from waste electrical and electronic equipment (WEEE) in the form of molecular recovery compounds. While almost quantitative recovery of the metal can be achieved from these products by cementation or electrowinning, this treatment increases the environmental and economic costs of the recovery process. Instead, the Wilton-Ely group is working with Professor Serpe and a synthetic organic chemist, Professor Christopher Braddock (Imperial College London), to valorise these products directly in catalysis (**Figure 1**).

End-of-life TWCs contain around 4 g of palladium (200 times the concentration in mined ore) and this metal content can be recovered in high yield through the use of *N,N*-dimethylperhydrodiazepine-2,3-dithione ( $\text{Me}_2\text{dazdt}$ ) and iodine to form the recovery product  $[\text{Pd}(\text{Me}_2\text{dazdt})_2]^{2+}$  (**Figure 1**). This complex was found to catalyse important C–H oxidative functionalisation transformations in higher yield, more rapidly and under milder conditions than those previously reported (4). The related recovery product,  $[\text{PdI}_2(\text{Me}_2\text{dazdt})]$  was then shown to undergo ligand exchange with

dithiocarbamate ligands with trimethoxysilyl-terminated units suitable for the functionalisation of silica-coated  $\text{Fe}_3\text{O}_4$  nanoparticles. The resulting catalyst system was used to transform benzo[*h*]quinoline to 10-methoxybenzo[*h*]quinoline before being magnetically recovered and reused (5). These reports demonstrated the great potential for valorising the molecular recovery products obtained from TWCs using benign, low-energy solvometallurgical routes. This will become even more significant with the planned end to the sale of new petrol and diesel cars in the UK in 2030, necessitating a range of recovery solutions for the millions of existing TWCs.

Most WEEE is currently sent to landfill with little attempt to recover the valuable metal content. This is despite the fact that the amount of gold in printed circuit boards ( $50\text{--}700\text{ g tonne}^{-1}$ ) is far higher than that found in primary mined ores or concentrates ( $1\text{--}10\text{ g tonne}^{-1}$ ), which rely on highly polluting and environmentally damaging processes. Serpe and Deplano have patented (14) a low-energy process to recover gold as the molecular product  $[\text{AuI}_2(\text{Me}_2\text{dazdt})]\text{I}_3$  using  $\text{Me}_2\text{dazdt}$  and iodine as part of a selective, three-stage metal leaching and recovery approach from WEEE. This solvometallurgical method employs common organic solvents and environmentally-friendly reagents under mild conditions.

Very recently (3), it has been demonstrated that this recovery product can be used as an effective homogeneous catalyst for a range of catalytic reactions, allowing an existing mild and effective recovery process to be connected with a major catalytic application of gold. Using SIM cards as the e-waste source,  $[\text{AuI}_2(\text{Me}_2\text{dazdt})]^+$  was produced and found to show comparable catalytic activity to current Au(III) catalysts for a range of important gold-catalysed transformations. These included cyclisation of propargylic amides, addition reactions of electron-rich arenes to carbonyl compounds and oxidative cross-coupling reactions of arenes with aryl silanes. This was the first example of the direct application in homogeneous catalysis of gold recovery products sourced from e-waste. A preliminary indicative cost analysis suggests that even unoptimised, small-scale production of the catalyst,  $[\text{AuI}_2(\text{Me}_2\text{dazdt})]^+$ , from certain types of WEEE leads to a significantly lower cost than commercial catalysts derived from environmentally-damaging mining.

The wider aim of these studies is to demonstrate that molecular recovery products from mild, low-impact processes based on end-of-life materials

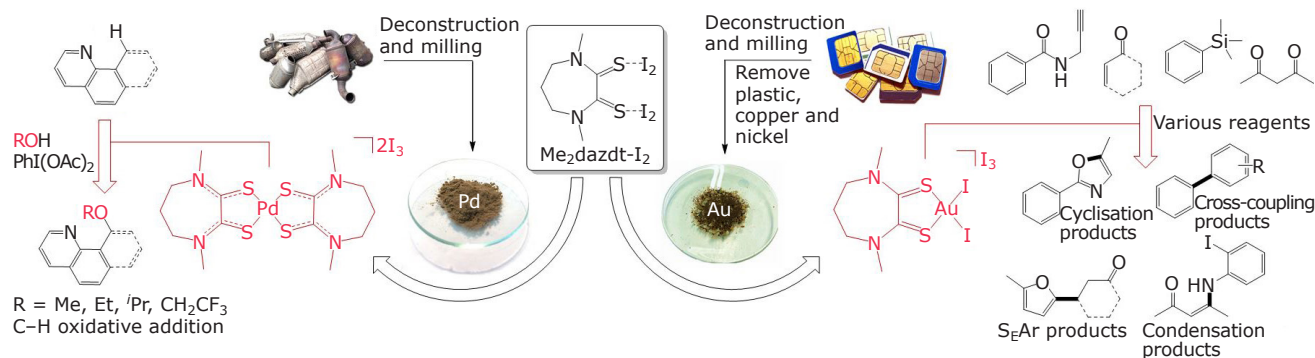


Fig. 1. Catalysis using palladium and gold compounds recovered from end-of-life sources

can be used to replace homogeneous catalysts derived from mining. If adopted more widely, this would not only improve sustainability, reduce waste and relieve pressure on primary sources, but also have cost and supply chain security benefits.

## Acknowledgements

James Wilton-Ely thanks Angela Serpe, Christopher Braddock, Sean McCarthy, Khairil Jantan and the Wilton-Ely group as well as the EPSRC CDT in Next Generation Synthesis and Reaction Technology (EP/S023232/1) for funding.

## References

1. S. McCarthy, D. C. Braddock and J. D. E. T. Wilton-Ely, *Coord. Chem. Rev.*, 2021, **442**, 213925
2. S. McCarthy, A. L. W. Jie, D. C. Braddock, A. Serpe and J. D. E. T. Wilton-Ely, *Molecules*, 2021, **26**, (17), 5217
3. S. McCarthy, O. Desauay, A. L. W. Jie, M. Hassatzky, A. J. P. White, P. Deplano, D. C. Braddock, A. Serpe and J. D. E. T. Wilton-Ely, *ACS Sustain. Chem. Eng.*, 2022, **10**, (48), 15726
4. K. A. Jantan, C. Y. Kwok, K. W. Chan, L. Marchiò, A. J. P. White, P. Deplano, A. Serpe and J. D. E. T. Wilton-Ely, *Green Chem.*, 2017, **19**, (24), 5846
5. K. A. Jantan, K. W. Chan, L. Melis, A. J. P. White, L. Marchiò, P. Deplano, A. Serpe and J. D. E. T. Wilton-Ely, *ACS Sustain. Chem. Eng.*, 2019, **7**, (14), 12389
6. A. Al Ghatta, J. D. E. T. Wilton-Ely and J. P. Hallett, *Green Chem.*, 2021, **23**, (4), 1716
7. A. Al Ghatta, X. Zhou, G. Casarano, J. D. E. T. Wilton-Ely and J. P. Hallett, *ACS Sustain. Chem. Eng.*, 2021, **9**, (5), 2212
8. A. Al Ghatta, J. D. E. T. Wilton-Ely and J. P. Hallett, *ACS Sustain. Chem. Eng.*, 2020, **8**, (6), 2462
9. A. Al Ghatta, J. D. E. T. Wilton-Ely and J. P. Hallett, *ACS Sustain. Chem. Eng.*, 2019, **7**, (19), 16483
10. A. Al Ghatta, J. D. E. T. Wilton-Ely and J. P. Hallett, *ChemSusChem*, 2019, **12**, (19), 4452
11. S. Eminov, J. D. E. T. Wilton-Ely and J. P. Hallett, *ACS Sustain. Chem. Eng.*, 2014, **2**, (4), 978
12. J.-M. Collinson, J. D. E. T. Wilton-Ely and S. Díez-González, *Catal. Commun.*, 2016, **87**, 78
13. J.-M. Collinson, J. D. E. T. Wilton-Ely and S. Díez-González, *Chem. Commun.*, 2013, **49**, (97), 11358
14. P. Deplano, M. L. Mercuri, L. Pilla, A. Serpe and M. Vanzi, Sardegna Ricerche Cagliari, 'Process for Recovering Noble Metals from Electric and Electronic Wastes', *European Patent* 1,964,936, 2008

# Additive Manufacturing of Platinum Alloys

## Practical aspects during laser powder bed fusion of jewellery items

**Ulrich E. Klotz\* and Frank R. König**

Research Institute for Precious Metals and Metals Chemistry (fem), Katharinenstrasse 17, 73525 Schwäbisch Gmünd, Germany

\*Email: [klotz@fem-online.de](mailto:klotz@fem-online.de)

### PEER REVIEWED

Received 25th July 2022; Revised 7th November 2022; Accepted 21st November 2022; Online 22nd November 2022

Additive manufacturing of jewellery alloys has been actively investigated for the past 10 years. Limited studies have been conducted on gold and platinum jewellery alloys. Platinum is of increased interest due to the technological challenges in investment casting. In the present paper, typical platinum jewellery alloys have been tested by laser track experiments on sheet materials. The effect of alloy composition on width and depth of the laser tracks was studied by metallography. Optimum parameters of the laser powder bed fusion (PBF-LB) process were determined for a typical 950Pt jewellery alloy by the preparation of dedicated test samples. Densities of >99.8% were reached for a wide range of processing parameters. However, for real jewellery parts the resulting density was found to depend significantly on the part geometry and on the chosen support structure. The supports must take into account the geometrical orientation of the part relative to the laser build direction and the orientation on the build plate. Local overheating gives rise to porosity in these areas. Therefore, the supports play an important role in thermal management and must be optimised for each part. The design of suitable supports was successfully demonstrated for a typical jewellery ring sample.

## 1. Introduction

Many different additive manufacturing processes exist for metals, polymers and ceramic materials. The present paper focuses on PBF-LB technology, the most widely used process for additive manufacturing of metallic alloys. The process is also known under different brand names using the same technology, such as selective laser melting (SLM) or direct metal laser sintering (DMLS). The PBF-LB of platinum alloy jewellery items has gained increasing interest in recent years. Pioneering work on the additive manufacturing of precious metals was done by Zito *et al.* (1–8). So far, most studies have focused on gold alloys (9–12). The effect of PBF-LB process parameters on 18 karat yellow gold was studied by Klotz *et al.* (9). Surface treatment of the powder allowed a reduction in porosity from 3% or 4% before treatment to below 1% after surface treatment. The addition of alloying elements, especially germanium, resulted in a reduction of porosity to 0.3%. At the same time, the surface roughness was reduced significantly.

Finishing and polishing of complex shaped jewellery is a crucial production step. Fletcher *et al.* (11) compared polishing techniques of LBPF produced jewellery items. Automated techniques are not sufficient to achieve the desired lustre and manual polishing remains necessary. A more fundamental work by Ghasemi-Tabasi *et al.* (12) describes a method to find optimum PBF-LB parameters using a so-called translation rule. The concept of normalised enthalpy is used to take into account the differences in thermal and optical properties among the different materials. Pogliani and Albertin (13) presented a case study for the production of a small series of jewellery by PBF-LB technology. They provide problem-solving insights into the technology in production.

Only a few publications present results on PBF-LB of platinum alloys (3, 4, 6, 14, 15). The first studies with platinum alloys were done by Zito *et al.* in 2014 (3). Platinum was found to be easier to work than gold due to its lower thermal conductivity. The addition of silicon and germanium further improved the surface quality and reduced porosity. A continuation of the work in 2015 (4) focused on the dimensional accuracy and mechanical properties of PBF-LB parts compared to cast parts. Flat products in platinum alloys can be produced with higher detail than curved objects, which is opposite to the observations in investment casting. Gold alloys allowed higher surface quality and better dimensional accuracy than platinum alloys. The geometry of the part (pave setting vs. ring) influenced the dimensional accuracy compared to the computer aided design (CAD) model. Again the work was conducted with non-standard alloy compositions that included 0.2–0.4% silicon and germanium (7).

The most comprehensive study on platinum alloys so far was published in 2018 (6). It provides a 1:1 comparison of the properties of several different jewellery items produced by PBF-LB or investment casting. The case study not only compares the technical aspects of the processes but also the production cost, production time and carbon dioxide footprint of both technologies. The investment casting process of platinum alloys is rather challenging and struggles with casting defects such as shrinkage porosity, microporosity or investment reactions (16–18). On the other hand, the physical properties of platinum alloys, particularly the reflectivity of infrared laser light, are more similar to steel or titanium alloys (19). This makes the PBF-LB process of platinum alloys much easier compared to gold or silver alloys. The authors (6) conclude that platinum PBF-LB parts show higher surface quality, less porosity and therefore less repair effort during finishing compared to their counterparts produced by investment casting. The commercial benefits of PBF-LB are slightly shorter production times, lower production cost and lower environmental impact. The advantages of PBF-LB are particularly noticeable with production quantities of 500 g platinum alloy per week.

Laag and Heinrich (15) studied the powder manufacturing of different platinum alloys by gas atomisation in the Nanoval process. They provide mechanical properties and surface roughness data of parts produced by PBF-LB and PBF-LB plus hot isostatic pressing (HIP) in comparison to parts produced by metal injection moulding (MIM).

PBF-LB results in higher density and smaller grain size than MIM, but these results were achieved for different alloys.

The present work is divided into two parts. The first part deals with the study of laser tracks on alloyed metal sheet in order to study the laser to alloy interaction. The alloy compositions include many commercial 950Pt alloys but also alloys of lower platinum content. The effect of alloy composition and the role of alloying elements on the melting behaviour was studied systematically by determining the width and depth of the laser tracks. This is the most comprehensive study so far on the role of platinum alloy compositions in PBF-LB processing. In the second part of this work PBF-LB trials were conducted with a commercially available 950Pt-In-Au-Ir alloy powder (alloy 951Pt P1, C.HAFNER GmbH + Co KG, Germany). The PBF-LB process parameters were optimised for minimum porosity. The effect of support structures was studied and effects on alloy chemistry and defects are described in detail.

## 2. Experimental

### 2.1 Laser Tracks on Metal Sheet Samples

A Concept Laser MLab R machine (GE Additive, USA) with a maximum laser power of 100 W was used in this study. The laser power was set to 95 W and kept constant for all tests. Despite the relatively low laser power a sufficient energy density could be achieved because of the small spot size (30  $\mu\text{m}$ ) of the machine.

Metal sheets of commercially available platinum alloys were obtained from C.HAFNER, Agosi AG, Germany and WIELAND Edelmetalle GmbH, Germany. Alloys that were not commercially available were prepared by induction melting from pure elements, except for ruthenium that was alloyed *via* a platinum-ruthenium master alloy. Precious metals were obtained from C.HAFNER. Additional alloying elements were provided by HMW Hauner GmbH & Co KG, Germany. All pure elements were used in a purity of at least 99.99%. Samples of approximately 40 g were melted in a centrifugal casting machine (TCE10, Topcast Srl, Italy) after evacuation to approximately  $10^{-2}$  mbar and backfilling with argon to about 300 mbar. The composition of all alloys is given in **Table I**. Some of the alloys were obtained as commercial alloys and used without further modification. The origin and manufacturing of each alloy is described in the column "Remarks".



**Table I Composition of Sheet Material for Laser Track Tests**

Alloy	Platinum, mass%	Alloying elements, mass%	Remarks
Pt-Ru	bal.	Ru: 1 / 3 / 5	Pt-5Ru from C.HAFNER, diluted with platinum to 1% and 3% Ru, respectively
Pt-Co	bal.	Co: 1 / 3 / 5	Pt-5Co from C.HAFNER, diluted with platinum to 1% and 3% Co, respectively
Pt-Cu	bal.	Cu: 4 / 4.7 / 20 / 40 / 60 / 80	Pt-4Cu and Pt-4.7Cu from Agosi and C.HAFNER, respectively. Alloys of higher Cu content prepared from pure elements
Pt-Pd	bal.	Pd: 20 / 40 / 60 / 80	Alloys prepared from pure elements
Pt-Ir	bal.	Ir: 10 / 20	Alloys from C.HAFNER
Pt-W	bal.	W: 5	Alloy from WIELAND Edelmetalle
Pt-Cu-Pd	60	Cu: 10 / 20 / 30, Pd: bal.	Alloys prepared from pure elements
Pt-Cu-Ga	95.5	Cu: 1.9, Ga: 2.7	Alloy from C.HAFNER
Pt-Cu-Pd	60	Pd: 10, Cu: bal.	Alloy from WIELAND Edelmetalle
Pt-Ru-X	95	Au: 1.5 / 3.5, Ru: bal.; Co: 1.5 / 3.5, Ru: bal.; Cu: 1.5 / 3.5, Ru: bal.	Alloys prepared pure elements and Pt-5Ru master alloy from C.HAFNER
Pt-Ru-Cu-X	95	Cu: 2.0, Ru: 1.0, X: 2.0; X = Ga, In, Sn, Ge, Zn	Alloys prepared from pure elements and Pt-5Ru master alloy from C.HAFNER
Pt-In-Au-Ru	95.2	In: 2.5, Au: 1.5, Ru: 1.0	Alloy from C.HAFNER
Pt-In-Au-Ir	95.1	In: 2.7, Au: 2.0, Ir: 0.2	Alloy from C.HAFNER

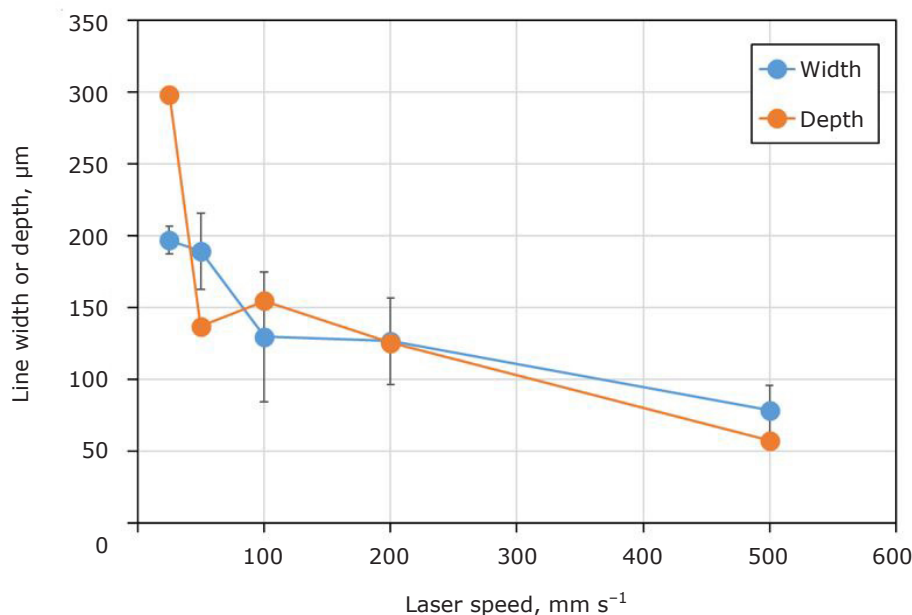


Fig. 1. Effect of laser speed on the line width and depth for 950PtInAuRu

Immediately after melting the alloy samples were cast into a copper mould of approximately 4 mm × 12 mm × 40 mm. The cast ingots were cold rolled with polished rolling mill to a thickness of approximately 1 mm. The sample surface was used in the as-rolled condition to apply the laser tracks. The laser tracks on metal sheets were produced in the Concept Laser Mlab R machine at a laser power of 95 W with a laser speed

between 25 mm s<sup>-1</sup> and 500 mm s<sup>-1</sup>. A set of laser tracks with a length of 5 mm was produced on each metal sheet (Figure 1). Each set of laser tracks was repeated three times. The width of the lines was measured by optical microscopy and averaged over the length of all three lines of the same speed. The depth of the tracks was measured in metallographic cross-sections in a scanning electron microscope (SEM). Samples for

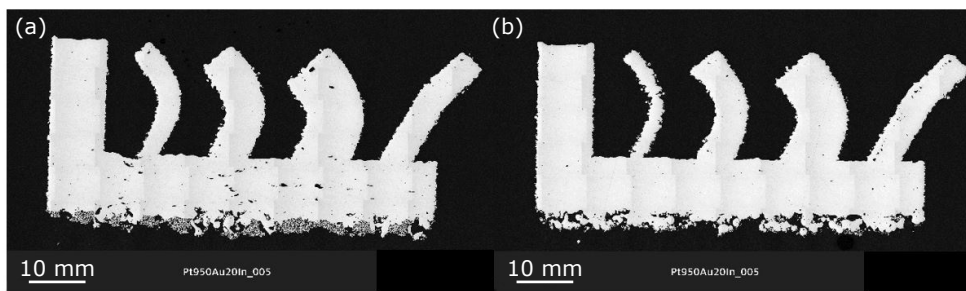


Fig. 2. Typical metallographic section of the test samples: (a) hatch distance 27  $\mu\text{m}$ , laser speed 600  $\text{mm s}^{-1}$ ; (b) hatch distance 63  $\mu\text{m}$ , laser speed 500  $\text{mm s}^{-1}$

SEM were produced by standard metallographic techniques as described in Section 2.3.

## 2.2 Laser Powder Bed Fusion Experiments

Concerning the PBF-LB trials with alloyed powder, a two-step scanning routine was applied where the contour scan was made prior to the hatch scan. This was found to be beneficial for gold alloys in terms of reducing the surface roughness (9). The contour scan speed was 600  $\text{mm s}^{-1}$  for all tests. The hatch scan parameters were varied to find optimum parameters with minimum porosity in a test part. The hatch distance and the laser speed were changed from 27  $\mu\text{m}$  to 63  $\mu\text{m}$  and 100  $\text{mm s}^{-1}$  to 600  $\text{mm s}^{-1}$ , respectively. The powder was provided as alloyed powder. It had a size distribution of 10–45  $\mu\text{m}$  ( $d_{10}/d_{90}$  value) and was applied with a rubber lip wiper in layers of 20  $\mu\text{m}$ .

The test part for the PBF-LB trials has an angular shape with wires and plates of different diameters similar to the one described in (9). The support structure and the slicing of the model was done with the software AutoFab. The part was oriented in a 45° angle relative to the movement of the recoater. After optimisation of the process parameters, jewellery parts were produced with these optimum parameters. An optimisation of the support structures was found to be necessary for some parts depending on their geometry.

## 2.3 Microstructure Investigation and Porosity Measurement

The test parts (metal sheets samples and PBF-LB parts) were embedded in epoxy (Epofix) and metallographically prepared. Grinding was done with grit P320, P600 and P1200 paper followed by subsequent polishing with 9  $\mu\text{m}$  and 3  $\mu\text{m}$  diamond paste. The last polishing step was done with 0.04  $\mu\text{m}$  oxide polishing suspension. SEM images were obtained by a GeminiSEM 300 instrument (ZEISS, Germany) equipped with an energy

dispersive X-ray (EDX) detector X-Max 150 (Oxford Instruments plc, UK) for local chemical analysis.

The porosity measurement was conducted by image analysis with the software AxioVision (ZEISS) on a stitched light optical image recorded at 5 $\times$  objective lens (Figure 2). The horizontal part of the test sample was selected as region of interest (ROI). In order to determine the porosity the image was binarised using a threshold value at the minimum of the histogram. The porosity value is given as the percentage of black pixels inside the ROI.

## 3. Results

### 3.1 Laser Tracks on Metal Sheets

The laser tracks were made to identify the effect of alloy composition on the laser-material interaction. The simplicity of the materials production and testing procedure allowed testing of many different alloys as opposed to tests with powder. At constant laser power the width of the laser tracks decreases with increasing laser speed, because the energy input per length unit becomes smaller (Figure 1). The data points indicate the mean value from five individual measurements on each of three lines. The maximum and minimum width is represented by the error bars. The inserted SEM image shows a typical laser track in cross-section. The cold rolled microstructure of the metal sheet allowed a clear identification of the melting zone and of the heat-affected zone. The depth was measured as the distance from the averaged metal sheet surface to the maximum depth of the laser track. The depth is generally more prone to changes than the width because there might be a change from the conduction mode to the keyhole mode, which mainly affects the depth but hardly the width (please see Section 4.1 for an explanation of conduction and keyhole mode).

The effect of alloy composition was studied for binary platinum-palladium and platinum-copper alloys with a platinum content from 100% to 20% (Figure 3) at a laser speed of 100  $\text{mm s}^{-1}$ . The addition of palladium

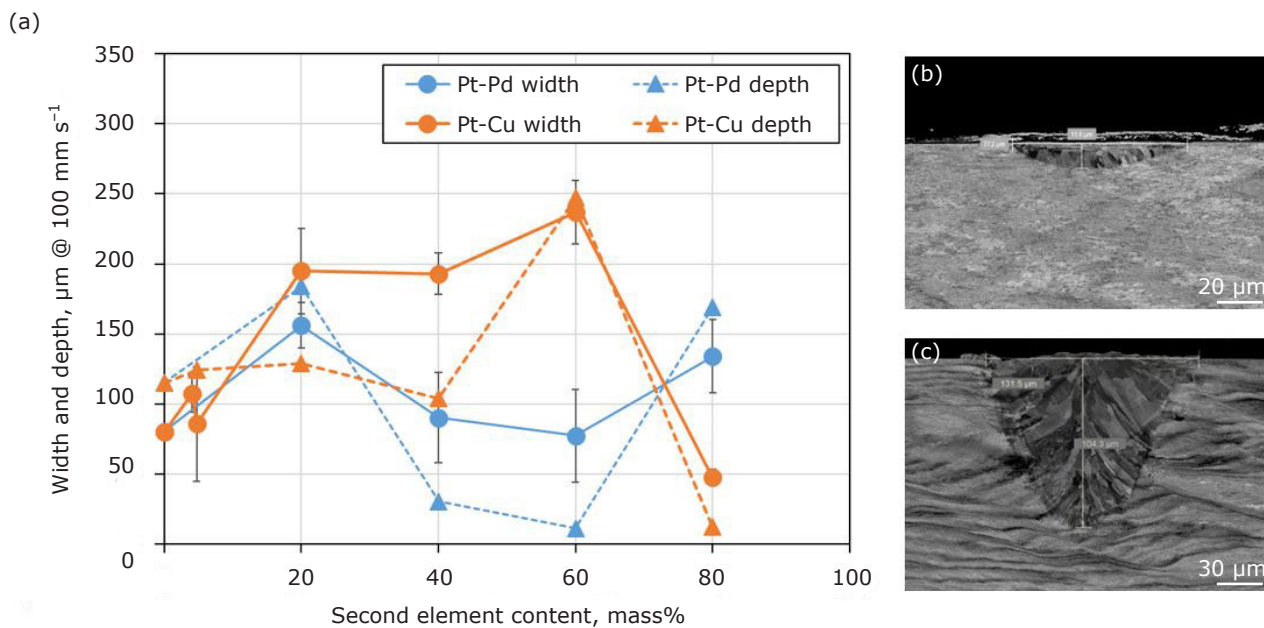


Fig. 3. (a) Effect of alloy composition on track width and depth in binary platinum-palladium and platinum-copper alloys; the micrographs for: (b) Pt-60Pd and (c) Pt-60Cu show typical examples for conduction mode and transition mode, respectively

and copper shows a different effect on width and depth of the laser tracks. Palladium tends to lower both values in an intermediate concentration range of 40–60%. Especially the depth shows a pronounced minimum. (Figure 3(b)) shows the very flat laser track, which is a typical example for the so-called conduction mode. For higher palladium contents the depth increases again. Tests at a laser speed of  $200 \text{ mm s}^{-1}$  showed similar results. The addition of copper shows the opposite trend to increase melt pool width and depth, especially in the intermediate concentration range (Figure 3(c)). However, the trends are affected by scatter of the experimental data.

A series of ternary alloys with 60% platinum was studied in the platinum-palladium-copper system (Figure 4). If palladium is exchanged by copper, both width and depth increase which results in a change from conduction mode (Figure 4(b)) to keyhole mode. With 270–290  $\mu\text{m}$  the depth is maximum for 20–30% copper (Figure 4(c)) where a typical keyhole mode occurs. For the binary platinum-copper alloy, the depth significantly decreases again to about 100  $\mu\text{m}$ .

The effect of cobalt, ruthenium, copper and gold is shown in Figure 5. These elements were added in smaller amounts according to the compositions of typical alloys used in the jewellery and watch industry. No significant effect of these alloying additions on the width and the depth of the laser tracks was found. The values are very similar

to pure platinum. A similar result was obtained for alloys with 95% platinum. Figure 5 shows compositions based on 95Pt-Ru where ruthenium is gradually replaced by gold, copper or cobalt. The width and depth are not much affected by such changes of the chemical composition.

The addition of further elements was studied with alloys based on 95Pt-1.5Cu-3.5Ru. Ruthenium was partly replaced by 2% gallium, indium, tin, germanium or zinc (Figure 6). According to the binary phase diagrams, these elements strongly decrease the liquidus temperature and increase the melting range. The effect in the laser track experiments shows strong differences. The addition of indium and zinc has no significant effect, neither on track width nor track depth. Gallium and tin have an intermediate to strong effect, while germanium has the strongest effect. The track depth increases by a factor of six due to the addition of 2% germanium as shown in Figure 6(b). The alloy with the addition of gallium was prone to hot cracking (Figure 6(c)), which was not the case for the addition of other alloying elements.

### 3.2 Process Parameter Optimisation in Laser Powder Bed Fusion

One of the objectives of the laser track tests was to obtain a first impression of the effect of the laser speed on the PBF-LB process. The results for the

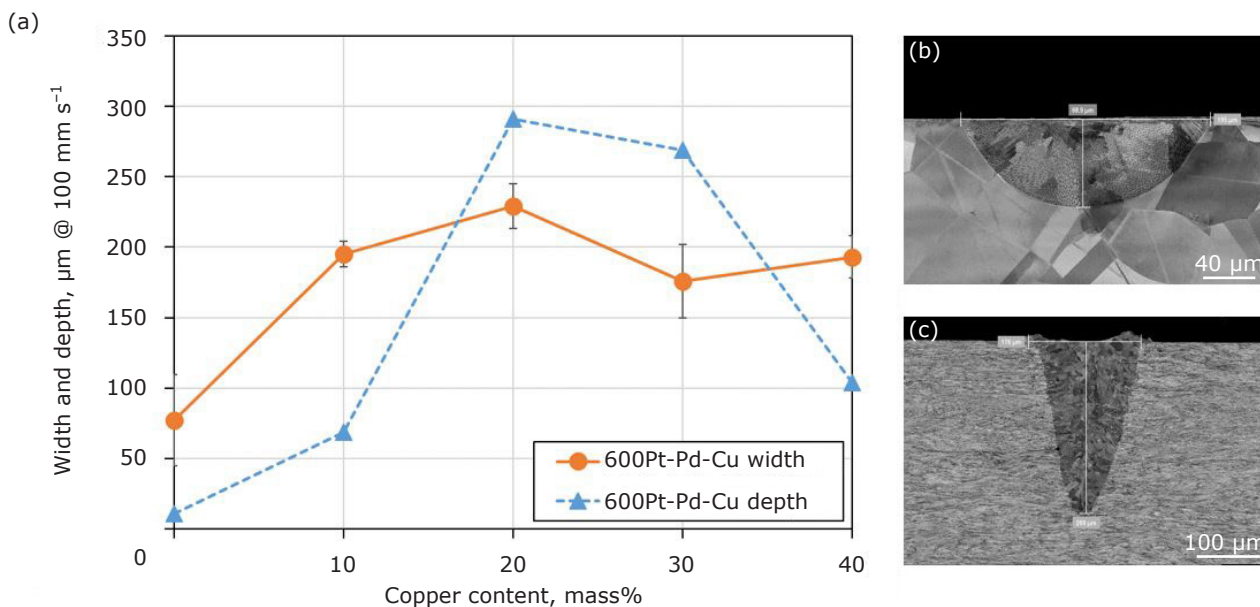


Fig. 4. (a) Effect of alloy composition on track width and depth in ternary platinum-palladium-copper alloys with a platinum content of 60%; SEM images of metallographic cross-sections of the alloys: (b) 60Pt-30Pd-10Cu and (c) 60Pt-10Pd-30Cu

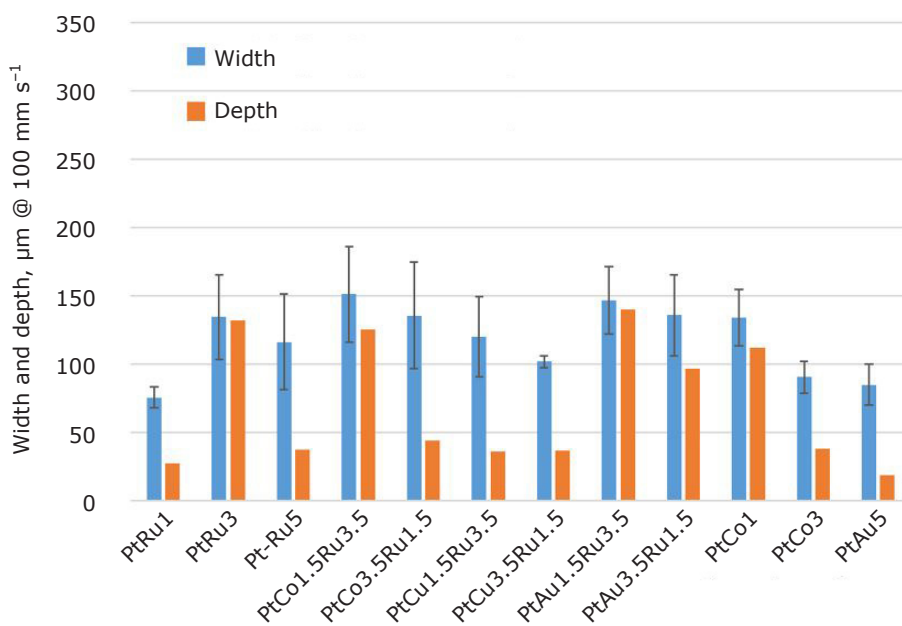


Fig. 5. Effect of alloy composition on track width and depth in platinum-X alloys of high platinum content

commercial alloys are shown in **Figure 7**. The error bars show the mean absolute deviation (MAD) of the average width. Taking into account the MAD most alloys show a width of 100–150  $\mu\text{m}$ . The 950Pt-W alloys are closer to 150  $\mu\text{m}$ . Alloys with similar composition obtained from two manufacturers are marked by #1 and #2. However, the results show significant scatter. The depth values show a larger variation than the width values. By far the highest width and depth were obtained for 950Pt-Ga-Cu. This alloy showed the smallest MAD of all alloys tested.

PBF-LB experiments on the alloy 950Pt-Au-In-Ru were conducted with alloyed powder, since it is commercially available as powder. It was provided by C.HAFNER. **Figure 2** shows two test samples produced by different sets of laser parameters. The part shown in **Figure 2(b)** was built with the optimum process parameters resulting in minimum porosity.

Generally, the porosity of this 950Pt alloy was very small (**Figure 8**) compared to other precious metal alloys (10, 19). For all hatch distances and

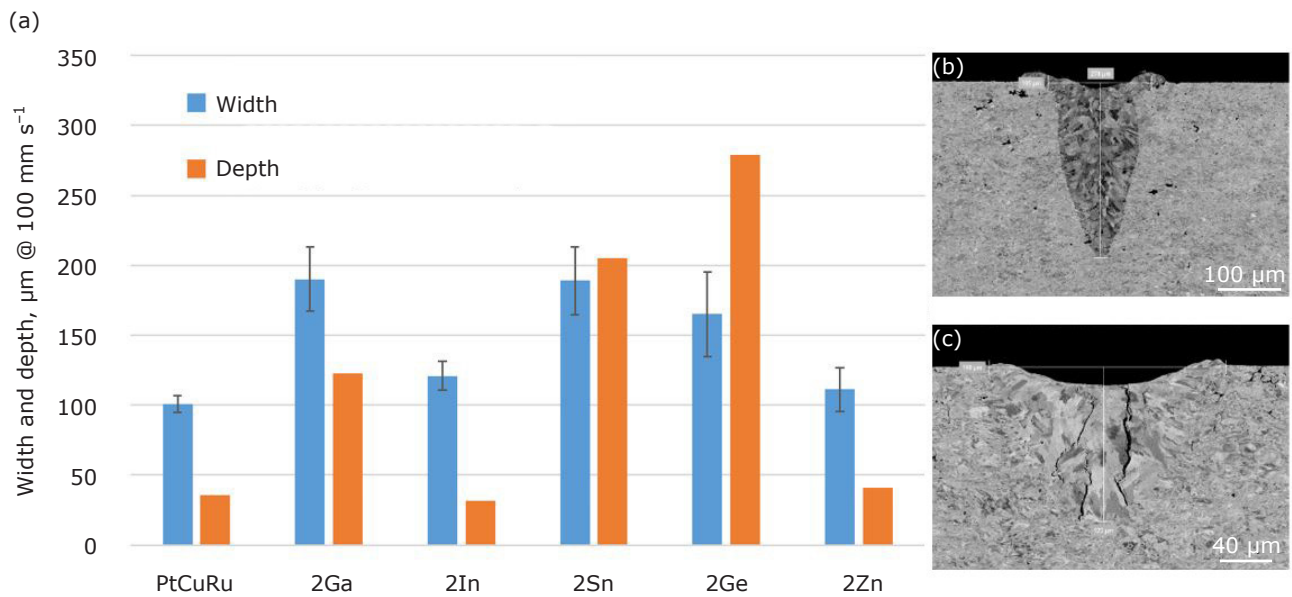


Fig. 6. (a) Effect of the addition of solidus suppressing elements in ternary 95Pt-1.5Cu-3.5Ru-X alloys; (b) effect of germanium; (c) effect of gallium. X stands for gallium, indium, tin, germanium or zinc that replace ruthenium in the alloy

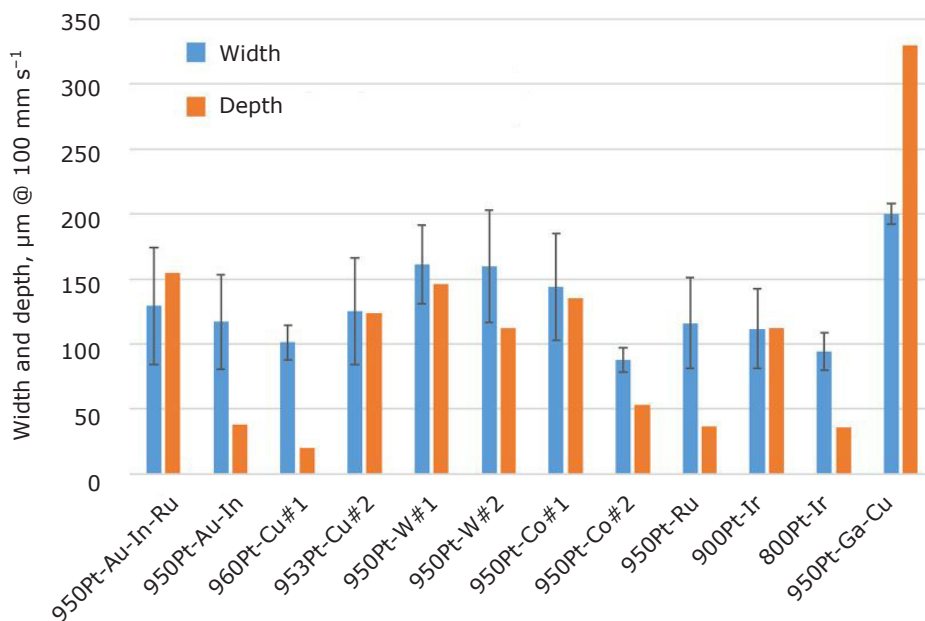


Fig. 7. Evaluation of laser track width and depth of technical alloys at a laser speed of  $100 \text{ mm s}^{-1}$ . Some alloy sheets were obtained from different manufacturers as indicated by the hash sign

laser speeds up to  $500 \text{ mm s}^{-1}$  the porosity was below 0.4%. The porosity increases with increasing laser speed and decreasing hatch distance. At  $600 \text{ mm s}^{-1}$  a significant increase is observed for most hatch distances.

The lowest porosity of below 0.1% (99.9% density) was achieved for a hatch distance of  $63 \mu\text{m}$ . At this hatch distance, the porosity levels are nearly independent of the laser speed. For all hatch distances and laser speeds up to  $500 \text{ mm s}^{-1}$  the porosity was below 0.4%. The porosity increases

with decreasing hatch distance and increasing laser speed. Decreasing hatch distance and increasing laser speed result in gas pores and lack-of-fusion porosity, respectively. At  $600 \text{ mm s}^{-1}$  a significant increase is observed and the process tends to become unstable. A hatch distance of  $63 \mu\text{m}$  and a laser speed of  $500 \text{ mm s}^{-1}$  were identified as optimum parameters throughout this study. These parameters provided the lowest porosity at a very high process speed (high hatch distance and laser speed).



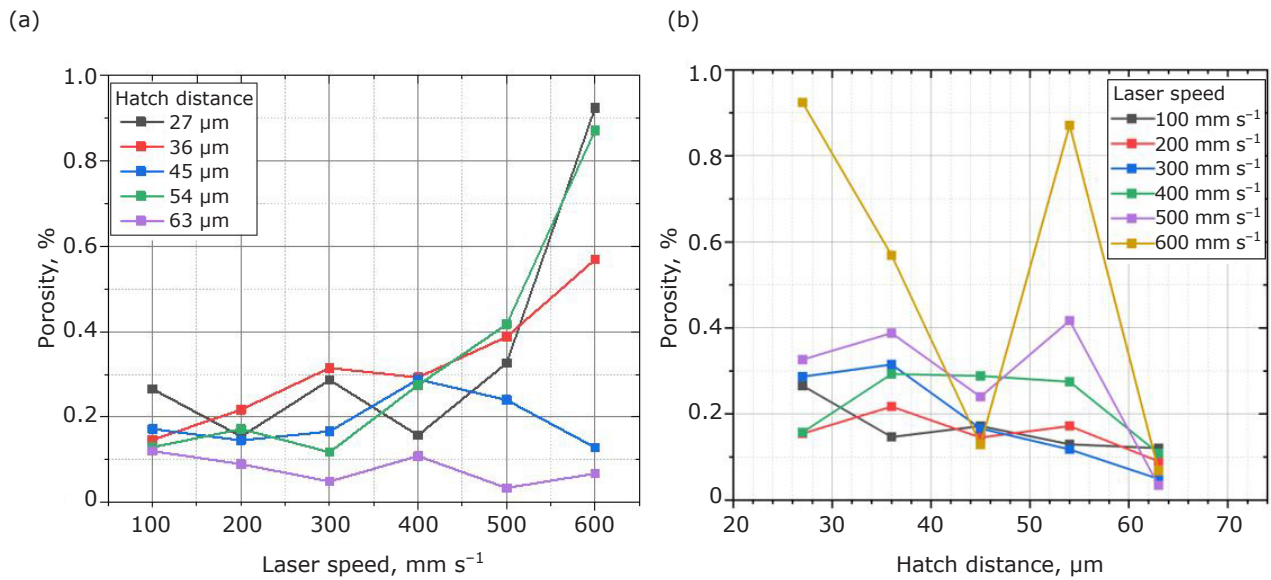


Fig. 8. (a) Effect of laser speed; and (b) effect of hatch distance. Laser power 95 W

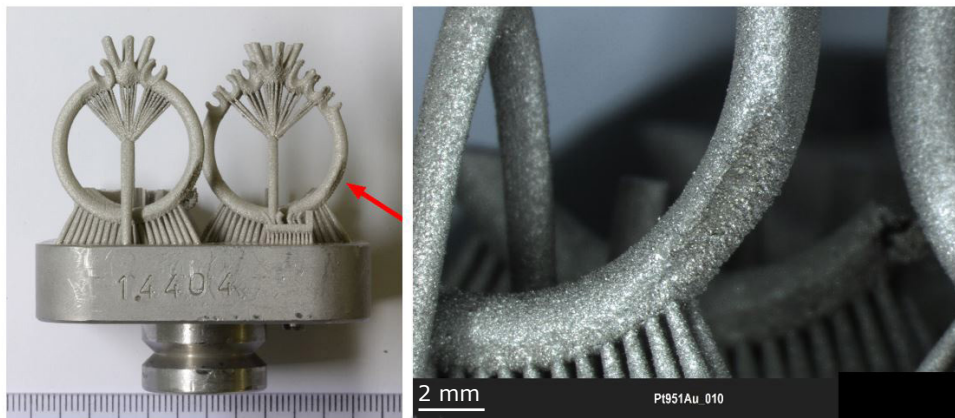


Fig. 9. As manufactured rings with standard support structure. The arrow marks defects on one side of the ring shank

### 3.3 Design of Support Structures for Jewellery Parts

Two jewellery designs, typical engagement rings with three or seven stones, were provided by project partners for additive manufacturing. The rings were supported by columnar hollow supports in areas with an inclination less than 45° to the build plate (Figure 9). The supports were positioned symmetrically on both sides of the ring. The recoater applied the powder on the build plate perpendicular to the plane of the ring shank. The laser direction was from right to left. Defects occurred on the right side in unsupported areas of the ring shank. Over a certain length of the ring shank, material is missing, but only on the right, outer side of the ring shank. The problem starts at the end of the support structure and it ends at a build angle of 72° (Figure 10).

In order to understand the problem, the additive manufacturing process was interrupted at a height of 7 mm, which is in the problematic region of the ring shank. An SEM investigation of the last built layer (Figure 11) indicates a perfect surface on the left side of ring. On the right side however, the surface appears highly porous. The surface is uneven with significant balling of the melt pool. The view on the outer surface of the ring shank and a metallographic section through the centre of the ring shank (Figure 12) show powder particles that stick to the surface. The powder particles themselves show a layer of much finer particles indicating a kind of condensate on the surface. Local chemical analysis by EDX showed an enrichment of the condensate with the alloying components gold and indium compared to the ring shank material.

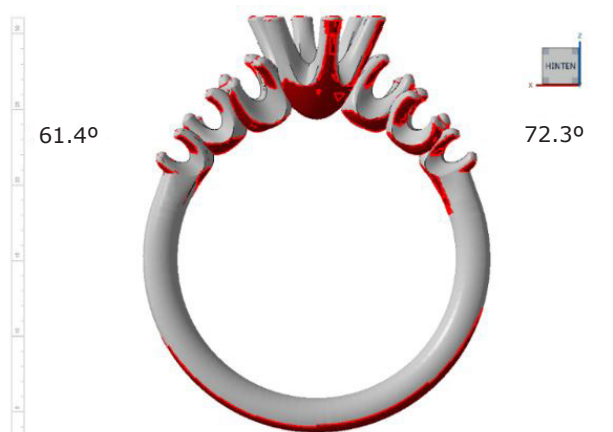


Fig. 10. Critical regions with possible excessive heating are shown in red

## 4. Discussion

### 4.1 Laser Track Tests on Metal Sheet

Two main modes of laser-metal interaction can be distinguished (20). In the conduction mode, no vaporisation of the material occurs and the melt pool depth is relatively small (**Figure 3(b)**). If the laser energy increases, i.e. the speed decreases, material evaporates and the melt pool becomes significantly deeper. **Figure 3(c)** shows a typical example of this transition mode. The transition mode occurs over a wide range of processing parameters (20). In the keyhole mode the material under the laser is strongly

heated causing more evaporation due to internal reflection of the laser light in the deep keyhole. This increases the absorption of laser light and turns the material into a black body (21). Such conditions result in very deep laser tracks (**Figure 4(c)**), often associated with typical keyhole porosity.

In the present study, the laser track experiments showed a certain amount of scattering in the width and depth measurements, which is a result of a change from conduction to transition mode and sometimes even to the keyhole mode. Such behaviour has been observed on different materials with different machines (22). Metallographic evaluation of such changes is quite time and material consuming. Therefore, the fraction of conduction mode was evaluated by qualitative assessment of the surface appearance of the laser tracks.

For the width, such scattering could be well described by measuring the average width over 15 mm of total track length. However, width is not much affected by changing the laser parameters. The determination of fluctuation in depth was not feasible as the amount of metallographic work would have been too much. It is known from literature (23–26) that the interaction of laser energy and the formation and size of a melt pool depends on several material properties, among which reflectivity, thermal conductivity, surface tension, viscosity, enthalpy of melting, liquidus temperature

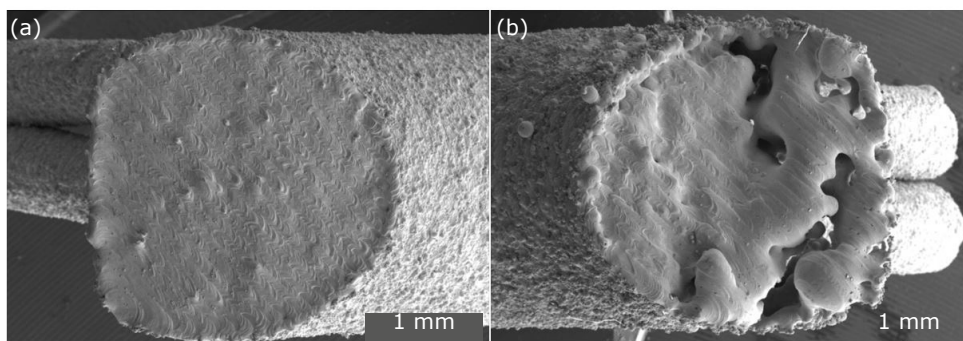


Fig. 11. Interrupted build job at a height of approximately 7 mm: (a) surface of the left side of the ring shank according to **Figure 9**; (b) surface of the right side of the ring shank according to **Figure 9**

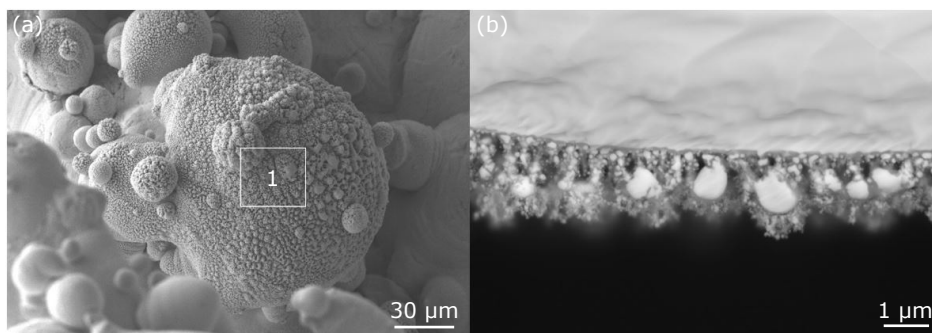


Fig. 12. Detail of the surface area of the right ring shank as marked in **Figure 11**

and melting range are the most important. By alloying, such properties can be strongly influenced (27–31). Therefore, it is not surprising that the higher alloyed materials (for example 60Pt-Pd-Cu alloys) showed a more pronounced effect on melting depth than the lower alloyed 95% platinum alloys. It is also not surprising that elements with strong effect on liquidus and solidus can strongly affect the melting depth even in small additions. The effects of the different alloying elements on the material properties and the resulting melting depth are discussed in the following paragraph.

The effect of the addition of melting point suppressing elements on the melting interval can be assessed based on the binary phase diagrams of platinum with these elements. However, in a multicomponent system such estimation might not be sufficient. Therefore, thermodynamic calculations of 95% platinum alloys were performed using the Thermo-Calc software package and the TCNOBL1 database (Thermo-Calc Software AB, Sweden), **Figure 13(a)**. The diagram shows a combination of five isopleth sections of the quaternary systems in the platinum-rich corner around the liquidus-solidus region. The liquidus and the solidus line of each system are plotted using the same colour. The ternary alloy 95Pt-1.5Cu-3.5Ru is plotted for an X-value of zero. This alloy has a very small melting range (difference between solidus and

liquidus temperature). If ruthenium is exchanged for one of the X elements both solidus and liquidus temperature are lowered and the melting interval increases. However, the extent of the reduction of solidus and liquidus temperature strongly depends on the element X. Indium and tin have the weakest effect on lowering solidus and liquidus temperature. The effect of zinc is slightly higher and that of gallium even more. Germanium has by far the strongest effect, especially on the solidus line, which is very much reduced for even small additions of germanium.

During the PBF-LB process, the very high cooling rate promotes the segregation of some alloying elements, which affects the actual solidus temperature. Scheil simulations consider the effect of limited diffusion in the solid phase and effects on the solidus temperature. Thermo-Calc offers a Scheil simulation with solute trapping that takes into account the conditions during additive manufacturing. The difference between equilibrium solidification (**Figure 13(a)**) and non-equilibrium solidification (**Figure 13(b)**) in terms of solidus temperature is significant. Zinc shows a relatively small difference between equilibrium and non-equilibrium solidification, because the eutectic reaction involving the PtZn phase above 1600°C (32) limits further lowering of the solidus temperature. This is supposed to limit the extension of the melt pool. Eutectic reactions also occur in the platinum-gallium and platinum-germanium systems.

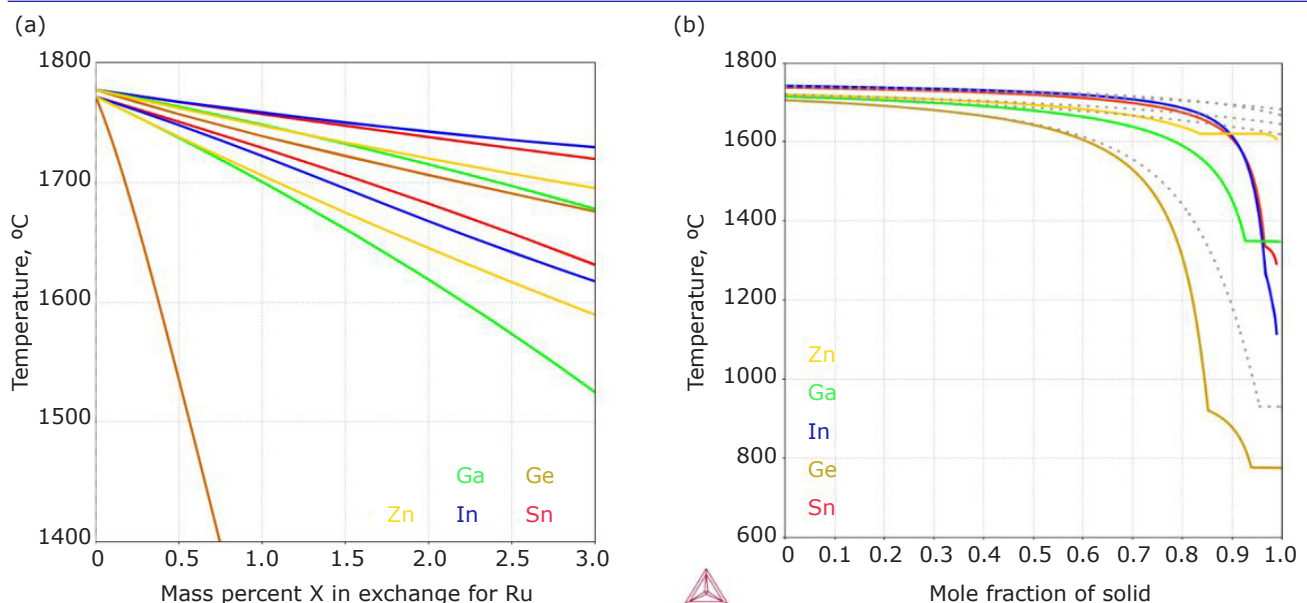


Fig. 13. Thermo-Calc calculations using TC\_V2022a and the TCNOBL1 database: (a) effect of the addition of low melting elements to 95Pt-1.5Cu-Ru-X alloys on the liquidus and solidus line; (b) Scheil calculation with solute trapping for a scanning speed of 100 mm s<sup>-1</sup> for alloys 95Pt-1.5Cu-1.5Ru-2X. Dotted lines represent equilibrium cooling conditions



However, the eutectic temperatures are much lower. The lower temperature results in a much deeper melt pool.

## 4.2 Laser Powder Bed Fusion Parameter Optimisation

Suitable PBF-LB parameters of the chosen 951PtP1 alloy could be determined to obtain a porosity below 0.1%. The porosity is a factor of 10 lower compared to surface treated 18 karat 3N gold alloys that were produced using the same machine (9). Staiger (33) investigated the width and depth of laser tracks on metallic sheet material and found that the width and depth of a 951PtP1 alloy was comparable to austenitic stainless steel and grade 5 titanium. 18 karat palladium white gold showed slightly higher width and depth compared to 951PtP1, while 18 karat yellow and red gold showed much lower width and depth of the laser lines. The similarity of 951PtP1 to austenitic stainless steel and grade 5 titanium is due to its similar infrared light reflectivity and similar thermal conductivity.

The porosity of parts produced by PBF-LB is a function of scan speed (34, 35). At low scan speed, i.e. high-energy tendency the porosity is relatively high due to keyhole porosity. Keyholing could be achieved on 951PtP1 sheet only at extremely low scan speed (25–50 mm s<sup>-1</sup> at 95 W) (33). According to Tang *et al.* (35) the lowest porosity is achieved in a medium range scan speed. For 950Pt alloys, this was achieved in the present study at 100–600 mm s<sup>-1</sup> (hatch distance 63 μm, laser power of 95 W, **Figure 8**). If the scan speed is further increased, Tang *et al.* (35) describe an increase of porosity due to lack of fusion. This work showed lack of fusion in 951PtP1 for hatch distances below 63 μm. The previous study on 18 karat yellow gold (9) found that lack of fusion pores emerge throughout the complete range of process parameters. Fully dense gold parts could be achieved at much higher laser powers of 375 W (12).

## 4.3 Optimisation of the Support Structure

The condensation of material that was observed on the defective ring shank (**Figure 12**) requires an initial evaporation of alloying elements. This is a clear indication of localised excessive heating of the material. To identify the reason for such overheating, the process conditions were analysed in detail. It appears that the laser works from right to left during the hatch scan. The different

curvature of the ring on the left and right sides relative to the laser direction results in insufficient heat dissipation on the right side of the ring shank. The laser scans from right to left. Therefore, it first encounters an unsupported powder bed with limited heat dissipation on the right side of the ring shank. As a consequence, about 50% of the ring shank cross-section (**Figure 11**) is locally overheated, which results in the evaporation of the lower melting elements (gold, indium) of the alloys. The left ring shank however does not suffer from such overheating because the laser starts on a well supported powder bed. On the very left side of the left ring shank the already lasered layer provides sufficient heat dissipation to prevent overheating.

In order to prevent the observed ring shank defects, sufficient heat dissipation has to be ensured on the right side of the ring shank by additional supports. The critical angle that requires additional supports was determined to be approximately 61° and 72° on the left and the right side of the ring shank, respectively. The critical angles on either side were determined by optical quality control of the rings. The supports should reach up to 6 mm and 8 mm on the left and the right side of the ring, respectively. Such regions are marked in red in **Figure 10**. These angles are much larger than a conventional rule of thumb that only surfaces with an angle below 45° should require supports.

Finally, all regions with smaller angles relative to the building plate were supported. **Figure 14** shows the support structures before and after optimisation. With optimised supports the ring could be manufactured without defects (**Figure 15**). Polishing and stone setting resulted in perfect finish.

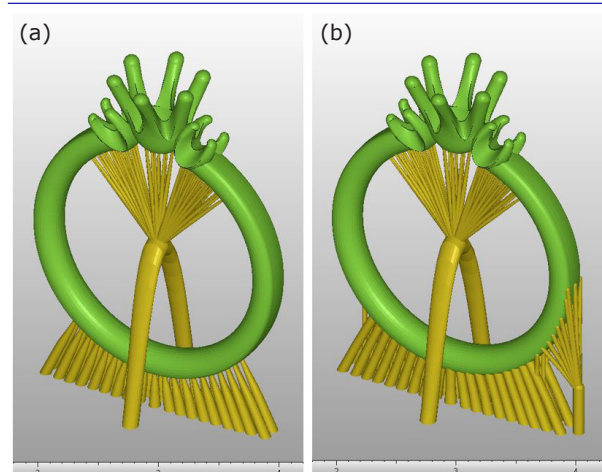


Fig. 14. CAD model of the ring with: (a) the original support structure; and (b) the optimised support structure. Arrows indicate the additional supports

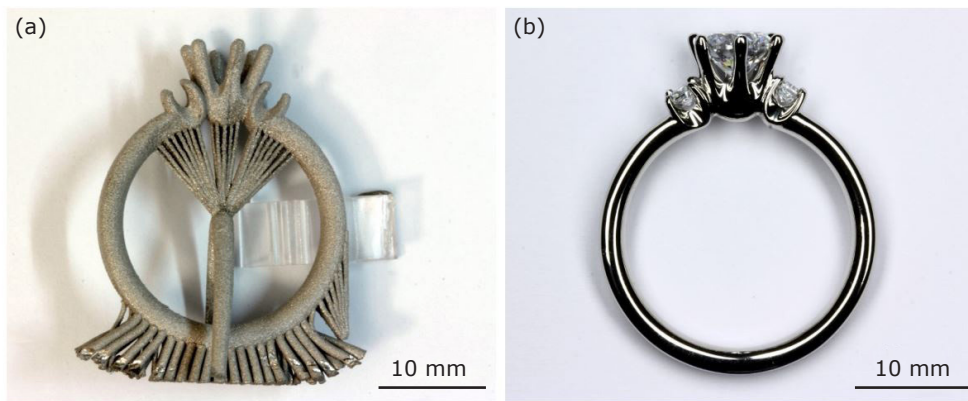


Fig. 15. Final ring (outer diameter 23 mm) with optimised support structure: (a) after the laser powder bed fusion process; and (b) after polishing and stone setting

## 5. Summary and Conclusions

Experiments with laser tracks on sheet materials showed a transition of the laser-material interaction from conduction to transition mode for most of the alloys tested. The transition mode can be unstable resulting in a very large scatter of the width and depth values of the laser tracks. A stable keyhole mode was only reached for alloys that contained high amounts of germanium, gallium or tin. Laser track experiments on metal sheets allow the testing of many different alloys with reduced experimental effort. However, due to the large scatter they are difficult to evaluate and barely useful for a determination of suitable parameters for PBF-LB. They allow the effect of alloying additions on the laser-material interaction to be studied.

The additive manufacturing of 950Pt alloys by PBF-LB technology was successfully demonstrated. The optimum process parameters were a hatch distance of 63  $\mu\text{m}$  and a laser speed of 100–600  $\text{mm s}^{-1}$  at a laser power of 95 W (Nd:YAG laser with 1064 nm wavelength and a spot size of 30  $\mu\text{m}$ ). For such parameters a residual porosity below 0.1% could be reached. A smaller hatch distance resulted in gas porosity. 950Pt alloys can be processed with similar parameters to austenitic stainless steel (316L).

Jewellery ring samples were prepared with conventional support structures. However, it appeared that the design of the supports must take into account machine-specific laser scanning procedures. Additional supports were required at positions where the laser encounters an unsupported powder bed if the orientation of the parts was below approximately 72° relative to the build plate. Otherwise, excessive heating resulted in the evaporation of material causing defective surfaces. Therefore, careful design of the support structures must be considered as part of PBF-LB process optimisation.

## Acknowledgements

This research project was supported by the Federal Ministry for Economic Affairs and Energy (BMWi) through the AiF (IGF no. 20670N) based on a decision taken by the German Bundestag. We kindly acknowledge the support of the members of the users committee, in particular the provision of 951PtP1 alloy powder and 3D CAD models by C. Hafner GmbH+Co.KG and Christian Bauer Schmuck GmbH+Co.KG, respectively. We thank our colleagues at fem for their contribution, namely Dario Tiberto and Daniel Blessing for additive manufacturing trials, metallography and SEM.

## References

1. D. Zito, A. Carlotto, A. Loggi, S. Bortolamei, A. Molinari and I. Cristofolini, 'Latest Developments in Selective Laser Melting Production of Gold Jewelry', in 26th Santa Fe Symposium on Jewelry Manufacturing Technology, Albuquerque, New Mexico, USA, 20th–23rd May, 2012, pp. 537–562
2. D. Zito, A. Carlotto, A. Loggi, P. Sbornicchia, D. Maggian, M. Fockele, P. Unterberg, A. Molinari and I. Cristofolini, 'Optimization of the Main Selective Laser Melting Technology Parameters in the Production of Precious Metal Jewelry', in 27th Santa Fe Symposium on Jewelry Manufacturing Technology, Albuquerque, New Mexico, USA, May, 2013, pp. 1–20
3. D. Zito, A. Carlotto, P. Sbornicchia, A. Molinari, I. Cristofolini, P. Unterberg and M. Fockele, 'Optimization of SLM Technology Main Parameters in the Production of Gold and Platinum Jewelry', in 28th Santa Fe Symposium on Jewelry Manufacturing Technology, Albuquerque, USA, 18th–21st May, 2014, pp. 439–469
4. D. Zito, A. Carlotto, A. Loggi, P. Sbornicchia, D. Bruttomesso and S. Rappo, 'Definition and Solidity of Gold and Platinum Jewelry Produced



- Using Selective Laser Melting (SLM™) Technology', in 29th Santa Fe Symposium on Jewelry Manufacturing Technology, Albuquerque, New Mexico, USA, May, 2015, pp. 455–491
5. D. Zito, V. Allodia, P. Sbornicchia, S. Rappo and L. Fiorese, 'Direct 3D Metal Printing: A Trip through New Opportunities and Innovative Alloys', in 30th Santa Fe Symposium on Jewelry Manufacturing Technology, Albuquerque, New Mexico, USA, May, 2016, pp. 473–514
  6. D. Zito, V. Allodia, F. Trevisan, M. G. M. Rossini, A. Rossini and M. Mazza, 'Potential and Innovation of the Selective Laser Melting Technique in Platinum Jewelry Production', in 32nd The Santa Fe Symposium on Jewelry Manufacturing Technology, Albuquerque, New Mexico, USA, May, 2018, pp. 625–684
  7. D. Zito, Progold SPA, 'Use of Gold Powder Alloys for Manufacturing Jewellery Items by Selective Laser Melting', *US Patent* 10,638,819; 2020
  8. D. Zito, E. Saccardo, P. Sbornicchia, V. Allodia and G. A. C. Arque, 'Innovative Printing Strategy for High-Resolution Jewelry Production by Selective Laser Melting', in 2022 Santa Fe Symposium on Jewelry Manufacturing Technology, Albuquerque, New Mexico, USA, May, 2022, pp. 629–666
  9. U. E. Klotz, D. Tiberto and F. Held, *Gold Bull.*, 2017, **50**, (2), 111
  10. U. E. Klotz, D. Tiberto and F. J. Held, *Galvanotechnik*, 2019, **110**, (8), 1436
  11. D. Fletcher and F. Cooper, 'The Precious Project: Polishing and Finishing of Additive Manufacturing (AM) Jewelry', in 2018 Santa Fe Symposium on Jewelry Manufacturing Technology, Albuquerque, New Mexico, USA, May, 2018, pp. 211–234
  12. H. Ghasemi-Tabasi, J. Jhabvala, E. Boillat, T. Ivas, R. Drissi-Daoudi and R. E. Logé, *Addit. Manuf.*, 2020, **36**, 101496
  13. C. Pogliani and A. Albertin, 'Case Study of Problems and Their Solutions for Making Quality Jewelry Using Selective Laser Melting (SLM) Technology', in 30th Santa Fe Symposium on Jewelry Manufacturing Technology, Albuquerque, New Mexico, USA, May, 2016, pp. 431–458
  14. J. Strauss, 'Additive Manufacturing of Precious Metals', in "ASM Handbook: Additive Manufacturing Processes", eds. D. L. Bourell, W. Frazier, H. Kuhn and M. Seifi, Vol. 24, ASM International, Materials Park, USA, 2020
  15. T. Laag and J. Heinrich, 'Advantages and Challenges of Platinum Group Metals Powder Processing', in 2018 Santa Fe Symposium on Jewelry Manufacturing Technology, Met-Chem Research, Albuquerque, New Mexico, USA, May, 2018, pp. 327–343
  16. U. E. Klotz and T. Drago, *Platinum Metals Rev.*, 2011, **55**, (1), 20
  17. T. Heiss, U. E. Klotz and D. Tiberto, *Johnson Matthey Technol. Rev.*, 2015, **59**, (2), 95
  18. U. E. Klotz, T. Heiss and D. Tiberto, *Johnson Matthey Technol. Rev.*, 2015, **59**, (2), 129
  19. U. E. Klotz, D. Tiberto and F. Held, 'Additive Manufacturing of 18-Karat Yellow-Gold Alloys', in 30th Santa Fe Symposium on Jewelry Manufacturing Technology, Albuquerque, New Mexico, USA, May, 2016, pp. 255–272
  20. S. Patel and M. Vlasea, *Materialia*, 2020, **9**, 100591
  21. B. Fotovvati, S. F. Wayne, G. Lewis and E. Asadi, *Adv. Mater. Sci. Eng.*, 2018, 4920718
  22. F. J. Held and U. E. Klotz, 'Effect of Material Properties and Process Parameters in Powder Bed Additive Manufacturing', in 2022 Santa Fe Symposium on Jewelry Manufacturing Technology, Albuquerque, New Mexico, USA, May 2022, pp. 233–262
  23. Z. Li, G. Yu, X. He, S. Li, C. Tian and B. Dong, *Opt. Laser Technol.*, 2020, **123**, 105914
  24. R. Fabbro, *J. Phys. D: Appl. Phys.*, 2010, **43**, (44), 445501
  25. W. E. King, H. D. Barth, V. M. Castillo, G. F. Gallegos, J. W. Gibbs, D. E. Hahn, C. Kamath and A. M. Rubenchik, *J. Mater. Process. Technol.*, 2014, **214**, (12), 2915
  26. A. M. Rubenchik, W. E. King and S. S. Wu, *J. Mater. Process. Technol.*, 2018, **257**, 234
  27. S. Mehmood, U. E. Klotz and G. Pottlacher, *Metall. Mater. Trans. A*, 2012, **43**, (13), 5029
  28. S. Mehmood, U. E. Klotz and G. Pottlacher, 'Thermophysical Properties of the Platinum-Copper System', EPD Congress, San Diego, USA, 27th February–3rd March, 2011, eds. S. N. Monteiro, D. E. Verhulst, P. N. Anyalebechi and J. A. Pomykala, John Wiley & Sons Inc, Hoboken, USA, 2011, pp. 167–173
  29. U. E. Klotz and Y. Plevachuk, *High Temp. High Press.*, 2016, **45**, (1), 3
  30. Y. Plevachuk, S. Mudry, V. Sklyarchuk, A. Yakymovych, A. Korolyshyn, I. Shtablavy, Y. Kulyk, U. E. Klotz, C. Liu and C. Leinenbach, *Int. J. Mater. Res.*, 2009, **100**, (5), 689
  31. Y. Plevachuk, S. Mudry, V. Sklyarchuk, A. Yakymovych, U. E. Klotz and M. Roth, *J. Mater. Sci.*, 2007, **42**, (20), 8618
  32. Z. Moser, *J. Phase Equilibria*, 1991, **12**, (4), 439
  33. R. Staiger, 'Einfluss der Prozessparameter und er Werkstoffeigenschaften bei der Additiven Fertigung von Metallischen Werkstoffen', Bachelor Thesis, HFU Hochschule Furtwangen University, Furtwangen, Germany, 2019
  34. H. Gong, K. Rafi, H. Gu, T. Starr and B. Stucker, *Addit. Manuf.*, 2014, **1–4**, 87
  35. M. Tang, P. C. Pistorius and J. L. Beuth, *Addit. Manuf.*, 2017, **14**, 39

---

## The Authors



Ulrich E. Klotz studied Physical Metallurgy at the University of Stuttgart, Germany, and earned his PhD from The Swiss Federal Institute of Technology (ETH) Zurich, Switzerland. From 1999 to 2007 he worked at the Swiss Federal Laboratories for Materials Testing and Research (Empa) in Dübendorf, Switzerland. Since 2007 he is Head of the Department of Physical Metallurgy at the Research Institute for Precious Metals and Metals Chemistry (fem), Germany. His research interests are thermodynamics and phase diagrams and processing technology including investment casting and additive manufacturing of precious metal alloys.



Frank König did an apprenticeship as material tester metal technology at vothec Labor GmbH and studied materials engineering at Aalen University, Germany. Now he is studying Metallurgy at the University of Leoben, Austria. Since 2019 he is responsible for the Additive Manufacturing Laboratory in the Department of Physical Metallurgy at the fem. His research interests are metallurgical processes including additive manufacturing and metal atomisation. Furthermore the process monitoring and optimisation with data analytics.

# Study on Technical Parameters and Suitability of Platinum-Based Metallic Glasses for Jewellery Applications

## Testing a series of platinum-based alloys for novel designs

### L.-Y. Schmitt\*

Research Institute for Precious Metals and Metal Chemistry (fem), Katharinenstrasse 17, 73525 Schwäbisch Gmünd, Germany

### N. Neuber

Saarland University, Campus C6.3, 66123 Saarbrücken, Germany

### M. Eisenbart

Research Institute for Precious Metals and Metal Chemistry (fem), Katharinenstrasse 17, 73525 Schwäbisch Gmünd, Germany

### L. Ciftci

Saarland University, Campus C6.3, 66123 Saarbrücken, Germany

### O. Gross

Amorphous Metal Solutions, Michelinstraße 9, 66424 Homburg, Germany

### U. E. Klotz

Research Institute for Precious Metals and Metal Chemistry (fem), Katharinenstrasse 17, 73525 Schwäbisch Gmünd, Germany

### R. Busch

Saarland University, Campus C6.3, 66123 Saarbrücken, Germany

\*Email: [Schmitt@fem-online.de](mailto:Schmitt@fem-online.de)

### PEER REVIEWED

Received 21st March 2022; Revised 15th June 2022; Accepted 5th July 2022; Online 13th July 2022

Jewellery-specific standardised tests as well as bulk metallic glass (BMG)-specific testing methods were performed on a series of platinum-based BMGs with and without phosphorus, to evaluate their suitability as jewellery items. Their mechanical properties (elasticity, Young's modulus and yield stress) were determined by three-point beam bending measurements. Hardness, wear and corrosion resistance were tested in comparison to state-of-the-art crystalline platinum-based jewellery alloys. The platinum-BMG alloys exhibit elastic elongation of about 2%. Compared to conventional crystalline platinum-alloys, their fracture strength of ca. 2 GPa and their hardness of ca. 450 HV1 is four and two times higher, respectively. However, the BMGs show less abrasion resistance in the pin-on-disc test than the conventional benchmark alloys due to adhesive wear and microcracking. Regarding the corrosion resistance in simulated body fluids, the BMG alloys reveal a slightly higher release of metals, while the tarnishing behaviour is comparable to the benchmark alloys. The phosphorus-free platinum-BMG alloy showed pronounced tarnishing during exposure to air at elevated temperature. The outstanding thermoplastic formability, a special feature of amorphous metals that can be crucial for enabling novel and filigree designs, was determined and quantified for all BMG alloys.

## 1. Introduction

Platinum-based BMGs have been the subject of research since 2005 and possess high potential for jewellery applications (1, 2). One advantage is that they show low liquidus temperatures of about 520°C due to their chemical composition in the vicinity of the phosphorus-platinum eutectic composition (2, 3). The absence of microstructural features in amorphous metals results in a high as-cast hardness, high mechanical strength, an outstanding surface quality and the absence of volume shrinkage during solidification (3, 4, 5). However, amorphous solidification requires very high cooling rates in comparison to conventional casting in order to inhibit crystallisation. This leads to a challenging casting process and ultimately limits the casting dimensions. The BMG alloys Pt<sub>42.5</sub>Cu<sub>27</sub>Ni<sub>9.5</sub>P<sub>21</sub> and Pt<sub>60</sub>Cu<sub>16</sub>Co<sub>2</sub>P<sub>22</sub> show a critical cooling rate of around 20 K s<sup>-1</sup> to successfully inhibit crystallisation and can be cast amorphously in diameters of about 20 mm (3), which is sufficient for their application as jewellery components.

Conventional platinum jewellery alloys challenge the casting process with their high melting temperatures of about 1850–2050°C and they reveal high shrinkage porosity (6, 7, 8) and low as-cast hardness. Binary jewellery alloys such as 95Pt-5Cu or 95Pt-5Ir possess as-cast hardness values less than 120 HV1 and ternary precipitation hardenable alloys such as 95Pt-2Ru-3Ga reach hardness values of about 200 HV1 (9). Work hardening, which is not applicable to investment cast parts, is required in order to reach a higher hardness (9).

Furthermore, BMGs show thermoplastic formability with high precision forming and enable new decorative designs (3, 10, 11). It has been shown that surface patterning of Pt<sub>57.5</sub>Cu<sub>14.7</sub>Ni<sub>5.3</sub>P<sub>22.5</sub> is possible with an accuracy in the nanometre range which can result in a superficial hologram effect (11). Hence, the properties of platinum-based BMGs make them attractive for jewellery and watchmaking and have led to numerous investigations on BMGs with high fineness (85Pt and 95Pt) for almost 20 years. The focus was laid on their glass forming ability and thermoplastic processability, but their corrosion and tarnishing resistance as well as wear resistance are not yet as intensively investigated as a huge variety of conventional platinum-based alloys (12). So far, good scratch (13) and wear resistance (2, 14)

are assumed for BMG alloys since they exhibit high hardness. For a better understanding of their applicability as jewellery items, this study focuses on technical aspects from alloy preparation to further manufacturing processes of alloys with a platinum content of around 85 wt%. A series of test procedures typically used for the characterisation of glassy metals in combination with standardised jewellery-specific tests was performed. The standard test procedures were carried out in comparison to conventional platinum jewellery alloys.

Mechanical properties such as elasticity limit, critical strains and wear resistance are in the scope of this work as well as the corrosion performance of the BMGs and benchmark alloys. Experiments in simulated body fluids and tarnishing tests for a few BMG alloys at elevated temperatures were conducted.

Since BMGs show the advantageous ability of plastic forming for novel designs (2), thermoplastic properties and the formability of the platinum-BMGs were characterised in this work to extend the understanding of their thermoplastic behaviour.

## 2. Materials and Methods

An overview of the investigated platinum-BMGs with their indications and compositions given in atomic percent (at%) are provided in **Table I** and weight percent (wt%) in **Table II**. The series of platinum BMG alloys chosen for this study consist of alloys from the platinum-copper-nickel/cobalt-phosphorus systems as well as nickel/cobalt and phosphorus-free systems. Throughout this work they will be named by their composition in atomic percent. Except the alloy Pt<sub>42.5</sub>Cu<sub>27</sub>Ni<sub>9.5</sub>P<sub>21</sub>, all BMGs reach a fineness of 85 wt% platinum. The conventional benchmark alloys and their compositions given in weight percent can be read in **Table III**. The benchmarks taken for the corrosion resistant tests are soft annealed. For the mechanical tests, they were taken in the as-cast and cold worked state. They are named with 'a.c' if they were tested in the as-cast state and are labelled with 'c.w' if the samples have undergone a cold work treatment. **Table IV** lists all alloys used in this work and the methods used on them.

The standardised tests were repeated three times for the glassy samples: once for the first alloy batch and twice for a second alloy batch. The conventional platinum-jewellery alloys were tested

**Table I The Compositions of the Platinum-BMG Alloys by Atomic Percent**

Alloy	at%								
	Pt	Cu	P	Ni	Co	Si	B	Ag	Ge
Pt <sub>42.5</sub> Cu <sub>27</sub> Ni <sub>9.5</sub> P <sub>21</sub>	42.50	27.00	21.00	9.50	-	-	-	-	-
Pt <sub>49.95</sub> Cu <sub>16.5</sub> Si <sub>6.4</sub> B <sub>24</sub> Ge <sub>3</sub>	49.95	16.50	-	-	-	6.40	24.00	-	3.00
Pt <sub>57.3</sub> Cu <sub>14.6</sub> P <sub>22.8</sub> Ni <sub>5.3</sub>	57.30	14.60	22.80	5.30	-	-	-	-	-
Pt <sub>57.8</sub> Cu <sub>19.2</sub> Ag <sub>1</sub> P <sub>20.6</sub> B <sub>1.4</sub>	57.80	19.20	20.60	-	-	-	1.40	1.00	-
Pt <sub>58.7</sub> Cu <sub>20.30</sub> Ag <sub>1</sub> P <sub>20</sub>	58.70	20.30	20.00	-	-	-	-	1.00	-
Pt <sub>60</sub> Cu <sub>16</sub> Co <sub>2</sub> P <sub>22</sub>	60.00	16.00	22.00	-	2.00	-	-	-	-

**Table II The Compositions of the Platinum-BMG Alloys by Weight Percent**

Alloy	wt%								
	Pt	Cu	P	Ni	Co	Si	B	Ag	Ge
Pt <sub>42.5</sub> Cu <sub>27</sub> Ni <sub>9.5</sub> P <sub>21</sub>	73.90	15.30	5.80	5.00	-	-	-	-	-
Pt <sub>49.95</sub> Cu <sub>16.5</sub> Si <sub>6.4</sub> B <sub>24</sub> Ge <sub>3</sub>	85.03	9.23	-	-	-	1.57	2.26	-	1.90
Pt <sub>57.3</sub> Cu <sub>14.6</sub> P <sub>22.8</sub> Ni <sub>5.3</sub>	85.18	7.07	5.38	2.37	-	-	-	-	-
Pt <sub>57.8</sub> Cu <sub>19.2</sub> Ag <sub>1</sub> P <sub>20.6</sub> B <sub>1.4</sub>	85.06	9.02	4.81	-	-	-	0.11	0.81	-
Pt <sub>58.7</sub> Cu <sub>20.30</sub> Ag <sub>1</sub> P <sub>20</sub>	85.02	9.58	4.90	-	-	-	-	0.80	-
Pt <sub>60</sub> Cu <sub>16</sub> Co <sub>2</sub> P <sub>22</sub>	86.57	7.52	5.04	-	0.87	-	-	-	-

**Table III The Compositions of the Benchmark Alloys by Weight Percent**

Alloy	wt%					
	Pt	Cu	Co	W	Ir	Pd
800PtIr	80.0	-	-	-	20	-
950PtW	95.0	-	-	5.0	-	-
953PtCu	95.3	4.7	-	-	-	-
600PtPd	60.0	30.0	-	-	-	10.0
950PtCo	95.0	-	5.0	-	-	-
960PtCu	96.0	4.0	-	-	-	-

**Table IV List of the Alloys and Conducted Testing Methods**

Alloy	Mechanic tests	Wear resistance and hardness	Nickel release	Artificial saliva	Annealing in air	Formability
Pt <sub>42.5</sub> Cu <sub>27</sub> Ni <sub>9.5</sub> P <sub>21</sub>	-	X	X	X	-	X
Pt <sub>49.95</sub> Cu <sub>16.5</sub> Si <sub>6.4</sub> B <sub>24</sub> Ge <sub>3</sub>	-	X	-	X	X	-
Pt <sub>57.3</sub> Cu <sub>14.6</sub> P <sub>22.8</sub> Ni <sub>5.3</sub>	-	X	X	X	X	X
Pt <sub>57.8</sub> Cu <sub>19.2</sub> Ag <sub>1</sub> P <sub>20.6</sub> B <sub>1.4</sub>	X	X	-	X	-	X
Pt <sub>58.7</sub> Cu <sub>20.30</sub> Ag <sub>1</sub> P <sub>20</sub>	X	X	-	X	X	X
Pt <sub>60</sub> Cu <sub>16</sub> Co <sub>2</sub> P <sub>22</sub>	X	X	-	X	-	X
800PtIr <sup>a</sup>	-	-	-	X	-	-
950PtW <sup>a</sup>	-	-	-	X	-	-
953PtCu <sup>a</sup>	-	-	-	X	-	-
600PtPd <sup>a</sup>	-	-	-	X	-	-
950PtCo <sup>a</sup>	-	X	-	X	-	-
960PtCu <sup>a</sup>	-	X	-	-	-	-

<sup>a</sup>Benchmark alloys



only once, since their properties are known and they serve in the comparative study as a reference.

## 2.1 Sample Preparation

The alloys were prepared from high purity elements of at least 99.95% purity and master alloys. The master alloys for the glassy samples were produced following the two-step procedure described in (15). The samples were produced by arc-melting followed by suction casting. A custom-built arc-melting furnace with a suction casting inset was used. The alloy was melted in a high purity titanium-gettered argon atmosphere on top of a water-cooled copper crucible and then sucked into the mould cavity.

A second preparation method was performed using a modified MC15 tilt-casting device (INDUTHERM Erwärmungsanlagen GmbH, Germany). Here, the pure elements were inductively melted in a zirconia-coated alumina crucible under argon (0.6 Ar) atmosphere and consequently the melt was poured into a water-cooled copper mould. The master alloy  $\text{Pt}_{49.95}\text{Cu}_{16.5}\text{Si}_{6.4}\text{B}_{24}\text{Ge}_3$  was prepared by arc melting and subsequently cast in a centrifugal casting machine using a silica crucible in an atmosphere of 700 mbar argon. The level of impurities was expected to be similar to those given by the initial raw materials. The alloy composition was validated with continuous control of the masses involved in the alloying process. All samples were cast in plates with a thickness of 1–2 mm and a surface area of about  $7\text{--}10 \times 10 \text{ mm}^2$ .

The samples were ground using coarse to fine grained silicon carbide paper (500 to 1200 grains per inch) and subsequently polished with an alumina dispersion with 1  $\mu\text{m}$  grain size. To verify amorphous structure X-ray diffraction analysis (XRD) with copper  $K_\alpha$ -radiation was performed in a Vantec-500 diffractometer (Bruker Corp, USA). A general area detector diffraction system (GADDS) configuration was used.

## 2.2 Three-Point Beam Bending

Three-point flexural bending tests were carried out using an Autograph AGG testing machine (Shimadzu, Japan) to determine Young's modulus, plastic limit and fracture strength. A three-point beam bending setup was chosen, which is used typically for metallic glasses. A more detailed description of the setup is given in (16). Due to the neutral plane in the middle of the beam, separating compressive and tensile strain, the propagation of

a single shear band throughout the whole sample is hindered. This allows a certain amount of plasticity compared to a tension mode test (17). The cast samples were ground and polished resulting in a well-defined geometry with a cross-section of  $0.6 \pm 0.05 \text{ mm} \times 2 \pm 0.05 \text{ mm}$ . The samples are bent at a deflection rate of  $0.3 \text{ mm min}^{-1}$  with a probed length of 15 mm. Based on classical beam-bending theory, the recorded load-displacement information was subsequently transformed into engineering stress-strain curves (18).

## 2.3 Hardness and Wear Resistance

To guarantee the same surface conditions, the samples were ground and polished prior to hardness testing according to the procedure described in Section 2.1. The Vickers hardness (HV) was measured according to ISO 6507-1:2018 (19) using a KB10 instrument from KB Prüftechnik GmbH, Germany. The indentation was set by a force of 9.807 N (1 kg).

The abrasive resistance was examined with a tribometer pin-disc machine (CSEM, Switzerland). The tribological system consisted of the sample and a 6 mm diameter ceramic alumina ball acting as a pin. The normal force on the pin was 2 N, the number of rotations of the sample was 10,000 and the rotation speed was 500 rpm. Considering the diameter of the friction track of 2 mm, the sliding speed of the pin on the disc was about  $52.4 \text{ mm s}^{-1}$ . Ambient conditions were  $23^\circ\text{C}$  and 50% RH. Afterwards, the wear marks were measured by profilometry, allowing a determination of the mark depth, and additionally investigated by scanning electron microscopy (SEM).

## 2.4 Corrosion Resistance

### 2.4.1 Metal Release in Simulated Body Fluids

For the metal release tests in simulated body fluids, samples of both BMG alloy batches were prepared as explained in Section 2.1 and the surface area in contact with the test solution was determined. The test solution for nickel release was prepared according to DIN EN 1811:2015-10 (20) and the alloys were immersed so that they were completely covered by solution. A second solution of artificial saliva was prepared according to ISO 10271:2020 (21) to test metal release. For both corrosion tests, the ratio of solution to sample surface amounted to  $1 \text{ ml cm}^{-2}$ . The samples were stored in the solution for  $7 \text{ days} \pm 2 \text{ h}$

at  $30 \pm 2^\circ\text{C}$  in a climatic chamber. Subsequently the released metal content was measured by inductively coupled plasma-optical emission spectrometry (ICP-OES) according to DIN EN 15605:2010-12 (22). The tarnishing caused by the corrosive attack was investigated by colorimetric analysis according to standard test DIN 5033-1:2017-10 (23) before and after the test.

The samples' colour is described by colour coordinates as follows: the luminescence  $[-L^*, +L^*]$  for black to white,  $[+a^* -a^*]$  for red or green appearance and  $[+b^*, -b^*]$  for yellow or blue. In the test daylight (D65) was used which was diffusely scattered by an integrating sphere on the surface of the sample. The measurements were performed with a  $10^\circ$  standard observer and a d/8 analysis geometry according to the standard test (23). The reflected light was split into its spectral components by a prism and these were then analysed by a photodiode array.

According to DIN 6174:2007-10 (24) the colour change can be described as the distance  $\Delta E$  between the coordinates of two colours and determined by Equation (i):

$$\Delta E = \sqrt{(\Delta L^*)^2 + (\Delta a^*)^2 + (\Delta b^*)^2} \quad (\text{i})$$

The Yellowness Index (YI) was determined according to standard ASTM D1925 (25).

### 2.4.2 Tarnishing in Air at Elevated Temperatures

The corrosion resistance was also evaluated by the investigation of tarnishing behaviour of the BMG alloys when exposed to air. Annealing experiments in air at elevated temperatures were performed for the phosphorus-free alloy  $\text{Pt}_{49.95}\text{Cu}_{16.5}\text{Si}_{6.4}\text{B}_{24}\text{Ge}_3$  containing silicon and boron and two platinum-BMGs  $\text{Pt}_{57.3}\text{Cu}_{14.6}\text{P}_{22.8}\text{Ni}_{5.3}$  and  $\text{Pt}_{58.7}\text{Cu}_{20.3}\text{Ag}_1\text{P}_{20}$ . The exposure at higher temperatures accelerates the kinetics of microstructural processes, making potential changes detectable in a reasonable experimental time window.

The alloy  $\text{Pt}_{49.95}\text{Cu}_{16.5}\text{Si}_{6.4}\text{B}_{24}\text{Ge}_3$  was annealed at 501 K ( $228^\circ\text{C}$ ) which corresponds to a homologous temperature about  $T_H = T/T_g = 0.88$ . To get an overview of the tarnishing behaviour of the platinum-BMGs, one candidate of each platinum-copper-silver/nickel-phosphorus alloy was chosen for the tests. Since the glass transition temperatures  $T_g$  of  $\text{Pt}_{57.3}\text{Cu}_{14.6}\text{P}_{22.8}\text{Ni}_{5.3}$  and  $\text{Pt}_{58.7}\text{Cu}_{20.3}\text{Ag}_1\text{P}_{20}$  differ by only 8 K, the average value was taken and to ensure the

same homologous temperature of 0.88, the annealing temperature of 449 K ( $176^\circ\text{C}$ ) was determined for both alloys. During the exposure time, the colour change was frequently measured. Alloy  $\text{Pt}_{49.95}\text{Cu}_{16.5}\text{Si}_{6.4}\text{B}_{24}\text{Ge}_3$  and the alloys  $\text{Pt}_{57.3}\text{Cu}_{14.6}\text{P}_{22.8}\text{Ni}_{5.3}/\text{Pt}_{58.7}\text{Cu}_{20.3}\text{Ag}_1\text{P}_{20}$  were annealed for 36 days at 501 K and at 449 K, respectively. The annealing tests of the  $\text{Pt}_{49.95}\text{Cu}_{16.5}\text{Si}_{6.4}\text{B}_{24}\text{Ge}_3$  alloy were performed twice with different samples to confirm the results. To increase the data accuracy shorter time intervals were chosen for the repeated measurement. Focused ion beam (FIB) was used to prepare samples imaged in SEM and chemical analysis was conducted by energy-dispersive X-ray spectroscopy (EDX).

## 2.5 Formability Tests

When metallic glasses are heated above their respective glass transition temperature, they can be thermoplastically formed in analogy to polymeric thermoplastics or conventional silicate glasses. The formability of an alloy is mainly defined by the temperature dependent viscosity,  $\eta$ , describing how well the material flows at a given temperature, in combination with the crystallisation time,  $t_x$ , defining the time window of deformation until the material crystallises at this temperature. The formability,  $F$ , is defined as Equation (ii) (26):

$$F = \frac{t_x}{3\eta} \quad (\text{ii})$$

The formability was determined for several platinum-phosphorus-based BMGs based on calorimetric measurements and thermomechanical measurements to determine the crystallisation and the temperature dependent viscosity, respectively. Further, thermophysical properties such as transition temperatures and enthalpies were determined by differential scanning calorimetry (DSC). A detailed description of the methodology used can be found in (27).

## 3. Results

XRD measurements were performed on the samples cross-section prepared as described in Section 2.1. **Figure 1** shows the patterns of all BMG alloys. No sharp peaks corresponding to crystalline peaks can be detected. Only two broad peaks are visible in the X-ray pattern, which is typical for amorphous structures. It should be

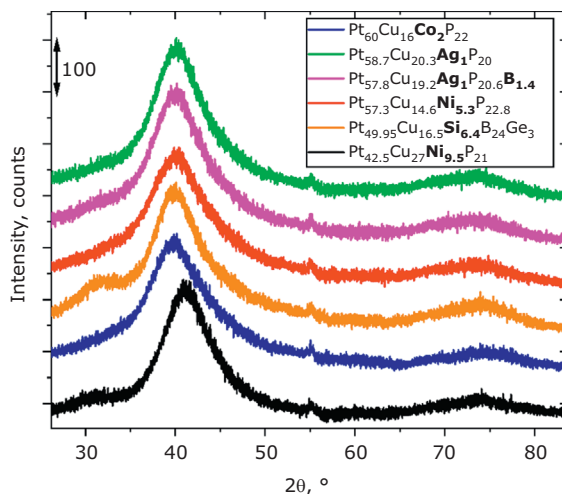


Fig. 1. XRD pattern of the platinum alloys in the glassy condition at room temperature

noted that the small peak appearing in each diffractogram at the same position at around 55° is due to a fault in the detector. For the two alloys Pt<sub>49.95</sub>Cu<sub>16.5</sub>Si<sub>6.4</sub>B<sub>24</sub>Ge<sub>3</sub> and Pt<sub>42.5</sub>Cu<sub>27</sub>Ni<sub>9.5</sub>P<sub>21</sub> a structural pre-peak in front of the first sharp diffraction peak (FSDP) can be observed. For the latter this pre-peak is associated with an increased degree of medium-range order (MRO) (28). The observable shift of the FSDP in this alloy is probably associated with the lower content of large platinum atoms, leading to a smaller average interatomic distance.

### 3.1 Mechanical Properties

In **Figure 2** the stress-strain curves of three nickel-free platinum-based BMG alloys obtained by three-point beam bending are displayed in comparison to those of three conventional crystalline platinum-

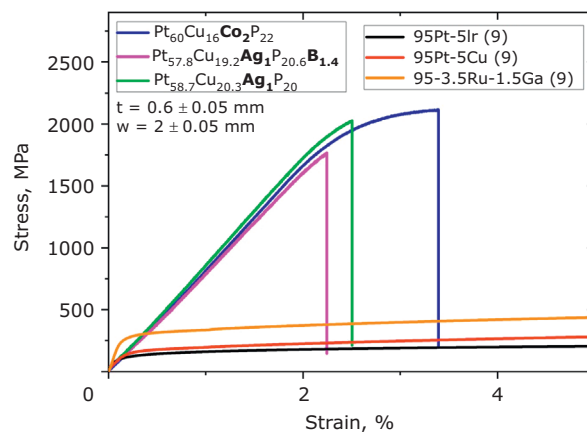


Fig. 2. Stress-strain curve of a selected number of amorphous platinum-based BMGs, tested in three-point-beam bending setup at a deflection rate of 0.33 mm min<sup>-1</sup>. The flexural elastic limit of 2% is reached for all samples, with some of them showing a slight plateau of plastic deformation before failure. The crystalline platinum alloys present pronounced plastic deformation (9)

alloys measured by tensile testing (reproduced from (9)). Each alloy composition reaches its elastic limit at 2% strain and with a strength of around 1.6 GPa ( $R_{p2}$ ). Above 2% strain, the Pt<sub>58.7</sub>Cu<sub>20.3</sub>Ag<sub>1</sub>P<sub>20</sub>, Pt<sub>57.8</sub>Cu<sub>19.2</sub>Ag<sub>1</sub>P<sub>20.6</sub>B<sub>1.4</sub> and Pt<sub>60</sub>Cu<sub>16</sub>Co<sub>2</sub>P<sub>22</sub> alloys exhibit plastic deformation before critical failure. Pt<sub>60</sub>Cu<sub>16</sub>Co<sub>2</sub>P<sub>22</sub> shows the highest plasticity and fractures at approximately 3.3% strain. The results of the three-point-beam bending experiments are provided in **Table V**. Maximal  $R_{p2}$  values are detected for the Pt<sub>58.7</sub>Cu<sub>20.3</sub>Ag<sub>1</sub>P<sub>20</sub> alloy. Compared to their high strength, the Young’s modulus of metallic glasses is relatively low, resulting in lower stiffness. In contrast to the platinum BMGs, the crystalline alloys demonstrate in the tensile tests significantly

**Table V Mechanical Properties Obtained by Three-Beam-Bending of Amorphous Cantilevers Compared to Those of Crystalline Platinum Alloys Measured by Tensile Tests**

Alloy, at%	Elasticity, $\epsilon$ , %	Elongation at fracture, $\epsilon F$ , %	Young’s-Modulus, E, GPa	Yield stress, $R_{p2}$ , MPa
Pt <sub>58.7</sub> Cu <sub>20.2</sub> Ag <sub>1</sub> P <sub>20</sub>	2.1	2.5	88.8 ± 7.3	1721
Pt <sub>57.8</sub> Cu <sub>19.2</sub> Ag <sub>1</sub> P <sub>20.6</sub> B <sub>1.4</sub>	2.1	2.3	82.5 ± 3.7	1604
Pt <sub>60</sub> Cu <sub>16</sub> Co <sub>2</sub> P <sub>22</sub>	2.0	3.4	88.1 ± 4.1	1660
95Pt-5Ir <sup>a</sup>	0.07	45	186	142
95Pt-5Cu <sup>a</sup>	0.07	15	129	171
95Pt-3.5Ru-1.5Ga <sup>a</sup>	0.10	22	184	299

<sup>a</sup>Benchmark tensile tests (9). Yield stress  $R_{p0.2}$ , MPa

lower yield strengths (<500 MPa) and a pronounced plasticity.

### 3.2 Wear Resistance and Hardness

The results of the wear resistance tests are depicted in **Figure 3**. For the BMG alloys, the mean values and standard deviations of three test series are plotted. All diagrams present the values for the BMG (black) in comparison to the conventional alloys (red). In **Figure 3(a)** the hardness values, given in HV1, are shown and the overall hardness values of the BMG alloys (around 450 HV1) are more than twice as high as those of the crystalline work hardened alloys (around 250 HV1) and about four times higher compared to the crystalline alloys in their as-cast state (around 100 HV1). The mean values of the wear mark depth depicted in **Figure 3(b)** reveal slightly higher values for the BMG alloys than those in the crystalline benchmarks. The mark depths of Pt<sub>57.8</sub>Cu<sub>19.2</sub>Ag<sub>1</sub>P<sub>20.6</sub>B<sub>1.4</sub> and Pt<sub>58.7</sub>Cu<sub>20.3</sub>Ag<sub>1</sub>P<sub>20</sub> are about 1 μm larger than those of the nickel and cobalt bearing BMGs. Pt<sub>57.3</sub>Cu<sub>14.6</sub>Ni<sub>5.3</sub>P<sub>22.8</sub> show the lowest wear mark depth. In **Figure 4** the wear mark depth is plotted against the hardness and lower values for the cold worked alloys compared to the softer as-cast state are discernible. Comparing the platinum BMGs among themselves, no evident correlation between hardness and wear mark depth can be observed.

In **Figure 5** details of the wear marks are shown for the BMG alloys Pt<sub>57.8</sub>Cu<sub>19.2</sub>Ag<sub>1</sub>P<sub>20.6</sub>B<sub>1.4</sub> (**Figure 5(a), 5(d)** and **5(g)**), Pt<sub>42.5</sub>Cu<sub>27</sub>Ni<sub>9.5</sub>P<sub>21</sub> (**Figure 5(b), 5(e)** and **5(h)**) and Pt<sub>49.95</sub>Cu<sub>16.5</sub>Si<sub>6.4</sub>B<sub>24</sub>Ge<sub>3</sub> (**Figure 5(c), 5(f)** and **5(i)**).

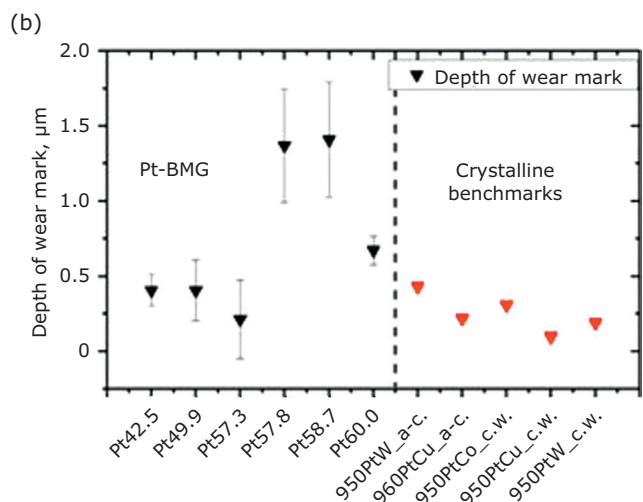
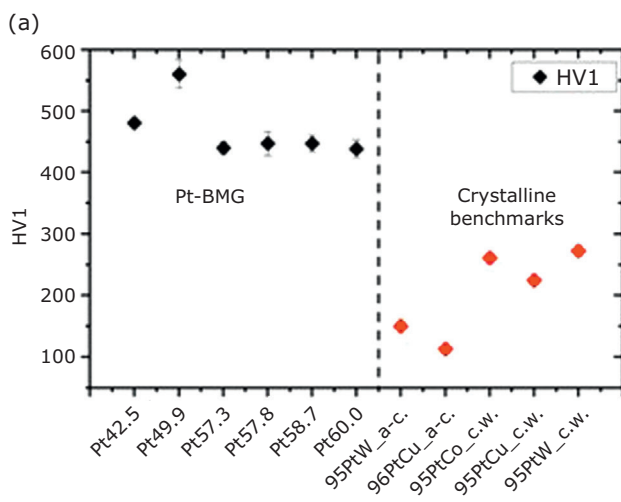


Fig. 3. Results of (a) hardness; and (b) abrasive damage of the platinum-BMG alloys in comparison to the conventional benchmark alloys

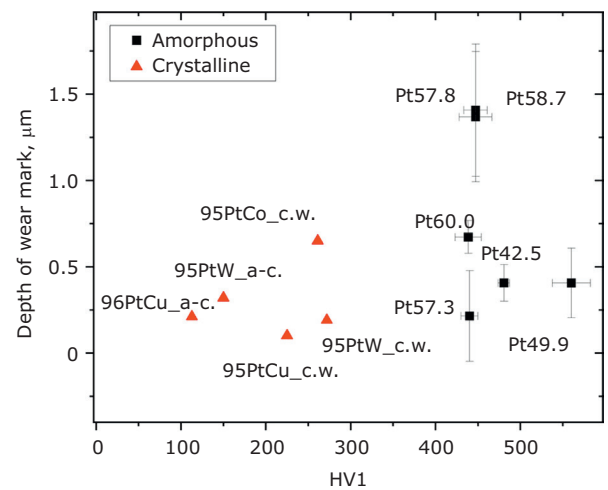


Fig. 4. Wear mark depth plotted against the hardness

In **Figure 5** different magnifications and different degrees of detail are shown hierarchically from the first to the last row. The positions of the magnifications are marked by a square. The overview images of abrasive attack of the alloys Pt<sub>57.8</sub>Cu<sub>19.2</sub>Ag<sub>1</sub>P<sub>20.6</sub>B<sub>1.4</sub> and Pt<sub>42.5</sub>Cu<sub>27</sub>Ni<sub>9.5</sub>P<sub>21</sub> display wear marks with flat pressed material at their respective edges. The marks of Pt<sub>57.8</sub>Cu<sub>19.2</sub>Ag<sub>1</sub>P<sub>20.6</sub>B<sub>1.4</sub> reveal peeled off particles and cracks in the border zone. In the detailed depiction of the mark centre of both alloys (**Figure 5(d)** and **5(e)**) where the applied load is maximal, scores next to deformed and flattened material can be observed. In the magnification shown in **Figure 5(g)** and **5(h)**, the surface appears coarse and rough and daubed material can be detected. In contrast, the overview image of Pt<sub>49.95</sub>Cu<sub>16.5</sub>Si<sub>6.4</sub>B<sub>24</sub>Ge<sub>3</sub> shows cracks in the centre



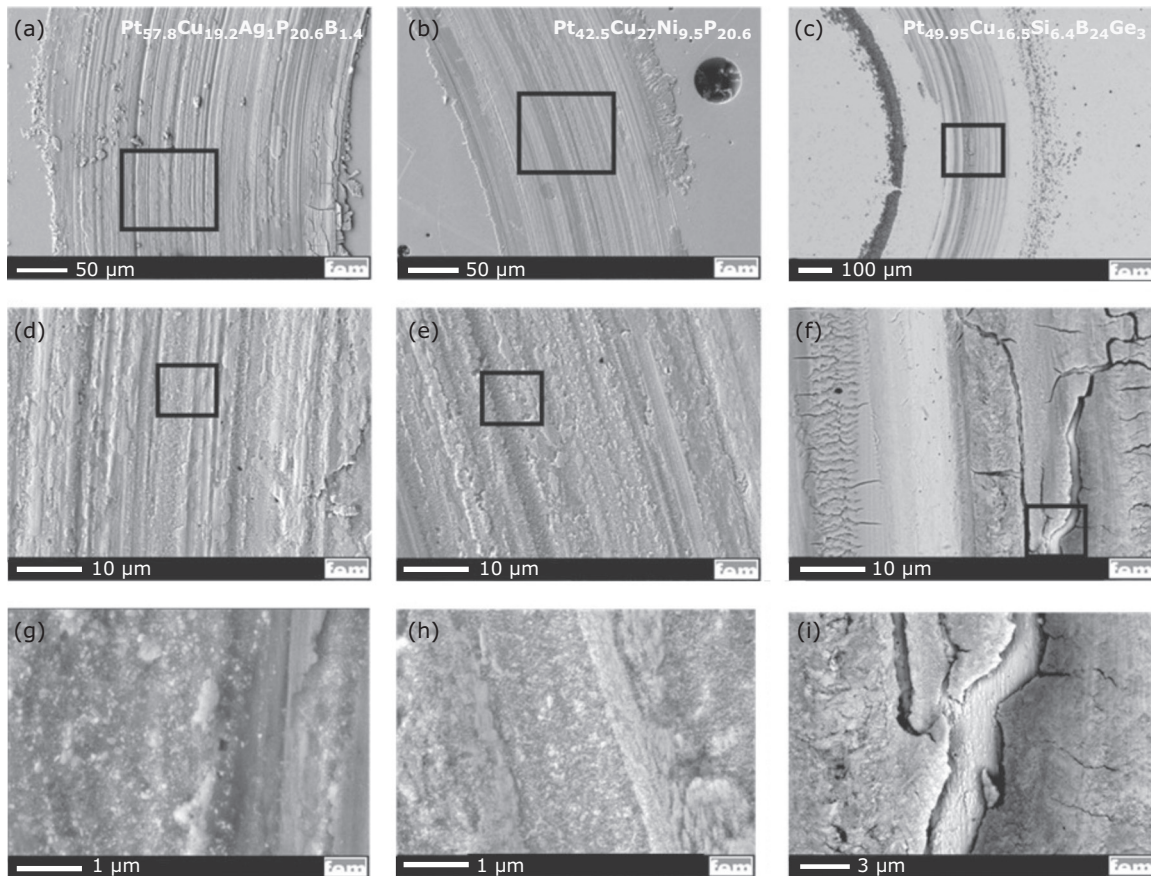


Fig. 5. SEM detail images of the wear marks of: (a)  $Pt_{57.8}Cu_{19.2}Ag_1P_{20.6}B_{1.4}$  at 50  $\mu m$ ; (b)  $Pt_{42.5}Cu_{27}Ni_{9.5}P_{20.6}$  at 50  $\mu m$ ; (c)  $Pt_{49.95}Cu_{16.5}Si_{6.4}B_{24}Ge_3$  at 100  $\mu m$ ; (d)  $Pt_{57.8}Cu_{19.2}Ag_1P_{20.6}B_{1.4}$  at 10  $\mu m$ ; (e)  $Pt_{42.5}Cu_{27}Ni_{9.5}P_{20.6}$  at 10  $\mu m$ ; (f)  $Pt_{49.95}Cu_{16.5}Si_{6.4}B_{24}Ge_3$  at 10  $\mu m$ ; (g)  $Pt_{57.8}Cu_{19.2}Ag_1P_{20.6}B_{1.4}$  at 1  $\mu m$ ; (h)  $Pt_{42.5}Cu_{27}Ni_{9.5}P_{20.6}$  at 1  $\mu m$ ; and (i)  $Pt_{49.95}Cu_{16.5}Si_{6.4}B_{24}Ge_3$  at 3  $\mu m$  BMG alloys. The positions of magnifications are marked by squares

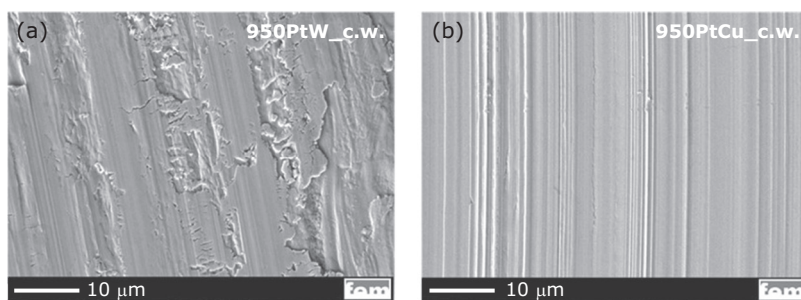


Fig. 6. SEM images of the wear marks of the cold worked benchmark alloys: (a) 950PtW; and (b) 950PtCu

of the marks (see **Figure 5(f)** and **5(i)**) together with an accumulation of apparently loose particles next to the wear tracks. Since less daubed-like regions and mainly cracks can be observed, the abrasive damage looks remarkably different to the other BMG alloys. Comparably, the abrasive damage of the cold worked benchmark alloys 950PtW and 950PtCu observed in SEM is reported in **Figure 6**. The chosen magnification corresponds to those of **Figure 5(d)**, **5(e)** and **5(f)**. Smooth and plastically deformed surfaces are visible. The

slightly harder 950PtW alloy also reveals partially removed material.

### 3.3 Corrosive Attack

#### 3.3.1 Metal Release in Simulated Body Fluids

Because the potentially hazardous to health element nickel is alloyed in three platinum BMG systems, their metal release was tested twice by



Table VI Alloys Bearing Nickel and Their Measured Release (20)		
Alloy, at%	Nickel release, $\mu\text{g cm}^{-2} \text{week}^{-1}$	Limit value, $\mu\text{g cm}^{-2} \text{week}^{-1}$
Pt <sub>42.5</sub> Cu <sub>27</sub> Ni <sub>9.5</sub> P <sub>21</sub>	0.09	0.5
	0.11	
Pt <sub>57.3</sub> Cu <sub>14.6</sub> Ni <sub>5.3</sub> P <sub>22.8</sub>	0.03	0.5
	0.04	

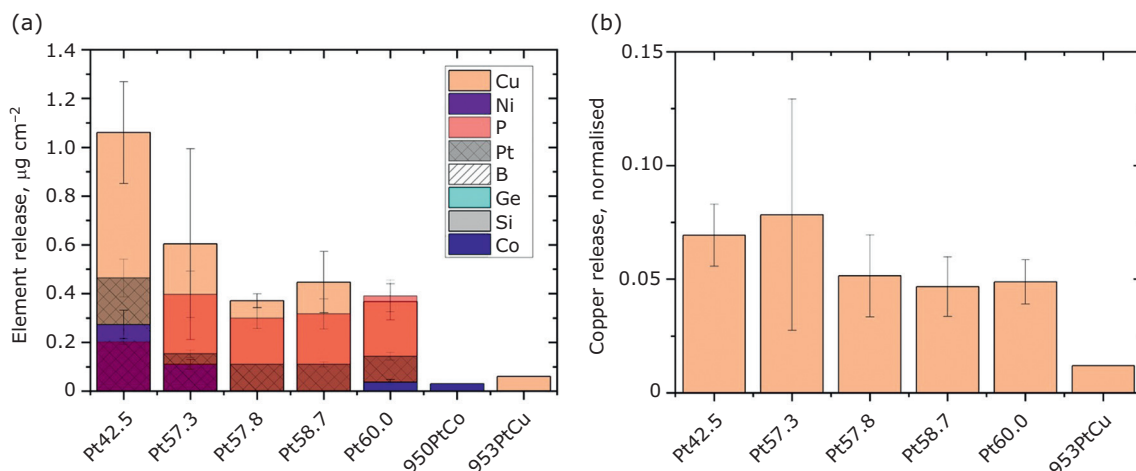


Fig. 7. (a) Element release of each BMG-alloy compared to 950PtCu and 950PtW; (b) copper release normalised to the initial copper content in wt%

the standardised test (20) to quantify the release of nickel in aqueous solution. The results, listed in **Table VI**, show a release of nickel far below the limit given by the industrial standard for jewellery applications. European legislation allows very low nickel release rates (20). Therefore, although not forbidden, most European jewellery manufacturers refrain from using nickel in their alloys.

As described in Section 2.4.1, the samples were stored in artificial saliva to determine the metal release. Metal release of the conventional benchmark alloys was only detectable for cobalt and copper. The results of element release for the BMGs and the benchmark alloys is plotted in **Figure 7(a)** and the value of copper-release normalised to the initial copper content is plotted in **Figure 7(b)**. Mean values and standard deviations from all tested samples (Batches 1 and 2) are depicted.

The BMG alloys release mainly copper and phosphorus. Comparing the other BMG alloys, a higher element release was detected for Pt<sub>42.5</sub>Cu<sub>27</sub>Ni<sub>9.5</sub>P<sub>21</sub>. The element releases of the other BMGs are similar and about four to seven times higher than for the conventional alloys. The platinum release of the conventional alloys lies below the detection limit. **Figure 7(b)** displays the copper release of all alloys normalised to their initial weight percent of copper. The differences

of normalised copper release between BMG and conventional alloys are lower due to higher copper content of the platinum BMG alloys.

As explained in Section 2.4.1, the change of colour caused by corrosive attack was determined. **Figure 8** compares the overall change in colour between the BMG alloys and the crystalline benchmark alloys. The results reveal similar

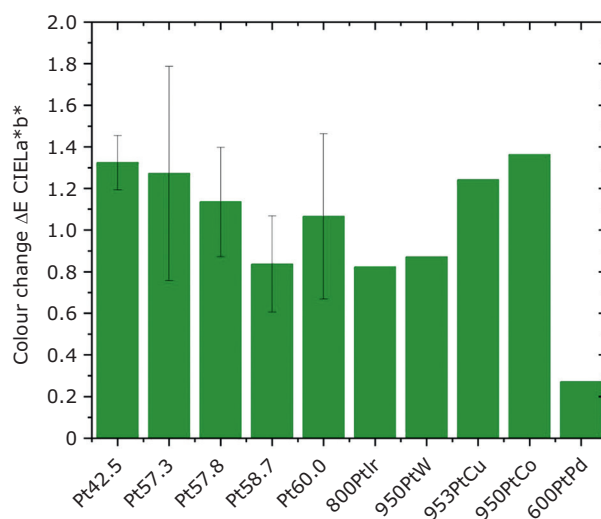


Fig. 8. Colour change of the BMG and the benchmark alloys caused by corrosive attack of artificial saliva

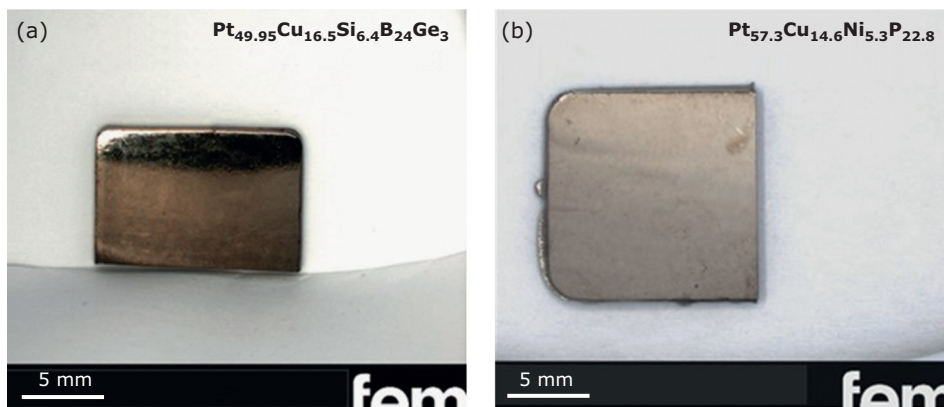


Fig. 9. Macroscopic images of the samples of: (a)  $Pt_{49.95}Cu_{16.5}Si_{6.4}B_{24}Ge_3$ ; and (b)  $Pt_{57.3}Cu_{14.6}Ni_{5.3}P_{22.8}$  alloy after exposure to air

changes of colour of the BMG alloys and the conventional crystalline jewellery alloys.

### 3.3.2 Exposure to Air

Exposure tests were performed on samples of the alloys  $Pt_{57.3}Cu_{14.6}Ni_{5.3}P_{22.8}$  and  $Pt_{58.7}Cu_{20.3}Ag_1P_{20}$  as well as two samples of  $Pt_{49.95}Cu_{16.5}Si_{6.4}B_{24}Ge_3$  alloy from different batches. The samples of  $Pt_{49.95}Cu_{16.5}Si_{6.4}B_{24}Ge_3$  and  $Pt_{57.3}Cu_{14.6}Ni_{5.3}P_{22.8}$  after the experiment are shown in Figure 9 and the calculated colour change of the platinum BMG alloys by exposure to air is shown in Figure 10. Macroscopically a pronounced colour change can be observed for  $Pt_{49.95}Cu_{16.5}Si_{6.4}B_{24}Ge_3$  whereas the  $Pt_{57.3}Cu_{14.6}Ni_{5.3}P_{22.8}$  sample surface retains a silver metallic lustre. The colour change of the  $Pt_{49.95}Cu_{16.5}Si_{6.4}B_{24}Ge_3$  alloy composition, which is about seven times more pronounced than that of the  $Pt_{57.3}Cu_{14.6}Ni_{5.3}P_{22.8}$  BMG, is clearly visible and appears brownish to the eye.

In Table VII the values for  $L^*$ ,  $a^*$ ,  $b^*$ , YI and  $\Delta E$  are given for the samples after annealing. To express the effect of tarnishing and to get an idea about the values and the corresponding lustre, the colour coordinates of an untreated 950PtCu alloy are given in comparison. Since this alloy was not annealed, no data after thermal treatment are given. Due to the brownness of the  $Pt_{49.95}Cu_{16.5}Si_{6.4}B_{24}Ge_3$  sample, the YI, which is commonly used to describe the lustre of gold and platinum-based jewellery, does not represent the colour here. However, it is given as additional information in Table VII. The  $a^*$  and  $b^*$  values of the  $Pt_{49.95}Cu_{16.5}Si_{6.4}B_{24}Ge_3$  samples differ slightly from those of the less tarnished samples and the benchmark reference. The luminescence  $L^*$ , which describes the brightness, reveals pronounced differences for the tarnished samples. Conventional

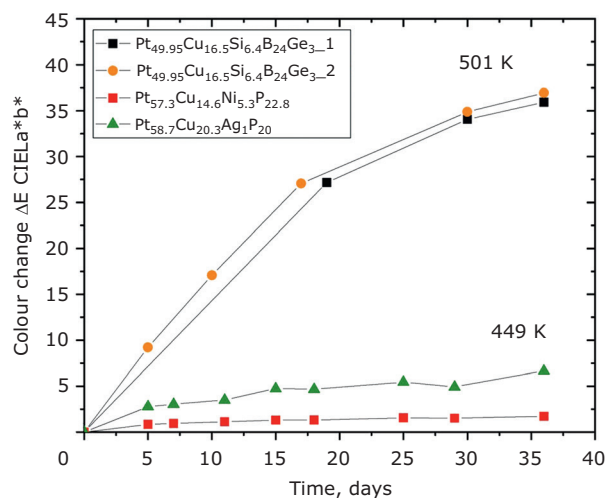


Fig. 10. Measured colour change of the BMG alloys  $Pt_{49.95}Cu_{16.5}Si_{6.4}B_{24}Ge_3$ ,  $Pt_{57.3}Cu_{14.6}Ni_{5.3}P_{22.8}$  and  $Pt_{58.7}Cu_{20.3}Ag_1P_{20}$

jewellery alloys reveal  $L^*$  values of about 85 (29). Compared to the brightness of a conventional platinum-jewellery alloy,  $Pt_{49.95}Cu_{16.5}Si_{6.4}B_{24}Ge_3$  possesses less than half after tarnishing in air.

Since the alloys  $Pt_{57.3}Cu_{14.6}Ni_{5.3}P_{22.8}$  and  $Pt_{58.7}Cu_{20.3}Ag_1P_{20}$  did not show any differences in their superficial appearance after the annealing experiments, only  $Pt_{49.95}Cu_{16.5}Si_{6.4}B_{24}Ge_3$  was examined in more detail. The SEM investigation of the surface after exposure to air is shown in Figure 11. The position of the cross-section prepared by FIB is shown in Figure 11(a). The SEM image of the FIB section is displayed in Figure 11(b). In addition to black boron-rich formations, which might not have been in solution before, small dendritic structures (marked with white arrow) are present. By using EDX, a carbon-rich phase was detected right underneath the surface with copper-oxide rich (dark) and a

**Table VII Colour Coordinates and Yellowness Index of Platinum-Based BMG Alloys Measured Before and After Annealing in Air Compared to an Intact Reference Sample of 950PtCu**

Alloy	Exposure time, days	L* (D65)	a* (D65)	b* (D65)	YI (D1925)	ΔE
<b>Pt<sub>49.95</sub>Cu<sub>16.5</sub>Si<sub>6.4</sub>B<sub>24</sub>Ge<sub>3</sub>_1</b>	0	76.82	0.03	3.99	10.35	35.93
	36	41.04	1.72	1.15	8.26	
<b>Pt<sub>49.95</sub>Cu<sub>16.5</sub>Si<sub>6.4</sub>B<sub>24</sub>Ge<sub>3</sub>_2</b>	0	78.17	-0.08	3.55	9.19	36.95
	36	40.75	0.83	-0.76	-0.17	
<b>Pt<sub>57.3</sub>Cu<sub>14.6</sub> Ni<sub>5.3</sub>P<sub>22.8</sub></b>	0	76.02	0.14	3.99	10.54	1.72
	36	75.50	0.19	4.77	12.34	
<b>Pt<sub>58.7</sub>Cu<sub>20.3</sub>Ag<sub>1</sub>P<sub>20</sub></b>	0	76.63	0.07	3.95	10.33	6.66
	36	72.20	0.80	8.08	20.65	
<b>950PtCu<sup>a</sup></b>	-	86.44	-0.3	3.22	7.71	-

<sup>a</sup>Untreated reference

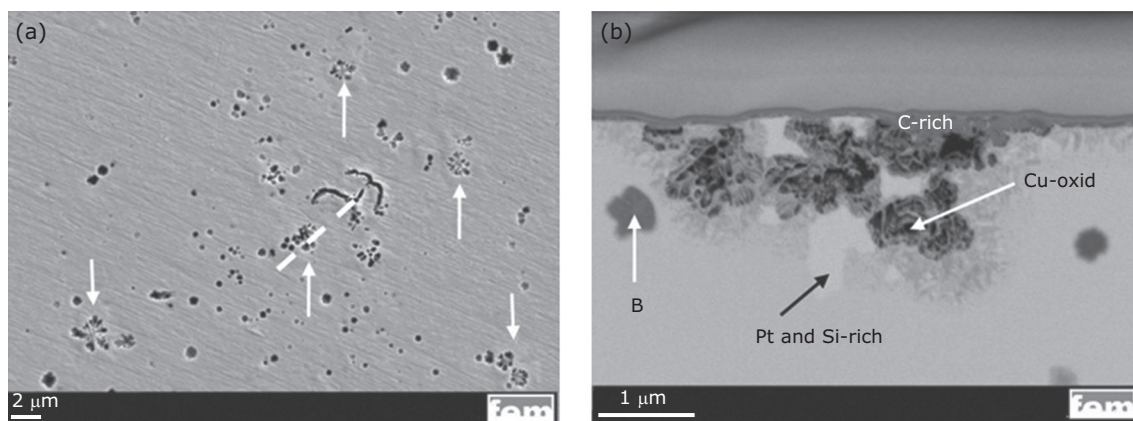


Fig. 11. SEM images of the surface of the Pt<sub>49.95</sub>Cu<sub>16.5</sub>Si<sub>6.4</sub>B<sub>24</sub>Ge<sub>3</sub> alloy: (a) after exposure to air in the overview with the marked position of the FIB section; and (b) the detail of the FIB section

brighter platinum and silicon phase in the adjacent surrounding bulky matrix. The amount of carbon underneath the surface might originate from an organic platinum compound formed during sample preparation.

### 3.4 Thermoplastic Properties

Calorimetry was used to determine the characteristic temperatures of the glass transition such as glass transition temperature,  $T_g$ , and following crystallisation,  $T_x$ , together with the melting event, where solidus temperature,  $T_s$ , and liquidus temperature,  $T_l$ , are determined. The characteristic temperatures of all alloys are

summarised in **Table VIII**. The glass transition temperatures are located within the small region between 501 K and 514 K. A larger spread can be seen in the onset of crystallisation, where the alloy Pt<sub>42.5</sub>Cu<sub>27</sub>Ni<sub>9.5</sub>P<sub>21</sub> shows the highest  $T_x$  at 597 K and Pt<sub>57.8</sub>Cu<sub>19.2</sub>Ag<sub>1</sub>P<sub>20.6</sub>B<sub>1.4</sub> shows the smallest value at 565 K. With respect to thermoplastic forming, the thermal stability of the supercooled liquid is of most interest. The thermal stability can be quantified by the width of the supercooled liquid region,  $\Delta T_x = T_x - T_g$ . Here, the alloy Pt<sub>42.5</sub>Cu<sub>27</sub>Ni<sub>9.5</sub>P<sub>21</sub> shows the highest stability with  $\Delta T_x = 83$  K. Nevertheless, this quantity is not a measure of the change in viscosity of the supercooled liquid, which is crucial for thermoplastic formability.

Table VIII Results of Differential Scanning Calorimetric Measurements with a Heating Rate of 0.33 K s <sup>-1</sup>								
Alloy	T <sub>g</sub> K	T <sub>x</sub> K	ΔT <sub>x</sub>	ΔH <sub>x</sub> kJ g <sup>-1</sup> atom <sup>-1</sup>	ΔH <sub>m</sub> kJ g <sup>-1</sup> atom <sup>-1</sup>	T <sub>s</sub> K	T <sub>l</sub> K	
Pt <sub>58.7</sub> Cu <sub>20.2</sub> Ag <sub>1</sub> P <sub>20</sub>	509	570	61	5.2	9.7	825	844	
Pt <sub>57.8</sub> Cu <sub>19.2</sub> Ag <sub>1</sub> P <sub>20.6</sub> B <sub>1.4</sub>	509	565	56	4.8	9.2	824	845	
Pt <sub>60</sub> Cu <sub>18</sub> Co <sub>2</sub> P <sub>22</sub>	506	573	67	7.3	10.7	824	882	
Pt <sub>42.5</sub> Cu <sub>27</sub> Ni <sub>9.5</sub> P <sub>21</sub>	514	597	83	6.6	10.5	779	874	
Pt <sub>57.3</sub> Cu <sub>14.6</sub> Ni <sub>5.3</sub> P <sub>22.8</sub>	501	577	76	7.3	11.4	735	833	

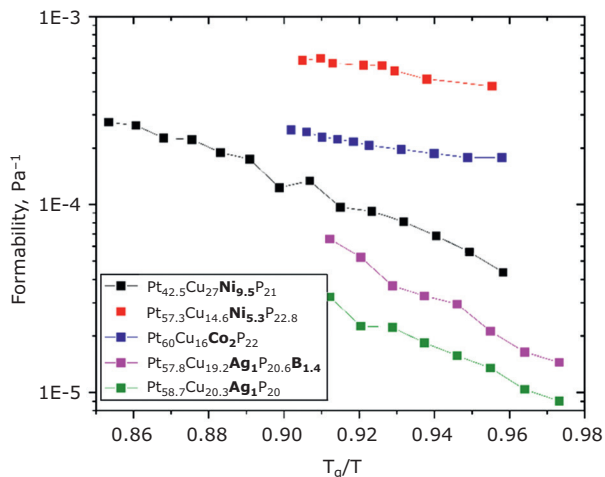


Fig. 12. Formability parameter over T<sub>g</sub>-nominated inverse temperature for several different platinum-based BMGs

The isothermal formability, *F*, includes both thermal stability and viscosity. In **Figure 12** the temperature dependent isothermal formability is shown as a function of inverse temperature, normalised to the glass transition temperature for 20 K min<sup>-1</sup>. Comparing the platinum BMG alloys among themselves, the systems based on platinum-copper-nickel/cobalt-phosphorus show better formability than the cobalt/nickel free platinum-copper-silver-(boron)-phosphorus alloys. The larger temperature range covered by Pt<sub>42.5</sub>Cu<sub>27</sub>Ni<sub>9.5</sub>P<sub>21</sub> originates from its large thermal stability. The superior formability of the other two platinum-copper-nickel/cobalt-phosphorus alloys is due to their steeper decrease in viscosity around the glass transition, i.e. they are kinetically more fragile (30). Still the formability of all tested platinum-based alloys is much higher than those reported in (31) for other families of metallic glasses.

### 4. Discussion

The investigation of mechanical properties by three-point beam bending reveals yield strength

values R<sub>p2</sub> of about 1600 MPa for all tested platinum BMG alloys. Deformation is mainly elastic for the majority of the platinum BMGs, in accordance with the literature (32). The strength of a series of conventional platinum jewellery alloys with 95 wt% platinum was previously measured by tensile testing, commonly used for crystalline alloys (9). Although the testing methods used for the different material classes are not identical, the magnitudes of strength are still comparable with each other. Studies on crystalline TiAl<sub>6</sub>V<sub>4</sub> using three-point beam bending (18) and tensile tests (33) reveal comparable results. For the majority of platinum jewellery alloys (9), yield strengths (R<sub>p0.2</sub>) of about 150 MPa to 300 MPa were detected, as shown for 95Pt-3Ru-1.5Ga, 95Pt-5Ir and 95Pt-5Cu in **Figure 2**. The maximum R<sub>p0.2</sub> of about 421 MPa was reached for 95Pt-2Ru-3Ga. Hence, the platinum BMG alloys demonstrate about eight times higher yield strength values (with about 2% elasticity) than conventional platinum-alloys. Furthermore, the BMG alloys exhibit Vickers hardness values more than twice as high as those of the crystalline work hardened alloys.

The abrasive behaviour of BMGs was investigated. Against expectation (2, 14), their high hardness does not result in higher wear resistance. The BMGs display a more pronounced abrasive damage than the crystalline benchmark alloys. The conventional crystalline alloys show mechanisms such as microploughing and wedge formation which may occur during abrasive attack (34) and which are not expected to be accompanied by a loss of material. Proof for microploughing as damage mechanism was shown for 950PtIr in a previous study (12). In this work, a similar mechanism was observed for the 950PtCu alloy.

SEM images of the platinum-phosphorus-based BMG alloys suggest that worn-off material is plastically deformed and sticks to the surface. This observation points towards an adhesive wear mechanism, which has already been suggested for platinum-phosphorus-based BMGs in the literature (35). This might result in a more

pronounced material loss if the worn material loses adhesion to the bulk material. In contrast, investigations reveal that the platinum-boron-based BMG is more prone to microcracking. Although the mechanism of the platinum-copper-silver-boron-phosphorus and platinum-copper-nickel-phosphorus alloys appears similar, the nickel-containing BMGs  $\text{Pt}_{42.5}\text{Cu}_{27}\text{Ni}_{9.5}\text{P}_{21}$  and  $\text{Pt}_{57.3}\text{Cu}_{14.6}\text{Ni}_{5.3}\text{P}_{22.8}$  show the smallest wear mark depths. Consequently, a positive effect of nickel on the abrasive resistance can be assumed. Furthermore, the cobalt containing alloy (2 at% cobalt) shows wear mark depths in between the nickel-free and nickel-containing BMGs. Hence, a composition dependant abrasive behaviour could be observed and the nickel containing alloys are suggested to be more suitable for application where abrasion resistance is important. In addition, it was shown that nickel release due to corrosive attack of body fluids is expected to lie far below the limit given by the industrial standard for jewellery applications, ensuring harmless applicability.

The different abrasive behaviour of the two material classes can be explained by extremely localised plastic deformation in BMGs. In the literature, the extent of plastic deformation of metallic glasses depends on the type of measurement. Compression experiments often lead to the formation of multiple shear bands resulting in a distinct plastic regime, for example  $\text{Pt}_{57.5}\text{Cu}_{17.7}\text{Ni}_{5.3}\text{P}_{22.5}$ , 20% plastic deformation (5). In contrast, the formation of a single shear band usually leads to catastrophic failure in tension experiments (36). Therefore, BMGs are often termed 'brittle' although they are highly ductile in a very localised area (shear band). Consequently, the adhesive wear observed for the platinum-phosphorus-based liquids suggest that the pin-on-disc experiments cause very localised plastic deformation leading to peeling off of material which is subsequently plastically deformed and flattened by the pin. This material is continuously transferred to the edges of the wear mark as seen in **Figure 5(a)** and **5(b)**. In contrast,  $\text{Pt}_{49.95}\text{Cu}_{16.5}\text{Si}_{6.4}\text{B}_{24}\text{Ge}_3$  shows the formation of microcracks suggesting significantly less ductile behaviour.

The corrosion tests reveal that the element release of the BMG alloys is slightly higher than that of the crystalline benchmark alloys. However, their tarnishing behaviour in artificial saliva is comparable. Pronounced element release is detected for the platinum-boron-based BMG alloy  $\text{Pt}_{49.95}\text{Cu}_{16.5}\text{Si}_{6.4}\text{B}_{24}\text{Ge}_3$  with a high scattering of data.

The oxidative behaviour of the  $\text{Pt}_{49.95}\text{Cu}_{16.5}\text{Si}_{6.4}\text{B}_{24}\text{Ge}_3$  alloy is noticeable with respect to tarnishing. Copper oxide was detected underneath the surface and adjacent to platinum-silicon rich phases after exposure to air at elevated temperatures. Oxidative attack has also been observed on a gold BMG in previous work (37). Growth of silica dendrites into the sample surface and copper oxide dendrites above were detected by annealing experiments in air at the homologous temperature,  $T_H$ , of about 0.88. The interplay of copper with silicon was concluded to play a crucial role for tarnishing (37). The platinum BMGs show a pattern of internal oxidation of copper compared to the gold BMG. Tarnishing was observed in this work only for the copper and silicon bearing alloy and it can be hypothesised that tarnishing occurs by a mechanism based on the interaction of copper and silicon. The interplay between these elements seems to be different for the platinum BMG compared to the gold BMG alloy. Analogous to the gold-based BMG, the reduction of copper or silicon content might reduce the tarnishing rate (38, 39). However, for a more detailed and in-depth understanding of the underlying mechanism further investigations are necessary.

Due to its worse performance, the  $\text{Pt}_{49.95}\text{Cu}_{16.5}\text{Si}_{6.4}\text{B}_{24}\text{Ge}_3$  alloy was excluded from the investigation of the mechanical and thermoplastic behaviour of the platinum BMG series.

The formability tests show outstanding formability of all platinum alloys due to a fast decrease of viscosity during heating above the glass transition temperature, called kinetically fragile behaviour, combined with a very good thermal stability against crystallisation (30, 40). Compared to other metallic glasses, for example iron- or zirconium-based glasses, the isothermal formability of the examined platinum-based BMGs is two to three orders of magnitude higher. A comparative analysis on thermoplastic formability within the different classes of BMGs is provided in (31). This superior formability together with their high strength predestines them for new innovative filigree and durable design applications in the jewellery sector.

## 5. Conclusions

The investigated BMG alloys, except  $\text{Pt}_{42.5}\text{Cu}_{27}\text{Ni}_{9.5}\text{P}_{21}$ , reach a fineness of 85 wt% platinum, which makes them interesting for jewellery manufacturing. The mechanical analysis of the platinum BMG series demonstrates for all tested alloys a strength and hardness which



exceed those of the crystalline benchmarks. These superior properties in the as-cast state enable near net shape casting without the need for subsequent thermomechanical treatment. In the context of filigree geometries, their mechanical properties are very valuable and ensure stability of form.

In comparison to platinum-based benchmark alloys, a more pronounced abrasive damage is expected for the platinum BMG alloys during their lifetime as jewellery items. Furthermore, a composition-dependent tribological behaviour among the platinum BMG alloys is observed, revealing favourable wear resistance associated with the content of nickel. In the context of corrosion behaviour, satisfactory maintenance of appearance during usage, similar to their crystalline counterparts, can be assumed for platinum-based BMG jewellery. The results indicate a higher risk of tarnishing for the phosphorus-free, platinum-boron-based alloy  $\text{Pt}_{49.95}\text{Cu}_{16.5}\text{Si}_{6.4}\text{B}_{24}\text{Ge}_3$  than for the other platinum-based BMGs. Interaction of copper and silicon is assumed to play a crucial role for the tarnishing mechanism.

The results of this work show the suitability of several platinum-based BMG alloys for jewellery application and demonstrate their beneficial properties. In addition to their outstanding elasticity and formability, their thermoplastic formability and high mechanical strength enable new designs, which should further enhance industrial interest and applicability of platinum BMGs.

## Acknowledgements

This work was financially supported by the German Federal Ministry for Economic Affairs and Climate Action (BMWK) under the IGF programme (project no. AiF-IGF 19979N). The members of the industrial user committee and colleagues in the working groups at LMW and fem are kindly acknowledged for their contribution to this work.

## References

1. J. Schroers and W. I. Johnson, 'Pt-Base Bulk Solidifying Amorphous Alloys', *US Patent* 7,582,172; 2009
2. J. Schroers, B. Lohwongwatana, W. L. Johnson and A. Peker, *Mater. Sci. Eng. A.*, 2007, **449–451**, 235
3. J. Schroers and W. L. Johnson, *Appl. Phys. Lett.*, 2004, **84**, (18), 3666
4. B. Lohwongwatana, W. L. Johnson and J. Schroers, 'Liquidmetal – Hard 18K and .850Pt Alloys that can be Processed like Plastics or Blown like Glass', in 21st Santa Fe Symposium on Jewelry Manufacturing Technology, Albuquerque, New Mexico, USA, 20th–23rd May, 2007, pp. 288–303
5. J. Schroers and W. L. Johnson, *Phys. Rev. Lett.*, 2004, **93**, (25), 255506
6. T. Heiss, U. E. Klotz and D. Tiberto, *Johnson Matthey Technol. Rev.*, 2015, **59**, (2), 95
7. J. Butler, *Platinum Metals Rev.*, 2011, **55**, (1), 2
8. U. E. Klotz, T. Heiss and D. Tiberto, *Johnson Matthey Technol. Rev.*, 2015, **59**, (2), 129
9. U. E. Klotz and T. Fryé, *Johnson Matthey Technol. Rev.*, 2019, **63**, (2), 89
10. Y. Saotome, Y. Fukuda, I. Yamaguchi and A. Inoue, *J. Alloys Compd.*, 2007, **434–435**, 97
11. G. Kumar, A. Desai and J. Schroers, *Adv. Mater.*, 2011, **23**, (4), 461
12. U. E. Klotz, T. Heiss and T. Fryé, *Johnson Matthey Technol. Rev.*, 2021, **65**, (3), 480
13. "Werkstoffkunde", eds. H.-J. Bargel and G. Schulze, 11th Edn., Springer Vieweg, Berlin, Germany, 2012
14. O. S. Houghton and A. L. Greer, *Johnson Matthey Technol. Rev.*, 2021, **65**, (4), 506
15. O. Gross, 'Precious Metal Based Bulk Glass-Forming Liquids: Development, Thermodynamics, Kinetics and Structure', Universität des Saarlandes, Germany, 2018
16. A. Kuball, B. Bochtler, O. Gross, V. Pacheco, M. Stolpe, S. Hechler and R. Busch, *Acta Mater.*, 2018, **158**, 13
17. P. E. Donovan, *Acta Metall.*, 1989, **37**, (2), 445
18. A. Kuball, O. Gross, B. Bochtler, B. Adam, L. Ruschel, M. Zamanzade and R. Busch, *J. Alloys Compd.*, 2019, **790**, 337
19. 'Metallic Materials – Vickers Hardness Test – Part 1: Test Method', ISO 6507-1:2018, International Organization for Standardization, Geneva, Switzerland, 2018
20. 'Reference Test Method for Release of Nickel from all Post Assemblies which are Inserted into Pierced Parts of the Human Body and Articles Intended to Come into Direct and Prolonged Contact with the Skin', DIN EN 1811:2015-10, Beuth Verlag GmbH, Berlin, Germany, 2015
21. 'Dentistry – Corrosion Test Methods For Metallic Materials', ISO 10271:2020, Beuth Verlag GmbH, Berlin, Germany, 2020
22. 'Copper and Copper Alloys – Inductively Coupled Plasma Optical Emission Spectrometry', DIN EN 15605:2010-12, Beuth Verlag GmbH, Berlin, Germany, 2010
23. 'Colorimetry – Part 1: Basic Terms of Colorimetry', DIN 5033-1:2017-10, Beuth Verlag GmbH, Berlin, Germany, 2017

24. 'Colorimetric Evaluation of Colour Coordinates and Colour Differences According to the Approximately Uniform CIELAB Colour Space', DIN 6174:2007-10, Beuth Verlag GmbH, Berlin, Germany, 2007
25. 'Standard Test Method for Yellowness Index of Plastics', ASTM D1925, 70th Edn., ASTM International, West Conshohocken, USA, May, 1977
26. J. Schroers, *Acta Mater.*, 2008, **56**, (3), 471
27. N. Neuber, O. Gross, M. Frey, B. Bochtler, A. Kuball, S. Hechler, I. Gallino and R. Busch, *Acta Mater.*, 2021, **220**, 117300
28. O. Gross, N. Neuber, A. Kuball, B. Bochtler, S. Hechler, M. Frey and R. Busch, *Comm. Phys.*, 2019, **2**, 83
29. G. Rakhtsaum, *Platinum Metals Rev.*, 2013, **57**, (3), 202
30. O. Gross, B. Bochtler, M. Stolpe, S. Hechler, W. Hembree, R. Busch and I. Gallino, *Acta Mater.*, 2017, **132**, 118
31. B. Bochtler, O. Kruse and R. Busch, *J. Phys.: Condens. Matter*, 2020, **32**, (24), 244002
32. J. J. Kruzic, *Adv. Eng. Mater.*, 2016, **18**, (8), 1308
33. P.-J. Arrazola, A. Garay, L.-M. Iriarte, M. Armendia, S. Marya and F. Le Maître, *J. Mater. Proc. Technol.*, 2009, **209**, (5), 2223
34. A. Hylén, P. Ölund, M. Ghadamgahi, S. Lille and E. Svensson, 'Understanding Wear Mechanisms – The Application Technology Behind WR-Steel®', Ovako AB, Stockholm, Sweden, 2021, 16 pp
35. M. A. Medina, O. Acikgoz, A. Rodriguez, C. S. Meduri, G. Kumar and M. Z. Baykara, *Lubricants*, 2020, **8**, (9), 85
36. C. Suryanarayana and A. Inoue, "Bulk Metallic Glasses", CRC Press, Boca Raton, USA, 2011
37. M. Eisenbart, 'On the Processing and the Tarnishing Mechanism of Gold-Based Bulk Metallic Glasses', Universität des Saarlandes, Germany, 2015
38. O. Gross, M. Eisenbart, L.-Y. Schmitt, N. Neuber, L. Ciftci, U. E. Klotz, R. Busch and I. Gallino, *Mater. Des.*, 2018, **140**, 495
39. N. Neuber, O. Gross, M. Eisenbart, A. Heiss, U. E. Klotz, J. P. Best, M. N. Polyakov, J. Michler, R. Busch and I. Gallino, *Acta Mater.*, 2019, **165**, 315
40. O. Gross, S. S. Riegler, M. Stolpe, B. Bochtler, A. Kuball, S. Hechler, R. Busch and I. Gallino, *Acta Mater.*, 2017, **141**, 109

## The Authors



Lisa-Yvonn Schmitt studied Material Science at the University of Saarland, Germany, until 2017 and then started working at fem research institute, Germany, as a project manager. Since summer 2021 she is also a PhD student at the Institute for Applied Materials (IAM-AWP) of Karlsruhe Institute of Technology (KIT), Germany. Her research topics are constitution and thermodynamics of platinum-alloys, bulk metallic glasses and sessile drop measurements of metallic melts.



Nico Neuber is a PhD student at the chair of metallic materials of Saarland University. He obtained a double bachelor's degree in Materials Science and Mechanical engineering at Saarland University and Oregon State University, USA, and a Master's degree in Materials Science in Saarbrücken, Germany. His research focuses on the connection of structure with the thermodynamic, kinetic and mechanical properties of metallic glasses and liquids mainly utilising synchrotron X-ray radiation based and calorimetric techniques. Further focus is put on processing technology and casting of amorphous metals.



Miriam Eisenbart graduated in 2009 in Mechanical Engineering from KIT. She then entered the metallurgy department of fem research institute where she worked on gold-based bulk metallic glasses and their mechanical behaviour as well as the development of copper alloys. In 2016 she was awarded her doctorate in engineering. Since 2019 she is the deputy head of the Physical Metallurgy department and has in recent years entered the research fields of additive manufacturing and digitalisation.



Ulrich E. Klotz studied Physical Metallurgy at the University of Stuttgart, Germany, and earned his PhD from The Swiss Federal Institute of Technology (ETH) Zurich, Switzerland. From 1999 to 2007 he worked at the Swiss Federal Laboratories for Materials Testing and Research (Empa), Switzerland. Since 2007 he is Head of the Department of Physical Metallurgy at the fem, Germany. His research interests are thermodynamics and phase diagrams and processing technology including investment casting and additive manufacturing of precious metals alloys.



Ralf Busch studied physics at the Georg-August-Universität Göttingen in Germany. He received his PhD in Göttingen in 1992. In 1993, he went to the California Institute of Technology in Pasadena, USA, as a Feodor Lynen Fellow of the Alexander von Humboldt Foundation. There he started to work in the field of bulk metallic glasses. In 1999, he accepted an Assistant Professorship in Materials Science in the Department of Mechanical Engineering at Oregon State University, USA, and became an Associate Professor there in 2004. He became Full Professor for Metallic Materials at Saarland University, Germany, in 2005.

# Moving from Fuel to Feedstock

## Selective hydrocarbon activation using rhodium and iridium complexes

**Paul A. Morton and  
Stephen M. Mansell\***

Institute of Chemical Sciences, School of  
Engineering and Physical Sciences, William  
Perkin Building, Heriot-Watt University,  
Edinburgh, EH14 4AS, UK

\*Email: [s.mansell@hw.ac.uk](mailto:s.mansell@hw.ac.uk)

### PEER REVIEWED

Received 23rd November 2022; Revised 10th February  
2023; Accepted 16th February 2023; Online 17th  
February 2023

Carbon-hydrogen bond activations and their subsequent functionalisation have long been an important target in chemistry because C–H bonds are ubiquitous throughout nature, making C–H derivatisation reactions highly desirable. The selective and efficient functionalisation of this bond into many more useful carbon-element bonds (for example, C–B, C–Si, C–O and C–S bonds) would have many uses in pharmaceutical and bulk chemical synthesis. Activation of the C–H bond is, however, challenging due to the high strength and low bond-polarity of this bond rendering its cleavage unfavourable. With the correct choice of reagents and systems, especially those utilising directing groups, kinetically and thermodynamically favourable catalytic processes have been developed. However, a key remaining challenge is the development of undirected, intermolecular reactions using catalysts that are both selective and active enough to make useful processes. In this review, the progress towards optimising Group 9 C–H activation catalysts is discussed, particularly focusing on undirected reactions that are kinetically more difficult, starting with a brief history of C–H activation, identifying the

importance of auxiliary ligands including the nature of anionic ligand (for example, cyclopentadienyl, indenyl, fluorenyl and trispyrazolylborate) and neutral ligands (such as phosphines, carbonyl, alkenes and *N*-heterocyclic carbenes (NHCs)) that contribute towards the stability and reactivity of these metal complexes. The tethering of the anionic ligand to strong  $\sigma$ -donating ligands is also briefly discussed. The focus of this review is primarily on the Group 9 metals rhodium and iridium, however, C–H activation using Group 8 and 10 metals are compared where useful. The most recent advances in this field include the development of C–H borylation of many small hydrocarbon substrates such as arenes, heterocycles and *n*-alkanes as well as the more challenging substrate methane.

### 1. Carbon-Hydrogen Activation

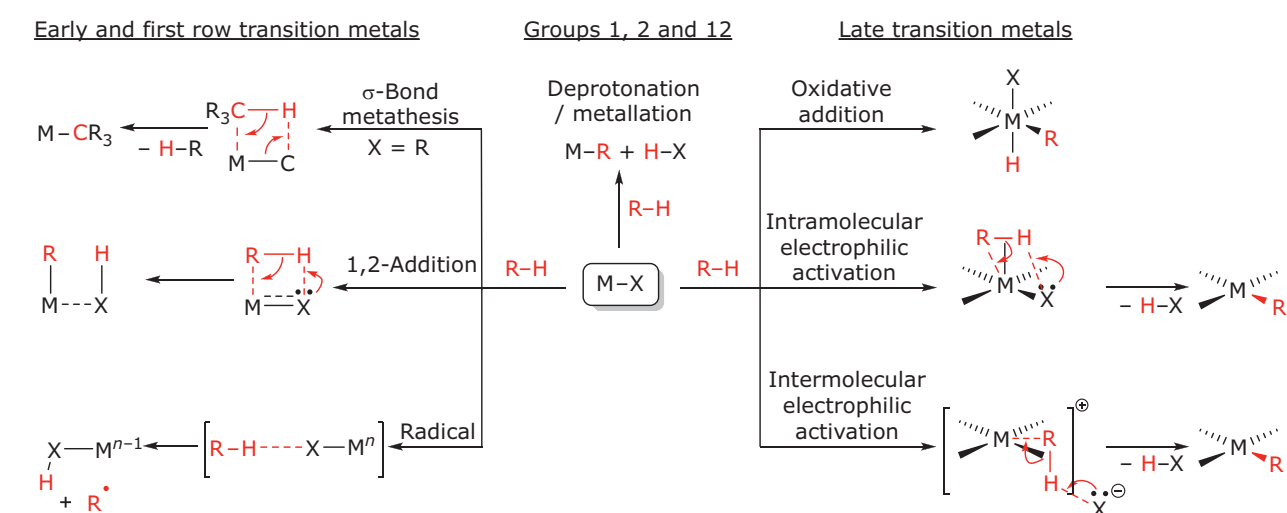
The C–H activation and functionalisation of small hydrocarbon molecules that feature relatively non-reactive C–H bonds, such as alkanes and aromatics, has long been of interest in chemistry due to their use as starting materials in many industrial syntheses (1). Hydrocarbons are cheap and highly abundant feedstocks currently derived from the petrochemical industry. Methane is a byproduct of oil extraction and must be burned when it cannot be transported due to its dangerous greenhouse gas potential. The use of hydrocarbons as fuels has unwanted side-effects due to the CO<sub>2</sub> released in combustion. If we are to move beyond fossil fuels, part of the solution may be to use these hydrocarbon feedstocks for building more useful and valuable compounds. Thus, if we can establish efficient transformations of C–H bonds, we can better utilise hydrocarbons as chemical building blocks rather than fuels. Additionally, because C–H bonds are ubiquitous in chemistry and biochemistry, these methods will also be applicable to other feedstocks

that could be renewable, bio-sourced or generated from waste products, further increasing the sustainability of this chemistry (2). One pertinent example is the hydrocarbons that are produced from Fischer-Tropsch processes (3, 4). These synthetic hydrocarbons could be carbon neutral, if derived from CO<sub>2</sub> and hydrogen produced using renewable energy, but will need functionalising if they are to be used as convenient chemical feedstocks.

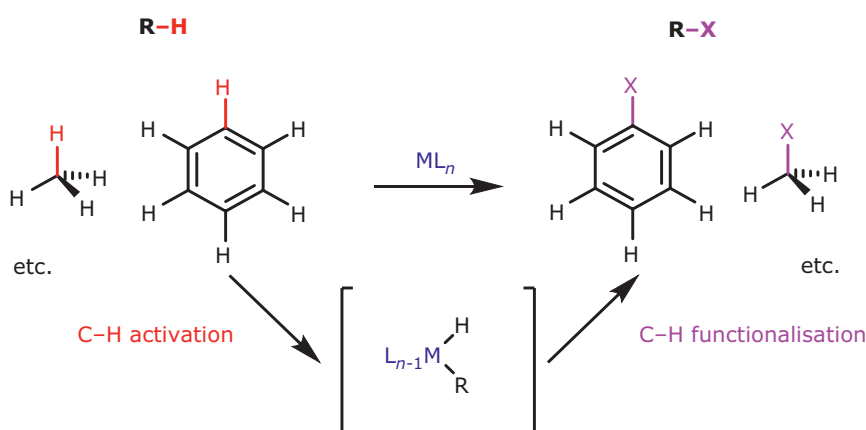
C–H activation remains difficult due to the strength and lack of polarity in carbon hydrogen bonds, particularly with respect to sp<sup>3</sup> carbon centres. This unfavorability in bond breakage can be overcome, however, using a number of approaches to generate thermodynamically and kinetically favourable reactions (**Scheme I**), even for intermolecular and undirected reactions (5). Strong bases can be used to deprotonate and then subsequently functionalise arenes in stoichiometric reactions, with directed *ortho* metalation (DoM) a particularly useful reaction (6), and modern

research has focused on developing better and more selective, albeit still stoichiometric, reagents and reactions (7).

Compared to stoichiometric reactions, catalytic C–H bond functionalisation has the advantage of reducing waste. Focusing on the late transition metals, electrophilic and oxidative addition pathways are commonly proposed, although  $\sigma$ -complex assisted metathesis pathways ( $\sigma$ -CAM) also need to be considered (8, 9). For oxidative addition, using metal complexes with a strongly electron-rich metal centre leads to the formation of strong metal-carbon and metal-hydrogen bonds (**Scheme II**). The requirement for an electron-rich metal centre makes the late transition metals attractive. To improve reactivity, these metal centres require the coordination of strongly electron-donating ligands to further increase the electron density on the metal centre. This subject has been covered in a plethora of reviews on C–H activation over the last few decades (10–13).

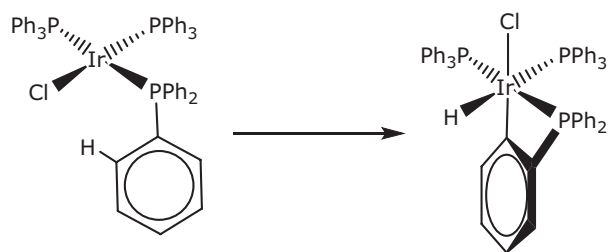


Scheme I. Generalisation of metal-based C–H activation pathways



Scheme II. C–H oxidative addition





Scheme III. An example cyclometallation reaction

The history of C–H activation began as long back as 1898 when Dimroth was able to show the mercuriation of benzene using  $\text{Hg}(\text{OAc})_2$  to give  $\text{Hg}(\text{Ph})\text{OAc}$ . Coincidentally, in 1908 Schorigin also used a mercury compound,  $\text{HgEt}_2$ , in combination with sodium and benzene to generate phenylsodium (7). C–H activation was then extended to aurations in 1931 with Kharasch and coworkers who used gold chloride salts for C–H insertion to form organogold compounds (14). Other early C–H deprotonations could be performed using organolithium and Grignard reagents, however, these reactions generally required nearby functional groups to acidify the C–H bond which both increased reactivity and brought about the selectivity in these reactions, giving rise to DoM.

The metals used in C–H activation moved away from these early C–H activation species to the more electron rich *d*-block metals and by the 1970s the process of intramolecular C–H activation, termed cyclometallation, was well known in the literature (15) with the first cyclometallations being performed in the late 1950s (16). Often aryl C–H bonds were involved (**Scheme III**) because aryl C–H bond activation is kinetically favoured over alkyl C–H bond activation due to pre-coordination of the electron rich arene as well as the formation of stronger M–aryl bonds compared to M–alkyl (17). Cyclometallation further favours the C–H activation product due to the high local concentration of C–H bonds present in ligands already attached to the metal centre and the chelate ring that is formed upon cyclometallation (18).

By the 1960s, Chatt and coworkers were able to demonstrate the more challenging intermolecular C–H activation reaction in the oxidative addition of a naphthalene C–H bond using a ruthenium 1,2-bis(dimethylphosphino)ethane (dmpe) complex, albeit forming a more kinetically and thermodynamically favoured M–aryl bond compared to an M–alkyl bond (19). This reaction was significant as it showed the capability of a low

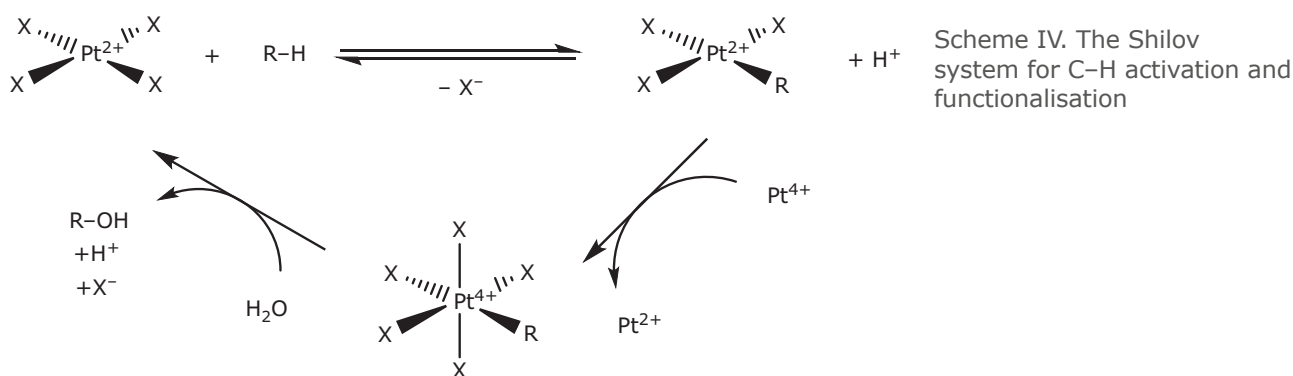
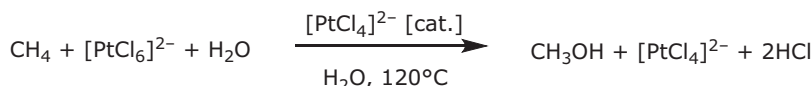
valent *d*-block complex to C–H activate a molecule that was not already bound to the metal centre. The less reactive tetrahydrofuran (THF) solvent molecule was, however, not C–H activated using this complex and it was not expected at that time that alkanes could be C–H activated (16, 20). Thus, the dual challenge of undirected  $\text{sp}^3$  C–H activation and the catalytic functionalisation of C–H bonds still remained.

## 2. Platinum Group Metals

The platinum group metals play a privileged role in catalysis due to their favourable properties including those that derive from their ‘soft’ bonding characteristics, as classified in the hard-soft Lewis acids and bases (HSAB) approach. This classification leads from the high covalency in their bonding, preference for soft ligands, such as those derived from carbon, and tolerance to oxygen and moisture. Additionally, they undergo two electron processes (oxidative addition and reductive elimination) and their properties can be modified easily using the ligands that are attached, which has proven crucial in developments throughout homogeneous catalysis (21).

### 2.1 A Brief Overview of Palladium and Platinum in Electrophilic Carbon-Hydrogen Activation: Historical Developments to the Modern Day

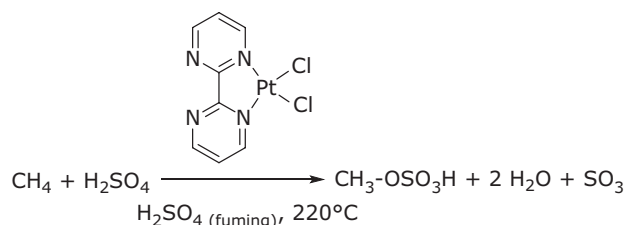
The Group 10 platinum metals (platinum and palladium) are important metals for C–H activations (22, 23). This has been seen since the late 1960s and early 1970s when Shilov and coworkers were able to develop metal complexes that were able to C–H activate alkanes in an undirected, intermolecular fashion; the so-called Shilov system (**Scheme IV**) (24). This system made use of a Pt(II) complex as the catalyst and a Pt(IV) complex as a stoichiometric oxidant because, although other oxidants were explored, platinum was shown to be able to deliver the best results. The work by Shilov was mostly unknown to western scientists due to the political split referred to as ‘The Iron Curtain’ at the time. The work by Bercaw and coworkers explored this chemistry further where they were able to follow the progress of Shilov through several international conferences. Bercaw and others were also able to explore the mechanism of this system in greater detail. This brought about knowledge of the active species involved, giving a more detailed answer to whether platinum nanoparticles were

**Overall reaction:**

the cause of activation. The answer was that while nanoparticles had an effect on H/D exchange, the system was still able to C–H activate the system on its own (25).

An example of more recent developments in platinum chemistry is shown by the work of the Periana group where they were able to synthesise a stable (2,2'-bipyrimidyl)Pt(II) dichloride catalyst, the so-called 'Periana System', for the functionalisation of methane to the methanol derivative methyl bisulfate,  $(\text{CH}_3)\text{HSO}_4$ , in  $\text{H}_2\text{SO}_4$  (Scheme V). This high yielding and relatively selective reaction was able to tolerate excess  $\text{SO}_3$  without forming the undesirable C–S bonded product methanesulfonic acid,  $\text{CH}_3\text{SO}_3\text{H}$ , however, the reaction is limited to a product methanol concentration of *ca.* 1 M. The authors also noted that the complex was stable for over 300 turnovers before there was any loss in activity when acid concentration is maintained, although further work was required to deduce why this was the case (23). Later work done by the Schüth group in 2016 showed the same reaction using another platinum catalyst,  $\text{K}_2\text{PtCl}_4$ . Under these reaction conditions the catalyst turnover frequency was  $25,000 \text{ h}^{-1}$  making this complex a potentially desirable catalyst for this process industrially. The authors also noted that platinum black was not an issue in these reactions, particularly as oleum in the reaction medium is capable of oxidising platinum black to Pt(IV) (26).

Palladium also plays a significant role in C–H activation and there is a plethora of examples of palladium complexes being used in organic syntheses (27). Palladium complexes used in C–H activation typically utilise a concerted metalation-



deprotonation (CMD) mechanism, or similar, as opposed to oxidative addition, where the reaction proceeds *via* the formation of a five- or six-membered palladacycle. This lowers the activation energy of the species to allow for the cleavage of the C–H bond. Therefore, the selection of directing groups in these reactions is important for achieving high reactivity in C–H bond activation (28, 29).

## 2.2 Ruthenium

Ruthenium complexes capable of C–H activation have long been known ever since the intermolecular C–H activations mentioned earlier performed by Chatt and coworkers. However, compared to other platinum metals, ruthenium has been relatively under-explored in C–H activation over the last couple of decades. An area where there has been interest in ruthenium C–H activation is in selective *meta*-C–H functionalisation through ruthenium catalysed  $\sigma$ -activation (30). This was reviewed in 2017 by Leitch and Frost where they were able to explore this reaction in more detail (31). The Frost group previously performed this reaction using a ruthenium *para*-cymene complex  $[\text{RuCl}_2(\text{p-cymene})]_2$  which selectively

C–H activated the *meta*-position of phenyl pyridine with an 80% yield in a sulfonation reaction. The high loadings of complex in this reaction were problematic. This was, however, tackled by the Ackermann group who were able to make use of a recyclable heterogeneous ruthenium catalyst on a silica support (32).

Research in ruthenium C–H activation was further expanded in a recent paper by the Baslé group, where they were able to perform phosphorus directed C–H borylation at the *ortho*-position of arylphosphines using a ruthenium NHC-tethered carboxylate complex. This reaction was highly selective and high yielding for a range of aryl phosphines, where the phosphine acted as a directing group in this reaction. The active site of this species was also brought about by the lability of the arene in the complex (33).

### 3. Rhodium and Iridium

Rhodium and iridium complexes, the focus of this review, are widely used in C–H activation reactions operating with several different distinct mechanisms depending on oxidation state, choice of ligands and substrate involved. Several of these mechanisms utilise similar ligands sets, so the choice of ligand set and the properties required will be discussed concurrently with the C–H activation processes.

#### 3.1 Ligand Choice and Selection with Respect to Carbon-Hydrogen Activation: Cyclopentadienyl/Pentamethylcyclopentadienyl Complexes

Cyclopentadienyl (Cp, C<sub>5</sub>H<sub>5</sub>), which is an aromatic and formally anionic ligand, and pentamethylcyclopentadienyl (Cp\*, C<sub>5</sub>Me<sub>5</sub>) were the ligands of choice for Group 9 C–H activation dating back to the first well-defined intermolecular C–H oxidative addition reactions in the early 1980s. This is because the ligands bound to a metal

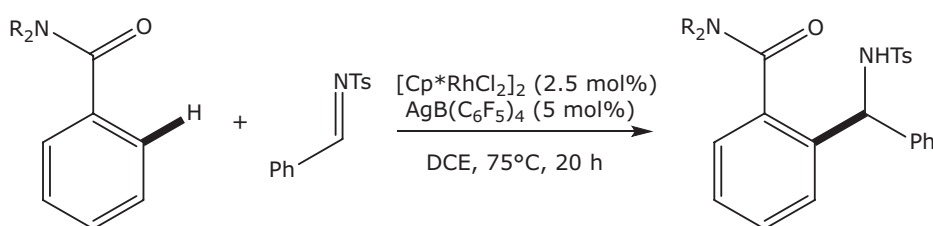
centre of a transition metal complex are important for controlling reactivity and Cp/Cp\* are useful ligands being able to bind strongly to the metal centre taking up three *cis* coordination sites. These anionic ligands are not easily dissociated from the metal complex, even at high temperatures, making these ligands excellent anchor groups and spectator ligands (34).

#### 3.2 Rhodium Complexes for Donor-Assisted Carbon-Hydrogen Activation

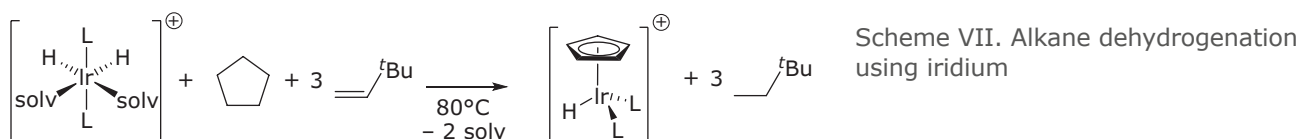
In general, with donor-assisted C–H activation catalysed by rhodium, two modes of activation are known: chelation-assisted C–H activation (35), particularly useful for the functionalisation of donor-substituted arenes; and the C–H activation of *N*-heterocycles (36). For chelation assisted C–H activation, a Rh(I) oxidative addition pathway is possible as well as a Rh(III) electrophilic pathway (35). Rh(III) chloride complexes featuring the Cp\* ligand are typically used here, with these complexes reacting akin to the palladium complexes mentioned earlier *via* a directed CMD reaction where the importance of the directing group is fundamental (37). The work of Bergman, Ellman and coworkers in this field is highlighted as these rhodium-catalysed processes are efficient means of C–C bond formation and the functionalisation of *N*-heterocycles (35, 36, 38). For example, {Cp\*RhCl<sub>2</sub>}<sub>2</sub> activated with a silver salt of a weakly coordinating anion in 1,2-dichloroethane (DCE) was used for the C–H activation of benzamide arenes where the amide was the directing group in this reaction (Scheme VI) (39). Amides are more useful motifs in the synthesis of biologically-relevant pharmaceuticals and natural products than earlier  $\alpha$ -branched amines that were used.

#### 3.3 Alkane Dehydrogenation Studies

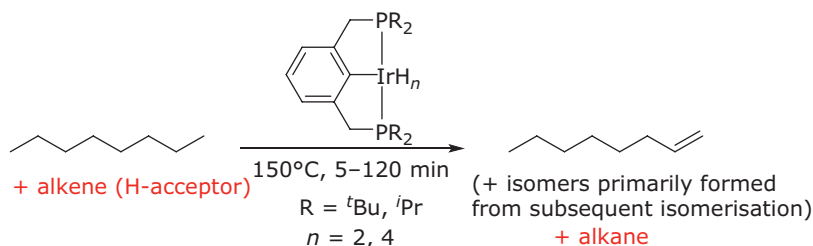
In 1979, Crabtree and coworkers utilised the high stability of iridium bonding to unsaturated hydrocarbons to drive the dehydrogenation of



Scheme VI. Biologically important C–H activation using a Rh(III) complex. Ts = *para*-tolylsulfonyl

L = PPh<sub>3</sub>

solv = acetone, water, alkene

Counter anion is typically [BF<sub>4</sub>]<sup>-</sup>*cis,cis,trans* isomer shown. All *trans* isomers were also observed.

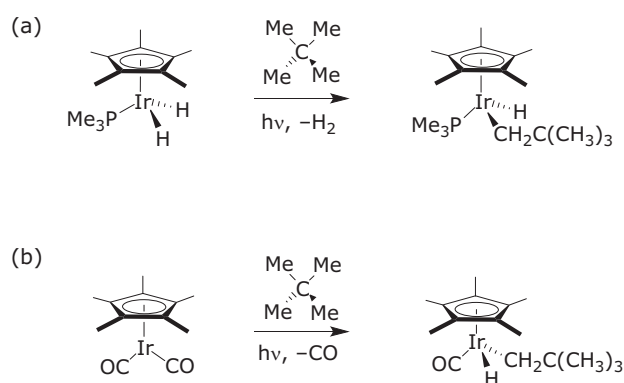
alkanes, although a hydrogen acceptor was needed making this reaction a transfer hydrogenation (40, 41). In particular, the high stability of the Ir–Cp fragment drives the dehydrogenation of cyclopentene and cyclopentane to the cyclopentadienyl ligand, thereby demonstrating C–H activation (**Scheme VII**).

Similar results were also achieved with rhenium hydride complexes [ReH<sub>7</sub>(PR<sub>3</sub>)<sub>2</sub>] (PR<sub>3</sub> = PPh<sub>3</sub> or PEt<sub>2</sub>Ph) (42), which could also be made catalytic generating cycloalkenes from cycloalkanes, albeit requiring the use of a hydrogen acceptor (42). Using [IrH<sub>5</sub>(P<sup>i</sup>Pr<sub>3</sub>)<sub>2</sub>], *n*-hexane could be converted into 1-hexene at room temperature (43). In these systems, turnover numbers up to 70 were achieved (44). Crabtree's system, modified with a chelating trifluoroacetate ligand, could also be used catalytically either thermally with a hydrogen acceptor, or photochemically without (45).

Rhodium phosphine complexes were subsequently found to catalyse the dehydrogenation of cyclohexane to cyclohexene, either photochemically (46) or thermally with a hydrogen acceptor (44, 47). However, the real breakthrough came when using thermally robust pincer ligands in combination with iridium metal centres (**Scheme VIII**) (48, 49). Subsequent research has driven further progress in this field (48, 50), including the combination of alkane dehydrogenation with alkene metathesis to effect 'alkane metathesis' *via* alkenes as intermediates (51).

### 3.4 Carbon-Hydrogen Oxidative Addition

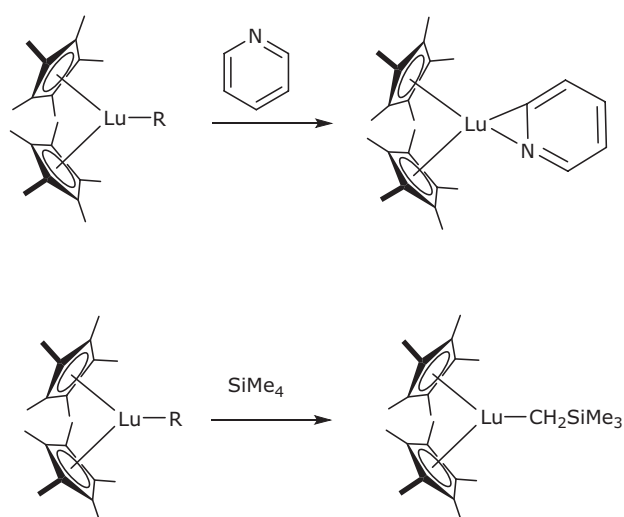
Cp\* iridium complexes capable of C–H activation were discovered in the early 1980s in seminal work by the Bergman and Graham groups where they were able to use highly electron-rich iridium complexes to stoichiometrically C–H activate neopentane (**Scheme IX**) (52, 53). The reactive, unsaturated 16 electron intermediate was generated using ultraviolet photolysis. This work showed that it was possible to activate sp<sup>3</sup> C–H bonds that were previously considered inert on molecules separate from the metal complex (termed intermolecular C–H activation) not just those bound to the transition metal centre (termed intramolecular C–H activation or cyclometallation).



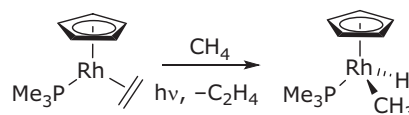
Scheme IX. Photolysis driven IrCp\* C–H activation

In parallel work, Cp\* ligands have also been utilised in C–H activation by  $\sigma$ -bond metathesis (**Scheme I**). In 1983, shortly after the work published by Graham and Bergman using iridium Cp complexes, Patricia Watson developed rare earth Cp\* complexes for intermolecular C–H activation using lutetium as the metal centre (54). A completely different mechanism of reactivity is in use here, termed  $\sigma$ -bond metathesis, enforced by the single accessible oxidation state of lutetium. Watson showed examples of intra- and intermolecular C–H activation of several species under mild conditions (**Scheme X**). It was also possible to form the intermolecular C–H activation product with tetramethylsilane to give (Cp\*)<sub>2</sub>Lu–CH<sub>2</sub>SiMe<sub>3</sub>. Again, it was the use of Cp\* as a stable, supporting ligand that controlled the coordination environment around the metal that led to the successful development of these C–H activation processes.

Returning to Group 9, investigations on the mechanism and thermodynamics of C–H activation using the [RhCp\*(PMe<sub>3</sub>)] fragment were carried out by Jones and coworkers (55, 56). These investigations revealed that [Cp\*Rh(H)(Ar)(PMe<sub>3</sub>)] complexes were stable below 60°C whereas the analogous alkyl complexes displayed irreversible reductive elimination at or about –20°C (56). Thus, photolysis of [Cp\*Rh(H)<sub>2</sub>(PMe<sub>3</sub>)] in liquid propane at –55°C followed by removal of the solvent at –40°C gave the *n*-propyl hydride complex (56). Competitive experiments using benzene:propane mixtures showed only a small



Scheme X. Cp\* Lutetium complex for intramolecular and intermolecular C–H activation



Scheme XI. RhCp C–H activation

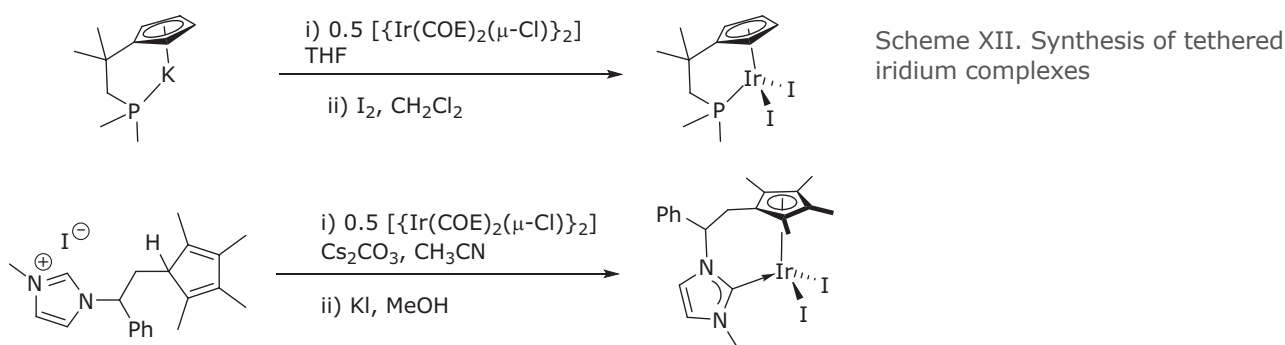
kinetic preference for benzene over propane (4:1) despite the thermodynamic preference for the formation of the phenyl hydride complex (56). Perutz and coworkers found that it was also possible to use ethene as a leaving group through photolysis of [MCp(PMe<sub>3</sub>)(C<sub>2</sub>H<sub>4</sub>)] (M = rhodium, iridium) to give a similar reactive fragment to that of Bergman *et al.* (57, 58) The group were also able to explore the C–H activation of methane several years later using photochemical generation of a reactive rhodium fragment, similar to the complex used by the Bergman and Graham groups (**Scheme XI**) (59).

### 3.5 Indenyl Complexes

Cp and Cp\* ligands are difficult to modify further (34). An exception to this is the benzannulated derivatives indenyl and fluorenyl that are readily available. Indenyl, just like Cp, has the ability to bind strongly to the metal centre through an  $\eta^5$ -interaction featuring bonding to all five carbon atoms of the five-membered ring. However, it is also possible for indenyl to 'ring-slip' to an  $\eta^3$  mode (where only three carbon atoms are coordinated) or even an  $\eta^1$ -interaction; this is known as the 'indenyl effect' (60). This change in hapticity was first shown by the Mawby group in 1969 where they observed that PPh<sub>3</sub> could coordinate to [Mo(C<sub>9</sub>H<sub>7</sub>)(Me)(CO)<sub>3</sub>] after ring slippage of the indenyl from  $\eta^5$  to  $\eta^3$  leaving a vacant site on the metal centre. The species then reverted back to  $\eta^5$  coordination after migratory insertion of the methyl to form [Mo(C<sub>9</sub>H<sub>7</sub>)(COMe)(CO)<sub>2</sub>(PPh<sub>3</sub>)] (61).

Foo and Bergman were able to use an indenyl phosphine iridium complex for the C–H activation of benzene in 1993 (62). As was hypothesised by the authors, it was found that the indenyl complex was more reactive than the Cp\* complex. Since then, there has been other uses of indenyl Group 9 complexes for C–H activation. A recent review (63) highlighted the work by the Rovis group who were able to use a heptamethyindenyl Rh(III) complex to catalyse the C–H activation and diastereoselective benzamidation of cyclopropenes (64). It was also





noted that different Cp analogues have differing stereochemical, steric and electronic properties leading to a change in the yields of the desired product.

### 3.6 Tethered Complexes

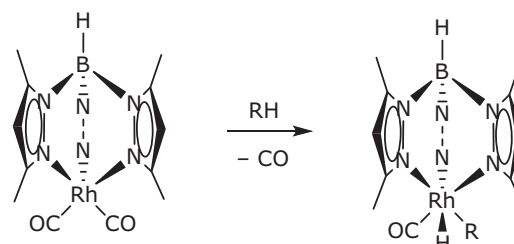
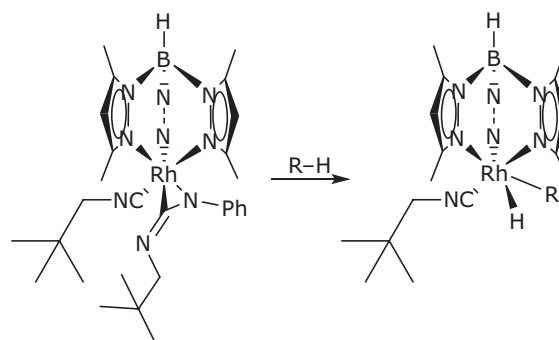
Tethered Cp ligands are well established in the literature and combine the advantages of Cp with those of another donor group (65, 66). Tethered species have the advantage of being more thermally stable, but there is also the advantage that the ligand is more rigid allowing for the preparation of an asymmetric catalyst when a chiral centre is present (67). In 1997, Bergman and coworkers were able to show C–H activation using an iridium complex formed from a phosphine tethered to a Cp ligand (Scheme XII). This complex was found to have an advantage over non-tethered complexes because the tethered phosphine could readily dissociate from the metal and then immediately reattach as the Cp is a stable supporting ligand and will not dissociate at high temperatures. The small bite angle effect (68) of the complex is also potentially advantageous, brought about by the rigidity of the ligand structure (69, 70). Contrastingly, a rhodium dihydride complex of the tethered ligand  $[C_5H_4SiMe_2CH_2PPh_2]^-$  did not show C–H activation under photochemical conditions (71). The Royo group in 2008 synthesised the first Cp\*-type tethered NHC ligand, a synthetically more challenging goal, to give an Ir(III) metal complex (Scheme XII) (72). The work of Danopoulos and coworkers is also highlighted as they were able to synthesise tethered iridium and rhodium indenyl/fluorenyl NHC complexes (73, 74).

### 3.7 Tp/Tp\* – Trispyrazolyborates

Amongst many Cp-mimics, (hydrotris(pyrazolyl) borate) (Tp) ligands are especially useful. These ligands bind to the metal centre as a

tridentate ligand through nitrogen donors (75, 76). These ligands were first explored for C–H activation in the early 1990s where Jones and coworkers were able to use a Tp complex,  $[Rh\{HB(3,5\text{-dimethylpyrazolyl})_3\}(CNR)]$  ( $PhN=C=NR$ ) ( $R = \text{neopentyl}$ ), to C–H activate a range of substrates (Scheme XIII) (77, 78).

Later, these ligands found use in mechanistic studies of C–H activation at room temperature. In 1997, the  $[RhTp^*(CO)_2]$  complex ( $Tp^* = HB-Pz^*_3$ ,  $Pz^* = 3,5\text{-dimethylpyrazolyl}$ ) was used in a collaborative project by the Harris, Bergman and Frei groups (Scheme XIV) (79). The  $Tp^*$  complex was seen as a better complex to study this reaction compared to Cp analogues because the  $Tp^*$  complex has a high quantum yield of



30% as opposed to the Cp complex which had a quantum yield of *ca.* 1% for the formation of the activated intermediate. This allowed the team to use ultrafast spectroscopy with picosecond and femtosecond time resolutions to access the inter/intramolecular processes that take place faster than diffusion. Further work was done in 2002 to report the role of hydrocarbon structure on the process of C–H activation as well as to compare with [RhCp(CO)<sub>2</sub>] (80). In 2018, the role of sterics and electronics was studied for Tp' complexes (Tp, Tp\* or Tp<sup>tBu</sup> = tris(3,5-dimethyl 4-*t*-butylpyrazolyl) borate) vs. Cp'(Cp or Cp\*) Rh(CNR)(carbodiimide) in the C–H activation of cyclic alkanes (81).

## 4. Borylation

### 4.1 Metal Boryls and Stoichiometric Borylation

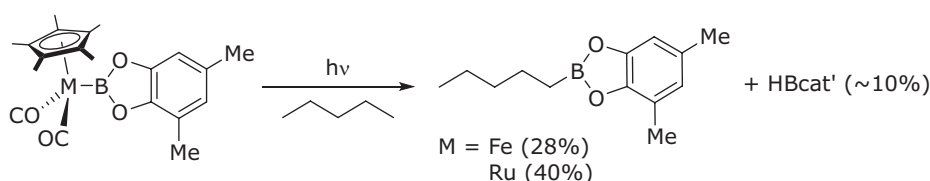
A major problem with many of the C–H activation reactions listed previously was the difficulty in converting the M–C species generated into new species whilst still yielding reactive metal complexes that can complete a catalytic cycle. The use of metal boryls was found to be an especially useful route forward. Firstly, reactions of C–H bonds (such as those in methane) with tetraalkoxydiboron(4) compounds, B<sub>2</sub>(OR)<sub>4</sub>, generate alkylboronate esters (R–B(OR)<sub>2</sub>) and H–B(OR)<sub>2</sub> and are thermodynamically downhill (82, 83). Even the reaction of C–H bonds with HB(OR)<sub>2</sub> (the byproduct of the previous reaction) are approximately thermoneutral (82), and so can be driven by release of the H<sub>2</sub> gas that is formed. Secondly, boryls are electron donating ligands that facilitate oxidative addition (often favoured in iridium borylation) and  $\sigma$ -CAM pathways (as proposed in rhodium-catalysed borylation) (84) of C–H bonds, with the nominally empty *p*-orbital on boron also facilitating C–H bond cleavage and C–B bond formation (82, 84). This means that reactions of metal boryls with arenes and alkanes can occur generating a catalytic cycle.

It is also fortunate that the organoboronic esters that are formed from C–H activation of metal boryl

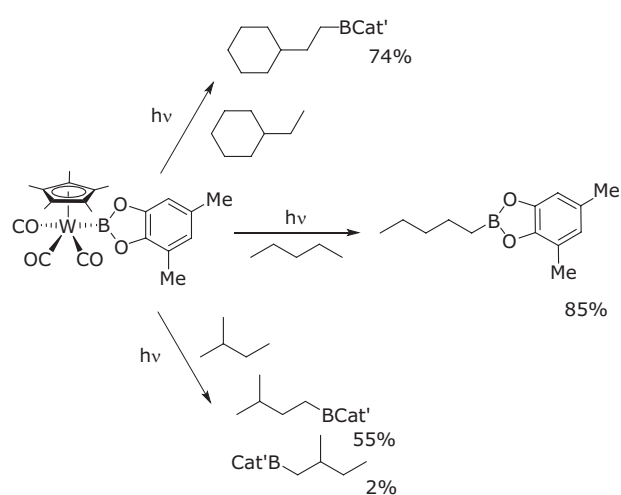
complexes are valuable as chemical intermediates in many chemical reactions including Suzuki–Miyaura coupling reactions. Additionally, drugs that contain boron are now being developed successfully, including Bortezomib, a proteasome inhibitor that has activity against a variety of cancers (85). The requirements for a catalyst that can accomplish C–H borylation was highlighted in a review by Hartwig in 2012 (86), identifying the need for catalysts that are both site selective with excellent functional group tolerance and have high turnover numbers. The versatility of these borylated arene intermediates was underscored because they can be further reacted with a wide range of organic reagents producing products that can be used in materials and medicinal applications.

The selective boron-functionalisation of alkanes using transition metals was pioneered by the Hartwig group using transition-metal boryl complexes (87, 88). The group was able to successfully synthesise pentyl-Bcat' {cat' = substituted catecholate 1,2-O<sub>2</sub>C<sub>6</sub>H<sub>2</sub>-3,5-(CH<sub>3</sub>)<sub>2</sub>} by the stoichiometric reaction of heteroleptic Cp\* metal-carbonyl boryl complexes with pentane (**Scheme XV**). Similar iron and ruthenium complexes were able to form pentyl-Bcat' in 28% and 40% yield, respectively, with the formation of trace amounts of HBcat' (~10%).

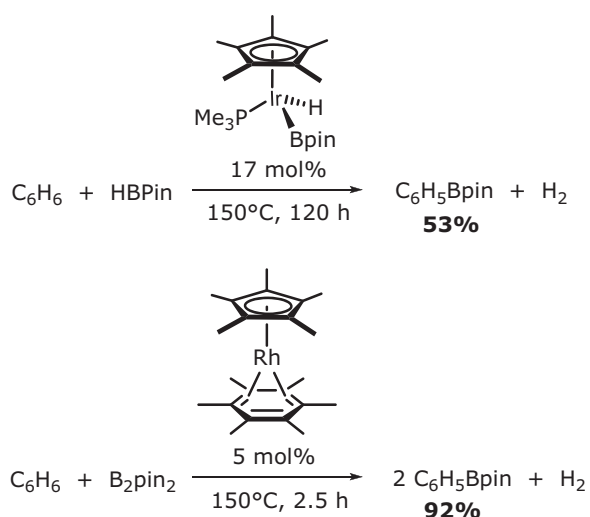
The reaction with the analogous tungsten complex was found to be the best with pentyl-Bcat' formed in 85% yield (**Scheme XVI**), therefore, the scope of the tungsten reaction was explored further. The group found that the complex was selective for the borylation of the least hindered sp<sup>3</sup> carbon of selected molecules. Ethylcyclohexane was selectively borylated at the terminal sp<sup>3</sup> position of the molecule to yield (2-cyclohexyl)-1-ethylboronate ester in 79% yield. The borylation of isopentane was selective for the least hindered terminal site (55% yield) instead of the most sterically hindered terminal carbon (2% yield). Cyclohexane was also borylated, however, the yield for this reaction was only 22%, suggesting that the reaction is selective for sp<sup>3</sup> carbons over sp<sup>2</sup> carbon centres.



Scheme XV. Cp\* metal carbonyl complex for C–H borylation



Scheme XVI. Further early stoichiometric C–H borylations using tungsten



Scheme XVII. C–H borylation of arenes using rhodium and iridium Cp complexes. The rhodium-catalysed reaction generates and uses HBPin to give two equivalents of PhBpin

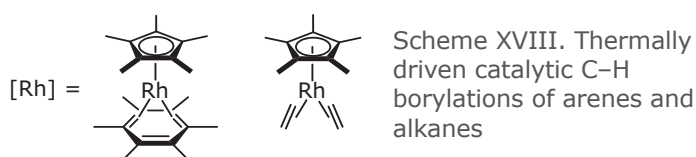
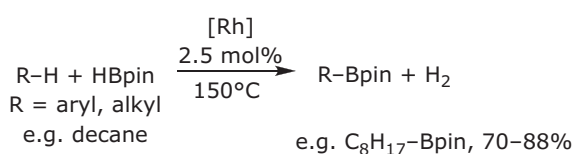
## 4.2 Catalytic Borylation

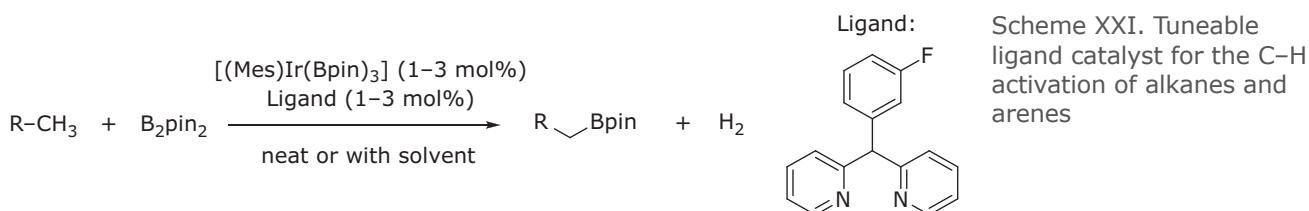
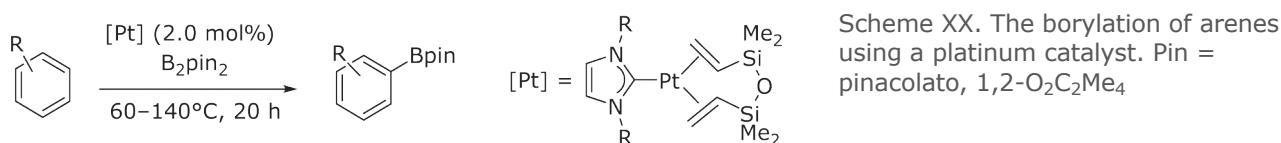
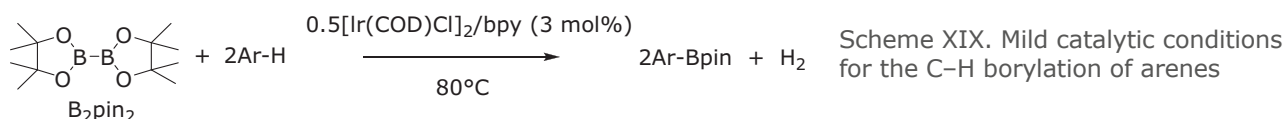
At a similar time, Smith and coworkers were also probing the challenge of C–H activation and the borylation of arenes (89). Using an IrCp\* complex, they were able to develop a catalytic

reaction, albeit under quite severe conditions (Scheme XVII). RhCp\* catalysts were quickly shown to be superior, utilising  $[\text{RhCp}^*(\text{C}_6\text{Me}_6)]$  as a precursor (Scheme XVII) (90, 91).

The first thermally-driven catalytic borylation of alkanes were realised by Hartwig and coworkers in 2000 (Scheme XVIII) (91). This reaction was able to occur, albeit at relatively high temperatures, to give organoboronic esters in good yields using both  $\text{B}_2\text{Pin}_2$  and HBPin as a source of boryl fragments.

In 2001, Hartwig, Miyaura and coworkers were able to exemplify the mild, catalysed direct borylation of arenes with  $\text{B}_2\text{Pin}_2$  using an iridium catalyst (Scheme XIX) (92). The group made a serendipitous discovery of a very effective catalyst by reacting a commercially available Ir(I) complex with 2,2'-bipyridine (bpy). The catalyst was able to efficiently borylate arene substrates at 80°C using  $\text{B}_2\text{Pin}_2$  making use of both Bpin groups. The reaction gave yields of 93% with turnover numbers as high as 8000. The reaction also took place at room temperature using this catalyst, however, the catalyst loading needed to be much higher (92). This finding led to much research into iridium-catalysed C–H borylation using bidentate nitrogen ligands based on bipyridine and phenanthroline (93), and iridium-catalysed arene borylation has even been performed on >70 kg of the borylated product (94). Other metal complexes were inferior to iridium complexes, such as  $\text{Pt}(\text{dba})_2/\text{bpy}$  and  $[\text{RhCl}(\text{COD})]_2/\text{bpy}$ . The platinum complex was unable to catalyse this reaction and the rhodium complex was only able to form PhBPin in 20% yields at temperatures over 150°C (92). Other ligands were tried, and it was found that 1,10-phenanthroline catalysed the reaction in high yields whereas pyridine,  $\text{PPh}_3$  and tetramethylethylenediamine (TMEDA) were unable to generate a catalytically active metal complex. Further research showed that with the correct choice of ligand, platinum catalysts can be successful. Work performed by Furawa *et al.* used an NHC platinum complex for the C–H activation and borylation of sterically congested positions of hydrocarbon substrates (Scheme XX) (95).





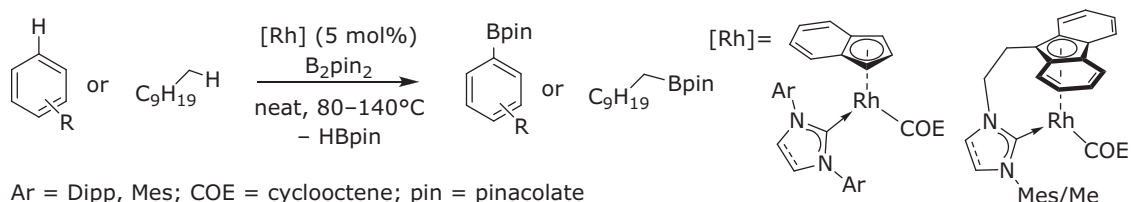
The substrate scope of iridium- and rhodium-catalysed C–H borylations has greatly improved since the work of the early 2000s. The Hartwig group have been able to expand the substrate scope of these reactions to ethers, amines, amides and heteroarenes. The scope, regioselectivity and mechanism of the borylation of heteroatoms were explored, in 2014, using an iridium tetramethylphenanthroline complex (96, 97). There have been many more examples of C–H activation and borylation of arenes since then, but the efficient borylation of alkanes remains very difficult (98, 99). A catalyst system involving the 2-methylphenanthroline ligand (5 mol%) with [Ir(mesitylene)(Bpin)<sub>3</sub>] (2.5 mol%) and B<sub>2</sub>pin<sub>2</sub> allowed the stoichiometric C–H borylation of sp<sup>3</sup> C–H bonds to be achieved (cycloalkanes were used as the solvent, primary C–H bonds are favoured, with secondary bonds functionalised only if the primary sites are absent or blocked), an important advance on previous processes that required excess substrate (100). Another recent successful example was demonstrated by the Schley group in 2020 where they were able to use an iridium catalyst with a tuneable ligand scaffold (**Scheme XXI**) (101).

Using the catalyst system designed by the Schley group, it was found that the C–H activation and borylation of *n*-octane could be performed in near quantitative yields to give octyl-Bpin. The group also found that their ligand system is tolerant to a range of substrates including ethers, esters and

tertiary amines. Secondary and branched alkanes, however, showed poor catalytic performance. It was found that although these functional groups were low yielding this reaction could be performed in cyclohexane with negligible competitive solvent borylation. The use of five equivalents of substrate gave high yields in cyclohexane which is useful compared to the typical requirement for neat substrate.

The active species of this reaction is relatively unknown. It was postulated that the ligand binds to the iridium metal centre through the nitrogen atoms and then forms a further bond through the cyclometallation of the phenyl to give an  $\kappa^3$ -binding mode, which looks analogous to the  $\eta^5$ -Cp\* ligand. The other explanation for the enhanced reactivity of this complex is that the complex can install a pinacol group on the sp<sup>2</sup> carbon proximal to the metal centre by borylation. This would be similar to the secondary coordination sphere interactions between boryls and substrate in alkane borylation like that proposed by the Hartwig group.

The work of Mansell, Morton, Evans and coworkers has focused primarily on indenyl rhodium NHC complexes for catalytic C–H activation and borylation (**Scheme XXII**) (102). It was observed that the NHC used in this reaction played a critical role in the rate of these reactions. The saturated NHC 1,3-bis(2,6-diisopropylphenyl)-4,5-dihydroimidazol-2-ylidene (SIDipp) complex was able to perform both arene and alkane borylation in better yields than both the saturated and



Scheme XXII. C–H borylation using indenyl rhodium NHC complexes, both tethered and non-tethered

unsaturated mesityl-substituted NHC complexes. Further work by the group has investigated the scope of these complexes for the borylations of a range of ether, ester and amide substrates. It was anticipated that the tethering of the NHC to a fluorenyl moiety through a C<sub>2</sub>H<sub>4</sub> linker would enable the formation of better catalysts for C–H activation, however, these complexes were both synthetically challenging to achieve in good yields and performed comparatively worse in the C–H borylation of arenes.

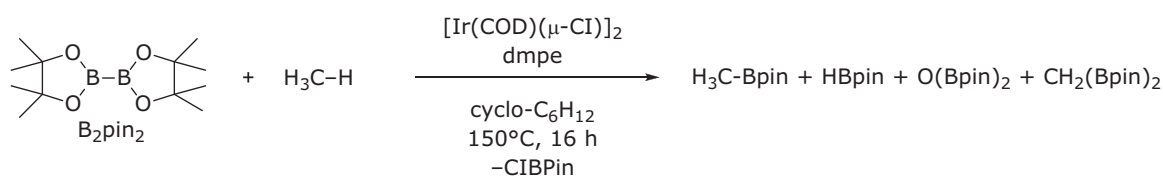
## 4.2 Methane Borylation

Methane functionalisation is a key challenge due to the high abundance and therefore low cost of methane but represents a particularly challenging goal for C–H activation. A lot of methane is flared at the point of extraction if it cannot be readily transported by pipeline (common in areas far from end users) to avoid releasing methane into the atmosphere due to methane's high global warming potential. However, this is a waste of a valuable resource, so facile and economic conversion into

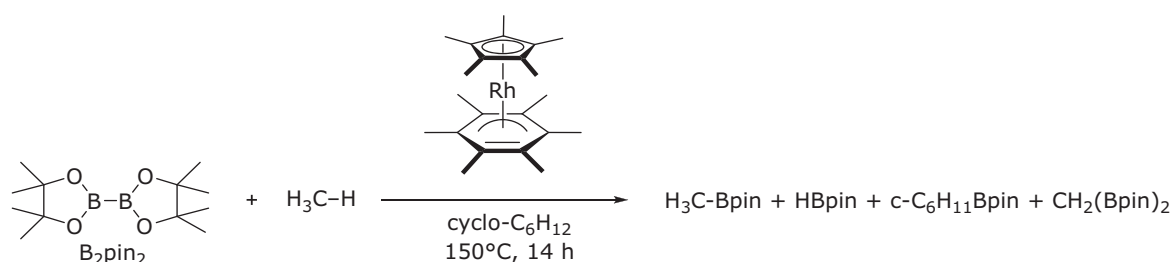
a liquid product would be very useful. Methane is a more challenging substrate to borylate compared to arenes due to its non-polar nature with unreactive, strong sp<sup>3</sup> C–H bonds. Methane is also poorly soluble in many polar and non-polar solvents. The solvents must also be less reactive to C–H activation than methane. The most significant issue with the borylation of methane is the chemoselectivity where any new borane species formed will be potentially more reactive than the bonds in methane, leading to poor selectivity such as overfunctionalisation and overoxidation.

The Mindiola and Sanford groups were able to independently identify catalysts for the C–H activation and borylation of methane (100, 103, 104). The Mindiola group utilised an iridium catalyst with the softer Lewis basic dmpe (Me<sub>2</sub>PC<sub>2</sub>H<sub>4</sub>PMe<sub>2</sub>)<sub>2</sub> ligand (Scheme XXIII). The group were able to overcome the chemoselectivity problems associated with methane borylation to synthesise methyl-BPin with a yield of 52% and a turnover number of 104.

The Sanford group made use of [RhCp\*(C<sub>6</sub>Me<sub>6</sub>)] to borylate methane (Scheme XXIV). This work followed density functional theory calculations



Scheme XXIII. C–H borylation of methane by the Mindiola group



Scheme XXIV. C–H borylation of methane by the Sanford group



done by Hall and coworkers in 2005 where they suggested that Cp\*Rh complexes were capable of performing this reaction (84).

## 5. Conclusions

Platinum group metals have long been associated with C–H activation, from the early days of the Shilov system where platinum was used for the catalytic functionalisation of alkanes, to the complexes of the early 1980s where well defined intermolecular C–H activations were performed using rhodium and iridium cyclopentadienyl complexes. Research has now progressed into the realm of catalytic C–H activation and functionalisation, with noble metal complexes still being used and developed. The correct choice of ligands is very important to the design and functionality of complexes for C–H activation, with anionic ligands being purposefully chosen and partnered with the correct neutral co-ligands to create the desired properties. An efficient catalyst for C–H functionalisation brings about the possibility of numerous applications. The products of borylation, boronate esters, are useful chemical intermediates in many medicinal and material syntheses, and progress towards the synthesis of these through C–H borylation is well underway with the selectivity, scope and scale of these reactions increasing. Progress towards the borylation of methane is still a challenge and since the seminal works of both Sanford and Mindiola there have been few additional examples of methane borylation (105).

The drive towards greater sustainability has been seen in many parts of society and is of no less importance here for C–H activation, particularly due to the cost and scarcity of these noble metals. Therefore, it is easy to see that the next challenge in C–H activation will be to perform these reactions in a more sustainable way. This would require the synthesis of much better and longer-lived catalysts or complexes that can be easily reused. Alternatively, C–H activation could be performed using less scarce metals such as iron, the second most abundant element in the earth's crust. Iron has begun to show promise in recent years for a number of C–H activation and functionalisation reactions (106). There are also a few rare examples of metal-free pathways for C–H activation, however, these reactions remain underexplored (107, 108). It can easily be envisioned that platinum metals will continue to be used as the metals of choice for C–H activation due to their reliability and their great diversity of use within these reactions.

However, work should continue to make these reactions more sustainable by designing more robust catalyst systems.

## Acknowledgements

The authors thank the Engineering and Physical Sciences Research Council (EPSRC, PhD studentship to Paul A. Morton), the Scottish Funding Council (Saltire Emerging Researcher Scheme, travel funding for Paul A. Morton) and the Royal Society of Chemistry (Research Fund grant R21-6824221494) for funding. The authors would also like to thank Johnson Matthey plc for the award of platinum group metal materials used in their research.

## References

1. T. Gensch, M. J. James, T. Dalton and F. Glorius, *Angew. Chem. Int. Ed.*, 2018, **57**, (9), 2296
2. J. F. Hartwig, *J. Am. Chem. Soc.*, 2016, **138**, (1), 2
3. F. S. Zeman and D. W. Keith, *Philos. Trans. A Math. Phys. Eng. Sci.*, 2008, **366**, (1882), 3901
4. S. J. Davis, N. S. Lewis, M. Shaner, S. Aggarwal, D. Arent, I. L. Azevedo, S. M. Benson, T. Bradley, J. Brouwer, Y.-M. Chiang, C. T. M. Clack, A. Cohen, S. Doig, J. Edmonds, P. Fennell, C. B. Field, B. Hannegan, B.-M. Hodge, M. I. Hoffert, E. Ingersoll, P. Jaramillo, K. S. Lackner, K. J. Mach, M. Mastrandrea, J. Ogden, P. F. Peterson, D. L. Sanchez, D. Sperling, J. Stagner, J. E. Trancik, C.-J. Yang and K. Caldeira, *Science*, 2018, **360**, (6396), eaas9793
5. J. F. Hartwig and M. A. Larsen, *ACS Cent. Sci.*, 2016, **2**, (5), 281
6. V. Snieckus, *Chem. Rev.*, 1990, **90**, (6), 879
7. R. E. Mulvey, F. Mongin, M. Uchiyama and Y. Kondo, *Angew. Chem. Int. Ed.*, 2007, **46**, (21), 3802
8. R. N. Perutz and S. Sabo-Etienne, *Angew. Chem. Int. Ed.*, 2007, **46**, (15), 2578
9. R. N. Perutz, S. Sabo-Etienne and A. S. Weller, *Angew. Chem. Int. Ed.*, 2022, **61**, (5), e202111462
10. T. Dalton, T. Faber and F. Glorius, *ACS Cent. Sci.*, 2021, **7**, (2), 245
11. T. Rogge, N. Kaplaneris, N. Chatani, J. Kim, S. Chang, B. Punji, L. L. Schafer, D. G. Musaev, J. Wencel-Delord, C. A. Roberts, R. Sarpong, Z. E. Wilson, M. A. Brimble, M. J. Johansson and L. Ackermann, *Nat. Rev. Methods Prim.*, 2021, **1**, 43
12. O. Baudoin, *Angew. Chem. Int. Ed.*, 2020, **59**, (41), 17798

13. L. Guillemard and J. Wencel-Delord, *Beilstein J. Org. Chem.*, 2020, **16**, 1754
14. M. S. Kharasch and H. S. Isbell, *J. Am. Chem. Soc.*, 1931, **53**, (8), 3053
15. S. Trofimenko, *Inorg. Chem.*, 1973, **12**, (6), 1215
16. R. H. Crabtree, *J. Organomet. Chem.*, 2015, **793**, 41
17. R. H. Crabtree, *J. Chem. Soc. Dalton Trans.*, 2001, (17), 2437
18. M. Albrecht, *Chem. Rev.*, 2010, **110**, (2), 576
19. J. Chatt and J. M. Davidson, *J. Chem. Soc.*, 1965, 843
20. R. H. Crabtree, "The Organometallic Chemistry of the Transition Metals", 5th Edn., John Wiley & Sons Inc, Hoboken, USA, 2009
21. P. W. N. M. van Leeuwen, "Homogeneous Catalysis: Understanding the Art", Kluwer Academic Publishers, Dordrecht, The Netherlands, 2004
22. J. A. Labinger, *Chem. Rev.*, 2016, **117**, (13), 8483
23. B. G. Hashiguchi, S. M. Bischof, M. M. Konnick and R. A. Periana, *Acc. Chem. Res.*, 2012, **45**, (6), 885
24. A. E. Shilov and G. B. Shul'pin, *Chem. Rev.*, 1997, **97**, (8), 2879
25. J. A. Labinger and J. E. Bercaw, *J. Organomet. Chem.*, 2015, **793**, 47
26. T. Zimmermann, M. Soorholtz, M. Bilke and F. Schüth, *J. Am. Chem. Soc.*, 2016, **138**, (38), 12395
27. J. He, M. Wasa, K. S. L. Chan, Q. Shao and J.-Q. Yu, *Chem. Rev.*, 2016, **117**, (13), 8754
28. Y.-F. Zhang, H.-W. Zhao, H. Wang, J.-B. Wei and Z.-J. Shi, *Angew. Chem. Int. Ed.*, 2015, **54**, (46), 13686
29. N. Kuhl, M. N. Hopkinson, J. Wencel-Delord and F. Glorius, *Angew. Chem. Int. Ed.*, 2012, **51**, (41), 10236
30. P. B. Arockiam, C. Bruneau and P. H. Dixneuf, *Chem. Rev.*, 2012, **112**, (11), 5879
31. J. A. Leitch and C. G. Frost, *Chem. Soc. Rev.*, 2017, **46**, (23), 7145
32. S. Warratz, D. J. Burns, C. Zhu, K. Korvorapun, T. Rogge, J. Scholz, C. Jooss, D. Gelman and L. Ackermann, *Angew. Chem. Int. Ed.*, 2017, **56**, (6), 1557
33. J. Thongpaen, R. Manguin, T. Kittikool, A. Camy, T. Roisnel, V. Dorcet, S. Yotphan, Y. Canac, M. Mauduit and O. Baslé, *Chem. Commun.*, 2022, **58**, (86), 12082
34. T. Piou, F. Romanov-Michailidis, M. Romanova-Michaelides, K. E. Jackson, N. Semakul, T. D. Taggart, B. S. Newell, C. D. Rithner, R. S. Paton and T. Rovis, *J. Am. Chem. Soc.*, 2020, **142**, (16), 7709
35. D. A. Colby, A. S. Tsai, R. G. Bergman and J. A. Ellman, *Acc. Chem. Res.*, 2012, **45**, (6), 814
36. D. A. Colby, R. G. Bergman and J. A. Ellman, *Chem. Rev.*, 2010, **110**, (2), 624
37. A. P. Walsh and W. D. Jones, *Organometallics*, 2015, **34**, (13), 3400
38. J. C. Lewis, R. G. Bergman and J. A. Ellman, *Acc. Chem. Res.*, 2008, **41**, (8), 1013
39. K. D. Hesp, R. G. Bergman and J. A. Ellman, *Org. Lett.*, 2012, **14**, (9), 2304
40. R. H. Crabtree, J. M. Mihelcic and J. M. Quirk, *J. Am. Chem. Soc.*, 1979, **101**, (26), 7738
41. R. H. Crabtree, M. F. Mellea, J. M. Mihelcic and J. M. Quirk, *J. Am. Chem. Soc.*, 1982, **104**, (1), 107
42. D. Baudry, M. Ephritikhine and H. Felkin, *J. Chem. Soc., Chem. Commun.*, 1980, (24), 1243
43. H. Felkin, T. Fillebeen-khan, R. Holmes-Smith and L. Yingrui, *Tetrahedron Lett.*, 1985, **26**, (16), 1999
44. A. S. Goldman and K. I. Goldberg, 'Organometallic C-H Bond Activation: An Introduction', in "Activation and Functionalization of C-H Bonds", eds. K. I. Goldberg and A. S. Goldman, ACS Symposium Series, ch. 1, Vol. 885, American Chemical Society, Washington, DC, USA, 2004, pp. 1-43
45. M. J. Burk and R. H. Crabtree, *J. Am. Chem. Soc.*, 1987, **109**, (26), 8025
46. K. Nomura and Y. Saito, *J. Chem. Soc., Chem. Commun.*, 1988, (3), 161
47. J. A. Maguire and A. S. Goldman, *J. Am. Chem. Soc.*, 1991, **113**, (17), 6706
48. K. I. Goldberg and A. S. Goldman, *Acc. Chem. Res.*, 2017, **50**, (3), 620
49. F. Liu, E. B. Pak, B. Singh, C. M. Jensen and A. S. Goldman, *J. Am. Chem. Soc.*, 1999, **121**, (16), 4086
50. A. Kumar, T. M. Bhatti and A. S. Goldman, *Chem. Rev.*, 2017, **117**, (19), 12357
51. A. S. Goldman, A. H. Roy, Z. Huang, R. Ahuja, W. Schinski and M. Brookhart, *Science*, 2006, **312**, (5771), 257
52. J. K. Hoyano and W. A. G. Graham, *J. Am. Chem. Soc.*, 1982, **104**, (13), 3723
53. A. H. Janowicz and R. G. Bergman, *J. Am. Chem. Soc.*, 1982, **104**, (1), 352
54. P. L. Watson, *J. Chem. Soc., Chem. Commun.*, 1983, (6), 276
55. W. D. Jones and F. J. Feher, *J. Am. Chem. Soc.*, 1984, **106**, (6), 1650
56. W. D. Jones and F. J. Feher, *Acc. Chem. Res.*, 1989, **22**, (3), 91

57. D. M. Haddleton and R. N. Perutz, *J. Chem. Soc., Chem. Commun.*, 1986, (23), 1734
58. D. M. Haddleton and R. N. Perutz, *J. Chem. Soc., Chem. Commun.*, 1985, (20), 1372
59. M. G. Partridge, A. McCamley and R. N. Perutz, *J. Chem. Soc., Dalt. Trans.*, 1994, (24), 3519
60. J. M. Blacquiere, *ACS Catal.*, 2021, **11**, (9), 5416
61. A. J. Hart-Davis and R. J. Mawby, *J. Chem. Soc. A*, 1969, 2403
62. T. Foo and R. G. Bergman, *Organometallics*, 1992, **11**, (5), 1801
63. V. B. Kharitonov, D. V. Muratov and D. A. Loginov, *Coord. Chem. Rev.*, 2019, **399**, 213027
64. N. Semakul, K. E. Jackson, R. S. Paton and T. Rovis, *Chem. Sci.*, 2017, **8**, (2), 1015
65. H. Butenschön, *Chem. Rev.*, 2000, **100**, (4), 1527
66. B. Royo and E. Peris, *Eur. J. Inorg. Chem.*, 2012, (9), 1309
67. F. Hanasaka, Y. Tanabe, K. Fujita and R. Yamaguchi, *Organometallics*, 2006, **25**, (4), 826
68. S. M. Mansell, *Dalton Trans.*, 2017, **46**, (44), 15157
69. S. R. Klei, T. D. Tilley and R. G. Bergman, *Organometallics*, 2002, **21**, (23), 4905
70. S. R. Klei, J. T. Golden, T. D. Tilley and R. G. Bergman, *J. Am. Chem. Soc.*, 2002, **124**, (10), 2092
71. L. Lefort, T. W. Crane, M. D. Farwell, D. M. Baruch, J. A. Kaeuper, R. J. Lachicotte and W. D. Jones, *Organometallics*, 1998, **17**, (18), 3889
72. A. Pontes da Costa, M. Viciano, M. Sanaú, S. Merino, J. Tejada, E. Peris and B. Royo, *Organometallics*, 2008, **27**, (6), 1305
73. S. P. Downing and A. A. Danopoulos, *Organometallics*, 2006, **25**, (6), 1337
74. S. P. Downing, P. J. Pogorzelec, A. A. Danopoulos and D. J. Cole-Hamilton, *Eur. J. Inorg. Chem.*, 2009, (13), 1816
75. S. Trofimenko, *Chem. Rev.*, 1993, **93**, (3), 943
76. Y. Jiao, J. Morris, W. W. Brennessel and W. D. Jones, *J. Am. Chem. Soc.*, 2013, **135**, (43), 16198
77. D. D. Wick, T. O. Northcutt, R. J. Lachicotte and W. D. Jones, *Organometallics*, 1998, **17**, (20), 4484
78. W. D. Jones and E. T. Hessell, *J. Am. Chem. Soc.*, 1993, **115**, (2), 554
79. S. E. Bromberg, H. Yang, M. C. Asplund, T. Lian, B. K. McNamara, K. T. Kotz, J. S. Yeston, M. Wilkens, H. Frei, R. G. Bergman and C. B. Harris, *Science*, 1997, **278**, (5336), 260
80. M. C. Asplund, P. T. Snee, J. S. Yeston, M. J. Wilkens, C. K. Payne, H. Yang, K. T. Kotz, H. Frei, R. G. Bergman and C. B. Harris, *J. Am. Chem. Soc.*, 2002, **124**, (35), 10605
81. J. Guan, A. Wriglesworth, X. Z. Sun, E. N. Brothers, S. D. Zarić, M. E. Evans, W. D. Jones, M. Towrie, M. B. Hall and M. W. George, *J. Am. Chem. Soc.*, 2018, **140**, (5), 1842
82. I. A. I. Mkhaliid, J. H. Barnard, T. B. Marder, J. M. Murphy and J. F. Hartwig, *Chem. Rev.*, 2010, **110**, (2), 890
83. E. C. Neeve, S. J. Geier, I. A. I. Mkhaliid, S. A. Westcott and T. B. Marder, *Chem. Rev.*, 2016, **116**, (16), 9091
84. J. F. Hartwig, K. S. Cook, M. Hapke, C. D. Incarvito, Y. Fan, C. E. Webster and M. B. Hall, *J. Am. Chem. Soc.*, 2005, **127**, (8), 2538
85. J. Adams and M. Kauffman, *Cancer Invest.*, 2004, **22**, (2), 304
86. J. F. Hartwig, *Acc. Chem. Res.*, 2011, **45**, (6), 864
87. K. M. Waltz and J. F. Hartwig, *Science*, 1997, **277**, (5323), 211
88. K. M. Waltz, X. He, C. Muhoro and J. F. Hartwig, *J. Am. Chem. Soc.*, 1995, **117**, (45), 11357
89. C. N. Iverson and M. R. Smith, *J. Am. Chem. Soc.*, 1999, **121**, (33), 7696
90. J.-Y. Cho, C. N. Iverson and M. R. Smith, *J. Am. Chem. Soc.*, 2000, **122**, (51), 12868
91. H. Chen, S. Schlecht, T. C. Semple and J. F. Hartwig, *Science*, 2000, **287**, (5460), 1995
92. T. Ishiyama, J. Takagi, K. Ishida, N. Miyaoura, N. R. Anastasi and J. F. Hartwig, *J. Am. Chem. Soc.*, 2002, **124**, (3), 390
93. L. Xu, G. Wang, S. Zhang, H. Wang, L. Wang, L. Liu, J. Jiao and P. Li, *Tetrahedron*, 2017, **73**, (51), 7123
94. A. J. Lyons, A. Clarke, H. Fisk, B. Jackson, P. R. Moore, S. Oke, T. O. Ronson and R. E. Meadows, *Org. Process Res. Dev.*, 2022, **26**, (5), 1378
95. T. Furukawa, M. Tobisu and N. Chatani, *J. Am. Chem. Soc.*, 2015, **137**, (38), 12211
96. M. A. Larsen, R. J. Oeschger and J. F. Hartwig, *ACS Catal.*, 2020, **10**, (5), 3415
97. M. A. Larsen and J. F. Hartwig, *J. Am. Chem. Soc.*, 2014, **136**, (11), 4287
98. J. Hu, J. Lv and Z. Shi, *Trends Chem.*, 2022, **4**, (8), 685
99. R. Bisht, C. Haldar, M. M. M. Hassan, M. E. Hoque, J. Chaturvedi and B. Chattopadhyay, *Chem. Soc. Rev.*, 2022, **51**, (12), 5042
100. R. Oeschger, B. Su, I. Yu, C. Ehinger, E. Romero, S. He and J. Hartwig, *Science*, 2020, **368**, (6492), 736

101. M. R. Jones, C. D. Fast and N. D. Schley, *J. Am. Chem. Soc.*, 2020, **142**, (14), 6488
102. K. J. Evans, P. A. Morton, C. Luz, C. Miller, O. Raine, J. M. Lynam and S. M. Mansell, *Chem. Eur. J.*, 2021, **27**, (71), 17824
103. K. T. Smith, S. Berritt, M. González-Moreiras, S. Ahn, M. R. Smith, M.-H. Baik and D. J. Mindiola, *Science*, 2016, **351**, (6280), 1424
104. S. Ahn, D. Sorsche, S. Berritt, M. R. Gau, D. J. Mindiola and M.-H. Baik, *ACS Catal.*, 2018, **8**, (11), 10021
105. O. Staples, M. S. Ferrandon, G. P. Laurent, U. Kanbur, A. J. Kropf, M. R. Gau, P. J. Carroll, K. McCullough, D. Sorsche, F. A. Perras, M. Delferro, D. M. Kaphan and D. J. Mindiola, *J. Am. Chem. Soc.*, 2023, **145**, (14), 7992
106. P. Gandeepan, T. Müller, D. Zell, G. Cera, S. Warratz and L. Ackermann, *Chem. Rev.*, 2019, **119**, (4), 2192
107. C. V. Craescu, M. J. Schubach, S. Huss and E. Elacqua, *Trends Chem.*, 2021, **3**, (8), 686
108. A. Shamsabadi and V. Chudasama, *Org. Biomol. Chem.*, 2019, **17**, (11), 2865

---

## The Authors



Paul Morton is currently a PhD student at Heriot-Watt University, UK, under the supervision of Stephen Mansell. His research interests focus on the development of unconventional tethered-NHC rhodium complexes, as well as the synthesis of other non-tethered NHC rhodium systems. These complexes are applied to catalytic C–H functionalisation reactions, particularly C–H borylation.



Stephen Mansell is an Assistant Professor in the Institute of Chemical Sciences at Heriot-Watt University. The research interests of the Mansell group focus on harnessing main group and transition metal chemistry in unison in order to develop better catalysts. Specific targets include the application of transition metal phosphinine complexes as catalysts for hydrogen atom processes (hydrogen borrowing, acceptorless dehydrogenation) and rhodium NHC complexes for C–H bond activation and borylation.

# Electrochemical Synthesis of Monodisperse Platinum-Cobalt Nanocrystals

**Minimising environmental impact and increasing commercial viability**

## Daniel J. Rosen, Duncan Zavanelli

Department of Materials Science and Engineering, University of Pennsylvania, Philadelphia, USA

## Christopher B. Murray\*

Department of Materials Science and Engineering and Department of Chemistry, University of Pennsylvania, Philadelphia, USA

\*Email: [cbmurray@sas.upenn.edu](mailto:cbmurray@sas.upenn.edu)

### PEER REVIEWED

Received 30th November 2022; Revised 6th February 2023; Accepted 3rd March 2023; Online 28th March 2023

The synthesis of platinum-cobalt nanocrystals (NCs) using colloidal solvothermal techniques is well understood. However, for monodisperse NCs to form, high temperatures and environmentally detrimental solvents are needed. We report a room temperature, aqueous method of platinum-cobalt NC synthesis using electrochemical reduction as the driving force for nucleation and growth. It is found that colloidal NCs will form in both the presence and absence of surfactant. Additionally, we report a monodisperse electrochemical deposition of NCs utilising a transparent conducting oxide electrode. The methods developed here will allow for a synthetic method to produce nanocatalysts with minimal environmental impact and should be readily applicable to other NC systems, including single- and multi-component alloys.

## 1. Introduction

Platinum group metals (pgms) as NCs are widely studied for many applications, including spectroscopy (1–5), biology (6–8) and catalysis (9–15). Specifically of interest in catalysis is using NCs containing elements in addition to the pgms to reduce the amount of precious metal needed in the system. The use of solvothermally synthesised platinum-cobalt NCs to catalyse the electrochemical oxygen reduction reaction (ORR) is well reported as a method of providing high activity while minimising the precious metal loading of the catalyst (1, 16–20). However, many of the reports that propose these systems for use as cathode material in proton exchange membrane fuel cells (PEMFCs) (21, 22) utilise high-temperature reactions of up to 300°C and environmentally unfriendly solvents (1, 16, 20). Additionally, many of the chemicals typically used in the solvothermal colloidal synthesis are hazardous, and often require specialised and costly equipment for storage and handling like a glovebox; these include, for example, oleylamine, trioctylphosphine and cobalt(0) pentacarbonyl. For PEMFCs (23) to act as a viable, clean source of energy, as many steps of production as possible must follow proper green chemistry principles (24) and minimise potential hazards. Many reports have discussed methods to produce NCs following green methods; however, these often lack uniformity in size and morphology (25–31). In this report, we demonstrate a room temperature, aqueous synthesis of near monodisperse platinum-cobalt NCs using green electrochemical methods.



Electrochemical methods for the synthesis of single-component NC systems are well understood (27, 29, 31–45), and bimetallic NC systems are currently being investigated in the literature (27, 46–51). However, to the best of our knowledge, these systems lack uniformity in shape, size and composition (8, 27, 46–49, 51). In this report, we describe an electrochemical method capable of producing highly monodisperse and colloidally stable, sub-5 nm platinum-cobalt alloy NCs, which are catalytically superior in activity compared to pure platinum NCs (16, 20). The ability to produce NCs through green chemistry methods is key to being able to synthesise nanocatalysts with minimal environmental impact and at a lower cost. By creating more uniform species, we allow for the NCs to maintain a higher catalytic surface area and for a more uniform morphology of the NCs to be studied.

## 2. Methods

To perform the desired electrochemical synthesis of the alloy NCs, procedures were developed through the modification of previously reported methods (31, 37, 51). An overview of the synthetic

procedure is shown in **Figure 1**. As shown in **Figure 1(a)**, 60 mM of dimethylformamide (DMF) is added to the aqueous solution containing both the precious metal precursor and the cobalt precursor. A complete list of materials is included in Supporting Information Section S1. As seen in **Figure 1(b)**, the potential cycle taken to undergo the synthesis involves one high potential segment allowing for nucleation, followed by a milder hold segment at  $-500$  mV to allow for NC growth. The difference in reduction potential between the cobalt and platinum precursors can be overcome through the addition of small amounts of DMF, which selectively coordinates to the platinum surfaces allowing for the standard reduction potential of the platinum species ( $-730$  mV vs. RHE) to approach that of cobalt ( $-280$  mV vs. RHE) by nearly 200 mV (51). By briefly holding the electrolyte solution at  $-650$  mV, the reduction potential of both species is surpassed, allowing for the reduction of the ionic species and subsequent nucleation.

**Figure 1(c)** shows that the electrolyte solution takes on an orange hue before synthesis occurs. The electrolyte solution is magnetically stirred at 300 rpm during the electrochemical synthesis to avoid any concentration gradients in the electrolyte solution or

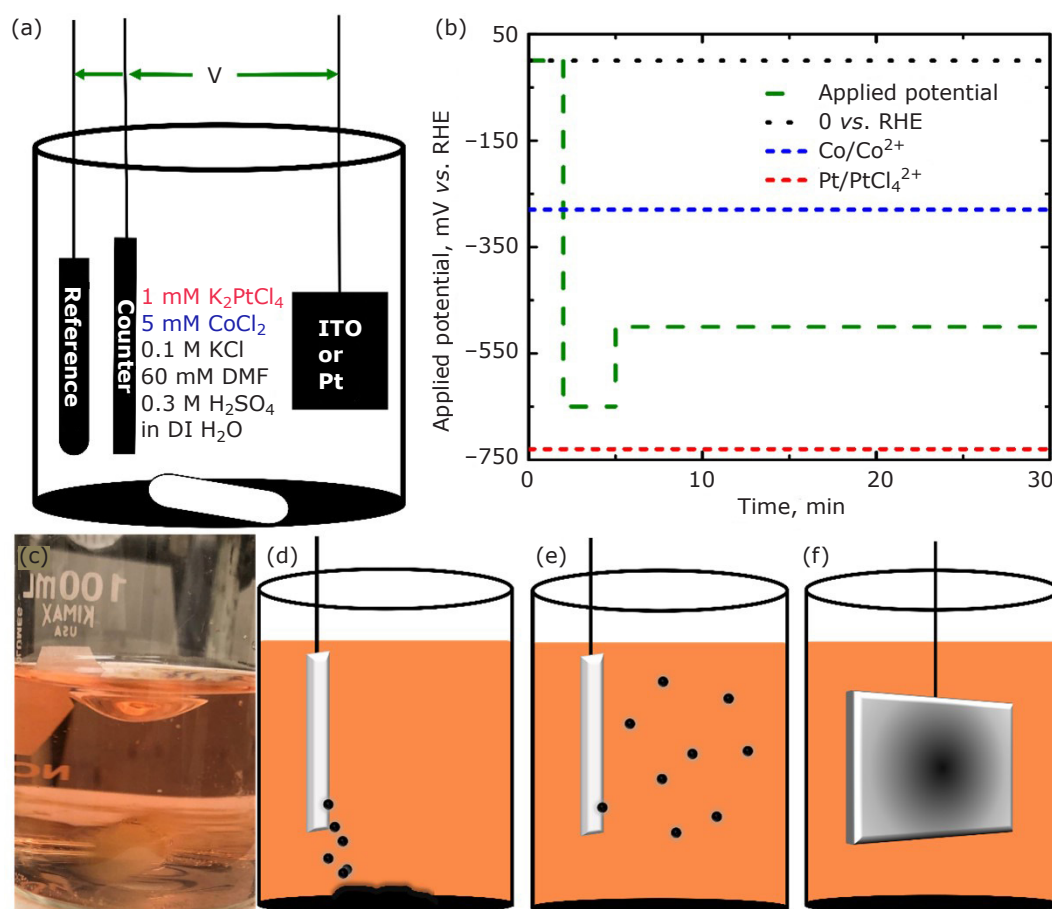


Fig. 1. (a) Schematic representation of reaction; (b) plot of potential cycle used for electrochemical synthesis, including lines for the standard reduction potential of both precursors; (c) image of starting electrochemical solution. Schematic representations of synthesis involving: (d) platinum working electrode with no surfactant; (e) platinum working electrode with a surfactant; and (f) ITO working electrode with no surfactant

overpotential barriers. Additionally, the electrolyte solution is purged with nitrogen before the reaction to minimise the effects of trace gas compounds that may be present and affect the reaction. The currents obtained during synthesis are shown in Figure S1 in the Supporting Information and demonstrate that our method of constant potential electrolysis for synthesis causes no unexpected variations in current density, but instead produces a uniform current throughout the synthetic process.

As stated in **Figure 1(a)** and shown in **Figure 1(d)–1(f)**, the working electrode used is either a platinum wire or a transparent conducting oxide (TCO) layer of indium tin oxide (ITO) on a glass substrate. For the cases of the platinum wire working electrode, we explore both syntheses without a surfactant (**Figure 1(d)**) and with the addition of 100 mM cetyltrimethylammonium bromide (CTAB) as a surfactant (**Figure 1(e)**). Without surfactant, the NCs do not aggregate, likely due to ionic stabilisation. We show that CTAB acts as a stabilising ligand during the reaction, allowing for colloidally stable NCs. In **Figure 1(f)**, the case of an ITO working electrode is shown, without the presence of surfactant, yielding a NC coating on the electrode. This case was tested without the presence of a surfactant to allow electrodeposition to occur onto the TCO layer.

### 3. Results and Discussion

We can compare the synthetic results of the platinum-cobalt alloy NCs formed in the cases shown in **Figure 1(d)–1(f)**; these include electrochemical synthesis without a stabilising agent, electrochemical synthesis with a stabilising agent and electrochemical deposition directly onto the electrode surface, respectively. We quantitatively compare monodispersity through size distribution from transmission electron microscopy (TEM), while a qualitative comparison is possible through the observation of change in the electrolytic solution. As shown in **Figure 2(c)**, the electrolyte solution begins as a transparent orange solution; as shown in Figure S3 in the Supporting Information, while the electrolyte solution with CTAB present is the same hue but cloudy due to the addition of a surfactant. **Figure 2** shows the results of electrochemical synthesis both without (**Figure 2(a)** and **2(b)**) and with (**Figure 2(c)** and **2(d)**) CTAB.

From **Figure 2(a)**, when lacking the presence of a surfactant, the NCs are unable to form a stable colloidal suspension. The NCs, as shown in

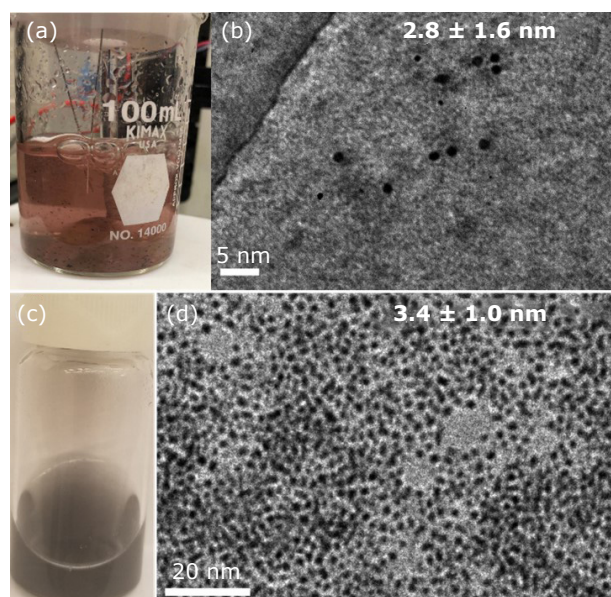


Fig. 2. Results of electrochemical synthesis without CTAB are shown in: (a) electrolytic solution after synthesis; and (b) TEM of NCs after synthesis. Results with CTAB are shown in: (c) electrolytic solution after synthesis; and (d) TEM of NCs after synthesis

**Figure 2(b)**, can also be seen to be sparse in the colloidal solution and not well-formed; the crystals have a dispersion of approximately 57%. In contrast, when the CTAB is added as a stabilising agent, the NCs form a stable, dilute, colloidal solution, as shown in **Figure 2(c)**. This signifies that the CTAB is not only able to act as a surfactant but also acts in the reaction as the ligand species. By having a stabilising ligand present during the reaction, we can produce NCs with a significantly higher level of monodispersity than previously reported in the literature (31, 47, 48, 51). As shown in **Figure 2(d)**, the NCs display a uniform spherical morphology, with a dispersion of approximately 29%. This demonstrates that the addition of stabilising ligands into the electrochemical solution before potential onset provides NCs with nearly double the monodispersity of NCs formed without CTAB.

In addition to the NCs produced through direct electrochemical synthesis, we tested the applicability of this synthetic method to electrodeposition. Electrodeposition provides the additional benefit of forming the NCs directly onto a useful substrate without the need for additional purification and transfer steps. In this work, we use ITO as a TCO electrode in place of the platinum working electrode used in electrosynthesis. This can be seen in **Figure 1(a)** and **1(f)**. The results obtained are summarised in **Figure 3**.

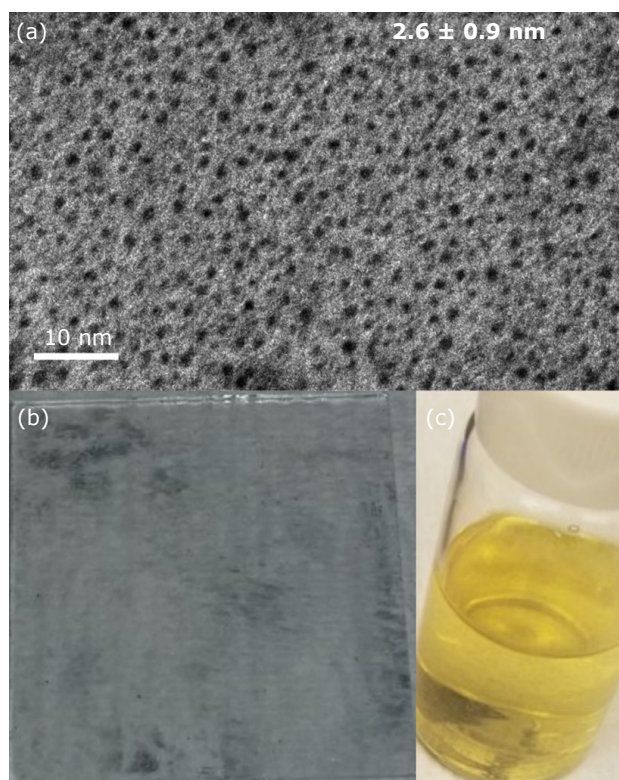


Fig. 3. (a) TEM of platinum-cobalt NCs after electrodeposition; (b) ITO slide with NCs deposited; (c) electrolytic solution after electrodeposition

As seen in **Figure 3(a)**, the NCs are smaller through electrodeposition than those formed through electrosynthesis, which is beneficial to catalytic purposes where a high surface area is desirable. However, at 35%, the dispersion of the NCs is higher than the NCs synthesised using CTAB. Again, we attribute this to the increase in the uniformity of the NCs provided by a stabilising ligand. The ITO slide after deposition, as shown in **Figure 3(b)**, indicates that while not completely uniform, the NCs can form a layer directly on the ITO slide. This, in combination with the colour change in the electrolytic solution from orange to yellow seen in **Figure 3(c)**, indicated that NCs were able to form and that the precursors used had been removed from the electrolytic solution during the deposition, indicating NCs formed with both platinum and cobalt, as neither forms a yellow solution individually. We attribute this to the synthesis of bimetallic NCs. To confirm that this is the case, we characterise the samples as shown in **Figure 4**. For this characterisation, we focus on the sample with the greatest synthetic uniformity: the electrosynthetic samples formed with CTAB as a stabilising agent.

From **Figure 4(a)**, we can see diffraction peaks indicative of the random alloy face-centered-

cubic crystal phase of platinum-cobalt NCs. These peaks are in correspondence to previous reports on this alloy (16, 20). The large background peak around  $43^\circ 2\theta$  is believed to be due to either stacking faults in the NCs, or some existence of a pure cobalt phase. No major peaks indicative of either pure platinum or cobalt are observed, implying no significant phase segregation during the synthesis. In the high-resolution scanning transmission electron microscopy (STEM) micrograph in **Figure 4(b)**, a face-centered cubic (fcc) lattice is observed, which is in correspondence with the crystal structure of the alloy NCs. This is also seen in **Figure 4(c)–4(d)**, which shows individual particle-resolved STEM micrographs. These micrographs show lattice correspondence to a fcc A1 crystal phase (16, 18, 20). A bimetallic structure is again observed in **Figure 4(g)** through energy dispersive spectroscopy (EDS), where the cobalt and platinum are uniform throughout the NCs. This implies that the NCs are indeed uniform alloys and do not suffer from any phase segregation. The presence of both platinum and cobalt on a larger scale at a near 1:1 ratio can be seen in the EDS spectra in Figure S2 in the Supporting Information.

#### 4. Conclusion

We have shown a green electrochemical method of NC synthesis capable of producing more uniform bimetallic alloy platinum-cobalt NCs than previously reported. The ability to synthesise catalytically relevant materials such as platinum-cobalt under green conditions is vital to ensure that in the process of producing catalysts to perform environmentally conscious tasks, we do not create harmful byproducts such as significant energy consumption to reach high temperatures or the release of harmful solvents into the environment. By producing small uniform NCs, we pave the way for pgm catalysts to be more economically viable to act as catalysts for applications such as PEMFCs. We believe that this method of NC synthesis will be readily applicable to many systems, allowing for green catalyst production for various applications. Through the understanding of electrochemical synthesis for both a direct synthesis method and an electrodeposition method, this work can be applied to systems where the catalyst can be directly electro-impregnated onto a support material. Through direct catalytic impregnation under green conditions, the methodology developed here will increase the commercial viability of pgm NCs for catalytic applications.



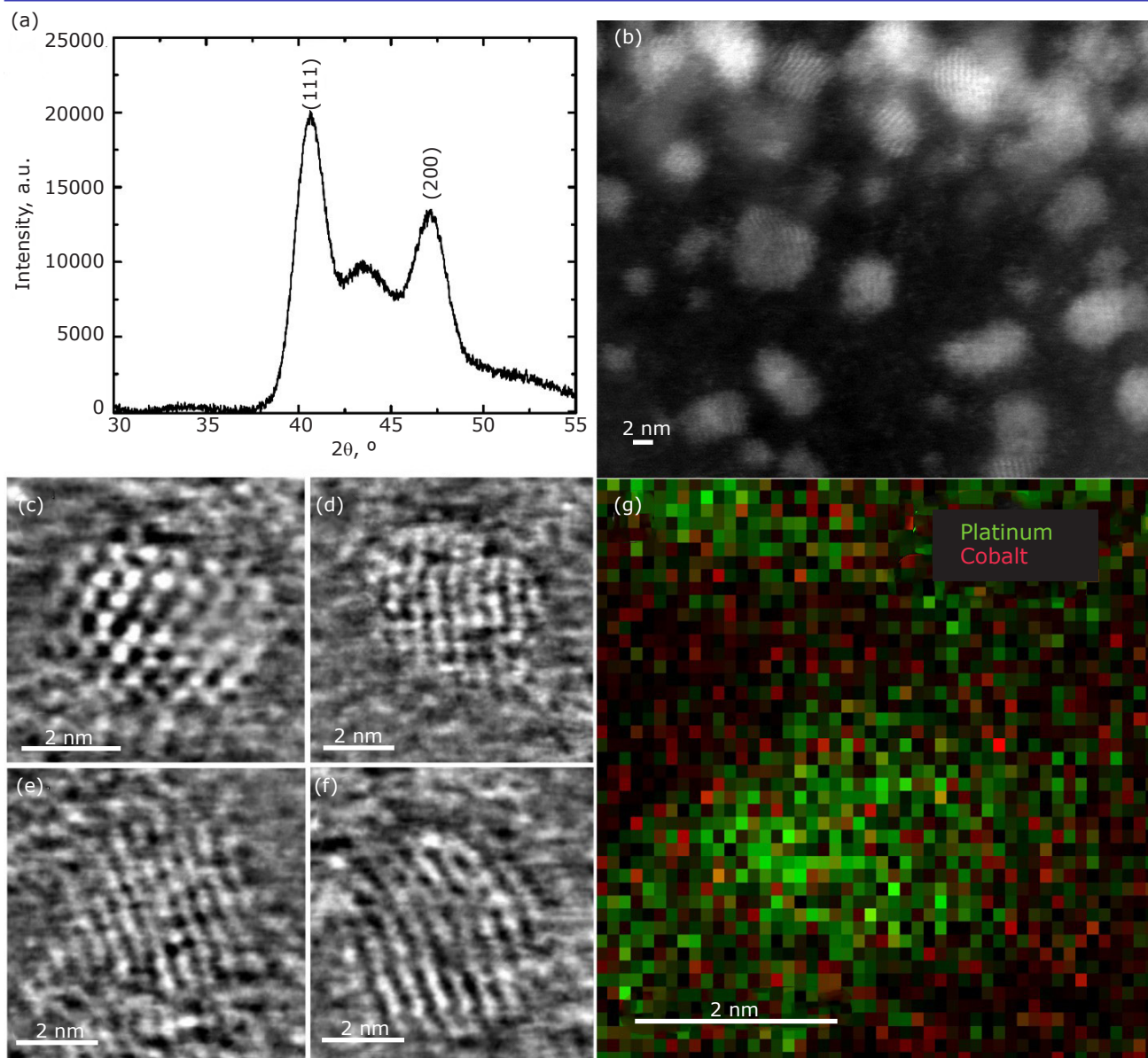


Fig. 4. (a) X-ray diffraction spectrum of electrosynthesised platinum-cobalt alloy NCs; (b) high-resolution STEM of platinum-cobalt alloy NCs; (c)–(f) Fourier filtered high-resolution STEM single particle imaging; (g) EDS of region shown in Figure S5 in the Supporting Information

### Glossary

CTAB	cetyltrimethylammonium bromide	PEMFC	proton exchange membrane fuel cell
DMF	dimethylformamide	pgm	platinum group metal
EDS	energy dispersive spectroscopy	RHE	reversible hydrogen electrode
ITO	indium tin oxide	STEM	scanning transmission electron microscopy
NC	nanocrystal	TCO	transparent conducting oxide
ORR	oxygen reduction reaction	TEM	transmission electron microscopy

## Acknowledgments

The authors acknowledge primary support from the Catalysis Center for Energy Innovation, an Energy Frontier Research Center funded by the US Department of Energy, Office of Science, Office of Basic Energy Sciences under Award No. DE-SC0001004. Daniel Rosen acknowledges support from the Vagelos Institute for Energy Science and Technology Fellowship Program. The authors acknowledge support from Johnson Matthey for Platinum Group Metal Award Scheme pgmAS34. Christopher Murray acknowledges the Richard Perry University Professorship at the University of Pennsylvania. This work was carried out in part at the Singh Center for Nanotechnology, which is supported by the NSF National Nanotechnology Coordinated Infrastructure Program under grant NNCI-2025608. Additional support to the Nanoscale Characterization Facility at the Singh Center has been provided by the Laboratory for Research on the Structure of Matter (MRSEC) supported by the National Science Foundation (DMR-1720530).

## Conflict of Interest

The authors declare no conflict of interest.

## References

1. A. C. Foucher, N. Marcella, J. D. Lee, D. J. Rosen, R. Tapper, C. B. Murray, A. I. Frenkel and E. A. Stach, *ACS Nano*, 2021, **15**, (12), 20619
2. D. J. Rosen, S. Yang, E. Marino, Z. Jiang and C. B. Murray, *J. Phys. Chem. C*, 2022, **126**, (7), 3623
3. A. Espinosa, G. R. Castro, J. Reguera, C. Castellano, J. Castillo, J. Camarero, C. Wilhelm, M. A. García and Á. Muñoz-Noval, *Nano Lett.*, 2021, **21**, (1), 769
4. X. Yin, M. Shi, J. Wu, Y.-T. Pan, D. L. Gray, J. A. Bertke and H. Yang, *Nano Lett.*, 2017, **17**, (10), 6146
5. B. T. Diroll, T. Dadosh, A. Koschitzky, Y. E. Goldman and C. B. Murray, *J. Phys. Chem. C*, 2013, **117**, (45), 23928
6. T. Geninatti, G. Bruno, B. Barile, R. L. Hood, M. Farina, J. Schmulen, G. Canavese and A. Grattoni, *Biomed. Microdevices*, 2015, **17**, (1), 24
7. K. Yan, F. Xu, W. Wei, C. Yang, D. Wang and X. Shi, *Colloids Surf. B: Biointerfaces*, 2021, **202**, 111711
8. P. Pandey, S. Merwyn, G. S. Agarwal, B. K. Tripathi and S. C. Pant, *J. Nanopart. Res.*, 2012, **14**, 709
9. S. Zhang, Y. Hao, D. Su, V. V. T. Doan-Nguyen, Y. Wu, J. Li, S. Sun and C. B. Murray, *J. Am. Chem. Soc.*, 2014, **136**, (45), 15921
10. M. Cargnello, D. Sala, C. Chen, M. D'Arienzo, R. J. Gorte and C. B. Murray, *RSC Adv.*, 2015, **5**, (52), 41920
11. M. Cargnello, V. V. T. Doan-Nguyen, T. R. Gordon, R. E. Diaz, E. A. Stach, R. J. Gorte, P. Fornasiero and C. B. Murray, *Science*, 2013, **341**, (6147), 771
12. C. Wang, J. Luo, V. Liao, J. D. Lee, T. M. Onn, C. B. Murray and R. J. Gorte, *Catal. Today*, 2018, **302**, 73
13. A. C. Foucher, S. Yang, D. J. Rosen, J. D. Lee, R. Huang, Z. Jiang, F. G. Barrera, K. Chen, G. G. Hollyer, C. M. Friend, R. J. Gorte, C. B. Murray and E. A. Stach, *J. Am. Chem. Soc.*, 2022, **144**, (17), 7919
14. Y. Kang, M. Li, Y. Cai, M. Cargnello, R. E. Diaz, T. R. Gordon, N. L. Wieder, R. R. Adzic, R. J. Gorte, E. A. Stach and C. B. Murray, *J. Am. Chem. Soc.*, 2013, **135**, (7), 2741
15. J. Luo, J. D. Lee, H. Yun, C. Wang, M. Monai, C. B. Murray, P. Fornasiero and R. J. Gorte, *Appl. Catal. B: Environ.*, 2016, **199**, 439
16. J. D. Lee, D. Jishkariani, Y. Zhao, S. Najmr, D. Rosen, J. M. Kikkawa, E. A. Stach and C. B. Murray, *ACS Appl. Mater. Interfaces*, 2019, **11**, (30), 26789
17. S. Wang, W. Xu, Y. Zhu, Q. Luo, C. Zhang, S. Tang and Y. Du, *ACS Appl. Mater. Interfaces*, 2021, **13**, (1), 827
18. D. Wang, H. L. Xin, R. Hovden, H. Wang, Y. Yu, D. A. Muller, F. J. DiSalvo and H. D. Abruña, *Nature Mater.*, 2013, **12**, (1), 81
19. R. Lin, T. Zheng, L. Chen, H. Wang, X. Cai, Y. Sun and Z. Hao, *ACS Appl. Mater. Interfaces*, 2021, **13**, (29), 34397
20. D. J. Rosen, A. C. Foucher, J. D. Lee, S. Yang, E. Marino, E. A. Stach and C. B. Murray, *ACS Mater. Lett.*, 2022, **4**, (5), 823
21. M. Liu, X. Xiao, Q. Li, L. Luo, M. Ding, B. Zhang, Y. Li, J. Zou and B. Jiang, *J. Colloid Interface Sci.*, 2022, **607**, (1), 791
22. P. Gao, M. Pu, Q. Chen and H. Zhu, *Catalysts*, 2021, **11**, (9), 1050
23. M. M. Whiston, I. L. Azevedo, S. Litster, K. S. Whitefoot, C. Samaras and J. F. Whitacre, *Proc. Natl. Acad. Sci. USA*, 2019, **116**, (11), 4899
24. P. T. Anastas and J. B. Zimmerman, *Environ. Sci. Technol.*, 2003, **37**, (5), 94A
25. S. Terada, H. Ueda, T. Ono and K. Saitow, *ACS Sustain. Chem. Eng.*, 2022, **10**, (5), 1765
26. Y.-W. Peng, C.-P. Wang, G. Kumar, P.-L. Hsieh, C.-M. Hsieh and M. H. Huang, *ACS Sustain. Chem. Eng.*, 2022, **10**, (4), 1578



27. A. Ahmed and S. Arya, 'Green Synthesis of Nanomaterials via Electrochemical Method', in "Advances in Green Synthesis", eds. Inamuddin, R. Boddula, M. I. Ahamed and A. Khan, *Advances in Science, Technology & Innovation*, Springer, Cham, Switzerland, 2021, pp. 205–216
28. N. Arshi, F. Ahmed, M. S. Anwar, S. Kumar, B. H. Koo, J. Lu and C. G. Lee, *Nano*, 2011, **6**, (4), 295
29. M. N. Groves, C. Malardier-Jugroot and M. Jugroot, *Chem. Phys. Lett.*, 2014, **612**, 309
30. S. P. Nayak, L. K. Ventrapragada, S. S. Ramamurthy, J. K. Kiran Kumar and A. M. Rao, *Nano Energy*, 2022, **94**, 106966
31. P. Yu, Q. Qian, X. Wang, H. Cheng, T. Ohsaka and L. Mao, *J. Mater. Chem.*, 2010, **20**, (28), 5820
32. C.-J. Huang, Y.-H. Wang, P.-H. Chiu, M.-C. Shih and T.-H. Meen, *Mater. Lett.*, 2006, **60**, (15), 1896
33. C.-J. Huang, P.-H. Chiu, Y.-H. Wang and C.-F. Yang, *J. Colloid Interface Sci.*, 2006, **303**, (2), 430
34. M. K. Rabinal, M. N. Kalasad, K. Praveenkumar, V. R. Bharadi and A. M. Bhikshavartimath, *J. Alloys Compd.*, 2013, **562**, 43
35. Q.-S. Chen, Z.-N. Xu, S.-Y. Peng, Y.-M. Chen, D.-M. Lv, Z.-Q. Wang, J. Sun and G.-C. Guo, *J. Power Sources*, 2015, **282**, 471
36. V. V. Yanilkin, G. R. Nasretdinova, Y. N. Osin and V. V. Salnikov, *Electrochim. Acta*, 2015, **168**, 82
37. G. R. Nasretdinova, Y. N. Osin, A. T. Gubaidullin and V. V. Yanilkin, *J. Electrochem. Soc.*, 2016, **163**, (8), G99
38. D.-W. Chou, C.-J. Huang and N.-H. Liu, *J. Electrochem. Soc.*, 2016, **163**, (10), D603
39. V. V. Yanilkin, N. V. Nastapova, G. R. Nasretdinova, R. R. Fazleeva and Y. N. Osin, *Electrochem. Commun.*, 2016, **69**, 36
40. M. Hasan, W. Khunsin, C. K. Mavrokefalos, S. A. Maier, J. F. Rohan and J. S. Foord, *ChemElectroChem*, 2018, **5**, (4), 619
41. Y.-Y. Yu, S.-S. Chang, C.-L. Lee and C. R. C. Wang, *J. Phys. Chem. B*, 1997, **101**, (34), 6661
42. S. Huang, H. Ma, X. Zhang, F. Yong, X. Feng, W. Pan, X. Wang, Y. Wang and S. Chen, *J. Phys. Chem. B*, 2005, **109**, (42), 19823
43. W. Pan, X. Zhang, H. Ma and J. Zhang, *J. Phys. Chem. C*, 2008, **112**, (7), 2456
44. N. Vilar-Vidal, M. C. Blanco, M. A. López-Quintela, J. Rivas and C. Serra, *J. Phys. Chem. C*, 2010, **114**, (38), 15924
45. O. A. Petrii, *Russ. Chem. Rev.*, 2015, **84**, (2), 159
46. Z. Wang, C. Li, K. Deng, Y. Xu, H. Xue, X. Li, L. Wang and H. Wang, *ACS Sustain. Chem. Eng.*, 2019, **7**, (2), 2400
47. A. L. Querejeta, M. C. del Barrio and S. G. García, *J. Electroanal. Chem.*, 2016, **778**, 98
48. G. R. Nasretdinova, R. R. Fazleeva, Y. N. Osin, V. G. Evtjugin, A. T. Gubaidullin, A. Y. Ziganshina and V. V. Yanilkin, *Electrochim. Acta*, 2018, **285**, 149
49. C. Garcia, P. Lecante, B. Warot-Fonrose, D. Neumeyer and M. Verelst, *Mater. Lett.*, 2008, **62**, (14), 2106
50. M. T. Reetz and W. Helbig, *J. Am. Chem. Soc.*, 1994, **116**, (16), 7401
51. S. Shen, F. Li, L. Luo, Y. Guo, X. Yan, C. Ke and J. Zhang, *J. Electrochem. Soc.*, 2018, **165**, (2), D43

## The Authors



Daniel Rosen is a PhD Candidate in the Christopher B. Murray Group at the University of Pennsylvania, USA. His work focuses on the synthesis and properties of transition metal NCs with a particular emphasis on the role of platinum group metals in catalysis. Previously, he obtained his bachelor's degrees in Physics and Applied Mathematics from Shippensburg University of Pennsylvania, USA.



Duncan Zavenelli recently graduated from the University of Pennsylvania with his bachelor's degree in Materials Science and Engineering. While at the University of Pennsylvania, he focused on novel synthetic routes for NC synthesis under the supervision of Christopher B. Murray. He is now a PhD Candidate at Northwestern University, USA, where he works in the group of G. Jeffery Snyder on the microstructure and interfaces of thermoelectric materials.



Christopher B. Murray is the Richard Perry University Professor of Chemistry and Materials Science and Engineering at the University of Pennsylvania. His expertise is in synthesis, characterisation and self-assembly of monodisperse NCs. Before coming to the University of Pennsylvania, he obtained his PhD in Physical Chemistry at Massachusetts Institute of Technology (MIT), USA, and served as Manager of the Nanoscale Materials and Devices Department at the Thomas J. Watson Research Center, IBM Corp, USA.

---

# “Practical Guidelines for the Chemical Industry: Operation, Processes, and Sustainability in Modern Facilities”

**By Kiran R. Golwalker (Consulting Chemical Engineer, India) and Rashmi Kumar (Dwarkadas J. Sanghvi College of Engineering, India), Springer Nature Switzerland AG, 2022, 297 pp, ISBN: 978-3-030-96580-8, £109.99, €126.72, US\$137.27**

## Reviewed by Mahmud Juned

Johnson Matthey, Pimlico Industrial Area, West Bradford Road, Clitheroe, BB7 4QB, UK

Email: [mahmud.juned1@matthey.com](mailto:mahmud.juned1@matthey.com)

## NON-PEER REVIEWED FEATURE

Received 17th April 2023; Online 14th June 2023

## Introduction

This book is a body of work to give insight to designers, technicians and production-based engineers working in the chemical industry as well as some general guidelines for safe and efficient running of chemical plants. There are specific guidelines on operational equipment including the use of pressure vessels, appropriate materials of construction and efficient handling of process fluids.

The authors are both located in India. Golwalker is a consultant chemical engineer working in private practice and has had much experience commissioning chemical plant in India, Kenya, Thailand and Indonesia. Kumar has experience from a long teaching career of around 25 years and is now an Assistant Professor of Chemical

Engineering at the D. J. Sanghvi College of Engineering in Mumbai, India.

## Overview of Chapters

The book is split into nine chapters. The structure of the book is convenient for those with little knowledge and for non-specialists in chemical engineering. The order of the subjects suggests that safety is understood to be a high priority as it shows up early in the guidelines. Furthermore, the order of the chapters would generally be the direction and format one would use when designing equipment or sections of a chemical plant.

Each chapter has an introduction and some examples to give the reader a good insight into best practice. A brief description on what each category involves is provided below. It is to note that there are references for further reading if one would like to find out more around certain sections which is especially useful.

## Chapter 1: Management Functions

Management functions cover a wide set of roles and activities in the chemical industry. The range of functions include how to be successful in management, marketing, surveying, procurement, planning, commissioning, delivery and maintenance.

The chapter covers general steps that one would look to take to be able to manage a chemical plant or commission a new one, such as process selections and how to utilise research and development.

## **Chapter 2: HAZID, HAZOP and Ensuring Safety**

This could easily be one of the most important sections of the book and is quite concise in its explanations of each safety point. The chapter considers steps when carrying out hazard identification (HAZID) or hazard and operability (HAZOP) studies, discusses operational safety and suggests procedures to take. The case studies in this chapter go a long way towards understanding safety and its application on a practical level.

## **Chapter 3: Materials of Construction**

This chapter aids in teaching the reader the importance of proper material selection. The correct choice of material for the application will minimise risk, process failure under work and potentially unsafe conditions. It also covers the basics of properties that need to be considered when going over material selections, such as physical, volumetric, mechanical and thermal properties.

This section also encompasses common materials such as the various carbon steel alloys and stainless steel alloys with different compositions. Common causes of failure in relation to material construction are also addressed in this section as well as methods to control those failures.

## **Chapter 4: Pressure Vessels**

Due to pressure vessels being so abundant in the chemical industry for applications such as carrying out reactions, storage of fluids and heat recovery, they have been given their own chapter in this book. The chapter describes the different classifications of pressure vessels, addresses important considerations when designing pressure vessels and presents the relevant codes and standards.

## **Chapter 5: Piping Design and Pumping Systems**

Similar to pressure vessels, this book has a section specifically for this topic covering their high abundance in the chemical industry as well as the various different pipes and pumps. This chapter outlines a guide on piping, important considerations

when designing vessels as well as the codes and standards surrounding pipes and pumps.

Interestingly, in comparison to other chapters in this book, this chapter also describes simple formulations to assist with designing pipes. This has not been seen elsewhere prior to this chapter.

In terms of pump systems, there are many examples of where to use specific types of pumps and the issues and failures that can occur with them. This gives a great insight into types of pumps and their application.

## **Chapter 6: Cooling and Heating Systems**

Controlling temperature is a vital part of chemical plants and this chapter discusses the types of systems for cooling and heating that are available and appropriate. The chapter also talks about practical considerations, expected observations during operation, maintenance and specific safety procedures for this type of unit operation.

## **Chapter 7: Cogeneration of Steam and Power, Steam Traps, and Heat Exchangers**

A substantial number of chemical plants utilise steam for heating. This chapter covers efficient ways of creating steam, the drainage of condensate and the potential for recycling condensate.

There are some notes to take away in terms of safety when it comes to steam due to the amount of pressure required on certain equipment. Different steam traps and types of floats are considered and discussed and the design considerations required when commissioning steam heated equipment are described.

## **Chapter 8: Process Control and Instrumentation**

Proper control of operations is a vital part of creating a safe, efficient and sustainable working chemical plant. Proper implementation of control allows minimal breakdown, optimal product quality, effective troubleshooting and prevents damage to the organisation's reputation. This chapter addresses the process parameters that should be considered when selecting those which need monitoring. It mentions advantages of implementing process control as well as some problems with hardware.

It is important to understand the sampling systems that are required for the chemical plant and what is critical for the plant to work. Process control can

be used as a preventative measure. However, there are still limitations to process control. These are mentioned in this chapter as well as some examples.

## Chapter 9: Practical Considerations and Guidelines for Project Managers, Plant Managers and Plant Engineers

The book mentioned a lot of detail in individual chapters. This final chapter discusses scope, conditions for performance, precautions to take when considering future capacity and such things as location. These guidelines can be used by project managers, plant managers and maintenance engineers to commission instruments, equipment or process units into a plant.

This chapter although not specific to an area (Europe, Asia or the Americas) reminds the reader that there will still be regulatory requirements that each plant must adhere to depending on the permissions required for the chemical plant to run in the area where it is commissioned. In addition to statutory permissions, the chapter compiles a list of things to consider when sending out purchase orders for new equipment and what to include in the scope during the initial project management stage.

It is to note that capacity expansions need to be considered to allow the chemical plant to have a certain degree of reasonable expansion. In addition, a guide to modernising any legacy equipment is also mentioned here.

This final chapter encompasses a lot of the smaller roles such as introducing changes into a system, managing resources as well as subjects like guidelines for certain job roles in the workplace. It also includes what to look for in employees when hiring for a chemical plant.

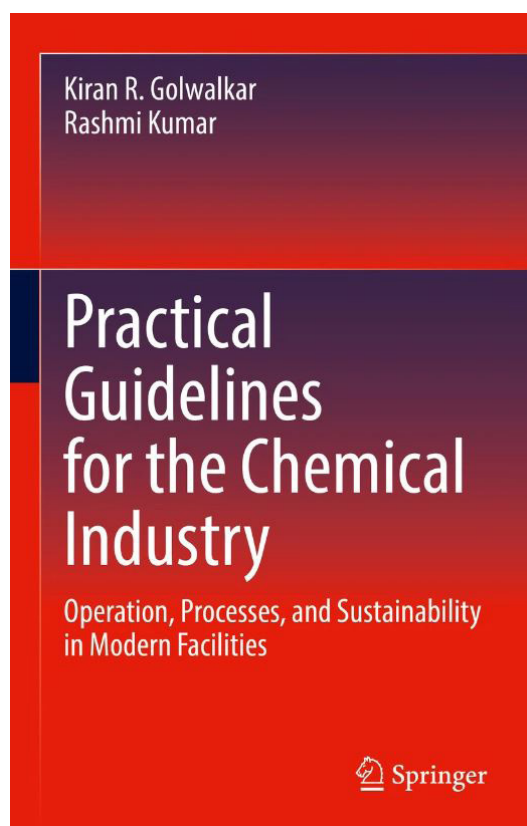
### Discussion

Most chapters give a general overview of the respective chapters with further reading as an optional extra at the end of each chapter. Although the book is labelled as practical guidelines for the chemical industry, it also includes a lot of the work required in the preparation and design steps of commissioning a plant. In my opinion, the chapters are well formatted to follow the standard order when designing a plant. However, I believe that these chapters can be further simplified into three categories: preparation (Chapters 1 and 2); specification(s) (Chapters 3, 4, 5, 6 and 7) and application (Chapters 8 and 9). This would make it a little easier to find specific information.

This book is a great resource for those who have studied chemical engineering and have just started to work in the chemical industry (early career). This is also a great read for those already in the industry who would like to understand a little more about the reasoning as to why certain things are designed the way they are (experienced employees without necessarily a chemical engineering background, but active in the chemical industry).

### Conclusion

This book is a well-structured approach to the chemical industry. It incorporates all the relevant information required to use as a guide towards preparing, commissioning and maintaining a chemical plant. As stated in the discussion, those who would benefit from this book are those who have a technical background in the chemical industry and would like to close the gap between theoretical and practical application. This is definitely a useful book to have on your shelf as a chemical engineer to reference from time to time. It will also help those who are new to the industry. I believe this is a great foundation book although additional books may still be needed to aid with actual design calculations when it comes down to the direct design work.



“Practical Guidelines for the Chemical Industry: Operation, Processes, and Sustainability in Modern Facilities”



## The Reviewer



Mahmud Juned is currently a Process Engineer at Johnson Matthey, UK. He has a BEng in Chemical Engineering from the University of Hull, UK, following which he completed his MSc in Advanced Chemical Engineering at the University of Leeds, UK. He is an associate member of the Institution of Chemical Engineers with the title AMIChemE working towards his chartership. Juned's professional career started in a technical role at Johnson Matthey before pursuing a role as a process engineer and process development engineer in the aerospace and aviation industry. He gained around three and a half years' experience in aerospace, specialising in platinum plating and ceramic vibro-polishing, before returning to Johnson Matthey.

---

## “PGM Market Report May 2023”

### A return to more balanced conditions is expected

#### Alison Cowley

Johnson Matthey, Orchard Road, Royston,  
Hertfordshire, SG8 5HE, UK

Email: [Alison.Cowley@matthey.com](mailto:Alison.Cowley@matthey.com)

#### NON-PEER REVIEWED FEATURE

Received 15th May 2023; Online 22nd June 2023

Johnson Matthey’s annual review of the platinum group metal (pgm) markets was published on 15th May 2023, providing an outlook for pgm supply and demand for 2023. The report contains a comprehensive review of developments in the automotive market, covering production and powertrain trends and their implications for pgm use as well as an update on future emissions legislation. It also features an in-depth discussion of the ruthenium and iridium markets in view of increasing interest in the use of these metals in the net zero transition.

#### Prices and Supplies

The first quarter of 2023 saw steep falls in palladium and rhodium prices (**Figure 1**). After a series of liquidity squeezes between 2019 and 2022, both markets are now returning to more normal conditions, with rhodium in a small surplus and the palladium market close to balance. In contrast, platinum is forecast to shift into a small deficit in 2023 due to greater adoption of trimetal catalysts on gasoline vehicles and robust industrial demand.

Johnson Matthey’s forecasts for all three metals show an increase in primary pgm supplies in 2023 in line with improved smelter availability in South Africa and some incremental growth at mines currently implementing expansion programmes.

Although Russian pgm output could fall, Norilsk Nickel is expected to maintain supplies by mobilising stocks of refined pgm that were not sold in 2022.

Secondary supplies should also grow modestly in line with a gradual recovery in new vehicle registrations. However, there is some downside risk to the estimates if falling palladium and rhodium prices cause scrap collectors to ‘hoard’ spent catalytic converters in the hope that their value will increase in future. Scrap flows in China fell sharply during the first quarter of 2023 due to an increase in hoarding, but activity is expected to normalise once the market adjusts to lower price levels.

#### Demand

Demand for pgms is forecast to remain relatively robust, especially for platinum which could see double-digit gains. Automotive platinum consumption should enjoy another year of strong growth, mainly due to ongoing platinum-for-palladium substitution on gasoline autocatalysts. However, rhodium use will be flat while palladium automotive demand will fall slightly, leaving total pgm consumption on vehicles only slightly higher than in 2022. While several large automotive markets will enforce tighter emissions legislation in 2023, autocatalyst pgm loadings are forecast to rise only modestly.

On the industrial front, demand in the chemicals sector is expected to remain buoyant for at least another year but a downturn in the electronics industry is currently affecting pgm use in electronic components, hard disks and display glass. Johnson Matthey’s forecasts reflect industry expectations of a recovery in the electronics sector during the second half of 2023; if this does not materialise, there could be some downside



Fig. 1. Platinum, palladium and rhodium prices

to the reported demand numbers. More broadly, the outlook for major world economies remains clouded by high inflation, elevated interest rates and increased geopolitical instability, escalating the risk that planned capacity expansions in the glass, chemical and petroleum sectors could be delayed or cancelled.

Jewellery demand, primarily for platinum, is forecast to be broadly stable in 2023. There are signs that the Chinese market could be bottoming out, but manufacturers in this region remain pessimistic about the outlook for platinum jewellery and have redeployed equipment and workers. This means there is little prospect of any material increase in Chinese jewellery demand in 2023 but there should be some growth in the US and Indian markets.

Johnson Matthey’s forecast allows for positive investment demand for both platinum and

palladium in 2023. During the first quarter of 2023, platinum benefited from a fall in yen-denominated prices which triggered renewed buying of large bars in Japan. There was also significant buying of platinum exchange traded funds (ETFs) in South Africa, where electricity shortages (and the resulting risk to mine production) encouraged a rotation out of mining equities and into underlying commodities. Palladium also saw some modest ETF buying, perhaps reflecting recent falls in the price which have created a more attractive entry point.

The ‘minor pgms’, ruthenium and iridium, are forecast to see strong growth in demand in 2023 with increased use of ruthenium in chemical catalysts (Figure 2) and growing consumption of iridium in a variety of electrochemical processes (Figure 3). Following a period of market tightness, availability is currently adequate to meet consumer

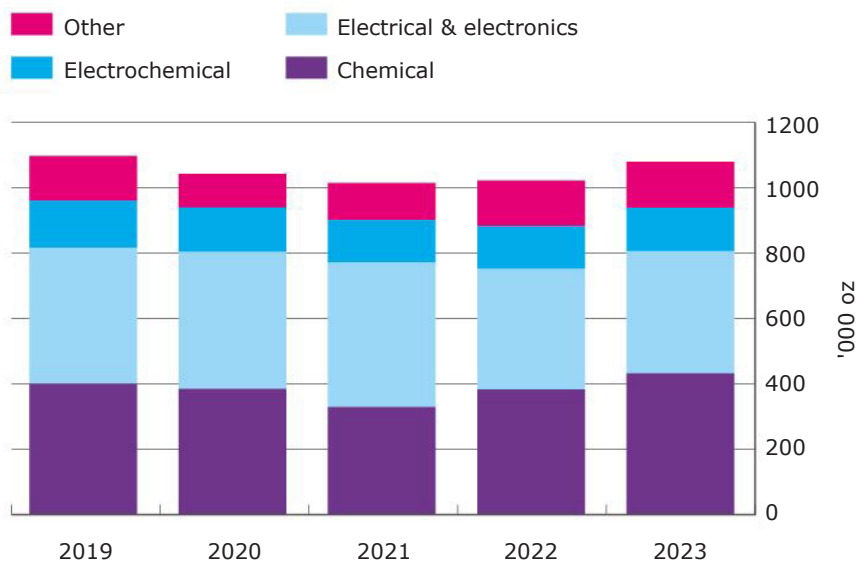


Fig. 2. Industrial demand for ruthenium

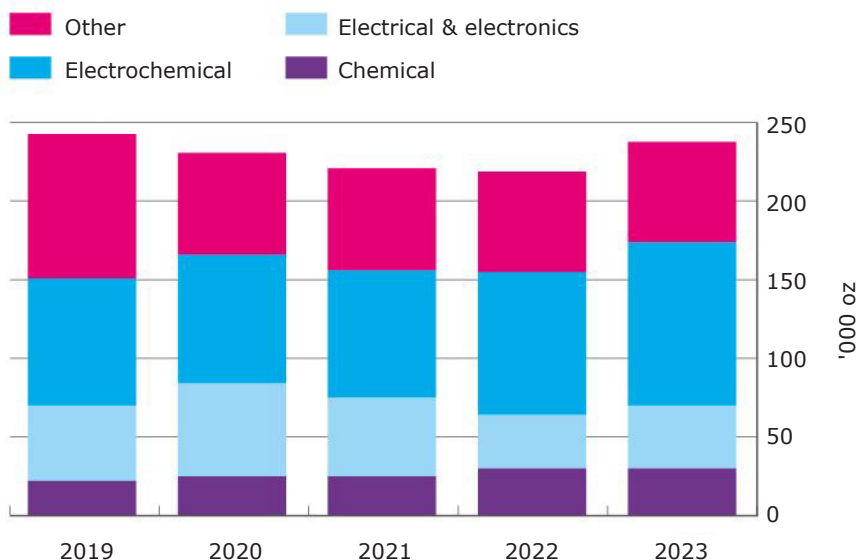


Fig. 3. Industrial demand for iridium

demand. Higher prices are stimulating efforts to minimise metal consumption *via* higher efficiencies and improved recoveries from in-process scrap. There has also been some substitution of iridium with platinum in crucibles used to grow electronic crystals.

### Summary

Overall, a return to more balanced conditions in the pgm markets is expected during 2023. While

the figures show the platinum market in a small deficit, there are ample market stocks available to meet consumer demand. For palladium and rhodium, the risk of renewed liquidity crises has receded in view of the subdued outlook for gasoline vehicle production, along with platinum-for-palladium substitution in autocatalysts and technical developments which released significant quantities of rhodium from the fibreglass industry during 2021–2022.

### The Author



Alison Cowley has worked in Johnson Matthey's Market Research department since 1990 and currently holds the post of Principal Analyst. She is Johnson Matthey's specialist on mining and supplies of the platinum group metals (pgms) and the author of the annual "PGM Market Report".

## Advertisement

# Johnson Matthey Virtual Platinum Group Metal Conference 2023

## Are platinum group metals critical to the future of sustainable technologies?

### Emma R. Schofield

Johnson Matthey, Blounts Court, Sonning Common, Reading, RG4 9NH, UK

Email: [Emma.schofield@matthey.com](mailto:Emma.schofield@matthey.com)

### NON-PEER REVIEWED FEATURE

Received 9th June 2023; Online 30th June 2023

Join us for our online conference, where we will be asking important questions about the future of platinum group metals (pgms), their contribution to technology development and the net zero transition. The conference brings together industry and academics, professional organisations and policymakers, to discuss the critical role pgms have to play in the technologies of the future.

## Agenda

### The Global Impact of Changes in PGM Supply and Demand

08:00–11:00 BST, 18th July 2023

How will the availability of pgms be affected by the net zero transition? Are pgms really the scarce metals they are often made out to be? This session offers unique insight into upcoming changes forecast in pgm markets and asks what the impacts are likely to be around the world.

### Future Applications of Rhodium and Palladium

16:00–19:00 BST, 18th July 2023

What are the new technologies that will take advantage of the increasing availability of rhodium and palladium? Global experts present their ideas in talks and a Pitch Battle.

### PGMs: A Circular Economy

08:00–11:00 BST, 19th July 2023

There's more to the circular economy of pgms than high recycling rates. Leaders in their fields talk about pgm life cycle and answer questions on the circular traceability of metals.

### PGM Technologies Enabling the Net Zero Transition

Part 1: 08:00–11:00 BST, 20th July 2023

Part 2: 16:00–19:00 BST, 20th July 2023

Explore how pgm technologies, from polymer-electrolyte membrane fuel cells to electrolyzers, are driving the energy transition and discover the associated challenges. Join in the discussion on how the availability of the critical materials pivotal to batteries and fuel cells will affect the transition to global net zero.

With excellent speakers, panellists and participants, we're expecting interesting presentations and thought-provoking discussions. For those you're unable to make, presentations will be recorded and posted on the Johnson Matthey YouTube channel following the conference. You can register for the conference on the conference website. A link is available in the online version of this feature.



**Johnson Matthey Virtual Platinum  
Group Metal Conference 2023**



## Johnson Matthey Highlights

### A selection of recent publications by Johnson Matthey R&D staff and collaborators

#### NON-PEER REVIEWED FEATURE

Received 22nd June 2023; Online 6th July 2023

#### Integration of Multi-Scale Porosimetry and Multi-Modal Imaging in the Study of Structure-Transport Relationships in Porous Catalyst Pellets

S. Mousa, V. Novak, R. S. Fletcher, M. Garcia, N. Macleod, M. Corfield and S. P. Rigby, *Chem. Eng. J.*, 2023, **452**, 139122

Batches of methanol synthesis catalyst pellets, made from various feed types, were characterised using multiscale porosimetry data and multi-modal imaging. This combined approach led to improvements in mutual interpretation. A simple random pore-bond network was used to model the impact on mass transfer of controlled modifications to the void space. Percolation analysis of overcondensation data was used to generate the characteristic parameters for the model. The method revealed the impact of different pellet fabrication parameters on tortuosity and the differential significance of certain sets of pores on mass transfer.

#### Computational Investigation of $\alpha$ -SiO<sub>2</sub> Surfaces as a Support for Pd

C. J. Lombard, C. G. C. E. van Sittert, J. N. Mugo, C. Perry and D. J. Willock, *Phys. Chem. Chem. Phys.*, 2023, **25**, (8), 6121

Dispersion-corrected DFT was used to study the interaction between palladium and periodic models of SiO<sub>2</sub> surfaces ( $\alpha$ -SiO<sub>2</sub> (001), (100) and (101)). The modelled surfaces contained isolated siloxane and silanol functional groups. The authors estimated the affinity of the surfaces towards the adsorption of palladium atoms. The model was used to calculate the geometries of the Pd<sub>1</sub>/ $\alpha$ -SiO<sub>2</sub> (*hkl*) adsorption site on each surface and to characterise the surface energies of the  $\alpha$ -SiO<sub>2</sub> (*hkl*) surfaces. Pd<sub>1</sub>(g) was predicted to

show a preference for adsorption near strained four-membered siloxane rings or on a vicinal silanol group of  $\alpha$ -SiO<sub>2</sub> (101).

#### Recognizing the Best Catalyst for a Reaction

A. Lazaridou, L. R. Smith, S. Pattisson, N. F. Dummer, J. J. Smit, P. Johnston and G. J. Hutchings, *Nat. Rev. Chem.*, 2023, **7**, (4), 287

Heterogeneous catalysis provides access to materials which impact the wellbeing of society. Therefore, improvements to catalysts are constantly needed. An issue with this is that new catalysts are often assessed under different conditions which makes determining the best catalyst difficult. To combat this, the authors used a data set based on all reactions under kinetic control to determine a set of key performance indicators (KPIs). The KPIs were normalised and plots of the normalised KPIs were used to highlight the best catalyst. This was achieved using two case studies: acetylene hydrochlorination and selective oxidation of methane to methanol.

#### Co<sub>3</sub>O<sub>4</sub>/TiO<sub>2</sub> Catalysts Studied *in situ* During the Preferential Oxidation of Carbon Monoxide: The Effect of Different TiO<sub>2</sub> Polymorphs

T. M. Nyathi, M. I. Fadlalla, N. Fischer, A. P. E. York, E. J. Olivier, E. K. Gibson, P. P. Wells and M. Claeys, *Catal. Sci. Technol.*, 2023, **13**, (7), 2038

An incipient wetness impregnation technique was used to support Co<sub>3</sub>O<sub>4</sub> nanoparticles on different TiO<sub>2</sub> polymorphs. The resulting Co<sub>3</sub>O<sub>4</sub>/TiO<sub>2</sub> catalysts were characterised *in situ* using magnetometry and PXRD. The best catalytic performance was observed when Co<sub>3</sub>O<sub>4</sub> nanoparticles were supported on P25, with 72.7% carbon monoxide conversion to CO<sub>2</sub> at 200°C and a 91.9% degree of reduction (DoR) of Co<sub>3</sub>O<sub>4</sub> to Co<sup>0</sup> at 450°C. A DoR of 85.9% was seen for the rutile-support catalyst under reaction conditions. In the rutile- and P25-supported catalysts, unwanted CH<sub>4</sub> was formed over the Co<sup>0</sup>. This was

not observed for anatase-supported catalysts. The study reveals the impact of various TiO<sub>2</sub> polymorphs on the crystal phase and chemical transformations of Co<sub>3</sub>O<sub>4</sub>.

### Catalytic, Z-Selective, Semi-Hydrogenation of Alkynes with a Zinc–Anilide Complex

G. Baker, A. White, I. Casely, D. Grainger and M. Crimmin, *ChemRxiv*, 2022, 16 pp

The authors report on the reversible activation of H<sub>2</sub> with a molecular zinc anilide complex which was investigated through DFT calculations and stoichiometric experiments. The results demonstrate that H<sub>2</sub> activation occurred with addition across the zinc–nitrogen bond *via* a four-membered transition state. At modest temperatures, the resulting zinc hydride complex was observed to be effective for the hydrozincation of C=C bonds. The hydrozincation of alkynes was faster than the equivalent alkene substrates as shown through competition experiments. The results from this study were applied to create a novel catalytic system for the semi-hydrogenation of alkynes.

### Interfacial Chemistry in the Electrocatalytic Hydrogenation of CO<sub>2</sub> over C-Supported Cu-Based Systems

D. Gianolio, M. D. Higham, M. G. Quesne, M. Aramini, R. Xu, A. I. Large, G. Held, J.-J. Velasco-Vélez, M. Haevecker, A. Knop-Gericke, C. Genovese, C. Ampelli, M. E. Schuster, S. Perathoner, G. Centi, C. R. A. Catlow and R. Arrigo, *ACS Catal.*, 2023, **13**, (9), 5876

Plane-wave DFT simulations and *operando* X-ray spectroscopic techniques were used to explain the enhanced activities of zinc-containing copper nanostructured electrocatalysts in the electrocatalytic CO<sub>2</sub> hydrogenation reaction. Zinc was shown to alloy with copper in the bulk of the nanoparticles with no metallic zinc segregated. Several surface Cu(I) ligated species were identified which responded to the potential for CO<sub>2</sub> hydrogenation. The validity of this mechanism was confirmed but the performance was shown to decline after successive applied cathodic potentials, until the hydrogen evolution reaction becomes the

main reaction pathway. DFT simulations suggest that Cu–Zn–O neighbouring atoms can activate CO<sub>2</sub> and Cu–Cu sites supply hydrogen atoms for the hydrogenation reaction.

### Transient CO Oxidation as a Versatile Technique to Investigate Cu<sup>2+</sup> Titration, Speciation and Sites Hydrolysis on Cu–CHA Catalysts: The Cu Loading Effect

U. Iacobone, I. Nova, E. Tronconi, R. Villamaina, M. P. Ruggeri, J. Collier and D. Thompsett, *Top. Catal.*, 2023, *in press*

In this study, a dry transient carbon monoxide oxidation protocol with pre-stored NH<sub>3</sub> was applied to a group of Cu–CHA catalysts with variable copper loading. Investigation found that increasing the copper content had a positive impact on CO<sub>2</sub> production. The maximum carbon monoxide conversion was predicted through analysis of the integral CO<sub>2</sub> production. Further investigation showed asymptotic titration of the total catalyst Cu<sup>2+</sup> contents in the presence of water. This work demonstrated the effectiveness and versatility of the carbon monoxide oxidation protocol as a multipurpose technique to study Cu<sup>2+</sup> ions in Cu–CHA catalysts.

### Perspectives on Current and Future Iridium Demand and Iridium Oxide Catalysts for PEM Water Electrolysis

M. Clapp, C. M. Zalitis and M. Ryan, *Catal. Today*, 2023, **420**, 114140

The future iridium demand of the global PEMWE sector was investigated and the role of different catalyst strategies for the improvement of iridium utilisation in the anode catalyst were examined. Modelling demonstrated that iridium utilisation must significantly improve by 2050 to prevent iridium supply limiting the capacity expansion. In addition, the installed capacity of iridium in 2050 could increase by ~2.7 times if closed-loop iridium recycling is realised by 2035. The authors predict that if these two conditions are achieved, global PEMWE capacity could realistically reach 1.3 TW by 2050 while using only 20% of annual global primary iridium supply (**Figure 1**).

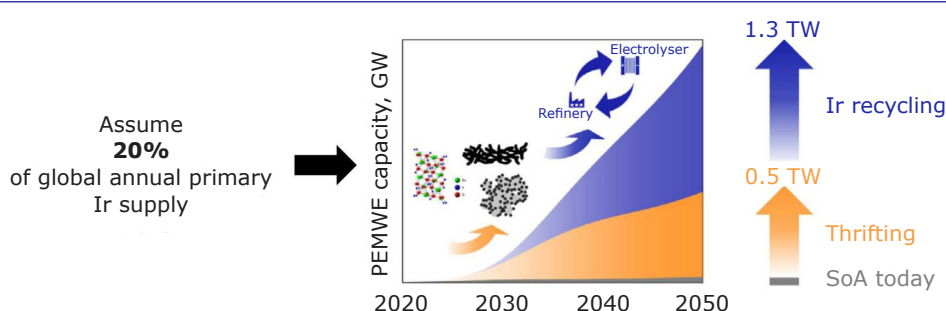


Fig. 1. Global PEMWE capacity over time. Reprinted from M. Clapp *et al.*, *Catal. Today*, 2023, **420**, 114140 under an Attribution-NonCommercial-NoDerivatives 4.0 International (CC BY-NC-ND 4.0) License

### Towards Improved Conversion of Wet Waste to Jet Fuel with Atomic Layer Deposition-Coated Hydrodeoxygenation Catalysts

W. Wilson McNeary, J. H. Miller, S. A. Tacey, J. Travis, G. D. Lahti, M. B. Griffin, K. L. Jungjohann, G. Teeter, T. Eralp Erden, C. A. Farberow, L. Tuxworth, M. J. Watson, A. A. Dameron and D. R. Vardon, *Chem. Eng. J.*, 2023, **467**, 143268

The commercialisation of wet waste-derived volatile fatty acid conversion into jet fuel-range hydrocarbons is threatened by the moderate alkane selectivity of platinum-based hydrodeoxygenation catalysts and high costs. With the aim of addressing this, ALD was utilised to apply TiO<sub>2</sub> overcoats to Pt/Al<sub>2</sub>O<sub>3</sub> catalysts. The new interface sites that this generated demonstrated a site time yield of the desirable *n*-alkane product eight times higher than an uncoated catalyst. Further calculations showed that under reducing conditions, oxygen vacancies were created at the platinum-TiO<sub>2</sub> interface for the ALD-coated catalyst. This led to increased selectivity and new Ti<sup>3+</sup> acid sites near the active metal. Results demonstrate that the utility of precious-metal catalysts can be maximised using TiO<sub>2</sub> ALD.

### Non-Carbon Greenhouse Gas Emissions for Hybrid Electric Vehicles: Three-Way Catalyst Nitrous Oxide and Ammonia Trade-Off

G. Brinklów, J. M. Herreros, S. Zeraati Rezaei, O. Doustdar, A. Tsolakis, A. Kolpin and P. Millington, *Int. J. Environ. Sci. Technol.*, 2023, *in press*

The three-way catalyst performance of a gasoline direct injection engine working under hybrid vehicle operation conditions was investigated. The abatement of both regulated and unregulated emissions was considered. Tailpipe NH<sub>3</sub> emissions were observed when the engine started while three-way catalyst temperatures were above 350°C. When the catalyst temperatures were below 150°C and the engine was started, N<sub>2</sub>O and tailpipe regulated emissions increased. This was explained due to the selectivity of NO to form NH<sub>3</sub> at higher temperatures and N<sub>2</sub>O at lower temperatures. A trade-off between regulated emissions (NH<sub>3</sub> and

N<sub>2</sub>O) was achieved by starting the engine when the three-way catalyst was within a targeted temperature range.

### Simulating Catalytic Reaction and Soot Oxidation in Coated Particulate Filters: A Simplified Modelling Framework Including Diffusion Effects

T. C. Watling, *Emiss. Control Sci. Technol.*, 2023, **9**, (2), 93

The author developed a simplified method for modelling catalysed particulate filters. The model incorporated the convection of gas through the particulate filter wall and soot cake from the inlet to the outlet channel, whilst avoiding the need to discretise in the through-wall direction. Even with the simplifications, the model revealed plausible predictions for soot oxidation and for the conversion of gaseous components. The model also included diffusion along the same axis. Diffusion through the wall was shown to be essential for NO<sub>2</sub> generated on the catalyst to be able to oxidise soot, however it had a smaller effect on the conversion of gaseous components.

### Ditopic Extractants to Separate Palladium(II) and Platinum(IV) Chloridometalates via Inner or Outer Sphere Binding

A. M. Wilson, R. A. Grant, R. J. Gordon, J. B. Love, C. A. Morrison, K. J. Macruary, G. S. Nichol and P. A. Tasker, *Solvent Extr. Ion Exch.*, 2023, **41**, (4), 401

The authors were able to recover and extract palladium and platinum from acidic chloride solutions using a single ditopic extractant (**L**). This was achieved by utilising differences in the coordination chemistries of Pt(IV) and Pd(II). For instance: the distinctions in kinetic stability of the outer-sphere assemblies [(**LH**)<sub>2</sub>·PtCl<sub>6</sub>] of Pt(IV) and the inner sphere complexes [Pd(**L**)<sub>2</sub>Cl<sub>2</sub>] of Pd(II); the dependence of rates of ligand exchange in the inner sphere on the oxidation state and coordination number; and dependence of the formation of outer-sphere complexes/assemblies of chloridometalates on their charge:radius ratios. The investigation demonstrates proof of concept for the use of ditopic reagents in platinum and palladium extraction and separation.

*Johnson Matthey Technology Review* is Johnson Matthey's international journal of research exploring science and technology in industrial applications

---

[technology.matthey.com](http://technology.matthey.com)

## Editorial team

**Editor** Sara Coles

**Editorial Assistant** Yasmin Stephens

**Senior Information Officer** Elisabeth Riley

Johnson Matthey Technology Review

Johnson Matthey Plc

Orchard Road

Royston

SG8 5HE

UK

**Tel** +44 (0)1763 253 000

**Email** [tech.review@matthey.com](mailto:tech.review@matthey.com)